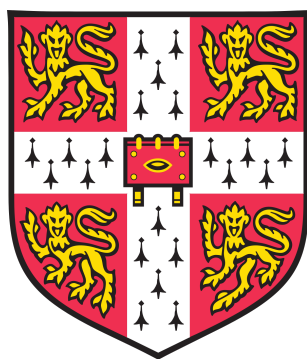

Holomorphic Hartree–Fock Theory Moving Beyond the Coulson–Fischer Point



This thesis is submitted for
the degree of
Doctor of Philosophy
March 2020

Department of Chemistry
University of Cambridge

Hugh Graham Alexander Burton
Robinson College, University of Cambridge

Declaration

This thesis describes research undertaken in the Department of Chemistry, University of Cambridge between October 2016 and March 2020 under the supervision of Dr Alex Thom. Chapters 1 and 2 provide an introduction to the topics studied in this thesis, while the remaining chapters are the result of my own work. The work in Chapters 4–8 has contributed towards the following publications:

- **Chapter 4:** H. G. A. Burton, M. Gross and A. J. W. Thom, *J. Chem. Theory Comput.* **14**, 607, (2018) — Ref. (1)
- **Chapter 5:** H. G. A. Burton, A. J. W. Thom and P.-F. Loos, *J. Chem. Theory Comput.* **15**, 4374, (2019) — Ref. (2)
- **Chapter 6:** H. G. A. Burton, A. J. W. Thom and P.-F. Loos, *J. Chem. Phys.* **150**, 041103 (2019) — Ref. (3)
- **Chapter 7:** H. G. A. Burton and A. J. W. Thom, *J. Chem. Theory Comput.* **15**, 4851, (2019) — Ref. (4)
- **Chapter 8:** H. G. A. Burton and A. J. W. Thom, (Submitted) “*Reaching Full Correlation through Nonorthogonal Configuration Interaction: A Second-Order Perturbative Approach*” — Ref. (5)

The derivation of Eq. (4.36) is the work of Prof. Mark Gross (DPMMS, University of Cambridge). The remainder of this thesis is all my own work.

This thesis is the result of my own work and includes nothing which is the outcome of work done in collaboration except as declared in the Preface and specified in the text. It is not substantially the same as any that I have submitted, or, is being concurrently submitted for a degree or diploma or other qualification at the University of Cambridge or any other University or similar institution except as declared in the Preface and specified in the text. I further state that no substantial part of my thesis has already been submitted, or, is being concurrently submitted for any such degree, diploma or other qualification at the University of Cambridge or any other University or similar institution except as declared in the Preface and specified in the text. It does not exceed the prescribed word limit for the relevant Degree Committee.

Hugh G. A. Burton

March 2020

Holomorphic Hartree–Fock Theory Moving Beyond the Coulson–Fischer Point

Hugh Graham Alexander Burton

Summary

Molecules with multiconfigurational wave functions play a key role across chemistry, including excited states, dissociating bonds, and reaction pathways. Recently, nonorthogonal configuration interaction (NOCI) using a basis of multiple Hartree–Fock (HF) states has been proposed to predict electronic energies in this type of system. However, NOCI has previously been hindered by the disappearance of HF states as the molecular structure changes, creating kinks and discontinuities in the energy. This thesis develops a new theory — holomorphic Hartree–Fock (h-HF) — to analytically extend HF states across all molecular structures. By removing the complex-conjugation of orbital coefficients from the conventional HF equations, h-HF theory forms the complex-analytic continuation of real HF theory. When real HF states disappear, their h-HF counterparts continue to exist with complex orbital coefficients and provide a continuous basis for NOCI.

To rigorously underpin h-HF theory, it is mathematically proved that every two-electron h-HF state must exist for all molecular structures. It is then shown that h-HF theory provides new insights into the nature of HF states in general. For example, enforcing particular symmetry conditions on the h-HF wave function is found to guarantee real h-HF energies even for a non-Hermitian effective Hamiltonian. Furthermore, by analytically continuing the electron–electron interaction itself into the complex plane, discrete h-HF states are shown to connect as multiple sheets of a continuous Riemann surface. These theoretical insights open entirely new avenues of research for electronic structure theory.

The guaranteed existence of h-HF states across all molecular structures now allows a general NOCI approach to be developed for computing potential energy surfaces. This NOCI approach is shown to provide a similar accuracy to state-of-the-art multireference methods for predicting static electron correlation, while requiring simpler computational optimisation. Finally, a rigorous second-order perturbative correction — NOCI-PT2 — is derived and shown to yield quantitative accuracy alongside equivalent multireference perturbation theories. Ultimately, the development of h-HF theory in this thesis allows NOCI and NOCI-PT2 to be established as quantitative approaches for predicting multireference potential energy surfaces in chemical processes.

Acknowledgements

First and foremost, I must thank Alex Thom for his continued support, supervision and guidance throughout the past four years. It has been a privilege to work alongside Alex, and I am very grateful for the opportunity.

I am also very grateful to Pierre-François Loos for his support in developing our ideas around \mathcal{PT} -symmetry and Riemann surfaces in quantum chemistry. He has been a constant source of inspiration since we started working together, and he has given me the confidence to explore new and unusual areas of electronic structure theory.

I thank Mark Gross for his support and enthusiasm in developing our ideas around algebraic geometry. I would not have achieved the rigorous mathematical proof for the number of holomorphic Hartree–Fock solutions without his expertise.

I thank Q-Chem Inc. and Evgeny Epifanovksy for inviting me to a summer internship where much of the computational code developed in this thesis was implemented. Visiting Q-Chem was a transformational step in my research career.

I thank the Thom Group: Charlie, Salvatore, Verena, Bang, David and Andreea, for their friendship, support and inspiration. I am also very grateful to the wider Theory Sector for creating such a positive environment in which to work. In particular, I thank Tom Sayer and George Trenins for many coffee breaks and lunches, and for the interesting discussions we've had across all subjects.

I acknowledge the Cambridge Trust for funding this research, and to Robinson College for providing financial support throughout.

Finally, I thank my family for their continued love and support. In particular, my parents for always inspiring me to push myself to the best of my abilities. My sisters, Clare, Joanna, Charlotte and Alice, for always being there for me and for reminding me that electronic structure theory is not always the most interesting topic of dinner conversation.

And lastly, to Rebecca for all of the fun we have together and the love she brings, and for her incredible patience as I have navigated the challenges of this PhD.

Contents

Declaration	i
Summary	iii
Acknowledgements	v
List of Figures	xiii
List of Tables	xvii
Introduction	xix
I Exposition	1
1 Overview of Electronic Structure Theory	3
1.1 Introducing Molecular Quantum Mechanics	3
1.1.1 Born–Oppenheimer Approximation	3
1.1.2 Antisymmetric Wave Functions and Slater Determinants	5
1.1.3 Operators and Matrix Elements	5
1.1.4 Projection to Finite Basis Sets	6
1.2 Hartree–Fock Theory	7
1.2.1 Fock Operator	8
1.2.2 Roothaan–Hall Equations	8
1.2.3 Electron Correlation Problem	9
1.3 Correlated Ground-State Methods	10
1.3.1 Configuration Interaction	11
1.3.2 Perturbation Theory	12
1.3.3 Coupled-Cluster Theory	15
1.4 Multireference Approaches	16
1.4.1 Multiconfigurational Self-Consistent Field	16
1.4.2 Multireference CI and CC	17

1.4.3	Multireference Perturbation Theory	18
1.5	Excited-State Methods	20
1.5.1	Configuration Interaction Singles	21
1.5.2	Equation-of-motion Coupled-Cluster	21
1.5.3	Excited-State CASSCF	22
2	Multiple HF Solutions and Nonorthogonal CI	25
2.1	Introduction	25
2.2	Multiple Hartree–Fock Solutions	26
2.2.1	Historical Overview	26
2.2.2	Symmetry in Hartree–Fock	27
2.2.3	Locating Multiple Hartree–Fock Solutions	30
2.3	Nonorthogonal Configuration Interaction	32
2.3.1	Introduction	32
2.3.2	Generating the NOCI Basis	34
2.3.3	Adding Dynamic Correlation to NOCI	36
2.3.4	Current Limitations	37
II	Development	41
3	Formulating Holomorphic Hartree–Fock	43
3.1	Context and Scope	44
3.2	Review of Prior Work	45
3.2.1	Single-Variable Hydrogen Dimer	45
3.2.2	Holomorphic Self-Consistent-Field Approach	46
3.3	Generalising Holomorphic Hartree–Fock	48
3.3.1	Complex-Analytic Hartree–Fock Energy	48
3.3.2	Holomorphic Orbital Constraint Manifold	52
3.3.3	Differential Geometry of the Holomorphic Energy	57
3.3.4	Extension to a Fundamental Theory of Hartree–Fock	61
3.4	Results and Discussion	63
3.4.1	Computational Details	63
3.4.2	Hydrogen Dimer	63
3.4.3	Links to Non-Hermitian Hartree–Fock	65
3.5	Concluding Remarks	66

4	Nature of Two-Electron Systems	69
4.1	Context and Scope	70
4.2	Overview of Algebraic Geometry	71
4.2.1	Affine Spaces	71
4.2.2	Projective Spaces	71
4.2.3	Intersection Theory	72
4.3	Enumerating Two-Electron h-RHF States	73
4.3.1	Homogenising the h-RHF Equations	73
4.3.2	Geometrically Decomposing the Constraint	74
4.3.3	Counting the h-RHF Stationary Points	77
4.3.4	Extension to h-UHF and Many-Electron Systems	80
4.3.5	Upper Bound for Real HF States	82
4.4	Results and Discussion	83
4.4.1	Computational Details	84
4.4.2	Dihydrogen Isoelectronic Sequence	85
4.4.3	Isomorphism of HHeH^{2+} and HHeH :	89
4.4.4	Double Bond Rotation of Ethene	90
4.5	Concluding Remarks	93
5	Real Energies in Holomorphic Hartree–Fock	95
5.1	Context and Scope	96
5.2	Review of \mathcal{PT} -Symmetric Hamiltonians	97
5.2.1	Spin-free \mathcal{PT} -Symmetry	97
5.2.2	Electron \mathcal{PT} -Symmetry	98
5.2.3	\mathcal{PT} -Doublet	99
5.3	\mathcal{PT} -Symmetry in Holomorphic Hartree–Fock	100
5.3.1	One-Electron Picture	102
5.3.2	Many-Electron Picture	103
5.3.3	Hartree–Fock \mathcal{PT} -Doublet	104
5.4	Extension to General Antilinear Operators	105
5.4.1	Time-Reversal Symmetry	105
5.5	Application to Hydrogen Dimer	106
5.5.1	Conditions for Real Energies	108
5.5.2	Real Orbital Coefficients	110
5.5.3	Complex Orbital Coefficients	112
5.5.4	Breaking Spatial Symmetry	115
5.6	Concluding Remarks	117
5.6.1	Scope for Future Development	118

6	Analytically Continuing the Hamiltonian	121
6.1	Context and Scope	122
6.2	Analytic Continuation of the Hubbard Model	123
6.2.1	Hubbard Dimer	123
6.2.2	Coulson–Fischer Points as Exceptional Points	127
6.2.3	Singularity in the Tight-Binding Limit	129
6.2.4	Hubbard Trimer	131
6.3	Complex Adiabatic Connection	133
6.3.1	Extension to Molecular Hamiltonians	134
6.3.2	Hydrogen Dimer	135
6.4	Concluding Remarks	136
6.4.1	Scope for Future Development	137
III	Recapitulation	139
7	General Approach for Multireference Molecules	141
7.1	Context and Scope	142
7.2	Theoretical Development	143
7.2.1	NOCI using h-HF States	143
7.2.2	Moving Past the Coulson–Fischer Point	144
7.2.3	Locating Relevant Hartree–Fock States	146
7.2.4	Combined Protocol	148
7.2.5	Algorithm Implementation	148
7.3	Results and Discussion	149
7.3.1	Computational Details	150
7.3.2	Hydrogen Dimer	150
7.3.3	Dissociation of the Fluorine Dimer	152
7.3.4	Torsional Rotation of Ethene	155
7.3.5	Distortion of Cyclobutadiene	159
7.4	Concluding Remarks	165
7.4.1	Scope for Future Development	165
8	Second-Order NOCI Perturbation Theory	169
8.1	Context and Scope	170
8.2	Theoretical Development	171
8.2.1	Prerequisites to NOCI Perturbation Theory	171
8.2.2	Defining the Reference Hamiltonian	172

8.2.3	Identifying the First-Order Interacting Space	173
8.2.4	Computing the Second-Order Energy	174
8.2.5	Intruder States and Imaginary Shifts	177
8.2.6	Algorithm Implementation	179
8.3	Results and Discussion	180
8.3.1	Computational Details	180
8.3.2	Hydrogen Dimer	180
8.3.3	Square H ₄ Symmetric Stretch	183
8.3.4	Fluorine Dimer	186
8.4	Concluding Remarks	188
8.4.1	Scope for Future Development	189
9	Concluding Remarks	193
	Appendices	197
A	Geometric Holomorphic HF Optimisation	199
B	\mathcal{T}-Symmetry for General Spins	205
C	Computing NOCI Matrix Elements	209
D	Active-Space Metadynamics	215
E	Benchmark Selected CI Calculations	219
	References	229

List of Figures

2.1	Classification of the eight HF formalisms according to the symmetries they conserve	28
3.1	Schematic comparison of the unitary and complex-orthogonal constraint surfaces	54
3.2	Topology of the h-HF energy for the hydrogen dimer	58
3.3	Energies of the h-HF solutions in minimal basis H_2	64
4.1	Decomposition of a constrained hemisphere into unconstrained affine subspaces	76
4.2	Constrained projective h-RHF energy for the minimal basis hydrogen molecule with two basis functions	78
4.3	Constrained projective h-RHF energy for the minimal basis linear H_3^+ cation with three basis functions	79
4.4	Comparison of upper bounds on the number of real RHF and UHF states	83
4.5	Bond length dependence of h-RHF and h-UHF states for the minimal basis HZ molecule	85
4.6	Evolution of h-RHF and h-UHF states in the minimal basis HZ molecule as the nuclear charge Q_Z is varied	87
4.7	Structure of RHF coalescence points in HZ forming a pitchfork bifurcation	88
4.8	Comparison of h-RHF states for $HHeH^{2+}$ and $HHeH$ in a minimal basis	89
4.9	h-RHF and h-UHF states for the double bond rotation of ethene in the minimal STO-3G basis	91
4.10	Sketch of the critical manifold of RHF coalescence points in ethene . . .	92
5.1	The h-HF energy for the multiple solutions of minimal basis H_2	107
5.2	UHF energy of H_2 illustrating \mathcal{T} - and \mathcal{PT} -symmetry for real orbital coefficients	111
5.3	Real and imaginary components of the h-RHF energy demonstrating the presence of \mathcal{PT} -symmetry for H_2	113

5.4	Real and imaginary components of the h-UHF energy demonstrating the presence of \mathcal{PT} -symmetry for H_2	114
5.5	Real and imaginary components of the h-UHF energy demonstrating the presence of \mathcal{T} -symmetry for H_2	115
5.6	Real and imaginary components of the h-RHF energy demonstrating the loss of \mathcal{PT} -symmetry in HZ.	116
5.7	Real and imaginary components of the h-UHF energy demonstrating the retention of \mathcal{T} -symmetry in HZ.	116
6.1	Holomorphic energy of the h-HF states in the Hubbard dimer for real U/t	124
6.2	Riemann surface representation of h-UHF states in the Hubbard dimer with complex U/t	126
6.3	Interconversion of symmetry-broken h-UHF states by following a path around the Coulson–Fischer point.	128
6.4	Phase rigidity of the h-UHF states in the Hubbard dimer for complex U/t , showing the singularity in the tight-binding limit.	130
6.5	h-HF energies of the h-RHF states in the two-electron periodic Hubbard trimer	131
6.6	Interconversion of h-RHF states by encircling the Coulson–Fischer point in the two-electron periodic Hubbard trimer	132
6.7	An example of a complex adiabatic connection pathway enabling the physical $\sigma_g^2 \rightarrow \sigma_u^2$ transition in H_2	135
7.1	Illustration of moving past the Coulson–Fischer point by perturbing the electron–electron interaction to complex values	146
7.2	Binding curve of the hydrogen dimer using h-HF and NOCI	151
7.3	Binding curve of the fluorine dimer using h-HF and NOCI	153
7.4	Schematic demonstrating the rotational torsion of ethene	155
7.5	Hartree–Fock and NOCI energies for the torsional rotation of ethene	156
7.6	Comparison of methods for the torsional barrier of ethene	157
7.7	Schematic demonstrating the modelled distortion of cyclobutadiene	160
7.8	Sketch of the occupied π molecular orbitals for the multiple RHF and UHF states of cyclobutadiene	161
7.9	Absolute h-HF and NOCI energies for the distortion of cyclobutadiene	162
7.10	Comparison of methods for the relative autoisomerisation barrier and first excited state of cyclobutadiene	163
8.1	NOCI-PT2 and CASPT2 energies for the hydrogen dimer	181
8.2	Assessment of NOCI-PT2 basis-set dependence for the hydrogen dimer	183

8.3	Singlet NOCI-PT2 binding curve for symmetric stretch of square H_4 . . .	184
8.4	Triplet NOCI-PT2 binding curve for symmetric stretch of square H_4 . . .	185
8.5	NOCI-PT2 binding curve for the fluorine dimer	187
E.1	Extrapolation of the selected CI variational energy for \mathcal{D}_{2h} ethene	220
E.2	Extrapolation of the selected CI variational energy for \mathcal{D}_{2d} ethene	223
E.3	Extrapolation of the selected CI variational energy for square cyclobuta- diene	226

List of Tables

3.1	Orbital coefficient constraints in real, complex, holomorphic, and fundamental HF	62
7.1	Comparison of correlation captured by multireference methods for the fluorine dimer	154
7.2	Initial geometry for ethene optimised at the RHF (cc-pVDZ) level in Angstroms.	155
7.3	Excitation energies for planar \mathcal{D}_{2h} ethene	158
7.4	Excitation energies for twisted \mathcal{D}_{2d} ethene	158
7.5	Initial geometry for cyclobutadiene optimised at the RHF (cc-pVDZ) level in Angstroms.	160
7.6	Total energy E_{tot} of the singlet ground state, and the first three vertical excitation energies for square cyclobutadiene.	164
C.1	Generalised Slater–Condon rules for evaluating nonorthogonal Hamiltonian matrix elements	213
C.2	Generalised Slater–Condon rules for evaluating nonorthogonal Fock matrix elements	213
C.3	Generalised Slater–Condon rules for evaluating nonorthogonal one-particle density matrix elements	213
E.1	Selected CI energies for the singlet states of \mathcal{D}_{2h} ethene	221
E.2	Selected CI energies for the triplet ground state of \mathcal{D}_{2h} ethene	222
E.3	Extrapolated FCI energy for the ground and excited states of \mathcal{D}_{2h} ethene	222
E.4	Selected CI energies for the singlet states of \mathcal{D}_{2d} ethene	224
E.5	Selected CI energies for the triplet ground state of \mathcal{D}_{2d} ethene	225
E.6	Extrapolated FCI energy for the ground and excited states of \mathcal{D}_{2d} ethene	225
E.7	Selected CI energies for singlet states of square cyclobutadiene	227
E.8	Selected CI energies for triplet ground state of square cyclobutadiene	228
E.9	Extrapolated FCI energy for the ground and excited states of square cyclobutadiene	228

Introduction

Theoretical and computational methods have the potential to transform chemical research. In principle, the properties and reactivity of any chemical system can be computed starting from the mathematical theory of electrons in molecules alone. For example, it is theoretically possible to predict the outcome of a chemical reaction or simulate processes such as protein folding or crystal nucleation to reveal microscopic insights that are impossible to achieve experimentally. However, while the required mathematics is well established, its exponential complexity makes it impossible to apply in practice.

A theoretical description of electrons and molecules begins in the framework of quantum mechanics. In a quantum description, the state of a system is described by a mathematical object, the ‘wave function’ Ψ , from which the probability of measuring any physical observable can be determined.⁶ Through this probabilistic view of the wave function, it is possible for an electron to be delocalised in space or in a superposition of different states. Identifying the wave function is achieved by solving the time-independent Schrödinger equation

$$\hat{H}\Psi = E\Psi$$

where \hat{H} is the so-called ‘Hamiltonian’ operator and E is the energy of the system. Crucially, the confinement of electrons in molecules restricts energies E to discrete values, representing ground and excited states with corresponding wave functions.⁶

The quantum view of electrons in molecules has been remarkably successful in explaining experimental observations such as the presence of spectral atomic emission lines or the origin of molecular bonding interactions.⁷ However, the incredible complexity of solving the Schrödinger equation means that only a single hydrogen atom can be solved exactly.⁶ Instead, theoretical chemists have turned their attention to developing a series of approximate methods to describe electronic and molecular quantum mechanics.⁸ At the most fundamental level, the Born–Oppenheimer approximation⁹ assumes that electrons respond instantaneously to nuclear motion, leading to the concept of an electronic potential energy surface.

The simplest approach to predicting the electronic potential energy surface is Hartree–

Fock (HF) theory.¹⁰ In the HF approach, the wave function is built from an antisymmetrised product of single-electron wave functions, known as molecular orbitals, and the electron repulsion is treated at the mean-field level where electronic motion is uncorrelated.⁸ Despite this mean-field approximation, HF theory has been widely applied as a computational tool and generally allows the calculation of ground-state energies to around 1% of the exact result.⁸ However, the remaining energy associated with correlated electronic motion is essential if chemically meaningful calculations are to be performed with comparable accuracy to experimental results.

The explosion of computational power and resources has seen the implementation of many approximate methods for predicting the electronic structure of molecules. In particular, the ability to perform ever larger calculations has enabled the development of many post-HF techniques to compute correlated electronic energies.¹¹ The most prominent methods include Møller–Plesset perturbation theory,¹² configuration interaction¹³ (CI) and coupled-cluster^{14–16} (CC). The accuracy and black-box nature of these methods for computing the ground state equilibrium energy of molecules has encouraged their widespread use for chemical systems

Despite the success of these computational methods, their accuracy often deteriorates away from the ground state equilibrium structure, limiting the ability to compute full molecular potential energy surfaces. In particular, many approximate methods break down if a molecule experiences competing electronic configurations, for example when a bond breaks during a chemical reaction. The primary cause of this breakdown is that a single HF wave function no longer provides a sufficiently accurate reference state for correlated post-HF methods.¹⁷ The most common solution is to use a ‘multireference’ approximation, of which the complete active space self-consistent-field (CASSCF) approach is by far the most popular.^{18,19} However, the practicality of CASSCF is limited by a high level of complexity in optimising the wave function, and the need for significant user knowledge and chemical intuition.

Alternatively, when multiple dominant configurations appear in the exact wave function, these configurations are reflected as additional stationary solutions to the HF equations.²⁰ In fact, the self-consistency of the HF equations allows many stationary HF states to be identified that are each built from a bespoke set of molecular orbitals.^{20–23} For example, in the hydrogen dimer, the ground HF state at equilibrium resembles the bonding σ_g^2 configuration, while stretching the bond lengths leads to an additional solution of lower energy where the electrons localise on opposite atoms to form a ‘diradical’ configuration.²⁴ Multiple HF states can therefore provide a natural description of multi-configurational systems,²⁵ while higher energy HF solutions are widely considered as mean-field approximations to excited states.^{26–30}

To exploit the HF description of competing electron configurations, recent research has focussed on constructing a linear combination of multiple HF solutions in a nonorthogonal configuration interaction (NOCI) expansion.^{25,31,32} In this approach, each HF state provides a mean-field description of each dominant configuration, allowing NOCI to successfully reproduce conical interactions, avoided crossings²⁵ and electron transfer processes.³³ Furthermore, since excited HF states are individually optimised, their inclusion in NOCI provides a promising approach for multi-electron excited states³¹ and core excitations.^{34,35}

Despite significant progress in the development of NOCI, its application to computing potential energy surfaces and reaction trajectories has been limited by the disappearance of HF states as the molecular structure changes.²⁵ While the self-consistency of the HF equations permits a number of solutions, there is no guarantee that these must exist for all molecular structures. The disappearance of the ‘diradical’ state in H₂ at the so-called ‘Coulson–Fischer’ point²⁴ is the prime example of this feature. In turn, the disappearance of HF states causes a sudden change in the size of the NOCI expansion that results in unphysical kinks and discontinuities in the energy.²⁵

To extend HF states across all molecular structures, Thom and Head-Gordon initially suggested that the HF stationary states may need to be located in the complex plane.²⁵ However, it is known that solutions to the complex HF equations are also not guaranteed to exist for all structures, and indeed additional complex HF states can emerge for structures with multireference character.^{36,37} In this thesis, a new approach is derived — holomorphic HF (h-HF) theory — where the HF equations are modified to ensure that every state exists across all geometries. Although proof-of-principle demonstrations of h-HF theory have previously been reported,^{38,39} little is understood about the general nature of h-HF solutions and no computational procedure exists for locating h-HF stationary states in larger molecules or combining them with NOCI.

The aim of this thesis is therefore to develop h-HF theory into a practical approach that allows smooth and continuous NOCI energy surfaces to be computed across all molecular geometries. To achieve this, a general h-HF formalism is derived by removing the complex conjugation of orbital coefficients from the real HF equations to create a complex-analytic function. The resulting h-HF equations then provide the complex-analytic continuation of the real HF equation and holomorphic self-consistent field (SCF) procedures can be defined to locate stationary states of the h-HF energy. Crucially, when real HF states disappear as the molecular structure changes, their h-HF counterparts are found to continue with complex orbital coefficients, providing a continuous basis for NOCI.

To rigorously underpin h-HF theory, it is mathematically proved that every two-

electron h-HF state must exist for all molecular structures. By forming the complex-analytic extension of real HF theory, h-HF is shown to provide new insights into the general nature of the wider HF approximation. For example, although the h-HF equations are inherently non-Hermitian, enforcing particular symmetry conditions on the h-HF wave function is found to guarantee real h-HF energies. These new symmetries provide alternative requirements to Hermiticity for ensuring real-valued energies in electronic structure theory. Furthermore, by analytically continuing the electron-electron interaction into the complex plane, multiple discrete h-HF states are shown to be connected as multiple sheets of a continuous Riemann surface. The conceptual unification of multiple h-HF energy levels in this way allows a ground-state wave function to be naturally evolved into an excited-state wave function along a ‘complex adiabatic connection’.

The guaranteed existence of h-HF states is then used to extend NOCI across all molecular structures. This is achieved by defining a general computational protocol for locating chemically relevant real HF states, identifying their h-HF counterparts across all molecular structures, and combining these states in a NOCI expansion. It is shown that this NOCI approach allows complete multireference potential energy surfaces to be computed for molecular dissociation and reaction barriers. Furthermore, the accuracy of NOCI is found to provide a promising alternative to CASSCF while avoiding the computationally challenging optimisation of the CASSCF wave function.

Finally, a rigorous perturbative correction to the NOCI wave function is derived to account for the remaining electron correlation. This NOCI-PT2 theory yields a similar degree of accuracy to existing multireference perturbation theories for typical chemical systems. By introducing NOCI-PT2 on top of the general NOCI procedure, this thesis now establishes the complete NOCI framework as a quantitative approach for predicting multiconfigurational potential energy surfaces. Ultimately, the derivation and development of h-HF theory in this thesis lays the foundations for using NOCI wave functions to predict electronic energies in chemical systems.

This thesis is structured in three parts. Part I provides an overview of the relevant background theory discussed throughout this thesis. In Part II, the h-HF approach is derived and its theoretical implications for the general nature of multiple HF states are explored. Part III then combines h-HF theory with NOCI and develops the NOCI-PT2 correction to establish a general multireference approach for computing smooth energy surfaces across all molecular structures.

Part I

Exposition

Chapter 1

Overview of Electronic Structure Theory

1.1 Introducing Molecular Quantum Mechanics

A quantum mechanical description of molecular systems starts with the time-independent Schrödinger equation⁸

$$\hat{H}\Psi(\mathbf{R}_1, \dots, \mathbf{R}_M, \mathbf{r}_1, \dots, \mathbf{r}_N) = E\Psi(\mathbf{R}_1, \dots, \mathbf{R}_M, \mathbf{r}_1, \dots, \mathbf{r}_N). \quad (1.1)$$

Here \hat{H} represents the Hamiltonian operator, the eigenvalue E is the total energy of the system and the eigenfunction Ψ is the total wave function in terms of the M nuclear positions \mathbf{R}_A and N electron positions \mathbf{r}_i .

Throughout this thesis only the non-relativistic description of quantum mechanics is considered, using atomic units unless otherwise stated. The molecular Hamiltonian therefore incorporates only the kinetic energy and Coulomb interaction of the nuclei and electrons, given by⁸

$$\hat{H} = - \sum_{A=1}^M \frac{1}{2m_A} \nabla_A^2 - \sum_{i=1}^N \frac{1}{2} \nabla_i^2 + \sum_{A<B}^M \frac{Z_A Z_B}{R_{AB}} - \sum_{i=1}^N \sum_{A=1}^M \frac{Z_A}{r_{iA}} + \sum_{i<j}^N \frac{1}{r_{ij}}, \quad (1.2)$$

where m_A (Z_A) is the mass (charge) of nucleus A , $R_{AB} = |\mathbf{R}_A - \mathbf{R}_B|$ is the distance between nuclei A and B , $r_{iA} = |\mathbf{r}_i - \mathbf{R}_A|$ is the distance between electron i and nucleus A , and $r_{ij} = |\mathbf{r}_i - \mathbf{r}_j|$ is the distance between electrons i and j .

In principle, if the exact wave function satisfying the time-independent Schrödinger equation can be identified, then all properties of the molecular system can be computed. However, solving Eq. (1.1) is practically impossible for anything beyond a single hydrogen atom, and a series of electronic structure approximations must be introduced.⁸

1.1.1 Born–Oppenheimer Approximation

The first level of approximation is the Born–Oppenheimer approximation,⁹ where the lighter relative mass of electrons compared to nuclei allows one to assume that electrons

spatially rearrange instantaneously in response to a change in nuclear positions. As a result, the total wave function can then be decomposed into the product of a nuclear wave function $\Psi_n(\mathbf{R}_1, \dots, \mathbf{R}_M)$ and an electronic wave function $\Psi_e(r_1, \dots, r_N; \mathbf{R}_1, \dots, \mathbf{R}_M)$ which depends parametrically on the nuclear positions, giving

$$\Psi(r_1, \dots, r_N, \mathbf{R}_1, \dots, \mathbf{R}_M) = \Psi_e(r_1, \dots, r_N; \mathbf{R}_1, \dots, \mathbf{R}_M) \Psi_n(\mathbf{R}_1, \dots, \mathbf{R}_M). \quad (1.3)$$

Substituting Eq. (1.3) into Eq. (1.1) using the Hamiltonian (1.2) leads to

$$\begin{aligned} E\Psi_n\Psi_e = & -\sum_A^M \frac{1}{2m_A} \Psi_e \nabla_A^2 \Psi_n - \sum_i^N \frac{1}{2} \Psi_n \nabla_i^2 \Psi_e \\ & + \sum_A^M \left[\Psi_n \nabla_A^2 \Psi_e + 2(\nabla_A \Psi_n) \cdot (\nabla_A \Psi_e) \right] \\ & + \left[\sum_{A<B}^M \frac{Z_A Z_B}{R_{AB}} + \sum_{i<j}^N \frac{1}{r_{ij}} - \sum_A^M \sum_i^N \frac{Z_A}{r_{iA}} \right] \Psi_n \Psi_e. \end{aligned} \quad (1.4)$$

Applying the Born–Oppenheimer approximation then involves ignoring terms involving any derivatives of Ψ_e with respect to the nuclear positions, specifically those on line 2 of Eq. (1.4). The resulting expression is now separable, and each arrangement of nuclear positions leads to the electronic Schrödinger equation

$$E_e(\mathbf{R}_1, \dots, \mathbf{R}_M) \Psi_e = \left[-\sum_i^N \frac{1}{2} \nabla_i^2 + \sum_{i<j}^N \frac{1}{r_{ij}} - \sum_A^M \sum_i^N \frac{Z_A}{r_{iA}} + V_N(\mathbf{R}_1, \dots, \mathbf{R}_M) \right] \Psi_e, \quad (1.5)$$

where $V_N(\mathbf{R}_1, \dots, \mathbf{R}_M)$ is the nuclear repulsion energy. This definition of the electronic energy E_e as a function of the nuclear positions is the central idea behind the concept of molecular potential energy surfaces in chemistry. Finally, the nuclear Schrödinger equation completes the Born–Oppenheimer approximation,

$$E\Psi_n\Psi_e = \left[-\sum_A^M \frac{1}{2m_A} \nabla_A^2 + E_e(\mathbf{R}_1, \dots, \mathbf{R}_M) \right] \Psi_n \Psi_e. \quad (1.6)$$

For the majority of chemistry, the Born–Oppenheimer approximation performs remarkably well and the molecular systems considered in this thesis will always remain within this approximation. Henceforth, only Eq. (1.5) is considered, dropping the ‘e’ subscript throughout and defining the electronic Hamiltonian as

$$\hat{H} = -\sum_i^N \frac{1}{2} \nabla_i^2 - \sum_A^M \sum_i^N \frac{Z_A}{r_{iA}} + \sum_{i<j}^N \frac{1}{r_{ij}} + V_N, \quad (1.7)$$

where all dependence on the nuclear positions becomes implicit.

1.1.2 Antisymmetric Wave Functions and Slater Determinants

In the absence of a magnetic field, the electronic Hamiltonian \hat{H} depends on only the electronic spatial coordinates. However, the wave function must also take into account the spin-angular momentum of electrons. To achieve this, an additional spin-coordinate σ is introduced that defines the component of the spin-angular momentum around a given axis. The complete set of electronic coordinates $\mathbf{x} = (\mathbf{r}, \sigma)$ then represents the tensor product space $\mathbb{R} \otimes \Omega$, where $\Omega = \{\alpha, \beta\}$ represents the space for particles with the total spin-angular momentum quantum number $S = \frac{1}{2}$.

Since electrons are fermionic particles, the Pauli exclusion principle dictates that the many-electron wave function must be antisymmetric with respect to the permutation of two electrons, i.e.

$$\Psi(\mathbf{x}_1, \dots, \mathbf{x}_i, \dots, \mathbf{x}_j, \dots, \mathbf{x}_N) = -\Psi(\mathbf{x}_1, \dots, \mathbf{x}_j, \dots, \mathbf{x}_i, \dots, \mathbf{x}_N). \quad (1.8)$$

Although a range of wave function structures are used,¹¹ the simplest way to satisfy this constraint is to build Ψ as a single ‘Slater’ determinant

$$\Psi(\mathbf{x}_1, \dots, \mathbf{x}_N) = \frac{1}{\sqrt{N!}} \begin{vmatrix} \psi_1(\mathbf{x}_1) & \psi_1(\mathbf{x}_2) & \cdots & \psi_1(\mathbf{x}_N) \\ \psi_2(\mathbf{x}_1) & \psi_2(\mathbf{x}_2) & \cdots & \psi_2(\mathbf{x}_N) \\ \vdots & \vdots & \ddots & \vdots \\ \psi_N(\mathbf{x}_1) & \psi_N(\mathbf{x}_2) & \cdots & \psi_N(\mathbf{x}_N) \end{vmatrix}, \quad (1.9)$$

where ψ_i are single-electron molecular spin-orbitals and the wave function antisymmetry arises clearly from the mathematical properties of determinants.⁸ Slater determinants provide the building blocks from which a wide range of wave function *ansätze* are built and will be widely employed throughout this thesis.

1.1.3 Operators and Matrix Elements

If the exact wave function is known, the value of *any* physical observable can be obtained as the eigenvalue of the associated operator \hat{O} . However, approximate wave functions require the evaluation of an observable’s expectation value

$$\langle \hat{O} \rangle = \frac{\langle \Psi | \hat{O} | \Psi \rangle}{\langle \Psi | \Psi \rangle} \quad (1.10)$$

where the ‘braket’ notation is defined using the inner product

$$\langle \Psi | \hat{O} | \Psi \rangle = \int \Psi^*(\mathbf{x}_1, \dots, \mathbf{x}_N) \hat{O} \Psi(\mathbf{x}_1, \dots, \mathbf{x}_N) \, d\mathbf{x}_1 \cdots d\mathbf{x}_N \quad (1.11a)$$

$$\langle \Psi | \Psi \rangle = \int \Psi^*(\mathbf{x}_1, \dots, \mathbf{x}_N) \Psi(\mathbf{x}_1, \dots, \mathbf{x}_N) \, d\mathbf{x}_1 \cdots d\mathbf{x}_N \quad (1.11b)$$

Most operators in electronic structure theory involve only one-electron $\hat{O}_1(i)$ terms depending on electron i and two-electron $\hat{O}_2(i, j)$ terms involving electrons i and j as

$$\hat{O} = \sum_i^N \hat{O}_1(i) + \sum_{i<j}^N \hat{O}_2(i, j). \quad (1.12)$$

Using the Slater–Condon rules,⁴⁰ the expectation value for a single Slater determinant can then be evaluated in terms of the orthogonal single-particle spin-orbitals as

$$\langle \hat{O} \rangle = \sum_i^N \langle \psi_i | \hat{O}_1 | \psi_i \rangle + \sum_{i<j}^N \left[\langle \psi_i \psi_j | \hat{O}_2 | \psi_i \psi_j \rangle - \langle \psi_i \psi_j | \hat{O}_2 | \psi_j \psi_i \rangle \right], \quad (1.13)$$

where the general notation for one- and two-electron integrals is introduced as

$$\langle \psi_i | \hat{O}_1 | \psi_j \rangle = \int \psi_i^*(\mathbf{x}_1) \hat{O}_1 \psi_j(\mathbf{x}_1) \, d\mathbf{x}_1 \quad (1.14a)$$

$$\langle \psi_i \psi_j | \hat{O}_2 | \psi_k \psi_l \rangle = \int \psi_i^*(\mathbf{x}_1) \psi_j^*(\mathbf{x}_2) \hat{O}_2 \psi_k(\mathbf{x}_1) \psi_l(\mathbf{x}_2) \, d\mathbf{x}_1 d\mathbf{x}_2 \quad (1.14b)$$

Considering the set of spin-orbitals as a basis, these terms can be represented as matrix elements $[\mathbf{O}_1]_{ij} = \langle \psi_i | \hat{O}_1 | \psi_j \rangle$ or components of a four-tensor $[\mathbf{O}_2]_{ijkl} = \langle \psi_i \psi_j | \hat{O}_2 | \psi_k \psi_l \rangle$.

The Hamiltonian \hat{H} is a typical example of an operator constructed from one- and two-electron operators, given by

$$\hat{H} = V_N + \sum_i^N \hat{h}(i) + \sum_{i<j}^N r_{ij}^{-1}, \quad (1.15)$$

where

$$\hat{h}(i) = -\frac{1}{2} \nabla_i^2 - \sum_A^M \sum_i^N \frac{Z_A}{r_{iA}}. \quad (1.16)$$

Expectation values of \hat{H} appear throughout electronic structure theory and the notation is usually simplified to

$$h_{ij} = \langle \psi_i | \hat{h}(1) | \psi_j \rangle \quad (1.17a)$$

$$\langle ij | kl \rangle = \langle \psi_i \psi_j | r_{12}^{-1} | \psi_k \psi_l \rangle, \quad (1.17b)$$

defining the one-electron and two-electron integrals used throughout this thesis. In addition, it is often convenient to introduce the anti-symmetrised two-electron integrals defined as

$$\langle ij || ij \rangle = \langle ij | ij \rangle - \langle ij | ji \rangle. \quad (1.18)$$

1.1.4 Projection to Finite Basis Sets

Expressions involving the many-electron molecular wave function Ψ are usually evaluated by projecting the single-electron orbitals into a finite-sized set of basis functions.

Most commonly used is a $2n$ -dimensional spin-orbital basis $\{\eta\} = \{\chi\} \otimes \{\alpha, \beta\}$ constructed as the product space of n spatial basis functions $\{\chi(\mathbf{r})\}$ and the two-component spin basis $\{\alpha(\sigma), \beta(\sigma)\}$. Each orbital can then be expanded as

$$\psi_i(\mathbf{x}) = \sum_{\mu}^{2n} \eta_{\mu}(\mathbf{x}) C_{i,\mu}^{\mu}. \quad (1.19)$$

Here the non-orthogonal tensor notation of Head–Gordon *et al.* is introduced⁴¹ with the metric tensor $S_{\mu\nu} = \langle \eta_{\mu} | \eta_{\nu} \rangle$ representing the overlap of the basis functions.

The most physically intuitive basis in which molecular electronic wave functions can be expanded is the set of atomic orbitals (AO) for each constituent atom. While the exact wave function can be expressed in a infinite basis that includes every AO — the complete basis set (CBS) limit — this cannot be computationally solved in practice. Instead, the electronic structure problem is usually projected into a truncated basis where only a subset of AOs are considered.⁸ The use of a truncated basis then allows wave functions and operators to be expressed through the framework of linear algebra.⁴² As a result, an ‘exact’ electronic energy can be evaluated within a given basis set, although the ‘true’ energy corresponds to the CBS limit.

Evaluating the one- and two-electron integrals required for electronic structure methods using physical ‘Slater’ orbitals is expensive for practical methods.⁸ Instead, these basis functions are usually approximated by taking a linear combination of Gaussian functions that are fitted to more accurate AOs.¹¹ The favourable properties of Gaussian functions then greatly simplifies the evaluation of the required electron integrals. Although a wide range of approximate basis functions have been developed, this thesis considers primarily the ‘minimal’ STO-3G basis set,⁴³ Pople’s basis sets,⁴⁴ and Dunning’s more advanced correlation-consistent basis sets.⁴⁵

1.2 Hartree–Fock Theory

Hartree–Fock (HF) theory is among the simplest methods in electronic structure theory, providing a mean-field description of the electronic energy.⁸ For a system of N electrons, the HF wave function is represented by a single Slater determinant constructed from a set of single-electron orbitals $\{\psi_i(\mathbf{x})\}$ as given in Eq. (1.9). Through the variational principle, the optimal set of spin-orbitals are those which minimise the expectation value of the energy, defining the HF energy⁴²

$$E_{\text{HF}} = \frac{\langle \Psi_{\text{HF}} | \hat{H} | \Psi_{\text{HF}} \rangle}{\langle \Psi_{\text{HF}} | \Psi_{\text{HF}} \rangle} = V_{\text{N}} + \sum_i^N h_{ii} + \sum_{i<j}^N \langle ij || ij \rangle. \quad (1.20)$$

1.2.1 Fock Operator

Optimising E_{HF} through the variational principle leads to the simultaneous eigenvalue equations known simply as the ‘‘Hartree–Fock’’ equations:⁸

$$\hat{F}\psi_i = \epsilon_i\psi_i. \quad i = 1, 2, \dots, N, \quad (1.21)$$

The single-particle eigenvalues ϵ_i define the molecular-orbital energies which, through Koopman’s theorem, can be interpreted as ionisation energies and electron affinities.⁸ Here the single-particle Fock operator has been introduced as

$$\hat{F}(\mathbf{x}_i) = \hat{h}(\mathbf{x}_i) + \sum_{j \neq i}^N \left(\hat{J}_j(\mathbf{x}_i) - \hat{K}_j(\mathbf{x}_i) \right), \quad (1.22)$$

where $\hat{J}_j(\mathbf{x}_1)$ and $\hat{K}_j(\mathbf{x}_1)$ define the Coulomb and exchange operators respectively

$$\hat{J}_j(\mathbf{x}_1)\psi_i(\mathbf{x}_1) = \psi_i(\mathbf{x}_1) \int \psi_j^*(\mathbf{x}_2) \frac{1}{r_{12}} \psi_j(\mathbf{x}_2) d\mathbf{x}_2, \quad (1.23a)$$

$$\hat{K}_j(\mathbf{x}_1)\psi_i(\mathbf{x}_1) = \psi_j(\mathbf{x}_1) \int \psi_j^*(\mathbf{x}_2) \frac{1}{r_{12}} \psi_i(\mathbf{x}_2) d\mathbf{x}_2. \quad (1.23b)$$

The contribution from the Coulomb operator can be classically interpreted as the spatially-averaged repulsion of an electron in ψ_i to every other electron. In contrast, the exchange contribution has no classical analogue and arises explicitly from the Pauli antisymmetry of the wave function.

Since Eq. (1.23a) and Eq. (1.23b) cancel each other when $i = j$, the summation restriction in Eq. (1.22) can be lifted to define a single Fock operator

$$\hat{F} = \hat{h} + \sum_k^N (\hat{J}_k - \hat{K}_k). \quad (1.24)$$

Expanding this expression in the molecular-orbital basis leads to the matrix element representation of the Fock operator

$$F_{ij} = h_{ij} + \sum_k^N \langle ik || jk \rangle. \quad (1.25)$$

Comparing Eq. (1.21) and Eq. (1.25) shows that the optimal set of orbitals are those which diagonalise the self-consistent Fock matrix built using the same orbitals. The HF approach can therefore be considered as a self-consistent single-particle description of electronic structure.

1.2.2 Roothaan–Hall Equations

In principle, the solutions to Eq. (1.21) provide the *exact* HF spin orbitals. However, the self-consistency of the Fock operator makes directly solving Eq. (1.21) impossible

for anything but a single atom. In practice these equations are solved by projecting the molecular orbitals into a finite basis set using Eq. (1.19). The only constraint on the orbital coefficients $C_{i\cdot}^{\mu\cdot}$ is that they satisfy the unitary normalisation constraint

$$\delta_{ij} = \langle \psi_i | \psi_j \rangle = \sum_{\mu\nu}^{2n} (C^*)_{i\cdot}^{\mu\cdot} S_{\mu\nu} C_{j\cdot}^{\nu\cdot}. \quad (1.26)$$

Representing the Fock matrix in this basis, the Hartree–Fock equations (1.21) can be expanded to give the Roothaan–Hall equations^{46,47} as

$$\sum_{\nu}^{2n} F_{\mu\nu} C_{i\cdot}^{\nu\cdot} = \sum_{\nu}^{2n} S_{\mu\nu} C_{i\cdot}^{\nu\cdot} \epsilon_i \quad (1.27)$$

where

$$F_{\mu\nu} = h_{\mu\nu} + \sum_{\sigma\tau}^{2n} \langle \mu\sigma || \nu\tau \rangle P^{\tau\sigma}, \quad (1.28)$$

and the one-particle density matrix $P^{\tau\sigma}$ has been introduced as

$$P^{\tau\sigma} = \sum_{i=1}^N C_{i\cdot}^{\tau\cdot} (C^*)_{i\cdot}^{\sigma\cdot}. \quad (1.29)$$

Although Eq. (1.27) appears to be a simple eigenvalue equation, the dependence of the Fock matrix on the density matrix, and in turn the orbital coefficients, means that this equation is non-linear and cannot be simply diagonalised. Instead, the optimal set of orbitals are identified using the iterative self-consistent field (SCF) approach as follows:

1. Begin with an initial set of coefficients $C_{i\cdot}^{\mu\cdot}$;
2. Evaluate the Fock matrix using Eq. (1.28);
3. Generate a new set of orbital coefficients from the eigenvectors of the Fock matrix;
4. Repeat steps 2–3 until self-consistency is reached.

The final optimised coefficients then represent the HF orbitals and are simultaneous eigenvectors of both the density matrix and the corresponding Fock matrix.

1.2.3 Electron Correlation Problem

Electron interactions in the HF approximation are only considered at the mean-field level, where each electron experiences a spatially-averaged repulsion from all other electrons. Therefore, although the HF energy accounts for a large portion of the true electronic energy, it is not exact.⁸ While same-spin electrons are correlated through the Pauli antisymmetry of a Slater determinant, electrons with opposite spins are completely uncorrelated under the HF approximation. This lack of correlation arises because the

single Slater determinant wave function includes no terms that account for the relative position of two electrons.⁸ The remaining ‘correlation’ energy represents the difference between the exact energy and the HF energy,⁴⁸ defined in a finite or infinite basis set as

$$E_{\text{corr}} = E_{\text{exact}} - E_{\text{HF}}. \quad (1.30)$$

Computing the correlation energy is the the central goal of most electronic structure techniques.

Electron correlation beyond the HF description can be broadly decomposed into two classifications. The first, *dynamic correlation*, accounts primarily for the instantaneous repulsion between electrons.¹¹ In this case the single determinant HF wave function provides a good approximate representation of the exact wave function. Much of the remaining error in the energy is associated with the failure of HF to describe the electron cusp in the exact wave function that occurs when the positions of two electrons converge. Correcting this cusp is challenging, although much of the dynamic correlation can be recovered using perturbation theory or other post-HF methods that build upon a single Slater determinant.¹¹ Furthermore, a complete description of dynamic correlation is known to converge slowly with the size of the underlying basis set.

In contrast, static correlation is associated with the qualitative breakdown of the single determinant wave function *ansatz*.¹¹ Static correlation effects become dominant in the presence of competing electron configurations, for example when the bonding and antibonding configurations become degenerate in the dissociation of the hydrogen dimer. These closely separated electron configurations can then interact strongly to significantly lower the energy below the single determinant energy. Accounting for static correlation requires the introduction of alternative wave function forms constructed as a combination of multiple determinants.¹¹

1.3 Correlated Ground-State Methods

For a given finite basis set, the exact wave function can be expanded as a combination of determinants built from every possible configuration of electrons in a set of orbitals. Usually the HF wave function is used to define a reference wave function $|\Psi_0\rangle$ with occupied orbitals (indexed by i, j, k , etc) and unoccupied virtual orbitals (indexed by a, b, c , etc). The full set of possible determinants, defining a Hilbert space,¹¹ is then given in terms of ‘excitations’ or ‘replacements’ from this reference wave function, e.g.

$$|\Psi_i^a\rangle = \hat{\tau}_i^a |\Psi\rangle. \quad (1.31)$$

Here $|\Psi_i^a\rangle$ represents a singly-excited Slater determinant with the occupied orbital i replaced by the virtual orbital a through the excitation operator $\hat{\tau}_i^a$. Analogous excitations

involving more electrons can be constructed to define a hierarchy of single, double, triple, and higher excitations. Through various combinations of these determinants, a range of post-HF methods have been developed to compute the remaining electronic correlation energy.

1.3.1 Configuration Interaction

Among the first correlated methods was the configuration interaction (CI) approach,¹³ where the wave function is built as a linear combination of Slater determinants as

$$|\Psi_{\text{FCI}}\rangle = |\Psi_0\rangle + \sum_{ia} c_i^a |\Psi_i^a\rangle + \sum_{\substack{i<j \\ a<b}} c_{ij}^{ab} |\Psi_{ij}^{ab}\rangle + \sum_{\substack{i<j<k \\ a<b<c}} c_{ijk}^{abc} |\Psi_{ijk}^{abc}\rangle + \dots \quad (1.32)$$

Including all excitations in a full CI (FCI) expansion provides the best approximation to the exact energy in a given basis. In practice, the FCI energy and wave function are identified by diagonalising the Hamiltonian matrix built in the basis of Slater determinants. However, the number of possible determinants grows rapidly with the size of the system, given for n spatial basis functions, N_α spin-up (α) electrons and N_β spin-down (β) electrons as

$$n_{\text{det}} = \binom{n}{N_\alpha} \binom{n}{N_\beta}. \quad (1.33)$$

Exact diagonalisation of the FCI Hamiltonian matrix is therefore restricted to only the smallest systems with a handful of atoms.

To overcome the prohibitive cost of exact diagonalisation, two types of computational approaches are generally taken. The first is to employ approximate diagonalisation schemes such as the Davidson algorithm⁴⁹ where only the lowest energy states are identified. Related approaches include stochastic FCI quantum Monte-Carlo (FCI-QMC),⁵⁰ which samples the FCI wave function to project out the ground-state, and iterative selected CI (sCI)^{51,52} schemes that incrementally grow the size of the diagonalised Hilbert space to locate the subset of determinants with the greatest contribution to the FCI wave function. Together, FCI-QMC and sCI methods have led to some of the most accurate electronic structure calculations to date.

The second approach involves truncating the number of determinants included in the CI expansion. Truncation is usually introduced by limiting the excitation level of determinants, for example in CI with singles and doubles (CISD)

$$|\Psi_{\text{CISD}}\rangle = |\Psi_0\rangle + \sum_{ia} c_i^a |\Psi_i^a\rangle + \sum_{\substack{i<j \\ a<b}} c_{ij}^{ab} |\Psi_{ij}^{ab}\rangle, \quad (1.34)$$

or by selecting a subset of determinants from all possible configurations within a certain 'active-space' of orbitals in a complete-active-space CI (CASCI).¹⁸ Often these

truncated CI methods are combined with iterative diagonalisation, FCI-QMC and s-CI methods to further increase the size of computationally tractable systems.⁵³ However, despite accurately describing wave functions for small molecular systems, the quality of the truncated CI wave function and energy decreases as the size of the system grows.¹¹ In addition, since truncated CI incorrectly describes the energy of separated non-interacting subsystems, it is not a ‘size-extensive’ description and subsequent correction terms are required.¹¹

1.3.2 Perturbation Theory

When the optimised HF wave function provides a good approximation to the true wave function, the remaining correlation energy can be considered as a small perturbation. Formal perturbation theory can be derived following the approach described in Ref. (54). The exact Hamiltonian is partitioned into a “reference” Hamiltonian \hat{H}_0 and the perturbation operator \hat{V} as

$$\hat{H} = \hat{H}_0 + \lambda\hat{V}. \quad (1.35)$$

The reference Hamiltonian is designed to have simple reference eigenfunctions

$$\hat{H}_0|\Psi_i^{(0)}\rangle = E^{(0)}|\Psi_i^{(0)}\rangle, \quad (1.36)$$

that should provide a good first-order approximation to the physical Hamiltonian.

To approximate the exact energies E_i and eigenfunctions $|\Psi_i\rangle$, the full Hilbert space can be partitioned into a “model” reference space and the remaining “external” space⁵⁴ with corresponding projectors \mathcal{M} and \mathcal{Q} satisfying the relations

$$\mathcal{M}^2 = \mathcal{M}, \quad \mathcal{Q}^2 = \mathcal{Q} \quad \text{and} \quad \mathcal{I} = \mathcal{M} + \mathcal{Q}. \quad (1.37)$$

Considering the ground state $|\Psi\rangle = |\Psi_0\rangle$ with energy $E = E_0$, the exact eigenvalue equation can be expanded as

$$\begin{pmatrix} \mathcal{M}\hat{H}\mathcal{M} & \mathcal{M}\hat{H}\mathcal{Q} \\ \mathcal{Q}\hat{H}\mathcal{M} & \mathcal{Q}\hat{H}\mathcal{Q} \end{pmatrix} \begin{pmatrix} \mathcal{M}|\Psi\rangle \\ \mathcal{Q}|\Psi\rangle \end{pmatrix} = E \begin{pmatrix} \mathcal{M}|\Psi\rangle \\ \mathcal{Q}|\Psi\rangle \end{pmatrix}. \quad (1.38)$$

In theory the wave function correction $\mathcal{Q}|\Psi\rangle$ can be eliminated by substituting

$$\mathcal{Q}|\Psi\rangle = -(\mathcal{Q}(\hat{H} - E)\mathcal{Q})^{-1}\mathcal{Q}\hat{H}\mathcal{M}(\mathcal{M}|\Psi\rangle), \quad (1.39)$$

leading to an effective eigenvalue equation expressed in the model space as

$$\underbrace{\left[\mathcal{M}\hat{H}\mathcal{M} - \mathcal{M}\hat{V}\mathcal{Q}(\mathcal{Q}(\hat{H} - E)\mathcal{Q})^{-1}\mathcal{Q}\hat{V}\mathcal{M} \right]}_{\hat{H}_{\text{eff}}} (\mathcal{M}|\Psi\rangle) = E(\mathcal{M}|\Psi\rangle). \quad (1.40)$$

Here the identity $Q\hat{H}_0\mathcal{M} = 0$ gives $Q\hat{H}\mathcal{M} = Q\hat{V}\mathcal{M}$.

Introducing the zeroth-order wave function $|\Psi^{(0)}\rangle = \mathcal{M}|\Psi\rangle$, the exact energy can be computed through the expectation value

$$E = \langle \Psi^{(0)} | \hat{H}_{\text{eff}} | \Psi^{(0)} \rangle = E^{(0)} - \langle \Psi^{(0)} | \hat{V} Q (\mathcal{Q}(\hat{H} - E)\mathcal{Q})^{-1} Q \hat{V} | \Psi^{(0)} \rangle. \quad (1.41)$$

However, the presence of the true energy E prevents Eq. (1.41) from being solved exactly. Instead, (1.39) can be solved by introducing the identity

$$(\mathcal{A} - \mathcal{B})^{-1} = \frac{1}{\mathcal{A}} \sum_{n=0}^{\infty} (\mathcal{B}\mathcal{A}^{-1})^n. \quad (1.42)$$

In the Rayleigh–Schrödinger formalism, this partitioning is defined as

$$\mathcal{A} = \mathcal{Q}(\hat{H}_0 - E^{(0)})\mathcal{Q} \quad \text{and} \quad \mathcal{B} = \mathcal{Q}(V - \delta E)\mathcal{Q}, \quad (1.43)$$

where $\delta E = E - E^{(0)}$. The wave function correction can then be expanded as

$$\mathcal{Q}|\Psi\rangle = \sum_{n=1}^{\infty} |\Psi^{(n)}\rangle \lambda^n, \quad (1.44)$$

where the power series expansion has been formalised by taking $V \rightarrow \lambda V$ and the first two terms are given by

$$\begin{aligned} |\Psi^{(1)}\rangle &= -(\mathcal{Q}(\hat{H}_0 - E^{(0)})\mathcal{Q})^{-1} \mathcal{Q}\hat{V}|\Psi^{(0)}\rangle \\ |\Psi^{(2)}\rangle &= -(\mathcal{Q}(\hat{H}_0 - E^{(0)})\mathcal{Q})^{-1} (\mathcal{Q}(\hat{V} - \delta E)\mathcal{Q}) (\mathcal{Q}(\hat{H}_0 - E^{(0)})\mathcal{Q})^{-1} \mathcal{Q}\hat{V}|\Psi^{(0)}\rangle \end{aligned} \quad (1.45)$$

Inserting this wave function expansion into the effective eigenvalue equation (1.40) then allows the exact energy to be expressed perturbatively as

$$E = \sum_{n=0}^{\infty} \lambda^n E^{(n)} \quad (1.46)$$

where the zeroth, first, and second-order corrections are given by

$$E^{(0)} = \langle \Psi^{(0)} | \hat{H}_0 | \Psi^{(0)} \rangle, \quad (1.47a)$$

$$E^{(1)} = \langle \Psi^{(0)} | \hat{V} | \Psi^{(0)} \rangle, \quad (1.47b)$$

$$E^{(2)} = \langle \Psi^{(1)} | \mathcal{Q}\hat{V} | \Psi^{(0)} \rangle = -\langle \Psi^{(0)} | \hat{V} \mathcal{Q} (\mathcal{Q}(\hat{H}_0 - E^{(0)})\mathcal{Q})^{-1} \mathcal{Q}\hat{V} | \Psi^{(0)} \rangle. \quad (1.47c)$$

1.3.2.1 Møller–Plesset Perturbation Theory

The most common perturbative correction to the HF energy is Møller–Plesset theory, where the reference Hamiltonian is defined as the one-electron Fock operator with the partitioning¹²

$$\hat{H}_0 = \hat{F} = \sum_i^N \hat{f}(i) \quad \text{and} \quad \hat{V} = \hat{H} - \hat{F}. \quad (1.48)$$

The reference HF determinant provides the zeroth-order wave function $|\Psi^{(0)}\rangle = |\Psi_{\text{HF}}\rangle$. Through the Rayleigh–Schrödinger perturbation theory framework, the zeroth and first order terms define the HF energy $E_{\text{HF}} = E^{(0)} + E^{(1)}$, given by

$$E^{(0)} = \langle \Psi^{(0)} | \hat{H}_0 | \Psi^{(0)} \rangle = \sum_i^N \epsilon_i \quad (1.49a)$$

$$E^{(1)} = \langle \Psi^{(0)} | \hat{V} | \Psi^{(0)} \rangle = V_N - \frac{1}{2} \sum_{ij}^N \langle ij || ij \rangle. \quad (1.49b)$$

Assuming the HF reference satisfies Brillouin’s theorem,⁸ the first-order wave function can be expanded in terms of double excitations from the reference HF determinant as

$$|\Psi^{(1)}\rangle = \sum_{\substack{i < j \\ a < b}} t_{ij}^{ab} |\Psi_{ij}^{ab}\rangle, \quad (1.50)$$

where the amplitudes are given by

$$t_{ij}^{ab} = \frac{\langle ab || ij \rangle}{\epsilon_a + \epsilon_b - \epsilon_i - \epsilon_j}, \quad (1.51)$$

and the indices i, j and a, b denote the HF canonical occupied and virtual molecular spin-orbitals respectively. Using Eq. (1.47c), the second-order Møller–Plesset (MP2) energy correction is then given by

$$E^{(2)} = -\frac{1}{4} \sum_{ijab} \frac{|\langle ij || ab \rangle|^2}{\epsilon_a + \epsilon_b - \epsilon_i - \epsilon_j}. \quad (1.52)$$

Crucially, this summation only contains terms that scale linearly with the number of electrons, and so the MP2 correlation energy is explicitly size-extensive. Furthermore, size-extensivity extends to all higher order terms, such as third order MP3, although these are more computationally expensive and are rarely included in practice.¹¹

As a perturbative approach, Møller–Plesset theory is not variational and is not necessarily systematically improvable because the perturbation expansion may become divergent.^{55,56} Furthermore, the MP2 approximation breaks down when the HF determinant does not provide a good reference wave function, for example when bond breaking introduces multireference character. MP2 is therefore thought to only account for dynamic electron correlation, while additional static correlation requires the introduction of multireference formalisms [see Section 1.4]. Finally, the rate of convergence of the perturbation expansion can depend strongly on both the choice of reference determinant⁵⁷ and basis set.^{58,59}

1.3.3 Coupled-Cluster Theory

A third prominent family of methods is the Coupled-Cluster (CC)^{14–16} framework, providing some of the most accurate electronic structure techniques. In CC theory, the wave function is expressed using the exponential form⁶⁰

$$|\Psi_{\text{CC}}\rangle = \exp(\hat{T})|\Psi_0\rangle \quad (1.53)$$

where $|\Psi_0\rangle$ is some reference wave function (usually the HF ground state) and \hat{T} is the “cluster operator” with the form

$$\hat{T} = \sum_k^N \hat{T}_k. \quad (1.54)$$

The k^{th} -term in this sum contains all k -fold excitations, e.g.

$$\hat{T}_1 = \sum_{ia} t_i^a \hat{\tau}_i^a, \quad \hat{T}_2 = \sum_{\substack{i<j \\ a<b}} t_{ij}^{ab} \hat{\tau}_{ij}^{ab}, \quad \dots \quad (1.55)$$

where $\hat{\tau}_i^a |\Psi_0\rangle = |\Psi_i^a\rangle$ represents an excitation from occupied orbital i to virtual orbital a , and the amplitudes $\{t_i^a, t_{ij}^{ab}, \dots\}$ parameterise the CC wave function. Using the intermediate normalisation $\langle \Psi_{\text{CC}} | \Psi_0 \rangle = 1$, the cluster amplitudes can be identified by self-consistently solving the projected CC equations

$$\langle \Psi_i^a | \hat{H} - E | \Psi_{\text{CC}} \rangle = 0, \quad \langle \Psi_{ij}^{ab} | \hat{H} - E | \Psi_{\text{CC}} \rangle = 0, \quad \dots \quad (1.56)$$

while the CC energy can be recovered through the projection

$$E_{\text{CC}} = \langle \Psi_0 | \hat{H} | \Psi_{\text{CC}} \rangle. \quad (1.57)$$

Although a variational optimisation of the CC energy is possible, its exponential complexity means it is rarely applied in practice.¹¹

When every excitation level is included in the cluster operator, the CC formalism is equivalent to FCI and the exact energy for the given basis is obtained. However, the power of the CC wave function *ansatz* is realised when the cluster operator is truncated at a given excitation level. In contrast to truncated CI wave functions, the exponentiation of the truncated cluster operator ensures that determinants of every excitation level always remain present in the CC wave function¹¹

$$|\Psi_{\text{CC}}\rangle = \left(1 + \hat{T} + \frac{1}{2} \hat{T}^2 + \dots \right) |\Psi_0\rangle, \quad (1.58)$$

although their relative contributions are not necessarily exact. As a result, the CC energy is explicitly size-extensive.⁶⁰ Truncation at the level of double excitations is by

far the most common approximation, describing important pairwise electron correlation and yielding the Coupled-Cluster singles-and-doubles (CCSD) approach.⁶¹ Since the computational cost increases at each truncation level, higher-order excitations are often accounted for perturbatively, and the success of CCSD with perturbative triples,⁶² CCSD(T), has led to the method being considered as the current “gold-standard” in electronic structure theory.

However, with close similarities to perturbation theory,^{60,63} CC theory also suffers from a lack of a variational energy. Furthermore, the exponential form relies on the presence of a dominant reference determinant such that the cluster amplitudes become increasingly small for higher excitations. The CC approximation therefore often breaks down in regions where the exact wave function has multireference character, or when state degeneracies occur. For example, the CCSD approach is known to overestimate the dissociation energy when single bonds are broken.⁶⁴ Handling this failure requires computationally expensive higher truncation levels, although numerous multireference or quasi-degenerate variations of CC theory have also been proposed.⁶⁵

1.4 Multireference Approaches

Single-reference methods such as truncated CI, truncated CC, or MP2 theory generally fail when the exact wave function contains multiple determinants with equally large coefficients.¹¹ The emergence of several dominant electronic configurations indicates that the reference HF determinant provides a poor approximation of the exact wave function, corresponding to the presence of strong static correlation effects. To overcome this failure, the most common solution is to introduce a multireference wave function through the multiconfigurational self-consistent field (MCSCF) framework.⁸ However, computationally tractable MCSCF methods usually provide only qualitative accuracy,¹¹ and the remaining dynamic correlation must be computed through the introduction of additional CI, CC or perturbation approaches.

1.4.1 Multiconfigurational Self-Consistent Field

When the exact wave function is dominated by several electronic configurations, a multiconfigurational wave function can be built as the truncated CI expansion

$$|\Psi_{\text{MCSCF}}\rangle = \sum_I^{n_{\text{ref}}} c_I |\Psi_I\rangle. \quad (1.59)$$

Here, $|\Psi_I\rangle$ represents a determinant with a particular arrangement of electrons in a common set of molecular orbitals defined by Eq. (1.19). The optimal wave function can

be obtained by simultaneously minimising the expectation value of the energy

$$E_{\text{MCSCF}} = \frac{\langle \Psi_{\text{MCSCF}} | \hat{H} | \Psi_{\text{MCSCF}} \rangle}{\langle \Psi_{\text{MCSCF}} | \Psi_{\text{MCSCF}} \rangle} \quad (1.60)$$

with respect to both the CI coefficients $\{c_I\}$ and the MO coefficients $\{C_{\cdot i}^{\mu}\}$.^{8,11} Crucially, this approach allows the underlying MOs to be tailored to a particular CI expansion, providing a highly flexible wave function *ansatz* that is well-suited to capturing the multireference character of the wave function.

Including all configurations in the MCSCF expansion leads to the exact FCI energy and wave function. In practice, the MCSCF wave function is expanded in a suitable subset of configurations that must be chosen *a priori*. The most common selection route is the complete active space (CAS) approach, where the MOs are partitioned into sets of inactive, active, and secondary orbitals.¹¹ The corresponding ‘‘CASSCF’’ wave function is then constructed from every combination of electrons in the active orbitals, while the inactive orbitals are doubly occupied and the secondary orbitals are unoccupied in all configurations.¹⁸ Since the active space is usually limited to a small number of correlated orbitals and electrons, e.g. a molecular π -system, the method is tractable for larger systems than the exact FCI approach. CASSCF has therefore become the method of choice for describing strongly correlated molecular systems.⁶⁶

However, optimising the highly nonlinear CASSCF wave function presents a difficult computational challenge. Usually this process requires second-order optimisation methods that often incur a significant computational demand.¹¹ Furthermore, CASSCF is ultimately limited by exponential scaling with the size of the active space, and its sensitivity to the choice of active orbitals restricts its applicability as a ‘black-box’ method. Recent developments in second-order MCSCF optimisation^{67,68} and automated active space selection^{69,70} have sought to alleviate these difficulties.

1.4.2 Multireference CI and CC

The MCSCF framework is very successful at capturing static correlation effects to provide qualitatively correct electronic energies. However, the remaining dynamic correlation requires large CI expansions in the MCSCF wave function that are often computationally intractable. Instead, the MCSCF wave function can be used to define a reference state for subsequent multireference CI (MRCI) or CC (MRCC) expansions that are more effective at capturing dynamic correlation. It is useful to briefly summarise the MRCI and MRCC approaches, although they will not be considered in this thesis.

For an optimised MCSCF state given by (1.59), the most general MRCI wave function

can be constructed using the set of excited determinants from each determinant⁷¹

$$|\Psi_{\text{MRCI}}\rangle = \sum_I^{n_{\text{ref}}} \left[c_I |\Psi_I\rangle + \sum_{ia} c(I)_i^a |(\Psi_I)_i^a\rangle + \sum_{\substack{i<j \\ a<b}} c(I)_{ij}^{ab} |(\Psi_I)_{ij}^{ab}\rangle + \dots \right], \quad (1.61)$$

where $|(\Psi_I)_i^a\rangle$ indicates a single replacement determinant constructed from the reference state $|\Psi_I\rangle$ and $c(I)_i^a$ denotes its corresponding coefficient in the MRCI wave function. Like single-reference CI, this wave function expansion is usually truncated at a given excitation level. For example, the multireference Single and Double Configuration Interaction (MRCISD) approach considers only single and double excitations from each reference determinant.⁷² In practice, the configuration expansion grows rapidly with the number of reference determinants and further approximations such as the use of ‘internally contracted’ configurations must be introduced.⁷³ For example, the corresponding internally-contracted MRCISD (ic-MRCISD) wave function is built as

$$|\Psi_{\text{ic-MRCI}}\rangle = \sum_{ia} t_i^a \hat{t}_i^a |\Psi_{\text{MCSCF}}\rangle + \sum_{\substack{i<j \\ a<b}} t_{ij}^{ab} \hat{t}_{ij}^{ab} |\Psi_{\text{MCSCF}}\rangle, \quad (1.62)$$

where the number of variational parameters is now equivalent to the single-reference CISD approach.

While MRCI can provide extremely accurate results for small molecules, it also suffers from a lack of size-consistency due to the use of a truncated CI expansion.⁷¹ Furthermore MRCI shows a slow convergence with respect to the size of the CI expansion.¹¹ Instead, there has been significant research in exploiting the size-consistency of CC theory applied to a reference MCSCF wave function in a MRCC expansion.^{16,65} While a full exposition of MRCC approaches is well beyond the scope of this thesis [see Refs. (16) and (65)], the most common formulations use the ‘Jeziorski and Monkhorst’ wave function constructed from reference-specific excitation operators as⁷⁴

$$|\Psi_{\text{JM}}\rangle = \sum_I^{n_{\text{ref}}} \exp(\hat{T}_I) |\Psi_I\rangle c_I. \quad (1.63)$$

However, these wave functions generally contain a large number of variational parameters that limit their applications to small active spaces.⁶⁵ Furthermore, MRCC often suffers from the presence of redundant parameters or intruder states that can cause numerical instabilities and convergence issues.⁶⁵

1.4.3 Multireference Perturbation Theory

To avoid the computationally difficult MRCI and MRCC methods, the remaining dynamical correlation effects can be approximated using multireference perturbation

theory. By far the most common approach is CASPT2, where Rayleigh–Schrödinger perturbation theory is applied using a CASSCF reference wave function to generate a second-order energy correction.^{75,76} The success of CASPT2 theory has led to its application for ground- and excited-states across a wide range of chemical systems, including organic radicals, reaction pathways, and transition metals.⁷⁷

Following the Rayleigh–Schrödinger approach with the reference wave function $|\Psi^{(0)}\rangle = |\Psi_{\text{CASSCF}}\rangle$, the second-order energy can be computed by identifying the first-order wave function $|\Psi^{(1)}\rangle$. This first-order wave function can be expanded using the first-order interacting space, defined as the set of determinants that can couple to $|\Psi^{(0)}\rangle$ through the Hamiltonian. For a CASSCF reference wave function, the full configuration space can be decomposed into four subspaces defined with the projectors \mathcal{M}_0 , \mathcal{Q}_K , \mathcal{Q}_{SD} , and $\mathcal{Q}_{\text{TQ...}}$.⁷⁸ Here $\mathcal{M}_0 = |\Psi^{(0)}\rangle\langle\Psi^{(0)}|$ projects onto the space spanned by the CASSCF reference wave function; \mathcal{Q}_K projects onto the CAS space that is orthogonal to $|\Psi^{(0)}\rangle$; \mathcal{Q}_{SD} projects onto the single and double excitations from $|\Psi^{(0)}\rangle$ that are not present in the CAS space; and $\mathcal{Q}_{\text{TQ...}}$ projects onto all higher-order excitations that are not yet accounted for. The first-order interacting space can then be identified as the subspace corresponding to the \mathcal{Q}_{SD} projector. Like the ic-MRCI approach, the perturbing functions in this first-order interacting space are usually constructed as contracted excitations,¹¹ giving

$$|\Psi^{(1)}\rangle = \sum_{ia} t_i^a \hat{\tau}_i^a |\Psi_{\text{CASSCF}}\rangle + \sum_{\substack{i<j \\ a<b}} t_{ij}^{ab} \hat{\tau}_{ij}^{ab} |\Psi_{\text{CASSCF}}\rangle. \quad (1.64)$$

Here i, j denote occupied inactive or active orbitals, a, b denote unoccupied active or virtual orbitals, and terms where all indices correspond to active orbitals are omitted. Using contracted configurations reduces the dimensionality of the first-order interacting space, although they make the matrix elements more complicated and introduce nonorthogonality between the perturbing configurations.^{11,77,78}

The success of single reference Møller–Plesset theory is largely due to the simplicity of the reference Fock operator. For a multiconfigurational reference wave function, a similar one-particle zeroth-order Hamiltonian can be constructed as the generalised Fock operator \hat{F}_G , defined in the spin atomic orbital basis as^{75,76}

$$F_G[\mathbf{P}_\Psi]_{\mu\nu} = h_{\mu\nu} + \sum_{\sigma\tau}^{2n} \langle\mu\sigma||\nu\tau\rangle (P_\Psi)^{\tau\sigma}. \quad (1.65)$$

Here \mathbf{P}_Ψ is the one-electron reduced density matrix of the multireference wave function $|\Psi_{\text{CASSCF}}\rangle$. However, to ensure that the reference Hamiltonian retains a simple structure and $|\Psi_{\text{CASSCF}}\rangle$ corresponds to an eigenfunction of \hat{H}_0 , the generalised Fock operator must be further modified as⁷⁸

$$\hat{H}_0 = \mathcal{M}_0 \hat{F}_G \mathcal{M}_0 + \mathcal{Q}_K \hat{F}_G \mathcal{Q}_K + \mathcal{Q}_{\text{SD}} \hat{F}_G \mathcal{Q}_{\text{SD}} + \mathcal{Q}_{\text{TQ...}} \hat{F}_G \mathcal{Q}_{\text{TQ...}}. \quad (1.66)$$

The zeroth-order energy is then defined as $E^{(0)} = \langle \Psi_{\text{CASSCF}} | \hat{H}_0 | \Psi_{\text{CASSCF}} \rangle$. Significantly, this zeroth-order Hamiltonian reduces to the Møller–Plesset form for a single determinant reference wave function.

Following the Rayleigh–Schödinger approach, the first-order wave function can be identified by solving the first-order perturbation equation

$$\sum_p (\hat{H}_0 - E^{(0)}) | \Psi_p \rangle t_p = -\hat{H} | \Psi_{\text{CASSCF}} \rangle, \quad (1.67)$$

where $| \Psi_p \rangle$ refers to an allowed contraction and $\mathcal{Q} \hat{V} | \Psi_{\text{CASSCF}} \rangle = \hat{H} | \Psi_{\text{CASSCF}} \rangle$. The optimal first-order wave function coefficients can be identified as the solution to the linear equations

$$\sum_{pq} \langle \Psi_q | \hat{H}_0 - E^{(0)} | \Psi_p \rangle t_p = -\langle \Psi_q | \hat{H} | \Psi_{\text{CASSCF}} \rangle, \quad (1.68)$$

where again the contracted nature of the expansion configurations means that the perturbing functions are not necessarily orthogonal and may contain linear dependencies.⁷⁸ In practice, the CASPT2 equations are generally solved using an iterative procedure.⁷⁷ Once the optimal first-order wave function has been identified, the second-order energy can be computed using Eq. (1.47c) as

$$E^{(2)} = -\sum_p t_p^* \langle \Psi_p | \hat{H} | \Psi_{\text{CASSCF}} \rangle. \quad (1.69)$$

While the CASPT2 approach works well in many circumstances, it is prone to the effects of intruder states in the perturbation expansion. Intruder states arise when first-order expansion configurations become nearly degenerate with the reference wave function, causing divergences and singularities along the potential energy surface.¹¹ The effects of intruder states in CASPT2 can be mitigated by introducing a real or imaginary shift in the reference Hamiltonian,^{79,80} or using the IPEA shift to modify the orbital energies based on their occupation number.⁸¹ However, these modifications introduce new parameters that must be defined empirically. Alternatively, NEVPT2 theory^{82,83} introduces the more sophisticated Dyllall zeroth-order Hamiltonian⁸⁴ that includes two-electron components to help avoid intruder-state effects.^{82,83}

1.5 Excited-State Methods

In addition to the ground state potential energy surface, excited electronic states play an important role across chemistry. Excited-state energies can in principle be obtained as the higher-energy eigenvalues of the exact FCI Hamiltonian. However, forming suitable approximations to exact excited-state energies remains a major challenge in

electronic structure theory. For example, methods must ensure a good representation of the excited-state wave function while avoiding variational collapse onto the ground state. In practice, several excited-state methods have been developed with varying degrees of accuracy and efficiency.^{85,86} For the sake of brevity, only the computational methods applied in this thesis will be summarised here.

1.5.1 Configuration Interaction Singles

The simplest excited-state approximation is the uncorrelated configuration interaction expansion using only single excitations (CIS).^{87,88} Starting from an optimised ground-state HF solution $|\Psi_0\rangle$, the CIS wave function is built as a linear combination of all singly-excited determinants as

$$|\Psi_{\text{CIS}}\rangle = \sum_{ia} c_i^a |\Psi_i^a\rangle. \quad (1.70)$$

The optimal excitation energies can be identified by diagonalising the corresponding Hamiltonian matrix with elements given by $H_{ia,jb} = \langle \Psi_i^a | \hat{H} | \Psi_j^b \rangle$.⁸⁵ Since the HF wave function satisfies Brillouin's theorem,⁸ these single excitations do not couple with the reference determinant and the ground-state energy remains uncorrelated. As a result, no correlation is introduced into either the ground- or excited-state wave functions and CIS defines an uncorrelated approach for excitation energies.⁸⁵ The popularity of CIS stems from the fact that it is computationally efficient and provides size-consistent variational estimates of the excited-state energies.⁸⁸

Despite the computational simplicity of CIS, the lack of electron correlation means that it often fails to provide sufficient accuracy beyond singly-excited electrons. Capturing excited-state electron correlation requires the introduction of double excitations and can be achieved perturbatively using the CIS(D) method.⁸⁹ Furthermore, since the orbitals used in the CI expansion are optimised for the HF ground state, CIS excitation energies are often overestimated when the exact excited-state wave functions involve a spatial rearrangement of electrons, for example in diffuse excited states or charge transfer states.⁹⁰ Recent attempts to improve excitation energies in these cases include relaxing the orbitals for each excited state in the orbital-optimised CIS (OO-CIS) approach.^{91,92}

1.5.2 Equation-of-motion Coupled-Cluster

Generalising the ground-state CC approach to excitation energies can be achieved through the equation-of-motion (EOM) formalism.^{63,93} Consider a given ground-state

CC wave function with the form $|\Psi\rangle = \exp(\hat{T})|\Psi_0\rangle$, where $|\Psi_0\rangle$ defines the HF reference determinant. In the EOM-CC approach, excited-state energies are computed by diagonalising the similarity-transformed Hamiltonian⁹⁴

$$\bar{H} = \exp(-\hat{T})\hat{H}\exp(\hat{T}) \quad (1.71)$$

in the space of excited determinants from the HF reference. The resulting eigenfunctions are represented by the operators \hat{R}_i with eigenvalues satisfying

$$\bar{H}\hat{R}_i = E_i\hat{R}_i. \quad (1.72)$$

Here \hat{R}_i defines an excitation operator with the corresponding excited-state wave function

$$|\Psi_i\rangle = \hat{R}_i \exp(\hat{T})|\Psi_0\rangle. \quad (1.73)$$

These wave functions are inherently multiconfigurational, allowing EOM-CC to describe excited states with multireference character.⁶³

Like the ground-state CC approach, EOM-CC is usually applied with a truncated excitation operator.⁶³ For example, the EOM-CCSD method is based upon the CCSD ground state and includes up to single and double excitations in the similarity-transformed Hamiltonian. However, only states dominated by determinants at the excitation level one less than the truncation level can be described properly by this approach. Since the computational cost of EOM-CC scales steeply with the truncation level, practical applications are limited to EOM-CCSD for which only single excitations can be accurately described.⁹⁵ Furthermore, EOM-CC relies on a good representation of the ground state and fails when the underlying single reference CC approximation breaks down.⁹⁴

1.5.3 Excited-State CASSCF

When exact excited states contain dominant contributions from several determinants, the application of multireference approaches is required.⁹⁴ The CASSCF framework provides a conceptually simple approach to both ground and excited states and is widely used for strongly correlated excited states.¹⁸ In principle, an excited-state CASSCF wave function can be identified by directly targeting higher-energy stationary points of the energy in a ‘state-specific’ formalism. However, state-specific CASSCF is susceptible to root-flipping and variational collapse onto the ground state if the state ordering changes in the iterative CI step of a CASSCF cycle.⁹⁶ Furthermore, unlike exact excited-state wave functions, individual CASSCF solutions are not guaranteed to be mutually orthogonal.⁹⁶

Alternatively, multiple excited states can be considered in the same CASSCF calculation using a state-averaged (sa) method.⁹⁷ The sa-CASSCF approach optimises a weighted average of the target state energies defined as

$$E_w = \sum_m W_m E_m = \sum_m W_m \sum_{IJ} (c_J^m)^* \langle \Psi_J | \hat{H} | \Psi_I \rangle c_I^m \quad (1.74)$$

where W_m is the weight for each target state. While sa-CASSCF is a powerful method for studying several excited states simultaneously, using the same set of orbitals for every state has been found to introduce a systematic bias towards the ground-state energy.⁹⁶ Furthermore, the resulting wave functions are not themselves stationary points of the energy and are inherently less accurate than a state-specific formalism. Finally, both state-averaged and state-specific CASSCF suffer from the computational challenges of selecting suitable active orbitals and the exponentially scaling number of configurations the active space size.

Chapter 2

Multiple Hartree–Fock Solutions and Nonorthogonal Configuration Interaction

2.1 Introduction

While HF theory is almost universally used to define a reference wave function for correlated methods, it is less widely appreciated that the HF equations can yield multiple stationary states.^{20,23} Additional solutions correspond to Slater determinants built from a bespoke set of orbitals and can represent local minima, maxima, or saddle points of the HF energy. Recently, several authors have sought to interpret higher energy HF states as mean-field approximations to physical excited states.^{23,26–29} Furthermore, multiple HF solutions are also found to resemble diabatic states with an electronic structure that is conserved as the molecular structure changes.²⁵ These solutions are not required to conserve the physical symmetries of the system,⁹⁸ and HF symmetry-breaking can lead to lower energies that correctly describe fragmented molecular systems such as bond dissociation.^{20,24}

When the exact wave function is dominated by several competing electronic configurations, HF states often correspond to each dominant configuration.^{25,33} This observation has inspired the combination of multiple HF states in a nonorthogonal CI (NOCI) expansion to construct a multireference alternative to CASSCF.²⁵ Significantly, using HF states to define the dominant configurations in a multireference wave function avoids the challenges associated with selecting the CASSCF active orbital space. NOCI expansions built in this way resemble physical adiabatic states, reproducing avoided crossings and conical intersections.²⁵ Furthermore, the bespoke orbitals of each HF state can lead to more compact NOCI expansions than orthogonal CI,³² while including higher-energy HF states provides accurate multielectron and core excitation energies.^{31,34,35} However, many current NOCI formalisms rely on the existence of HF states across all geometries and catastrophically fail when a HF solution disappears along a potential energy surface.²⁵

In the current chapter, the existence and properties of multiple HF states are reviewed before an outline of current NOCI methods is presented.

2.2 Multiple Hartree–Fock Solutions

2.2.1 Historical Overview

Indications that the HF equations could permit multiple stationary states were reported almost immediately after the derivation of the Roothaan–Hall approach.⁹⁹ The earliest examples of multiple HF solutions were related to the formation of ferromagnetic and antiferromagnetic states in a Fermi gas^{99,100} In these cases, the ‘normal’ HF state with a symmetric electron distribution is never the lowest energy state. Furthermore, at a certain electron density, a transition occurs between the ferromagnetic state with all electron spins parallel, and the antiferromagnetic state where spin-up (α) and spin-down (β) electrons form an alternating spin-density wave.¹⁰⁰ The physical significance of these multiple HF states was further developed by drawing parallels with the Mott metal-insulator transition and the Wigner crystallisation of high-density electrons.¹⁰¹

In the parlance of modern quantum chemistry,⁸ the ‘normal’ HF state represents a closed-shell restricted HF (RHF) solution, while the antiferromagnetic solutions correspond to an unrestricted HF (UHF) state where the α and β electrons adopt different spatial orbitals. Equivalent multiple HF states emerge in the hydrogen dimer where an RHF solution corresponding to the closed-shell σ_g^2 configuration is the lowest energy state at equilibrium but a ‘diradical’ UHF state emerges as the bond length extends towards dissociation.⁸ The RHF state cannot correctly describe dissociation to two open-shell radical hydrogen atoms and overestimates the electron repulsion energy for large bond lengths. In contrast, the UHF state predicts the correct energy by allowing the electrons to localise on opposite atoms in a ‘diradical-like’ configuration. The sudden appearance of this additional UHF solution occurs at the so-called Coulson–Fischer point²⁴ and equivalent states can be found in a wide range of molecular systems.^{102–105}

The consequence of allowing different orbitals for different spins in the UHF approach is that the wave function is no longer an eigenfunction of the S^2 spin-operator, becoming a ‘spin-contaminated’ combination of a singlet and triplet state. More generally, the occurrence of HF solutions with lower energies than the conventional RHF state is associated with the HF wave function breaking certain symmetries of the Hamiltonian.⁹⁸ This phenomenon leads to Löwdin’s “symmetry dilemma” where one must decide between variationally lower energies and good quantum numbers.¹⁰⁶

Assessing whether a converged HF state represents the lowest energy solution can be

achieved using stability analysis, where the eigenvalues of the orbital Hessian indicate whether a true energy minima has been located.^{107–112} Furthermore, by considering a constrained Hessian, the stability of a converged state can be determined with respect to an orbital rotation that conserves the symmetry of the wave function (e.g. RHF \rightarrow RHF) or that allows a particular symmetry to be broken (e.g. RHF \rightarrow UHF).¹¹³ In this sense, the emergence of a lower energy UHF state in the dissociation limit of H₂ corresponds to the onset of an instability in the orbital Hessian.

From a mathematical perspective, the work of Fukutome established a framework for understanding the existence of multiple solutions and identified upper and lower bounds on the possible number of solutions.²² By introducing perturbative expansions, Fukutome also classified each type of UHF Hessian instability in terms of their pattern of connectivity between different solutions.^{114,115} Similar instabilities can be classified with respect to closed-shell RHF spatial symmetry breaking, creating charge-density waves that resemble ‘ionic configurations’.^{116–118} Finally, by considering the possible combinations of conserved symmetries, Fukutome defined the eight families of HF states that are described more comprehensively in Section 2.2.2

Recent computational developments for locating many HF stationary points have led to renewed interest in exploiting multiple HF states.^{20,23,26,119} In particular, many authors have sought to interpret higher energy HF stationary states as mean-field approximations to excited states.^{26–29} Furthermore, multiple HF states have been found to produce approximate physical diabatic states in molecular systems.^{20,25} In this sense, broken-symmetry HF states are thought to contain ‘more correlation’ than a symmetry-pure HF ground-state.¹²⁰ The belief that multiple HF states represent different dominant configurations in the exact wave function has subsequently motivated their use as a basis for multireference NOCI expansions.^{25,31}

2.2.2 Symmetry in Hartree–Fock

The true N -electron (bare) Hamiltonian (1.7) conserves all the physical symmetries of a molecule and the exact wave function is therefore an eigenfunction of the S^2 and S_z spin operators, and the time-reversal \mathcal{T} , complex-conjugation \mathcal{K} and spatial point group symmetry operators. In contrast, the HF wave function is identified as the stationary point of the expectation value (1.20) and is not a true eigenfunction of the bare Hamiltonian. There is therefore no requirement that the HF wave function satisfies every symmetry of the true Hamiltonian. While allowing broken-symmetry HF wave functions can create a lower variational estimate of the exact ground state, it also leads to badly defined quantum numbers that obscure the physical interpretation of a state and are difficult to restore in post-HF approaches.^{121–124}

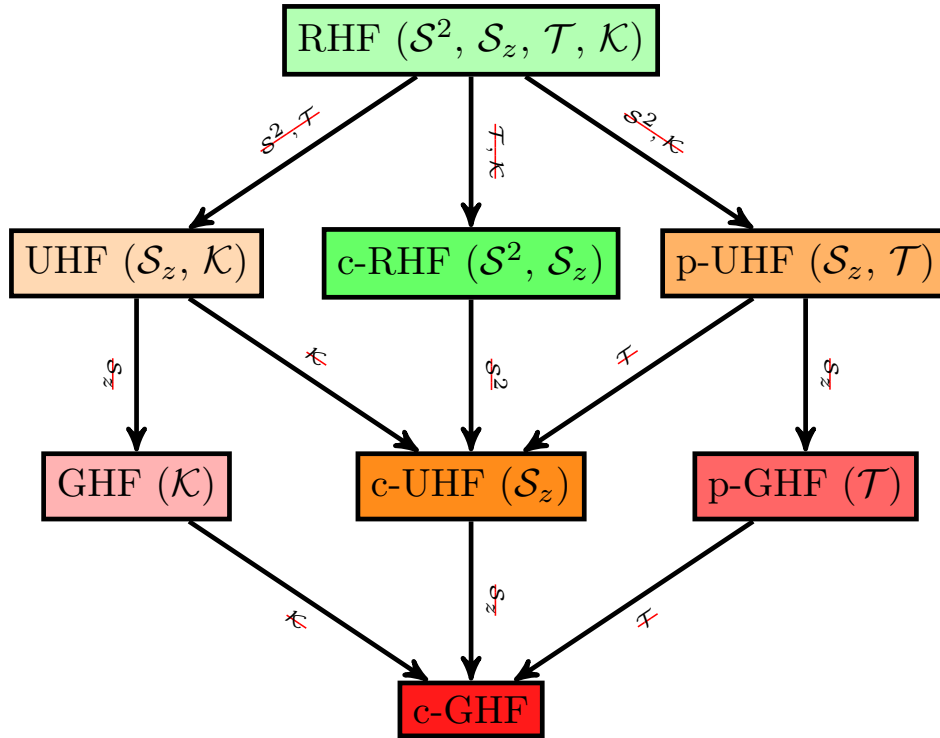


Figure 2.1: The eight families of HF solutions, along with their definition according to Stuber and Paldus⁹⁸ and the symmetries they conserve. XHF, p-XHF and c-XHF denote real, paired and complex XHF (where X = R, U and G). See main text for more details.

Symmetry-breaking in the HF wave function is induced by the self-consistency of the HF equations. In particular, since the optimal HF orbitals are in fact eigenvectors of the self-consistent Fock matrix, where the bare Hamiltonian is ‘dressed’ with the molecular orbitals, the symmetry of these orbitals (and in turn the HF wave function) is dictated by the Fock operator. The symmetry of the initial wave function is therefore retained throughout the SCF procedure and is reflected in the final wave function. As a result, symmetries can be conserved in the wave function by explicitly enforcing certain constraints on the HF equations, leading to the eight formalisms of HF summarised in Fig. 2.1.^{98,125,126}

These different formalisms are best illustrated by considering the structure of the occupied orbital coefficients for a state with an even number of electrons N , given as

$$\mathbf{C} = \begin{pmatrix} c_{1\alpha} & c_{2\alpha} \\ c_{1\beta} & c_{2\beta} \end{pmatrix} \in \mathbb{C}^{2n \times N} \quad (2.1)$$

where the first (last) $N/2$ columns \mathbf{c}_1 (\mathbf{c}_2) correspond to the spin-up (spin-down) electrons in a closed-shell state and each orbital contains contributions from α and β basis orbitals in general. Each submatrix in Eq. (2.1) has dimensions $n \times \frac{N}{2}$ and is expressed in the spatial orbital basis.

The real RHF approach is the most constrained HF formulation, where each orbital

must be real-valued with a spin component that is either aligned parallel (α) or antiparallel (β) to a common axis, and the spatial component of orbitals with opposite spin must be the same. In this case, the HF wave function is parameterised by a set of n spatial orbitals with coefficients c and the full orbital coefficient matrix takes the form

$$C_{\text{RHF}} = \begin{pmatrix} c & \mathbf{0} \\ \mathbf{0} & c \end{pmatrix} \in \mathbb{R}^{2n \times N}. \quad (2.2)$$

Constraining the orbital coefficients in this way ensures that the HF state forms an eigenfunction of the spin operators S^2 and S_z , \mathcal{K} and \mathcal{T} by definition. For open-shell systems, the restricted open-shell HF (ROHF) approach can be applied where all spin-paired electrons occupy the same spatial orbitals.^{127,128} Note that there is no condition for the spatial point group symmetry to be conserved in RHF or ROHF, although this can be enforced using additional constraints on the SCF procedure.

Allowing the different spins to occupy different spatial orbitals while retaining real values leads to the UHF approach with a coefficient matrix of the form

$$C_{\text{UHF}} = \begin{pmatrix} c_\alpha & \mathbf{0} \\ \mathbf{0} & c_\beta \end{pmatrix} \in \mathbb{R}^{2n \times N}. \quad (2.3)$$

Although the more flexible UHF wave function provides better energies for open-shell or diradical systems, the wave function is no longer an eigenfunction of S^2 or \mathcal{T} . As a result, it is possible for the wave function to become spin-contaminated and represent the combination of multiple spin-pure states.

Often even the UHF approach does not provide a sufficient level of flexibility to obtain the lowest possible HF energy. For example it fails to describe the energy of dissociating a bond into open-shell fragments with opposite spins.¹²⁶ When this is the case, the condition that orbitals must have pure α or β components can be lifted and the spin of electrons can be allowed to rotate to *any* orientation. This represents the real generalised HF (GHF) approach with orbital coefficients taking the form

$$C_{\text{GHF}} = \begin{pmatrix} c_{1\alpha} & c_{2\alpha} \\ c_{1\beta} & c_{2\beta} \end{pmatrix} \in \mathbb{R}^{2n \times N}. \quad (2.4)$$

As a result, the GHF wave function is longer required to be an eigenfunction of S_z and the only remaining symmetry, complex conjugation \mathcal{K} , is the result of retaining real-valued orbitals.

At each of the constraint levels RHF, UHF and GHF, the orbitals can be allowed to become complex-valued, leading to the complex RHF (c-RHF), complex UHF (c-UHF) and complex GHF (c-GHF) formalisms. When orbitals become complex, the \mathcal{K} -symmetry of the wave function is lost. However, these complex orbitals can introduce

multireference character into the wave function at the mean-field level and can remove singularities in the real HF energy.^{36,37,129,130} Furthermore, allowing complex orbital coefficients while enforcing time-reversal symmetry leads to the paired UHF and pair GHF approaches

$$\mathbf{C}_{\text{p-UHF}} = \begin{pmatrix} \mathbf{c} & \mathbf{0} \\ \mathbf{0} & \mathbf{c}^* \end{pmatrix} \in \mathbb{C}^{2n \times N} \quad \text{and} \quad \mathbf{C}_{\text{p-GHF}} = \begin{pmatrix} \mathbf{c}_1 & \mathbf{c}_2 \\ -\mathbf{c}_2^* & \mathbf{c}_1^* \end{pmatrix} \in \mathbb{C}^{2n \times N}. \quad (2.5)$$

The p-UHF variation is equivalent to the Kramers RHF approach defined for relativistic Hamiltonians.¹³¹

2.2.3 Locating Multiple Hartree–Fock Solutions

While in most cases only one HF solution is required to provide a reference state for a post-HF calculation, it is common for the SCF procedure to converge onto a stationary point that does not represent the global minimum.¹³² Renewed awareness of multiple solutions and recent interest in using higher energy solutions as mean-field excited-state approximations has led to the development of new computational approaches for locating the global minimum and converging the SCF procedure to higher energy stationary points. Two recent methods that are most extensively used in this thesis are the Maximum Overlap Method (MOM) introduced by Gilbert *et al.*²⁶ and the SCF Metadynamics approach of Thom and Head-Gordon.²⁰

2.2.3.1 Maximum Overlap Method

Converging higher energy stationary points is challenging for conventional SCF algorithms because *non-aufbau* ordering of the orbital eigenvalues must be achieved. Selecting the new occupied orbitals on each SCF iteration by occupying the lowest N energy orbitals will nearly always lead to convergence onto the lowest energy stationary point. To overcome this behaviour, the MOM approach introduces a selection procedure where the new occupied orbitals on each iteration are selected as the eigenvectors of the Fock matrix that have the greatest overlap with the occupied orbitals on the previous iteration.²⁶

The MOM procedure begins with an excited Slater determinant constructed by swapping an occupied and virtual orbital of the HF ground state. After the diagonalisation of the Fock matrix, an overlap matrix can be constructed between the old occupied orbital coefficients on the previous iteration ${}^{\text{old}}\mathbf{C}$ and new orbital coefficients ${}^{\text{new}}\mathbf{C}$ as

$$\Omega_{ij} = \sum_{\mu\nu} ({}^{\text{old}}\mathbf{C}^*)_{i\cdot}{}^{\mu} S_{\mu\nu} ({}^{\text{new}}\mathbf{C})_{\cdot j}{}^{\nu}. \quad (2.6)$$

The projection of the j th new orbital onto the previous occupied orbitals is then given by

$$p_j = \sum_{i=1}^N \Omega_{ij} \quad (2.7)$$

and the new occupied orbitals can be selected as those with the greatest weight $|p_j|$. Selecting the occupied orbitals in this way provides an entirely black-box alternative to the conventional *aufbau* ordering and can be applied to any of the HF formalisms outlined in the previous section.

Using the MOM procedure, an SCF calculation will converge onto the target excited state as long as the initial guess is sufficiently close to the desired stationary point.²⁶ The general applicability of MOM has been widely demonstrated for locating mean-field excited state approximations with great success.^{26-28,30} Furthermore, when the SCF procedure drifts far from the target state even with a good initial guess, a stricter orbital selection criteria can be introduced where the new occupied orbitals are always compared to the initial orbital coefficients, defining the Initial Maximum Overlap Method (IMOM).²⁹ The IMOM modification essentially ‘anchors’ the orbitals in the SCF procedure towards the initial guess orbitals, and provides significantly more robust optimisation in the case of nearly-degenerate states.²⁹

2.2.3.2 SCF Metadynamics

When an SCF calculation is believed to have converged onto a solution that is not a minimum (e.g. a saddle point or maximum), lower energy states can be identified by following the downhill directions indicated by stability analysis.¹¹³ However, identifying lower energy HF states in this way does not account for the fact that a converged stationary point may be a *local* minimum with no downhill directions. The SCF metadynamics approach provides an automated approach to break free from local minima and locate the globally lowest energy HF stationary state.²⁰ Once an initial HF state has been identified, a biasing potential is added to “fill in” the corresponding minimum in the HF energy surface and encourage subsequent SCF calculations to converge onto lower energy stationary states.

Defining SCF metadynamics requires a measure of the distance between the electron density during the SCF procedure and the electron density corresponding to previously identified solutions. Every possible Slater determinant is defined uniquely by its density matrix, denoted for an optimal HF state w as ${}^w P^{\mu\nu}$. The idempotency of the density matrix and the fact that its trace equals the number of electrons can then be exploited to

define the distance between two HF states (w and x) as

$$d_{wx}^2 = N - \sum_{\mu\sigma}^{2n} ({}^w P)^{\mu\sigma} ({}^x P)_{\sigma\mu}. \quad (2.8)$$

When the two densities are identical $d_{wx}^2 = 0$, while the maximum possible distance using this metric is N .

Once a set of HF states have been identified, a biasing Gaussian potential can be added to the HF energy surface by defining the Lagrangian

$$\mathcal{L} = E_{\text{HF}} + \sum_w N_w e^{-\lambda_w d_{0w}^2} \quad (2.9)$$

where N_w and λ_w correspond to the height and width of the bias potential and d_{0w}^2 is the distance between state w and the density currently undergoing optimisation. A biased Fock matrix can then be defined as

$$F'_{\mu\nu} = F_{\mu\nu} + \sum_w {}^w P_{\mu\nu} N_w \lambda_w e^{-\lambda_w d_{0w}^2} \quad (2.10)$$

and used in a conventional SCF calculation without further modification.²⁰ This biased Fock matrix encourages SCF convergence away from previously located solutions. Starting from initial values $N_w = \lambda_w = 1$, the parameters can be increased if the bias is insufficient. The bias is turned off when a density is close to an optimal solution to allow the unperturbed solution to be identified.

Although SCF metadynamics was primarily developed to locate the global minimum of the HF energy surface, combining it with methods for targeting excited states (including MOM) allows any type of HF stationary point to be identified. This has been most widely used to locate multiple HF states corresponding to diabatic states in molecular systems,^{25,33} and has been extended to construct an embedding approach for excited states.¹³³

2.3 Nonorthogonal Configuration Interaction

2.3.1 Introduction

Inspired by the diabatic nature of HF states, recent research has focussed on combining multiple HF solutions to construct multiconfigurational wave functions.^{25,31,32,134} Since each HF stationary state corresponds to an individually optimised Slater determinant built from a different set of molecular orbitals, multiple solutions are not required to be mutually orthogonal and the multiconfigurational expansion takes the form of

a nonorthogonal CI (NOCI) wave function.²⁵ In principle, combining individually optimised determinants allows NOCI to provide tailored description for each dominant configuration,²⁵ while also capturing orbital relaxation effects in excited-state wave functions.^{31,34,135} NOCI therefore represents a complementary approach to the orthogonal multireference methods described in Section 1.4, and has been found to recover adiabatic states with similar qualitative features to CASSCF.^{25,136} Significantly, NOCI avoids the need to select active orbitals in CASSCF, although a relevant set of nonorthogonal basis states must be identified instead.

The NOCI wave function is constructed as a linear combination of n_{det} mutually non-orthogonal basis states $\{|^x\Psi\rangle\}$ as

$$|\Psi_{\text{NOCI}}\rangle = \sum_x^{n_{\text{det}}} |^x\Psi\rangle c_x. \quad (2.11)$$

Each state $|^x\Psi\rangle$ corresponds to a single Slater determinant built from N occupied molecular orbitals (MOs), $\{|^x\psi_i\rangle\}$, which themselves are formed from a linear combination of $2n$ (non-orthogonal) atomic spin orbitals (AOs), $\{|\eta_\mu\rangle\}$, as

$$|^x\psi_i\rangle = \sum_\mu^{2n} C_{\cdot i}^{\mu \cdot x} |\eta_\mu\rangle, \quad (2.12)$$

where n is the size of the spatial basis set. The NOCI eigenstates are identified by solving the generalised eigenvalue problem

$$\sum_x^{n_{\text{det}}} (H^{wx} - ES^{wx}) c_x = 0, \quad (2.13)$$

where $H^{wx} = \langle {}^w\Psi | \hat{H} |^x\Psi \rangle$ and $S^{wx} = \langle {}^w\Psi | ^x\Psi \rangle$ are the Hamiltonian and overlap matrix elements in the non-orthogonal basis.²⁰ The matrix elements H^{wx} and S^{wx} are computed by building a biorthogonal set of orbitals using Löwdin's pairing approach^{137,138} and then applying the generalised Slater–Condon⁴⁰ rules as described in Appendix C. This approach allows the NOCI energy to be identified with a computational scaling of $\mathcal{O}(n_{\text{det}}^2 \max(N^3, n^2))$, which is not much greater than a single HF calculation.

As an inherently multireference approach, NOCI is well-suited to capturing static correlation effects. In particular, including all degenerate symmetry-broken HF states in the NOCI basis allows the partial restoration of broken symmetries, providing improved quantum numbers that allow physical interpretation of the wave function.^{31,139} Furthermore, the individual mean-field optimisation of HF states in the NOCI expansion enables a more balanced treatment of multi-electron excitations,³¹ core excitations,^{34,35} electronic coupling,¹⁴⁰ transition metal complexes,¹³⁹ and charge transfer processes.³³ The nonorthogonality of the NOCI basis can also lead to more compact multiconfigurational expansions that provide guess orbitals for active space methods,¹⁴¹ or trial nodal surfaces for quantum Monte-Carlo.^{142,143}

2.3.2 Generating the NOCI Basis

Among the advantages of NOCI over CASSCF is that it avoids the need to select an active set of molecular orbitals. However, a suitable set of expansion configurations must still be identified and can be more challenging than conventional CI. Since each basis state is often built from a different set of molecular orbitals, they cannot be easily related through the concept of electron excitation levels. Instead, current methods of constructing the NOCI basis include randomly searching the HF solution space^{20,25} or using orbital-relaxed excitations from a symmetry-pure HF state.³¹ Both of these approaches have their own advantages and disadvantages, and an optimal approach for identifying the NOCI basis remains an ongoing area of research.

2.3.2.1 Symmetry-Broken Determinants

Initial implementations of NOCI were focussed around exploiting the diabatic nature of symmetry-broken determinants to construct multireference wave functions.²⁵ The determinants used in the NOCI expansion therefore corresponded to low-lying HF states that could be identified using the SCF metadynamics approach.²⁰ In many cases these HF states were symmetry-broken solutions that can describe the correct energy in strongly correlated regions while retaining a mean-field wave function.²⁰ Crucially, including a suitable combination of symmetry-broken HF states in the NOCI expansion allows symmetry-pure wave functions to be recovered.¹³⁹ Furthermore, the superior energy of these symmetry-broken determinants allows the NOCI wave function to capture static electron correlation through a more efficient and compact multireference expansion.

Identifying multiple symmetry-broken HF states corresponding to local minima of the HF energy is made significantly easier using SCF metadynamics. However, as a stochastic method, there is no guarantee that SCF metadynamics will locate the global minimum or the most important determinants for the NOCI expansion. For example, once a symmetry-broken solution has been identified, its symmetry-related copies must often be computed by subsequently applying the relevant symmetry operators.¹³⁹ Furthermore, it is possible for symmetry-broken determinants to coalesce at a Coulson–Fischer point along the potential energy surface, leading to discontinuities in the NOCI energy.²⁵ Constructing the NOCI expansion basis using SCF metadynamics is therefore only a partially ‘black-box’ approach and can often be unreliable.

2.3.2.2 Spin-Flip

Spin-flip NOCI (SF-NOCI)³² targets strong static correlation by building the NOCI expansion basis using an approach inspired by the spin-flip family of methods.¹⁴⁴ Starting from an optimised high-spin ROHF wave function, an active space is defined as the set of all partially occupied orbitals. These ROHF orbitals are believed to provide a better estimate of statically correlated singlet and triplet orbitals than a conventional RHF wave function.¹⁴⁴ A set of active space configurations is then constructed using every possible arrangement of electrons in the active orbitals with $m_s = 0$. At this stage, the set of multiple determinants is equivalent to the spin-flip CAS approach.¹⁴⁵ Taking each spin-flipped determinant as an initial guess, the orbitals outside the active space are then optimised through a 'frozen active-space SCF' procedure, and the resulting partially-optimised determinants are used to define the NOCI basis.

Since every determinant has a different active space, these SCF optimisations cannot converge onto the same HF state and the size of the NOCI expansion basis is fixed by the number of active-space configurations. Furthermore, relaxing only the doubly-occupied closed-shell orbitals with frozen active orbitals ensures that spin-contamination is completely removed in the NOCI wave function. The resulting method is therefore well-defined given the multiplicity of the high-spin reference, and its performance has been demonstrated for predicting ferromagnetic coupling in bimetallic complexes.³² However, SF-NOCI relies on the identification of a suitable ROHF determinant from which to build the nonorthogonal configurations, and this is not always a trivial task.

2.3.2.3 Single Excitations

To target core excitation energies, an approach has been developed that generates the NOCI basis using single excitations (NOCIS).^{34,35} Core excitations present an interesting challenge as they require the relaxation of core orbitals when an electron has been removed. Starting from the ground-state HF solution, an electron in the target core orbital can be removed to generate a positively charged high-spin determinant. This determinant is then optimised at the ROHF level to relax the remaining orbitals in the presence of the vacant core orbital. Finally, a set of singly excited determinants are constructed by reattaching the electron in every possible virtual orbital.³⁴

Since each core orbital is doubly occupied, both the α and β excitations must be considered in this approach. In general the ROHF optimisation of the cationic state will differ depending on the spin of the removed electron. As a result, the combined set of neutral configurations will form two groups of determinants that are orthogonal to each other within each group but nonorthogonal to the determinants in the other

group. In this sense, the final combination of every possible excited state forms a NOCI expansion.³⁴ This approach has been shown to provide improved core excitations relative to alternative methods such as CIS and TD-DFT, and can be used to interpret x-ray absorption spectra.³⁴ However, like SF-NOCI, the use of partially-optimised determinants in NOCIS limits the accuracy of the electron correlation it can capture.

2.3.3 Adding Dynamic Correlation to NOCI

While current NOCI approaches can provide suitable multireference wave functions for capturing static correlation effects, their practical applications are limited by a lack of significant dynamic correlation. To reach quantitative accuracy, recent research has sought to introduce dynamic correlation through perturbative corrections^{134,146,147} or a nonorthogonal analogue of MRCI.¹⁴⁸ However, the lack of orthogonality between molecular orbitals of different NOCI determinants makes these approaches far more computationally expensive than their orthogonal counterparts.

2.3.3.1 NOCI-MP2 Perturbation Theory

Perturbatively adding dynamic correlation to the NOCI wave function was first introduced as the Δ SCF(2) method¹³⁴ and later renamed “NOCI-MP2”.¹⁴⁶ To overcome the ambiguity of defining a reference Hamiltonian for the NOCI wave function, a ‘perturb-then-diagonalise’ approach is taken where the basis states are perturbed before the NOCI problem is solved. In particular, each determinant in the NOCI basis is expanded to first-order using single-reference Møller–Plesset theory to give the modified NOCI basis $\{|^w\Psi\rangle\} = \{|^w\Psi^{(0)}\rangle + |^w\Psi^{(1)}\rangle\}$.¹³⁴ Retaining only the leading correction terms, the NOCI Hamiltonian and overlap matrix elements are then computed as

$$\langle ^w\Psi | \hat{H} | ^x\Psi \rangle = \langle ^w\Psi^{(0)} | \hat{H} | ^x\Psi^{(0)} \rangle + \frac{1}{2} \left(\langle ^w\Psi^{(0)} | \hat{H} | ^x\Psi^{(1)} \rangle + \langle ^w\Psi^{(1)} | \hat{H} | ^x\Psi^{(0)} \rangle \right) \quad (2.14a)$$

$$\langle ^w\Psi | ^x\Psi \rangle = \langle ^w\Psi^{(0)} | ^x\Psi^{(0)} \rangle + \frac{1}{2} \left(\langle ^w\Psi^{(0)} | ^x\Psi^{(1)} \rangle + \langle ^w\Psi^{(1)} | ^x\Psi^{(0)} \rangle \right), \quad (2.14b)$$

where the correction terms are averaged to ensure that the diagonal of the Hamiltonian corresponds to the MP2 energy of each determinant.¹⁴⁶ Through this expansion, NOCI-MP2 is able to capture dynamic correlation in ground and excited states while retaining accurate representations of conical intersections.¹³⁴

However, it was later realised that the original NOCI-MP2 matrix elements (2.14) lead to the loss of size-consistency in the NOCI diagonalisation.¹⁴⁶ This failure can be attributed to the absence of higher-order coupling terms. As a solution, Ref. (146) introduced two potential modifications to the Hamiltonian and overlap matrix elements between the reference states and first-order wave functions. In the first approach, referred

to as “*version 1*”, the overlap terms were simply ignored by defining $\langle {}^w\Psi^{(0)} | {}^x\Psi^{(1)} \rangle = 0$. Alternatively, the second approach, “*version 2*”, retained all overlap terms but redefined the coupling Hamiltonian matrix elements as

$$\langle {}^w\Psi^{(0)} | \hat{H} | {}^x\Psi^{(1)} \rangle = \langle {}^w\Psi^{(0)} | \hat{H} | {}^x\Psi^{(1)} \rangle + {}^wE_{\text{MP2}} \langle {}^w\Psi^{(0)} | {}^x\Psi^{(1)} \rangle, \quad (2.15)$$

where ${}^wE_{\text{MP2}}$ is the MP2 energy of the reference determinant w . The working equations for each version are summarised in Table II of Ref. (146). Size-consistent formulations of NOCI-MP2 have since been applied to study singlet-triplet gaps in biradical molecules¹⁴⁶ and dispersion interactions between bulky hydrocarbon molecules.¹⁴⁷

2.3.3.2 Nonorthogonal Configuration Interaction Singles and Doubles

As an alternative to perturbation theory, a nonorthogonal analogue of MRCISD has been proposed in Ref. (148). The resulting NOCISD wave function can in general be built using the combined set of single and double excitations from each reference as

$$|\Psi_{\text{NOCISD}}\rangle = \sum_w^{n_{\text{ref}}} \left[c_w |{}^w\Psi\rangle + \sum_{ia} (c_w)_i^a |({}^w\Psi)_i^a\rangle + \sum_{\substack{i<j \\ a<b}} (c_w)_{ij}^{ab} |({}^w\Psi)_{ij}^{ab}\rangle \right], \quad (2.16)$$

where the coefficients $\{c_w, (c_w)_i^a, (c_w)_{ij}^{ab}\}$ are determined by solving the corresponding generalised eigenvalue problem. In practice, directly solving the full eigenvalue problem is difficult due to the potential presence of redundancies and singularities in the overlap matrix. Instead, the authors propose a contracted scheme where the standard CISD problem for each reference determinant is iteratively solved and a subset of the eigenvectors are used to build a lower-dimensional generalised eigenvalue problem.¹⁴⁸ The corresponding NOCISD energies are then found to converge rapidly with respect to the number of retained eigenvectors for the systems studied. However, the NOCISD energy still retains a reasonably large error for many systems, although this is attributed to an inadequate reference NOCI wave function.¹⁴⁸

2.3.4 Current Limitations

Despite the recent developments in NOCI methods, it has not yet found widespread applications for molecular systems. The major limitation of current NOCI approaches is still the definition of a general scheme for identifying expansion determinants. While selecting configurations from active orbitals in CASSCF provides a flexible approach for a range of systems, the current NOCI selection schemes are much more specialised to specific chemical situations. Furthermore, one major advantage of NOCI is the ability to include symmetry-broken determinants that introduce additional variational flexibility

into the wave function.^{20,25} However, identifying symmetry-broken states is not easily automated and, while this can be achieved using SCF metadynamics, it is far from an optimal procedure. In contrast, systematic approaches that relax orthogonal excitations from of a symmetry-pure reference state (e.g. SF-NOCI or NOCIS) usually ignore the possibility of symmetry-broken solutions. This absence of symmetry-broken solutions prevents NOCI from being used to its full potential and leads to less substantial energy relaxation on top of orthogonal CI expansions.

The second major limitation of current NOCI methods arises from the need to identify the HF solutions across the full potential energy surface. Once a suitable set of symmetry-pure and symmetry-broken states has been identified, these solutions can coalesce and disappear at Coulson–Fischer points.²⁴ When a HF state disappears at a Coulson–Fischer point, there is a sudden change in the size of the NOCI basis that can lead to kinks or discontinuities in the NOCI energy.²⁵ These effects severely limit the applications of NOCI using multiple HF states and prevent the computation of smooth potential energy surfaces across all molecular geometries.

In the SF-NOCI method, coalescing HF states are avoided by using partially-optimised HF wave functions constructed through the spin-flip formalism.³² However, this type of approach relies on a smoothly evolving and well-defined spin-flip active space across all molecular geometries. In contrast, one recently proposed alternative involves extending fully-optimised HF states beyond Coulson–Fischer points by considering the real HF equations in the complex-plane.^{38,39} Using a modified ‘holomorphic’ HF energy function, preliminary studies have found that complex extensions of real HF states can be identified for all geometries in the minimal basis H₂ molecule.^{38,39} These complex extensions can in principle be used to define a continuous basis for NOCI that entirely removes the issues associated with states disappearing at a Coulson–Fischer point.³⁹ Developing this alternative approach into a general NOCI method for constructing potential energy surfaces is the primary focus of this thesis.

Finally, even if a suitable and continuous NOCI basis can be identified across all molecular structures, the NOCI expansion still accounts mainly for static correlation energy.³² While NOCI-MP2^{134,146,147} and NOCISD¹⁴⁸ provide useful routes towards incorporating additional dynamic correlation, there is still a large scope for improving post-NOCI approaches. For example, the current NOCI-MP2 perturbative correction requires *ad hoc* modifications to ensure that the NOCI matrix elements retain the correct symmetries and the energy remains size-extensive.^{134,146} Deriving a ‘diagonalise-then-perturb’ NOCI approach similar to CASPT2^{75,76} could provide a more rigorous and well-defined perturbative correction. Furthermore, this type of rigorous post-NOCI perturbation theory would reduce to CASPT2 for a suitably chosen orthogonal set

of expansion determinants, suggesting a promising route for extending the general accuracy of CASPT2 to NOCI wave functions. This form of perturbative correction to NOCI is explored in Chapter 8.

Part II

Development

Chapter 3

Formulating Holomorphic Hartree–Fock

Summary

Constructing multireference NOCI wave functions using multiple HF states has previously been hindered by the disappearance of HF solutions as the molecular structure changes, creating discontinuities in the NOCI energy.²⁵ To remove these discontinuities, holomorphic HF (h-HF) has recently been proposed in Refs. (38) and (39) as a way of extending HF solutions across all molecular structures. In h-HF theory, the complex conjugation of orbital coefficients is removed from the conventional HF equations to construct a complex-analytic continuation of real HF. When real HF states disappear, their h-HF counterparts continue to exist with complex-valued orbital coefficients and provide a continuous basis for NOCI. This chapter extends h-HF theory beyond the initial proof-of-principle studies into a general theoretical framework. The mathematical properties and differential geometry of the h-HF approximation are derived, laying the foundations for developing h-HF into a general computational tool for extending real HF states across all molecular structures.

3.1 Context and Scope

Predicting the energy of molecules with competing electronic configurations requires the use of multireference approaches that can account for strongly coupled configurations.^{71,94} Traditionally, such calculations have been approached using the MRCI and MCSCF frameworks, however these are known to suffer from a lack of size-consistency and high-order polynomial scaling.⁹⁴ Alternatively, the recently developed NOCI method exploits the existence of multiple HF solutions to define an entirely new multireference framework.^{25,31} In NOCI, each HF solution in the CI expansion is individually optimised at the mean-field level with its own bespoke set of orbitals, avoiding the coupled SCF and CI optimisation of MCSCF approaches.²⁵

However, the disappearance of real HF states at Coulson–Fischer points has been found to create unphysical discontinuities and ‘kinks’ in the NOCI energy that prevent the computation of molecular binding curves and reaction trajectories.²⁵ To remove these discontinuities, Thom and Head–Gordon suggested that HF states may need to be followed into the complex plane beyond the points at which they vanish.²⁵ The conventional way to extend HF theory into the complex plane is through complex HF (c-HF).³⁶ In c-HF, the molecular orbital coefficients are allowed to become complex variables and the SCF procedure optimises the energy with respect to the real and imaginary parts of these coefficients. However, while c-HF solutions are known to exist,^{36,37} they do not correspond to the required complex-valued extensions of real HF solutions beyond Coulson–Fischer points.

Instead an entirely new theory — holomorphic HF (h-HF) — has been proposed to extend real HF states into the complex plane.^{38,39} In the h-HF approach, the molecular orbital coefficients are allowed to become complex *without* introducing their complex-conjugates into the HF energy. As a result, the h-HF energy forms a complex-analytic function of the orbital coefficients, and is believed to retain a constant number of stationary points across all molecular structures. Crucially, when real HF states disappear at a Coulson–Fischer point, their holomorphic counterparts appear to smoothly continue with complex orbital coefficients.³⁸

While the original proof-of-principle studies provide a conceptual outline for h-HF, there are many mathematical properties of the theory still to be understood. For example, the mathematical properties of the h-HF energy function and the structure of the h-HF orbital constraint surface are yet to be formally derived. If NOCI is to be routinely applied to general molecular systems using h-HF states, then a rigorous mathematical formulation of h-HF will be essential. Formally deriving h-HF theory and understanding its mathematical properties therefore forms the focus of the current

chapter.

3.2 Review of Prior Work

3.2.1 Single-Variable Hydrogen Dimer

Hiscock and Thom first introduced h-HF theory in Ref. (38). Here, the existence of multiple UHF solutions in the hydrogen molecule are investigated using a minimal basis comprising a single atomic orbital on each hydrogen, for which an explicit energy function can be parametrised as a single-variable polynomial. For the $m_s = 0$ manifold, the α and β occupied orbitals can be constructed as

$$\psi_\alpha(\mathbf{r}, \sigma) = \psi_\alpha(\mathbf{r})\alpha(\sigma), \quad (3.1a)$$

$$\psi_\beta(\mathbf{r}, \sigma) = \psi_\beta(\mathbf{r})\beta(\sigma), \quad (3.1b)$$

where ψ_α and ψ_β represent spatial component of the α and β spin-orbitals respectively. To capture the symmetry breaking observed by Coulson and Fischer,²⁴ the spatial orbitals are expanded in terms of the (orthogonal) molecular orbital basis $\{\sigma_g(\mathbf{r}), \sigma_u(\mathbf{r})\}$ using the single complex parameter $z \in \mathbb{C}$ as

$$\phi_\alpha(\mathbf{r}) = \frac{1}{\sqrt{1+|z|^2}}\sigma_g(\mathbf{r}) + \frac{z}{\sqrt{1+|z|^2}}\sigma_u(\mathbf{r}), \quad (3.2a)$$

$$\phi_\beta(\mathbf{r}) = \frac{1}{\sqrt{1+|z|^2}}\sigma_g(\mathbf{r}) - \frac{z}{\sqrt{1+|z|^2}}\sigma_u(\mathbf{r}). \quad (3.2b)$$

Clearly, the RHF σ_g^2 state is recovered when $z = 0$, while any other finite z -value represents a symmetry-broken UHF state with the α and β electrons becoming localised on separate atoms. Note that, in this representation, the RHF antibonding σ_u^2 configuration corresponds to the limit $z \rightarrow \infty$ and is therefore ignored.

Using this parametrisation, the conventional HF energy is given by

$$E_{\text{HF}}(z) = \frac{2}{1+z\bar{z}}(h_{\text{gg}} + z\bar{z}h_{\text{uu}}) + \frac{1}{(1+z\bar{z})^2} \times \left[\langle \text{gg} | \text{gg} \rangle + 2z\bar{z} \langle \text{gu} | \text{gu} \rangle - (z^2 + \bar{z}^2) \langle \text{gg} | \text{uu} \rangle + (z\bar{z})^2 \langle \text{uu} | \text{uu} \rangle \right], \quad (3.3)$$

where \bar{z} denotes the complex conjugate of z and the one- and two-electron integrals are expressed in the molecular orbital basis. Since Eq. (3.3) is a rational function of two polynomials, it is tempting to apply the Fundamental Theorem of Algebra to prove that the number of stationary points must be constant regardless of the one- and two-electron integral values. However, in applying this theorem, it is understood that some roots can

appear in the complex plane. As a result, although Eq. (3.3) is a strictly real function, it must be considered as a complex function with a single complex variable z .

Crucially, the Fundamental Theorem of Algebra can only be applied to a complex-analytic polynomial function of a single complex variable. For a function to be a complex-analytic with well-defined complex derivatives — known as a *holomorphic* function — it must satisfy the Cauchy–Riemann conditions.¹⁴⁹ The simplest form of these conditions states that a complex differentiable function must have no dependence on \bar{z} . Clearly the conventional HF (3.3) fails this condition and the Fundamental Theorem of Algebra cannot be applied. There is therefore no guarantee that the number of real and complex HF stationary points is constant.

Instead, Hiscock and Thom suggest removing the complex conjugate (i.e. $\bar{z} \rightarrow z$) to construct a holomorphic complex polynomial that depends on only z , defining the ‘holomorphic’ HF energy as

$$\begin{aligned} \tilde{E}_{\text{HF}}(z) &= \frac{2}{1+z^2}(h_{\text{gg}} + z^2 h_{\text{uu}}) + \frac{1}{(1+z^2)^2} \\ &\times \left[\langle \text{gg} | \text{gg} \rangle + 2z^2 (\langle \text{gu} | \text{gu} \rangle - \langle \text{gg} | \text{uu} \rangle) + z^4 \langle \text{uu} | \text{uu} \rangle \right]. \end{aligned} \quad (3.4)$$

This energy function is now complex-valued in general, although when z is real, $\tilde{E}_{\text{HF}}(z)$ coincides exactly with $E_{\text{HF}}(z)$. All conventional real HF solutions therefore remain stationary points of the h-HF energy. As a holomorphic function, the Fundamental Theorem of Algebra can be applied to show that three stationary points exist *for all molecular structures* and finite z ; when the conventional UHF solutions disappear at the Coulson–Fischer point, their holomorphic counterparts continue to exist with complex z . Hiscock and Thom then illustrate the existence of these complex extensions for the real HF solutions in H_2 . Finally, they demonstrate that including the h-HF states in the NOCI basis removes unphysical discontinuities in the NOCI energy and recovers an entirely smooth binding curve.³⁸

3.2.2 Holomorphic Self-Consistent-Field Approach

In practice, the conventional HF equations are solved using the iterative SCF approach.⁸ To extend h-HF theory beyond the single-variable case, Burton and Thom introduced a holomorphic SCF procedure for h-UHF theory in Ref. (39). Working in an orthogonal spatial basis with dimension n , the conventional SCF approach is modified by introducing holomorphic one-particle density matrices as

$${}^{\alpha} \tilde{P}^{v\mu} = \sum_i^{N_{\alpha}} ({}^{\alpha} C)_{\cdot i}^v ({}^{\alpha} C)_{i \cdot}^{\mu}, \quad \text{and} \quad {}^{\beta} \tilde{P}^{v\mu} = \sum_i^{N_{\beta}} ({}^{\beta} C)_{\cdot i}^v ({}^{\beta} C)_{i \cdot}^{\mu}, \quad (3.5)$$

where the complex-conjugation of orbital coefficients has been removed *ad hoc* from the conventional density matrix (1.29). Using these density matrices, the h-UHF energy function can then be expressed as

$$\begin{aligned} \tilde{E}_{\text{HF}} = & V_{\text{N}} + \sum_{\mu\nu}^n \tilde{P}^{\nu\mu} h_{\mu\nu} \\ & + \frac{1}{2} \sum_{\mu\nu\sigma\tau}^n \left[\tilde{P}^{\nu\mu} \langle \mu\sigma | \nu\tau \rangle \tilde{P}^{\tau\sigma} - \left(\alpha \tilde{P}^{\nu\mu} \alpha \tilde{P}^{\sigma\tau} + \beta \tilde{P}^{\nu\mu} \beta \tilde{P}^{\sigma\tau} \right) \langle \mu\sigma | \tau\nu \rangle \right], \end{aligned} \quad (3.6)$$

where the total holomorphic density matrix is defined as $\tilde{P}^{\nu\mu} = \alpha \tilde{P}^{\nu\mu} + \beta \tilde{P}^{\nu\mu}$. Furthermore, the authors suggest removing the complex-conjugation of orbital coefficients from the holomorphic normalisation constraint to give

$$\sum_{\mu}^n (\alpha C)_{i\cdot}^{\cdot\mu} (\alpha C)_{\cdot i}^{\mu\cdot} = 1 \quad \text{and} \quad \sum_{\mu}^n (\beta C)_{i\cdot}^{\cdot\mu} (\beta C)_{\cdot i}^{\mu\cdot} = 1, \quad (3.7)$$

although no rigorous justification is provided.

Having constructed a density matrix form of the h-UHF energy function, holomorphic Fock matrices can then be introduced as

$$\alpha \tilde{F}_{\mu\nu} = h_{\mu\nu} + \sum_{\sigma\tau}^n \left[\tilde{P}^{\tau\sigma} \langle \mu\sigma | \nu\tau \rangle - \alpha \tilde{P}^{\tau\sigma} \langle \mu\sigma | \tau\nu \rangle \right], \quad (3.8a)$$

$$\beta \tilde{F}_{\mu\nu} = h_{\mu\nu} + \sum_{\sigma\tau}^n \left[\tilde{P}^{\tau\sigma} \langle \mu\sigma | \nu\tau \rangle - \beta \tilde{P}^{\tau\sigma} \langle \mu\sigma | \tau\nu \rangle \right]. \quad (3.8b)$$

Notably, these holomorphic Fock matrices are complex-symmetric rather than Hermitian, and can possess complex-valued eigenvalues corresponding to the holomorphic orbital energies.³⁹ As a result, the conventional *aufbau* selection of the new occupied orbitals on each iteration cannot be applied as the complex orbital eigenvalues are unorderable. Instead, Burton and Thom propose a modified holomorphic version of the MOM method²⁶ where the new occupied orbitals are selected as those with the greatest “holomorphic overlap” with the previous occupied orbitals, defined as

$$\Omega_{ij} = \sum_{\mu}^n (C^{\text{new}})_{i\cdot}^{\cdot\mu} (C^{\text{old}})_{\cdot j}^{\mu\cdot}. \quad (3.9)$$

A complex variant of the DIIS (direct inversion of the iterative subspace) extrapolation technique^{150,151} is then introduced to accelerate convergence of the holomorphic SCF procedure, although again no rigorous justification is provided.

Finally, the complete holomorphic SCF approach is defined as follows:

1. Begin with an initial set of (complex) coefficients $C_{i\cdot}^{\cdot\mu}$;
2. Form the one-particle holomorphic density matrices (3.5);

3. Construct the holomorphic Fock matrices (3.8) and apply DIIS extrapolation;
4. Diagonalise the holomorphic Fock matrices to generate a new set of orbitals;
5. Compute the holomorphic overlap (3.9) between old and new orbitals to select the new occupied orbitals;
6. Repeat steps 2–5 until convergence is reached.

Crucially, the similarity between the holomorphic and conventional SCF procedures ensures that the only increase in computational cost arises from handling complex, rather than real, orbital coefficients. The authors then apply this procedure to the H_2 , H_4^{2+} , and H_4 molecules, where complex-valued h-UHF extensions are identified for every real HF state that disappears at a Coulson–Fischer point.³⁹ They find that every real HF state remains a stationary point of the h-HF energy and, when real HF states vanish at a Coulson–Fischer point, their h-HF counterparts continue to exist with complex orbital coefficients. Furthermore, it is shown that combining multiple real HF states and their complex holomorphic counterparts in NOCI ensures smooth ground and excited states across all molecular structures, and these are found to provide accurate approximations to the corresponding FCI energies.³⁹

3.3 Generalising Holomorphic Hartree–Fock

The two original studies on h-HF theory provide a promising starting point for constructing complex extensions to real HF states that disappear at Coulson–Fischer points.^{38,39} However, developing the h-HF approach from a novel concept to a computational tool requires a deeper mathematical understanding of the theory itself. In the remainder of this chapter, a generalised derivation of h-HF theory from the conventional HF approach is presented, and its mathematical properties are characterised. This formal derivation lays the foundation for combining h-HF theory and NOCI into a general computational approach later in this thesis.

3.3.1 Complex-Analytic Hartree–Fock Energy

Before generalising h-HF theory, it is useful to consider the mathematical properties of the conventional HF approach and why solutions of the real HF equations disappear in the first place. For mathematical clarity (and without loss of generality), the orbitals are expanded in a real $2n$ -dimensional spin-orbital basis

$$\{\eta(\mathbf{x})\} = \{\chi(\mathbf{r})\} \otimes \{\alpha(\sigma), \beta(\sigma)\} \quad (3.10)$$

where $S_{\mu\nu} = \langle \eta_\mu | \eta_\nu \rangle$ defines the overlap (metric) tensor and n is the number of spatial basis functions. Using the nonorthogonal tensor notation of Head–Gordon *et al.*⁴¹ the molecular orbitals are parametrised by the coefficients $C_{:i}^{\mu\cdot}$ as

$$\psi_i(\mathbf{x}) = \sum_{\mu}^{2n} \eta_{\mu}(\mathbf{x}) C_{:i}^{\mu\cdot}, \quad (3.11)$$

and the orthonormalisation constraint is given by

$$\langle \psi_i | \psi_j \rangle = \sum_{\mu\nu}^{2n} (C^*)_{:i}^{\mu\cdot} S_{\mu\nu} C_{:j}^{\nu\cdot} = \delta_{ij}. \quad (3.12)$$

Building a single Slater determinant with this orbital parametrisation for a system of N electrons, and allowing complex orbital coefficients $C_{:i}^{\mu\cdot} \in \mathbb{C}$, the conventional (Hermitian) HF energy is given by

$$E = V_N + \sum_i^N \sum_{\mu\nu}^{2n} (C^*)_{:i}^{\mu\cdot} h_{\mu\nu} C_{:i}^{\nu\cdot} + \frac{1}{2} \sum_{ij}^N \sum_{\mu\nu\sigma\tau}^{2n} (C^*)_{:i}^{\mu\cdot} (C^*)_{:j}^{\sigma\cdot} \langle \mu\sigma || \nu\tau \rangle C_{:i}^{\nu\cdot} C_{:j}^{\tau\cdot}, \quad (3.13)$$

where $h_{\mu\nu}$ and $\langle \mu\nu || \sigma\tau \rangle$ denote the one- and two-electron integrals in the spin-orbital basis $\{\eta(\mathbf{x})\}$. Notably, the energy (3.13) is a fourth-order polynomial with respect to the orbital coefficients and their complex conjugates. This non-linearity represents the self-consistency in the HF equations. By introducing the Hermitian density matrix

$$P^{\nu\mu} = \sum_i^N C_{:i}^{\nu\cdot} (C^*)_{:i}^{\mu\cdot} \quad (3.14)$$

the energy (3.13) can be reduced to

$$E = V_N + \sum_{\mu\nu}^{2n} h_{\mu\nu} P^{\nu\mu} + \frac{1}{2} \sum_{\mu\nu\sigma\tau}^{2n} P^{\nu\mu} \langle \mu\sigma || \nu\tau \rangle P^{\tau\sigma}. \quad (3.15)$$

Conventional HF solutions are then identified as the stationary points of E with respect to changes in the density matrix or orbital coefficients under the orthogonality constraint (3.12).⁸

For real HF coefficients, Eq. (3.13) forms a real-analytic polynomial of the orbital coefficients $C_{:i}^{\mu\cdot} \in \mathbb{R}$ and real orbital gradients can be identified. Stationary points are then given as the roots of real polynomials representing the constrained derivatives of E with respect to the orbital coefficients.^{21,152} However, as these are polynomial functions of strictly real variables, the Fundamental Theorem of Algebra cannot be applied. Furthermore, the non-linearity of Eq. (3.13) means that the stationary points of the real HF energy cannot be mapped onto an exact linear eigenvalue problem, and there is no guarantee that the number of solutions is constant across all geometries.

Alternatively, when the orbital coefficients are extended to the complex plane $C_{.i}^{\mu} \in \mathbb{C}$, the energy (3.13) becomes a polynomial of several complex variables $\{C_{.i}^{\mu}\}$ and their complex conjugates $\{(C^*)_{.i}^{\mu}\}$. Therefore, Eq. (3.13) is not a complex-analytic function since its dependence on both the orbital coefficients and their complex conjugates violates the Cauchy–Riemann conditions.¹⁴⁹ As a result, there are no well-defined complex gradients or complex stationary points on the energy surface. The conventional HF energy surface must instead be considered as a function of the real variables $X_{.i}^{\mu}, Y_{.i}^{\mu} \in \mathbb{R}$, where $C_{.i}^{\mu} = X_{.i}^{\mu} + iY_{.i}^{\mu}$. By decomposing the complex orbital coefficients into these real and imaginary components, the HF energy is transformed from a non-complex-analytic real function of complex variables to a real-analytic function with twice as many variables. Consequently, even in the complex (Hermitian) HF framework, the HF energy function and its derivatives remain real-valued functions of real variables and there is still no guarantee that solutions must exist across all molecular geometries.

Instead, constructing an approach where the real-valued stationary points extend into the complex-plane requires a complex-analytic energy function of complex-variables. This complex-analytic function will then have well-defined derivatives with respect to the orbital coefficients represented by complex-analytic polynomials, and it is likely that a generalisation of the Fundamental Theorem of Algebra will be applicable (see Chapter 4). Such an approach can be achieved by allowing the orbital coefficients $C_{.i}^{\mu}$ to become complex-valued *without* introducing the complex conjugate in Eq. (3.13). This is equivalent to allowing the real component of $C_{.i}^{\mu}$ to become complex, i.e. $X_{.i}^{\mu} \in \mathbb{C}$, while keeping the imaginary component zero $Y_{.i}^{\mu} = 0$. The resulting h-HF energy \tilde{E} is then given by

$$\tilde{E} = V_N + \sum_i^N \sum_{\mu\nu}^{2n} C_{.i}^{\mu} h_{\mu\nu} C_{.i}^{\nu} + \frac{1}{2} \sum_{ij}^N \sum_{\mu\nu\sigma\tau}^{2n} C_{.i}^{\mu} C_{.j}^{\sigma} \langle \mu\sigma || \nu\tau \rangle C_{.i}^{\nu} C_{.j}^{\tau}, \quad (3.16)$$

where now $C_{.i}^{\mu} = X_{.i}^{\mu}$. This definition of the h-HF energy provides the generalisation to Eq. (3.3) for molecular systems with several degrees of freedom. Crucially, Eq. (3.16) now forms a complex-valued polynomial of several complex variables (without their complex conjugates) and satisfies the Cauchy–Riemann conditions. As a result, complex-gradients and stationary points can be defined although, as a complex-valued energy surface, the concept of ‘minima’ and ‘maxima’ is lost. Furthermore, as a fully complex-analytic function with stationary points represented by the roots of polynomial derivatives, it is reasonable to believe that every stationary state will exist across all geometries.

By introducing the generalised holomorphic density matrix

$$\tilde{P}^{\nu\mu} = \sum_i^N C_{.i}^{\nu} C_{.i}^{\mu}, \quad (3.17)$$

the density matrix form of the h-HF energy can be defined as

$$\tilde{E} = V_N + \sum_{\mu\nu} h_{\mu\nu} \tilde{P}^{\nu\mu} + \frac{1}{2} \sum_{\mu\nu\sigma\tau} \tilde{P}^{\nu\mu} \langle \mu\sigma || \nu\tau \rangle \tilde{P}^{\tau\sigma}, \quad (3.18)$$

providing the generalisation of the h-UHF energy defined in Ref. (39) . From the holomorphic density matrix, the holomorphic Fock matrix can be defined as

$$\tilde{F}_{\mu\nu} = h_{\mu\nu} + \sum_{\sigma\tau} \langle \mu\sigma || \nu\tau \rangle \tilde{P}^{\tau\sigma}. \quad (3.19)$$

Optimal stationary h-HF states are then given by the self-consistent eigenvectors of this Fock matrix

$$\sum_{\nu} \tilde{F}_{\mu\nu} C_{\cdot i}^{\nu} = \sum_{\nu} S_{\mu\nu} C_{\cdot i}^{\nu} \epsilon_{ii}, \quad (3.20)$$

where the orbital coefficients forming the density matrix are simultaneously the eigenvectors of the corresponding Fock matrix, and ϵ_{ii} is a diagonal matrix containing the eigenvalues of \tilde{F} . This self-consistent eigenvalue equation (3.20) provides the holomorphic equivalent of the Roothaan–Hall equations.^{46,47}

Furthermore, like the conventional HF equations, the holomorphic Fock and density matrices commute when self-consistency is reached. This can be demonstrated by expanding the density matrix in terms of the orbital coefficients and utilising the transpose of Eq. (3.20) to give

$$\begin{aligned} \sum_{\sigma\tau} \left[\tilde{F}_{\mu\sigma} \tilde{P}^{\sigma\tau} S_{\tau\nu} - S_{\mu\sigma} \tilde{P}^{\sigma\tau} \tilde{F}_{\tau\nu} \right] &= \sum_{\sigma\tau} \sum_i \left[\tilde{F}_{\mu\sigma} C_{\cdot i}^{\sigma} C_{\cdot i}^{\tau} S_{\tau\nu} - S_{\mu\sigma} C_{\cdot i}^{\sigma} C_{\cdot i}^{\tau} \tilde{F}_{\tau\nu} \right] \\ &= \sum_{\sigma\tau} \sum_i \left[S_{\mu\sigma} C_{\cdot i}^{\sigma} \epsilon_{ii} C_{\cdot i}^{\tau} S_{\tau\nu} - S_{\mu\sigma} C_{\cdot i}^{\sigma} \epsilon_{ii} C_{\cdot i}^{\tau} S_{\tau\nu} \right] \\ &= 0. \end{aligned} \quad (3.21)$$

As a result, defining the holomorphic analogue of the DIIS error vector as

$$\tilde{e}_{\mu\nu} = \sum_{\sigma\tau} \left[\tilde{F}_{\mu\sigma} \tilde{P}^{\sigma\tau} S_{\tau\nu} - S_{\mu\sigma} \tilde{P}^{\sigma\tau} \tilde{F}_{\tau\nu} \right], \quad (3.22)$$

justifies the use of the DIIS procedure^{150,151} for accelerating the holomorphic SCF method in Ref. (39) . The magnitude of this error vector also provides a metric for holomorphic SCF convergence.

Significantly, when the orbital coefficients are real, the h-HF equations reduce to the real HF equations and every real HF solution remains a stationary point of the h-HF energy. The h-HF framework can therefore be viewed as a “mathematically motivated” complex-analytic continuation¹⁵³ of the real HF equations that retains analytic working

equations while introducing a complex-valued energy. In contrast, the conventional complex HF equations provide a “physically motivated” extension of real HF that retains real-valued energies at the cost of losing analyticity. Since h-HF states are only needed to provide an intermediate basis for constructing the NOCI wave function, complex h-HF wave functions are only required to evolve smoothly and continuously from their real HF counterparts and there is no explicit need for real h-HF energies. Consequently, the generalised h-HF approach is ideally suited to the purpose of constructing complex continuations of real HF states beyond Coulson–Fischer points.

Finally, note that Eqs. (3.16)–(3.20) represent the most general form of h-HF theory where the orbital coefficients can take non-zero complex values for any spin-orbital in the molecular orbital expansion. This formalism represents the complex-analytic extension of the real GHF equations, defining the holomorphic GHF (h-GHF) approach. By applying restrictions on the orbital coefficients in the same way as those described in Section 2.2.2, it is possible to define holomorphic UHF (h-UHF) and holomorphic RHF (h-RHF) formalisms. For h-UHF theory, these restrictions recover the original h-HF equations presented in Ref. (39).

3.3.2 Holomorphic Orbital Constraint Manifold

In a departure from the conventional HF equations, the holomorphic Fock matrix (3.19) and density matrix (3.17) are both complex-symmetric rather than Hermitian matrices. This change in matrix symmetry affects the form of both the eigenvectors and eigenvalues of the Fock matrix, representing the single-electron orbitals and orbital energies respectively. For example, as complex-symmetric matrices can break Hermiticity, it is possible for these orbital eigenvalues to be complex-valued and the *aufbau* principle is lost.³⁹ In this section, the properties and consequences of this complex-symmetry are investigated in the context of the holomorphic molecular orbitals.

3.3.2.1 Complex-Orthogonality Constraint

At SCF convergence, the optimal holomorphic orbitals are represented as the eigenvectors of the complex-symmetric holomorphic Fock matrix (3.19). While a Hermitian matrix can always be diagonalised by a unitary transformation, the diagonalisation of a complex-symmetric matrix M ($= M^T$) requires a complex-orthogonal transformation V to give^{154,155}

$$\Lambda = V^T M V. \quad (3.23)$$

Here, Λ is a diagonal matrix containing the eigenvalues of M , V is a complex matrix with columns containing the eigenvectors of M , and $V^T V = I$. As a result, the eigenvectors

v_i of a complex-symmetric matrix (corresponding to the columns of V) form a complex-orthogonal set satisfying

$$v_i^\top v_j = \delta_{ij}, \quad (3.24)$$

where the complex-analytic continuation of the Euclidean inner product is used.

The complex-symmetry of the holomorphic Fock and density matrices therefore requires that the holomorphic orbital coefficients satisfy the complex-orthogonality constraint

$$\langle \psi_i^* | \psi_j \rangle = \sum_{\mu\nu} C_{i,\mu} S_{\mu\nu} C_{j,\nu}^* = \delta_{ij}, \quad (3.25)$$

in contrast to the conventional unitary constraint (3.12). In turn, this ensures the normalisation of the h-HF wave function with respect to the complex-symmetric inner product, i.e.

$$1 = \langle \Psi^* | \Psi \rangle = \int \Psi(\mathbf{x}_1, \dots, \mathbf{x}_N) \Psi(\mathbf{x}_1, \dots, \mathbf{x}_N) \, d\mathbf{x}_1 \cdots d\mathbf{x}_N. \quad (3.26)$$

Furthermore, the h-HF energy (3.16) can then be equated to an expectation value computed with the complex-symmetric inner product

$$\tilde{E}_{\text{HF}} = \frac{\langle \Psi^* | \hat{H} | \Psi \rangle}{\langle \Psi^* | \Psi \rangle} = \frac{\int \Psi(\mathbf{x}_1, \dots, \mathbf{x}_N) \hat{H} \Psi(\mathbf{x}_1, \dots, \mathbf{x}_N) \, d\mathbf{x}_1 \cdots d\mathbf{x}_N}{\int \Psi(\mathbf{x}_1, \dots, \mathbf{x}_N) \Psi(\mathbf{x}_1, \dots, \mathbf{x}_N) \, d\mathbf{x}_1 \cdots d\mathbf{x}_N}. \quad (3.27)$$

From this perspective, the complex (Hermitian) and holomorphic formalisms of HF theory can be differentiated purely by the choice of inner product, and whether the complex-conjugate is included.

Notably, the complex-symmetric inner product (3.24) — and by extension the orbital constraint (3.25) — is not positive-definite. While the normalisation of most vectors can be ensured by introducing a constant multiplicative factor

$$v_i \rightarrow v_i / \sqrt{v_i^\top v_i}, \quad (3.28)$$

it is also possible for non-zero vectors to become ‘quasi-null’ with $v_i^\top v_i = 0$.¹⁵⁴ Quasi-null vectors can usually be avoided by using suitable initial coefficients in the holomorphic SCF procedure, although subsequent sections will show that these quasi-null vectors play a key role in characterising the h-HF energy landscape.

It is useful to consider the topological differences between the real-orthogonal, unitary, and complex-orthogonal orbital constraint surfaces. Take the simple case of a two-dimensional vector $v = (x, y)^\top$ represented in an orthogonal basis. The real-orthogonality constraint $v^\top v = 1$ for $x, y \in \mathbb{R}$ is given by the circle $x^2 + y^2 = 1$ in the real xy -plane (red line in Fig. 3.1). Alternatively, if x, y are allowed to become complex, then the unitary constraint corresponds to a complex sphere $|x|^2 + |y|^2 = 1$ with $x, y \in \mathbb{C}$,

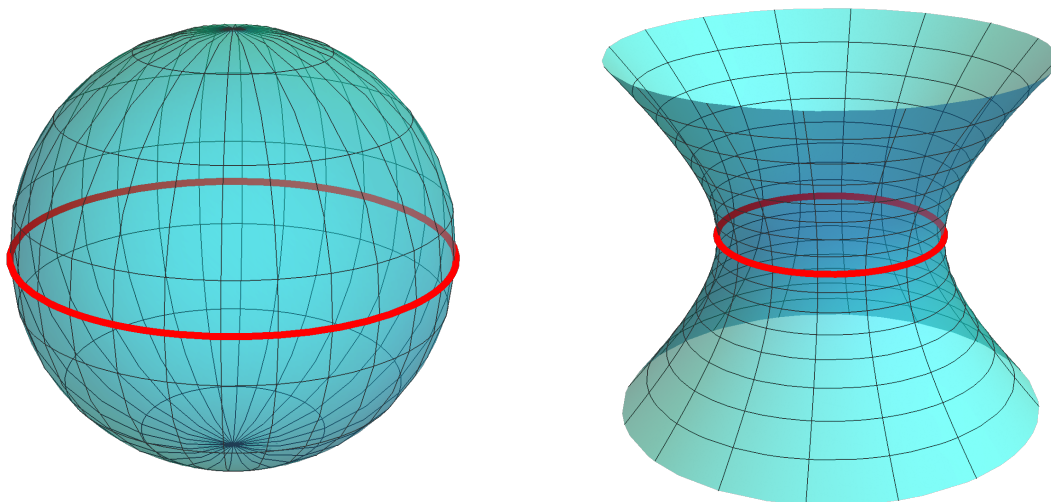


Figure 3.1: Schematic comparison of the unitary (left) and complex-orthogonal (right) constraint surfaces for a two-dimensional vector. The red circle represents the real-orthogonal constraint surface (see main text for details).

while the complex-orthogonality constraint defines the complex generalisation of the circle $x^2 + y^2 = 1$. These unitary and complex-orthogonal constraint manifolds are illustrated schematically in the left and right panels of Fig. 3.1 respectively. Significantly, in contrast to the real-orthogonal and unitary constraints, the complex-orthogonal constraint yields an *unbound* surface. In fact, it will be shown in Chapter 4 that points at the ‘infinite’ limit of this complex-orthogonal constraint surface correspond to quasi-null vectors, and that no quasi-null vectors exist elsewhere.

3.3.2.2 Properties of the Holomorphic Density Matrix

Like the conventional HF formalism, satisfying the molecular orbital constraint (3.25) has important consequences for the properties of the holomorphic density matrix. In particular, the density matrix conventionally represents a projector onto the space spanned by the occupied orbitals and is required to satisfy the idempotency condition.⁸ Complex-orthogonality of the molecular orbitals ensures that the holomorphic density matrix also retains idempotency

$$\sum_{\sigma\tau}^{2n} \tilde{P}^{\mu\sigma} S_{\sigma\tau} \tilde{P}^{\tau\nu} = \sum_{ij}^N C_{\cdot i}^{\mu\cdot} \underbrace{\left(\sum_{\sigma\tau}^{2n} C_{i\cdot}^{\sigma} S_{\sigma\tau} C_{\cdot j}^{\tau\cdot} \right)}_{\delta_{ij}} C_{j\cdot}^{\nu\cdot} = \tilde{P}^{\mu\nu}. \quad (3.29)$$

Furthermore, since the conventional density matrix is a projector onto the occupied orbital space, its trace must equal the total number of electrons. Again, the complex-orthogonality of orbitals ensures that this trace property is retained for the holomorphic

density matrix

$$\sum_{\mu\nu}^{2n} \tilde{P}^{\mu\nu} S_{\nu\mu} = \sum_i^N \sum_{\mu\nu}^{2n} C_{\cdot i}^{\mu\cdot} C_{i\cdot}^{\nu\cdot} S_{\nu\mu} = \sum_i^N \delta_{ii} = N. \quad (3.30)$$

Enforcing the complex-orthogonality constraint on the molecular orbital coefficients is therefore essential for retaining the idempotency and trace conditions on the holomorphic density matrix. Significantly, since the holomorphic density matrix can be considered as a complex-symmetric projector, it depends on only the subspace spanned by the occupied h-HF orbitals. In fact, the holomorphic density matrix is invariant to a complex-orthogonal occupied-occupied orbital transformation \mathbf{Q} since

$$\sum_i^N \left(\sum_j^N C_{\cdot j}^{\mu\cdot} Q_{ji} \right) \left(\sum_k^N Q_{ik} C_{k\cdot}^{\nu\cdot} \right) = \sum_{jk}^N C_{\cdot j}^{\mu\cdot} C_{k\cdot}^{\nu\cdot} \underbrace{\left(\sum_i^N Q_{ji} Q_{ik} \right)}_{\delta_{jk}} = \tilde{P}^{\mu\nu}. \quad (3.31)$$

3.3.2.3 Complex-Orthogonal Grassmannian Representation

Since the h-HF energy depends on only the holomorphic density matrix, and the holomorphic density matrix depends on only the space spanned by the occupied h-HF orbitals, the h-HF energy must be invariant to transformations among the occupied holomorphic orbitals. As a result, unique points on the h-HF energy surface are only defined up to a complex-orthogonal transformation of the occupied orbitals.

The mathematical structure of the full h-HF wave function constraint surface can be considered by expressing an optimal set of orbital coefficients \mathbf{C} as a complex-orthogonal transformation \mathbf{Q} of an initial set of coefficients $\mathbf{C}^{(0)}$ as

$$\mathbf{C} = \mathbf{C}^{(0)} \mathbf{Q}. \quad (3.32)$$

This transformation can be explicitly expanded in terms of the occupied \mathbf{C}_{occ} and virtual \mathbf{C}_{vir} blocks of the coefficient matrix as

$$\begin{pmatrix} \mathbf{C}_{\text{occ}} & \mathbf{C}_{\text{vir}} \end{pmatrix} = \begin{pmatrix} \mathbf{C}_{\text{occ}}^{(0)} & \mathbf{C}_{\text{vir}}^{(0)} \end{pmatrix} \begin{pmatrix} \mathbf{Q}_{\text{OO}} & \mathbf{Q}_{\text{VO}} \\ \mathbf{Q}_{\text{OV}} & \mathbf{Q}_{\text{VV}} \end{pmatrix}, \quad (3.33)$$

where \mathbf{Q}_{OO} , \mathbf{Q}_{VV} , \mathbf{Q}_{OV} , and \mathbf{Q}_{VO} represent occupied-occupied, virtual-virtual, occupied-virtual and virtual-occupied orbital transformations.

Exploiting this complex-orthogonal transformation reveals that a unique point in the space of h-HF wave functions is parametrised by the subspace spanned by the first N columns of \mathbf{Q} , representing the occupied orbitals expressed in the basis of the initial orbitals. Constraint surfaces with this structure correspond to the complex-orthogonal analogue of the Grassmann manifold $\text{Gr}(2n, N; \mathbb{C})$,^{156–158} where each point

represents the set of all $2n \times N$ complex-orthogonal matrices that can be interconverted through right multiplication by a complex-orthogonal matrix. Mathematically, this complex-orthogonal Grassmannian corresponds to a quotient manifold

$$\text{Gr}(2n, N; \mathbb{C}) = \frac{\text{St}(2n, N; \mathbb{C})}{\text{O}(2n; \mathbb{C})}, \quad (3.34)$$

where $\text{St}(2n, N; \mathbb{C})$ represents the complex-orthogonal Stiefel manifold comprising the set of all $2n \times N$ “tall-skinny” complex-orthogonal matrices

$$\text{St}(2n, N; \mathbb{C}) = \left\{ \mathbf{M} \in \mathbb{C}^{2n \times N} \mid \mathbf{M}^\top \mathbf{M} = \mathbf{I}_N \right\} \quad (3.35)$$

and $\text{O}(n; \mathbb{C})$ defines the complex-orthogonal group

$$\text{O}(2n; \mathbb{C}) = \left\{ \mathbf{M} \in \mathbb{C}^{2n \times 2n} \mid \mathbf{M}^\top \mathbf{M} = \mathbf{I}_{2n} \right\}. \quad (3.36)$$

Using the properties of the complex-orthogonal Grassmannian, a non-redundant parametrisation of the complex-orthogonal h-HF wave function can be constructed through an exponential representation of the complex-orthogonal transformation (3.32) as¹⁵⁵

$$\mathbf{Q} = \exp(\mathbf{X}), \quad (3.37)$$

Here \mathbf{X} is a complex-valued skew-symmetric matrix, i.e. $\mathbf{X} = -\mathbf{X}^\top$. Since the h-HF energy is invariant to both occupied-occupied and virtual-virtual orbital rotations, this non-redundant parametrisation requires \mathbf{X} to take the form

$$\mathbf{X} = \begin{pmatrix} \mathbf{0} & -\mathbf{X}_{\text{VO}}^\top \\ \mathbf{X}_{\text{VO}} & \mathbf{0} \end{pmatrix} \quad (3.38)$$

where only the occupied-virtual blocks are non-zero and \mathbf{X}_{VO} represents the virtual-occupied block. Note that, similar to the case of unitary orbital transformations,¹⁵⁹ the required matrix exponential (3.37) can be expanded as

$$\mathbf{Q} = \begin{pmatrix} \mathbf{V} \cos(\boldsymbol{\Sigma}) \mathbf{V}^\top + (\mathbf{I} - \mathbf{V} \mathbf{V}^\top) & -\mathbf{V} \sin(\boldsymbol{\Sigma}) \mathbf{U}^\top \\ \mathbf{U} \sin(\boldsymbol{\Sigma}) \mathbf{V}^\top & \mathbf{U} \cos(\boldsymbol{\Sigma}) \mathbf{U}^\top + (\mathbf{I} - \mathbf{U} \mathbf{U}^\top) \end{pmatrix}, \quad (3.39)$$

where $\mathbf{X}_{\text{VO}} = \mathbf{U} \boldsymbol{\Sigma} \mathbf{V}^\top$ is a complex-orthogonal singular-value decomposition.¹⁶⁰ Consequently, given an initial set of orbital coefficients, the complex-orthogonal h-HF wave function manifold can be parametrised using the $N \times (2n - N)$ components of \mathbf{X}_{VO} .

The independent variables in \mathbf{X}_{VO} provide the holomorphic extension of occupied-virtual orbital rotation angles, allowing non-redundant orbital transformations to be parameterised and providing a local coordinate system for the h-HF constraint surface. Note that, like their conventional counterparts, the real component of the holomorphic

orbital rotation angles take unique values in the range $[0, \pi)$, while in contrast to conventional HF, their imaginary components are unbound and can become infinite. In the next section, these local coordinates will allow explicit orbital derivatives of the h-HF energy to be derived.

3.3.3 Differential Geometry of the Holomorphic Energy

Having considered the structure of the h-HF orthonormalisation constraint surface, the differential geometry of the h-HF energy itself can now be derived and characterised. Understanding the properties of the h-HF energy surface provides a mathematical foundation informing the development of future algorithms for locating h-HF stationary states.

3.3.3.1 Properties of the h-HF Energy Surface

In contrast to conventional HF, the h-HF energy (3.16) is an inherently complex-valued function. As a result, there is no concept of minima or maxima on the h-HF energy surface. Regardless, stationary points corresponding to h-HF solutions remain well-defined as points where the gradient vanishes.

The polynomial form of Eq. (3.16) allows certain features of the h-HF energy to be recognised immediately. Firstly, the h-HF energy function is strictly real-valued for real orbital coefficients, since under these conditions Eq. (3.16) coincides exactly with the real HF energy function. Secondly, due to the polynomial form of Eq. (3.16), two sets of orbital coefficients related by complex-conjugation must have h-HF energies that are also related by complex-conjugation, i.e. $\tilde{E}_{\text{HF}}(\mathbf{C}^*) = \tilde{E}_{\text{HF}}(\mathbf{C})^*$. These features can be visualised by considering the h-RHF energy of the hydrogen dimer in the minimal molecular orbital basis $\{\sigma_{\text{g}}(\mathbf{r}), \sigma_{\text{u}}(\mathbf{r})\}$ where the single occupied spatial orbital can be represented using the complex rotation angle θ as

$$\phi(\mathbf{r}) = \sigma_{\text{g}}(\mathbf{r}) \cos \theta + \sigma_{\text{u}}(\mathbf{r}) \sin \theta. \quad (3.40)$$

The complex-conjugation symmetry and strictly real energies along the real θ -axis are then seen clearly in the complex h-RHF energy surface (green dashed line in Fig. 3.2). In fact, this line of real h-RHF energies is closely related to more fundamental symmetries of the h-HF energy that are explored in Chapter 5.

As a non-constant complex holomorphic function, the h-HF energy (3.16) must be unbound¹⁴⁹ and the conventional HF variational principle is lost. Notably, since the real energy function is recovered for real orbital coefficients, only h-HF states with complex orbital coefficients can possess non-variational energies. Regardless, it is useful

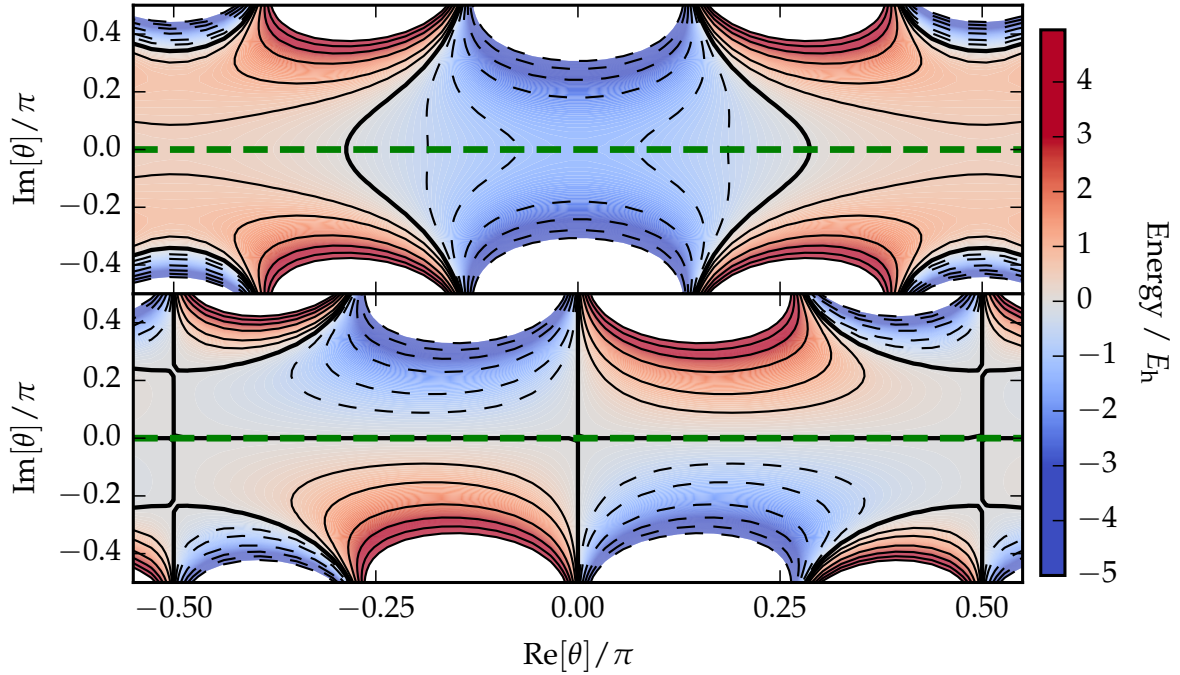


Figure 3.2: Real (top) and imaginary (bottom) components of the h-RHF energy for the minimal basis hydrogen dimer at a bond length of 0.75 \AA . The complex rotation angle θ corresponds to the spatial orbital parametrisation (3.40). When the orbital coefficients are real (dashed green) the h-HF energy coincides with the real HF energy and takes strictly real values.

to consider the conditions where the h-HF energy reaches its minimum (maximum) infinite limits.

Taking a fixed set of finite one- and two-electron integrals, the h-HF energy can only tend to positive or negative infinity if the orbital coefficients themselves become infinite. Since the orbital coefficients can nearly always be complex-orthonormalised through the transformation (3.28), the coefficients only tend to infinity in the limit of quasi-null vectors. In this special case, the orbital coefficients cannot be complex-orthonormalised and the h-HF energy must be considered more generally as the expectation value

$$\tilde{E}_{\text{HF}}(\mathbf{C}) = \frac{\langle \Psi^* | \hat{H} | \Psi \rangle}{\langle \Psi^* | \Psi \rangle}. \quad (3.41)$$

Since $\langle \Psi^* | \Psi \rangle = \det(\mathbf{C}_{\text{occ}}^{\text{T}} \mathbf{C}_{\text{occ}})$, this representation of the h-HF energy is the ratio of two complex polynomials, taking the form of a meromorphic function.¹⁴⁹

Singularities in the h-HF energy can now be identified as points where the denominator in Eq. (3.41) vanishes, i.e. $\det(\mathbf{C}_{\text{occ}}^{\text{T}} \mathbf{C}_{\text{occ}}) = 0$. These points occur if (and only if) at least one of the occupied orbitals becomes quasi-null. As a result, the unbounded limits of the h-HF energy coincide exactly with points where quasi-null orbitals arise, and these occur at the infinite limits of the complex-orthogonal orbital constraint surface described in Section 3.3.2. The asymptotic sign of the h-HF energy in these limits

depends on the specific one- and two-electron integrals for a system. Finally, since infinities in the h-HF energy only occur at the infinite limits of the complex-orthogonal constraint surface, it is reasonable to expect that the h-HF energy will be well-behaved in the regions close to the real axis where complex extensions of real HF states must originate.

3.3.3.2 Analytic Orbital Gradients of the Holomorphic Energy

Recall that only complex-orthogonal transformations between occupied and virtual orbitals lead to a change in the h-HF energy. Taking into account the complex-orthogonality constraint on the holomorphic energies requires that analytic orbital gradients must lie in the space tangential to the complex-orthogonal Grassmannian. For a given set of orbital coefficients $\mathbf{C} = (\mathbf{C}_{\text{occ}} \quad \mathbf{C}_{\text{vir}})$, the corresponding point on the complex-orthogonal Grassmannian is defined by the $2n \times N$ occupied orbital coefficient matrix \mathbf{C}_{occ} . Any vector \mathbf{T} in the tangent space at this point must then satisfy the constraint¹⁵⁶

$$\mathbf{C}_{\text{occ}}^{\text{T}} \mathbf{T} + \mathbf{T}^{\text{T}} \mathbf{C}_{\text{occ}} = \mathbf{0}, \quad (3.42)$$

where \mathbf{T} is represented in the covariant basis.⁴¹ A general vector \mathbf{T} expressed in the global covariant coordinate space in which the complex-orthogonal Grassmannian is embedded (i.e. the unconstrained orbital coefficient space) can be projected into this tangent space through the projector¹⁵⁶

$$\mathbf{\Pi}(\mathbf{C}_{\text{occ}}) = (\mathbf{I} - \mathbf{C}_{\text{occ}} \mathbf{C}_{\text{occ}}^{\text{T}}), \quad (3.43)$$

where the properties of the holomorphic density matrix are now essential (see Section 3.3.2.2). Alternatively, the virtual orbitals \mathbf{C}_{vir} span the space of orthogonal vectors to the point \mathbf{C}_{occ} and can be used to define a local basis for the tangent space. The general vector \mathbf{T} in the global covariant coordinate space can then be projected into this local basis as

$$\mathbf{t} = \mathbf{C}_{\text{vir}}^{\text{T}} \mathbf{T}, \quad (3.44)$$

where \mathbf{t} corresponds to the vector represented using the local coordinates.¹⁵⁷

Crucially, analytic orbital gradients of the h-HF energy must also be tangential to the complex-orthogonal Grassmannian. These analytic gradients can be derived by first considering the unconstrained gradient of the h-HF energy in the global coordinate space, given by

$$\begin{aligned} \frac{\partial \tilde{E}_{\text{HF}}}{\partial C_{\cdot i}^{\mu}} &= 2 \left(\sum_{\nu}^{2n} h_{\mu\nu} C_{\cdot i}^{\nu} + \sum_{\nu\sigma\tau}^{2n} \sum_j^N C_{\cdot i}^{\nu} \langle \mu\sigma || \nu\tau \rangle C_{\cdot j}^{\tau} C_{\cdot j}^{\sigma} \right) \\ &= 2 \sum_{\nu}^{2n} \tilde{F}_{\mu\nu} C_{\cdot i}^{\nu}. \end{aligned} \quad (3.45)$$

Here, the symmetries of the one- and two-electron integrals have been exploited. Projecting Eq. (3.45) into the local coordinates defined by the virtual orbitals then gives the constrained gradient

$$g_{ai} = 2 \sum_{\mu\nu}^{2n} C_a^\mu \tilde{F}_{\mu\nu} C_i^\nu, \quad (3.46)$$

where the indices i and a explicitly denote occupied and virtual orbitals respectively. This local representation corresponds to the h-HF energy gradient with respect to the occupied-virtual rotation angles in the exponential parametrisation (3.37) and (3.38).

Significantly, the local representation of the h-HF energy gradient is equivalent to the virtual-occupied block of the holomorphic Fock matrix, mirroring the analytic orbital gradients in real HF.^{161,162} While the holomorphic orbital gradient is complex-valued in general, h-HF stationary points occur when the magnitude of this local representation falls to zero, giving the convergence condition $|g_{ai}| = 0$. Alternatively, stationary points of the h-HF energy arise when the occupied-virtual block of the holomorphic Fock matrix vanishes, defining the holomorphic analogue of Brillouin’s theorem⁸

$$\sum_{\mu\nu}^{2n} C_a^\mu \tilde{F}_{\mu\nu} C_i^\nu = 0. \quad (3.47)$$

Note that, while these gradients have been derived for the most general form of h-GHF, applying the relevant symmetry constraints allows corresponding gradients for the h-UHF or h-RHF energy to be defined.

3.3.3.3 Geometric Optimisation of the h-HF Energy

Combining the Roothaan–Hall approach^{46,47} with DIIS extrapolation^{150,151} generally provides a robust way to optimise the HF energy. However, in certain cases the DIIS procedure suffers from slow oscillatory convergence or fails completely, particularly in the vicinity of Coulson–Fischer points.^{163,164} Furthermore, DIIS extrapolation can result in large steps in the orbital coefficient space through regions of high energy or steep gradients. While such behaviour helps to locate the global minimum, it can cause difficulties in converging higher energy stationary points, even with the addition of the non-*aufbau* Maximum Overlap Method.^{26,29}

To overcome these failures of DIIS, a number of second-order quasi-Newton algorithms have been developed to directly optimise the HF energy using analytic orbital derivatives. Initially these second-order SCF approaches were defined by combining orbital gradients with exact or approximate Hessians in standard second-order optimisation methods.^{161,165–167} However, the importance of respecting orbital orthogonality was later recognised, and the Geometric Direct Minimisation (GDM) approach was developed to explicitly optimise the HF energy on this constraint manifold.¹⁶⁴

Since h-HF solutions are required to form complex extensions of real HF states in the vicinity of Coulson–Fischer points, the holomorphic DIIS procedure is also likely to suffer from difficult SCF convergence. The analytic orbital gradients derived for the h-HF energy now create the possibility of optimising the h-HF energy using second-order quasi-Newton approaches. In particular, it is possible to combine these analytic gradients with the geometric structure of the complex-orthogonal constraint surface to derive a holomorphic analogue of the GDM approach and target holomorphic stationary points. Appendix A provides a detailed derivation for one potential algorithm that directly optimises the h-HF energy subject to the complex-orthogonal Grassmannian. The differential geometry of the h-HF energy derived in this chapter will provide the foundation for similar future algorithms to locate multiple h-HF stationary points with increasing reliability and efficiency.

3.3.4 Extension to a Fundamental Theory of Hartree–Fock

Until now, h-HF theory has been presented as an alternative to complex (Hermitian) HF for extending real HF in to the complex plane. Through this perspective, h-HF theory forms the complex-analytic continuation of real HF theory; when real HF states disappear at a Coulson–Fischer point, their h-HF counterparts continue with complex orbital coefficients. However, it is also interesting to consider how *complex* HF states may be extended beyond the points at which they vanish,³⁶ and whether an over-arching “fundamental” HF Theory can be developed. To derive a fundamental theory of HF, it is useful to again decompose the orbital coefficients into their real and imaginary components as

$$C_{.i}^{\mu} = X_{.i}^{\mu} + iY_{.i}^{\mu}. \quad (3.48)$$

In this representation, the real, complex, and holomorphic HF formalisms are distinguished simply by the constraint applied to the $X_{.i}^{\mu}$ and $Y_{.i}^{\mu}$, shown in Table 3.1.

Considering orbital coefficients with this decomposition, the most general form of HF theory can be derived by allowing both $X_{.i}^{\mu}$ and $Y_{.i}^{\mu}$ to become complex variables, creating the unintuitive situation where the “imaginary” part of the orbital coefficients is represented by a complex number. This “fundamental Hartree–Fock” theory forms the analytic continuation of complex HF into the complex-plane. In principle, the corresponding HF equations can be derived in a similar manner to the h-HF equations

HF Formalism	$X_{\cdot i}^{\mu\cdot}$	$Y_{\cdot i}^{\mu\cdot}$
Real	\mathbb{R}	0
Complex	\mathbb{R}	\mathbb{R}
Holomorphic	\mathbb{C}	0
Fundamental	\mathbb{C}	\mathbb{C}

Table 3.1: Constraint applied to the real and imaginary components of the orbital coefficients (3.48) in different formalisms of HF.

by introducing a new density matrix as

$$\begin{aligned}
\bar{P}^{\mu\nu} &= \sum_i^N (X_{\cdot i}^{\mu\cdot} + iY_{\cdot i}^{\mu\cdot})(X_{\cdot i}^{\nu\cdot} - iY_{\cdot i}^{\nu\cdot}) \\
&= \sum_i^N [(X_{\cdot i}^{\mu\cdot} X_{\cdot i}^{\nu\cdot} + Y_{\cdot i}^{\mu\cdot} Y_{\cdot i}^{\nu\cdot}) + i(Y_{\cdot i}^{\mu\cdot} X_{\cdot i}^{\nu\cdot} - X_{\cdot i}^{\mu\cdot} Y_{\cdot i}^{\nu\cdot})] \\
&= \bar{P}_{\text{Re}}^{\mu\nu} + i\bar{P}_{\text{Im}}^{\mu\nu}.
\end{aligned} \tag{3.49}$$

Note that \bar{P}_{Re} and \bar{P}_{Im} are both complex-symmetric matrices in general and the total density matrix \bar{P} is neither Hermitian nor complex-symmetric. The corresponding energy will therefore be a complex-valued function of complex variables, forming the complex-analytic extension of the complex HF energy. Furthermore, the orbital orthonormalisation constraint takes the form

$$\sum_{\mu\nu}^{2n} (X_{\cdot i}^{\mu\cdot} + iY_{\cdot i}^{\mu\cdot}) S_{\mu\nu} (X_{\cdot j}^{\nu\cdot} - iY_{\cdot j}^{\nu\cdot}) = \delta_{ij}, \tag{3.50}$$

and thus the orbital coefficients $C_{\cdot i}^{\mu\cdot}$ are neither complex-orthogonal or unitary.

In practice, the absence of Hermiticity or complex-symmetry in the fundamental HF density matrix — and its corresponding Fock matrix — means that optimising the energy using an iterative SCF approach is likely to present sufficient computational challenges to prohibit its practical application. For example, the well-understood Hermiticity and complex-symmetry of the complex and holomorphic HF density matrices provide essential properties such as well-defined eigenvectors and orthogonality constraints that will be lost in the fundamental HF approach. Nonetheless, deriving holomorphic and complex HF as subsets of one unified framework highlights the close theoretical relationship between all HF approaches. Furthermore, the framework of complex-analytically continuing complex HF states may yet prove useful if complex HF states are required to build a basis for NOCI.

3.4 Results and Discussion

The rigorous mathematical theory of h-HF derived in this chapter now provides the foundation for developing h-HF into a practical computational tool to support NOCI. For example, understanding the h-HF orbital constraint surface and analytic energy gradients paves the way for new algorithms to locate h-HF stationary states. In this section, the original h-HF case of the hydrogen dimer is briefly revisited to illustrate the key properties of h-HF theory. Furthermore, the close similarities between h-HF and the other non-Hermitian HF approaches are discussed, highlighting potential links between complex h-HF states and metastable resonances.

3.4.1 Computational Details

All h-HF calculations employed the Geometric Holomorphic SCF procedure outlined in Appendix A. Stationary states were first identified by initialising multiple SCF guesses at random points selected in the orbital coefficient space. States are then followed along all molecular structures by using the h-HF solutions at the previous geometry as the guess coefficients for the SCF optimisation at the next geometry. When a Coulson–Fischer point is reached, random complex perturbations of the orbital coefficients were used to generate new SCF guesses until the corresponding h-HF state is identified. For clarity, only stationary points with complex orbital coefficients are referred to as h-HF states and atomic units are used throughout.

3.4.2 Hydrogen Dimer

The hydrogen dimer in a minimal basis (STO-3G) presents the simplest molecular system to illustrate the h-HF approach. Exhaustively searching the orbital coefficient space in the dissociation limit yields a total of four real RHF (solid red) and a further four real UHF stationary points (blue solid), as shown in Fig. 3.3. In order of ascending energy, the RHF stationary points represent the bonding σ_g^2 , antibonding σ_u^2 and degenerate ionic $H^+ - H^- / H^- - H^+$ configurations, while the additional UHF solutions correspond to the low-energy diradical ${}^1H-H^{\cdot} / {}^1H-H^{\cdot}$ configurations and the degenerate $\sigma_g\sigma_u / \sigma_u\sigma_g$ configurations. As the molecular bond length is shortened, the diradical real UHF states coalesce with the σ_g^2 RHF state at the Coulson–Fischer point²⁴ and disappear at shorter bond lengths. Similarly, the ionic-like RHF states coalesce with the σ_u^2 state, although at a different bond length.

Extending the diradical UHF states beyond the Coulson–Fischer point in H_2 provided the first case-study of h-HF theory.^{38,39} Using the geometric holomorphic SCF

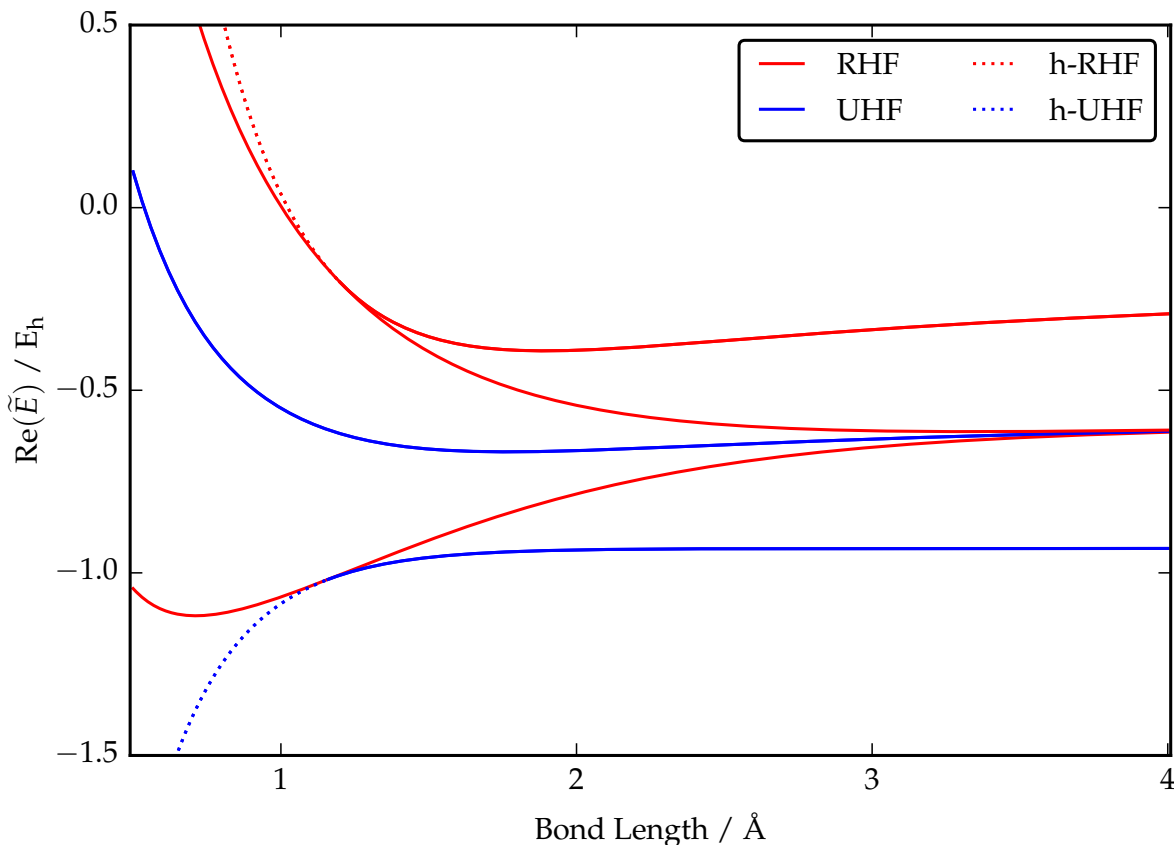


Figure 3.3: Stationary points of the h-UHF equations for the hydrogen dimer (STO-3G) located using the holomorphic SCF procedure. Eight solutions exist with degeneracies from bottom to top of two, one, two, one and two. When real RHF (solid red) and real UHF (solid blue) solutions disappear at a Coulson–Fischer point, their h-RHF (dashed red) and h-UHF (dashed blue) counterparts continue to exist across all bond lengths with complex orbital coefficients.

approach, complex-valued h-UHF (dashed blue) and h-RHF (dashed red) extensions to the diradical and ionic states respectively can now be identified beyond the Coulson–Fischer points at which they vanish. As a result, h-HF theory allows *every* real HF state to be analytically extended across all bond lengths. Furthermore, the orbital coefficients of these complex h-HF solutions form smooth continuations of the real HF states, providing suitable extensions for the NOCI basis beyond the Coulson–Fischer point.

The holomorphic energy of h-HF states in the hydrogen dimer also provides important insights for understanding the properties of the h-HF approximation. Firstly, complex h-HF states always exist in pairs with orbital coefficients and h-HF energies related by complex-conjugation. These pairs illustrate the complex-conjugation symmetry discussed in Section 3.3.3.1. Secondly, the complex h-HF states in H_2 appear to retain real-valued h-HF energies despite the holomorphic energy being a complex-valued function. The existence of stationary points with real h-HF energies implies the existence of additional symmetries under which the complex h-HF energy surface is

purely real-valued, and this feature is investigated further in Chapter 5. Finally, the complex h-UHF stationary points have non-variational h-HF energies which fall below the minimum real HF energy. However, since complex h-HF states are only designed to form a continuous basis for NOCI, non-variational h-HF energies are not a primary concern and the only requirement is that the h-HF wave function evolves smoothly along the binding curve.

3.4.3 Links to Non-Hermitian Hartree–Fock

The major difference between conventional HF and h-HF is the inherent non-Hermiticity of the holomorphic Fock and density matrices. However, using non-Hermitian Hamiltonians in quantum chemistry is not itself new; these Hamiltonians have been exploited extensively to describe metastable resonance phenomena.¹⁶⁸ In particular, non-Hermitian HF provides a mean-field approximation of resonance states^{168–170} and shares several features with h-HF theory.

Metastable molecular resonances correspond to electronic states with a finite lifetime, playing important roles in electron scattering and autoionisation processes.¹⁶⁸ A resonance state can be characterised by the complex Siegert energy

$$E_{\text{res}} = E_{\text{R}} - \frac{i\Gamma}{2}, \quad (3.51)$$

where E_{R} is the resonance energy and Γ is the decay width with a lifetime $\tau = \hbar/\Gamma$.¹⁶⁸ However, predicting resonance Siegert energies is challenging as the wave function of scattering electrons is not stationary.¹⁶⁸ The resonance wave function is therefore not square-integrable, preventing the application of standard electronic structure methods.

The issues associated with non-stationary wave functions can be overcome by analytically continuing the Hamiltonian operator into the complex plane, creating a non-Hermitian Hamiltonian with complex eigenvalues that correspond to Siegert energies.¹⁶⁸ For example, the *complex-scaling* approach introduces complex-valued electron coordinates $r \rightarrow re^{i\theta}$,¹⁷¹ transforming divergent resonances to square-integrable wave functions for a sufficiently large rotation θ .^{172,173} Alternatively, square-integrable wave functions can be obtained using *complex absorbing potentials* (CAPs) that create an absorbing boundary condition outside the molecular target.¹⁷⁴ These absorbing potentials are introduced through a parametrised molecular Hamiltonian

$$\hat{H}(\lambda) = \hat{H} - i\lambda\hat{W}, \quad (3.52)$$

where λ controls the CAP strength and \hat{W} is an absorbing one-particle operator. Resonance eigenvalues are then associated with the minimisation of $|\lambda dE_i(\lambda)/d\lambda|$, where $E_i(\lambda)$ represents the eigenvalues of $\hat{H}(\lambda)$.¹⁷⁴

Both the complex-scaling and complex-absorbing potentials use non-Hermitian complex-symmetric Hamiltonians with eigenfunctions that form a complex-orthogonal system.¹⁶⁸ Therefore, the non-Hermitian HF framework requires a complex-symmetric optimisation that is identical to the holomorphic SCF approach. In fact, the only substantial difference between non-Hermitian HF and h-HF theory is the use of analytically-continued Hamiltonians rather than the bare molecular Hamiltonian in h-HF theory. However, while complex wave functions and energies emerge in non-Hermitian HF from complex-scaling or CAP potentials, in h-HF theory these wave functions arise purely from the self-consistent feedback of complex orbital coefficients in the h-HF energy.

Identifying the relationship between h-HF theory and non-Hermitian HF raises possibilities for both theoretical frameworks. For example, given complex-valued stationary states can be located in h-HF using only the bare molecular Hamiltonian, these same states are also likely to exist in non-Hermitian HF methods. Since the real component of the h-HF stationary energies do not appear to lie in the continuum, these solutions may form an additional type of state alongside real bound states and complex resonances. In the other direction, the non-Hermitian HF framework may allow complex-valued h-HF continuations of real HF states to be interpreted as metastable resonance energies in the bound-state region of the spectrum. Furthermore, given h-HF states can have complex-valued orbital coefficients while retaining real orbital eigenvalues, interpreting h-HF energies as Siegert energies suggests the existence of true bound states with complex wave functions. Lastly, the mean-field nature of the HF approximation may mean that these complex h-HF states are simply unphysical artefacts with no correspondence to bound or resonances states.

Investigating the relationship between h-HF and non-Hermitian HF may therefore allow any chemical relevance of complex h-HF states to be assessed and understood. However, for the purpose of this thesis, the existence of h-HF states is only required to form a continuous basis for NOCI and the relationship between h-HF and non-Hermitian HF will not be considered further.

3.5 Concluding Remarks

In this chapter, a generalised form of the h-HF approach^{38,39} has been derived and its mathematical properties have been characterised. The resulting h-HF equations correspond to the analytic continuation of real HF into the complex plane, forming a complex-analytic function of several complex variables. General holomorphic density and Fock matrices can be defined, but these satisfy complex-symmetry rather than

Hermiticity. In turn, this complex-symmetry requires the holomorphic orbitals to be orthonormalised with respect to the complex-symmetric inner product, and the orbital constraint surface corresponds to the unbound complex-orthogonal Grassmannian. The differential geometry of the holomorphic orbital constraint and energy surface has been derived, providing analytic orbital gradients of the h-HF energy that have allowed a second-order h-HF optimisation scheme to be formulated in Appendix A. Furthermore, the complex-valued h-HF energy surface has unbound infinities when the orbitals become quasi-null, although these occur at the infinite limits of the complex-orthogonal Grassmannian.

The minimal hydrogen dimer has been used to illustrate the essential properties of h-HF states. In particular, when real HF states disappear at Coulson–Fischer points, their h-HF counterparts continue to exist with complex orbital coefficients. Mathematically understanding the holomorphic orbital constraint and energy surface therefore lays the foundation for developing h-HF theory into a general computational tool that allows a continuous basis for NOCI to be defined across all molecular structures. However, before a combined h-HF and NOCI approach can be developed, a number of theoretical questions must be addressed.

Firstly, although all current numerical h-HF results suggest that h-HF stationary states exist across all molecular structures, there is no mathematical guarantee that this must always be true. Gaining confidence that h-HF states *do* exist across all structures is essential if NOCI is to be applied as a general electronic structure method. To rigorously prove that h-HF states must exist across all geometries, it is sufficient to prove that the number of h-HF solutions depends on only the number of electrons and basis functions and not the value of the nuclear repulsion or one- and two-electron integrals. By extension, the number of h-HF states must then be independent of the molecular structure, and thus h-HF solutions cannot disappear as the molecular structure changes. The validity of this proposition is established through a mathematical proof for the existence of two-electron h-HF states in Chapter 4.

Secondly, the observation that complex h-HF states can retain real-valued energies in H_2 poses an interesting theoretical question for quantum chemistry. Electronic structure methods are almost universally defined using Hermitian operators as these rigorously ensure real-valued energies.⁸ However, the presence of real-valued h-HF energies with a complex non-Hermitian Fock operator suggests that certain symmetries in the HF wave function may provide an alternative condition to Hermiticity. Investigating this fundamental aspect of the HF approximation provides the focus of Chapter 5.

Finally, applying h-HF theory for larger molecules with high dimensional orbital rotation spaces will require improved methods for locating multiple real HF states

and their complex h-HF extensions. The SCF metadynamics²⁰ approach provides a promising approach for locating multiple real HF states, although there is no guarantee that the HF states with the greatest contribution to the NOCI wave function will be identified. Furthermore, moving smoothly past the Coulson–Fischer point and onto the complex h-HF extensions presents a more serious computational challenge. While complex h-HF states for small molecules can be identified through random guesses in the complex plane, this approach will not be suitable when the number of orbital rotations increases. Instead, the topology of complex h-HF states must be understood to allow the correct complex direction to be routinely identified, and this is investigated in Chapter 6.

Chapter 4

Nature of Two-Electron Systems

The work in this chapter has contributed to the publication Ref. (1)

Summary

Underpinning h-HF theory lies the belief that the number of solutions to the h-HF equations is constant for all geometries. If this holds true, then every state must exist across *all* molecular structures, allowing a basis for NOCI to be constructed with smooth and continuous energies. This chapter considers the validity of this conjecture by proving that the number of h-RHF and h-UHF stationary points is constant for two-electron systems. The full topology of h-RHF and h-UHF solutions is then explored in simple molecular systems, demonstrating the coalescence behaviour of real and complex stationary states. Since all real HF states are also solutions to the h-HF equations, this analysis also provides wider insights into the nature of real HF states in molecules.

4.1 Context and Scope

Having formalised the h-HF approach, this chapter investigates the existence of h-HF states across all molecular structures and the nature of Coulson–Fischer points where real HF states coalesce. Understanding the properties of h-HF stationary points is essential for creating a strong foundation for using multiple h-HF states as a continuous basis for NOCI.

To achieve this, the mathematical existence of h-HF solutions is investigated in the simplest class of molecules containing only two electrons. For these molecules, the h-HF wave function can be parameterised using only one RHF or two UHF spatial orbitals without needing to account for invariance with respect to occupied-occupied orbital rotations. In turn, the h-HF equations are expressed as a set of polynomial equations whose common solutions represent the h-HF solutions. Identifying the number of h-HF stationary points is then equivalent to counting the intersections of these polynomial equations. The mathematical framework of algebraic geometry provides the foundation for enumerating intersections between polynomial functions,^{175,176} and can be applied to establish the exact number of h-HF stationary points. In turn, this derivation proves that the number of h-RHF or h-UHF states is constant for all molecular geometries in two-electron systems.

Once the exact number of h-RHF and h-UHF states is known in two-electron systems, the topology of *all* HF states can be explored in a range of simple molecular systems. In particular, the influence of molecular structure and symmetry on the characteristics of h-HF solutions can be understood, providing insights into the properties of Coulson–Fischer points where real HF states disappear. Understanding these points informs the use of multiple h-HF states for NOCI expansions in later chapters.

Furthermore, since all real HF states are stationary points of the h-HF equations, investigating the nature of h-HF solutions reveals fundamental insights into the properties of real HF solutions. Despite the widespread use of HF reference states across electronic structure theory,¹¹ surprisingly little is known about the existence of multiple solutions.²⁰ For example, only a handful of studies have investigated the number of solutions to the HF equations,^{21–23} and even these have only produced wide-ranging upper and lower bounds. This sparsity of knowledge persists even though multiple HF states have important consequences for electronic structure calculations, particularly since the choice of reference state can heavily influence the quality of post-HF calculations using truncated excitations.^{177,178} Furthermore, inconsistencies in the choice of reference HF states can lead to kinks or discontinuities in post-HF energy surfaces, resulting in unphysical behaviours in molecular simulations.¹¹⁹ Investigating the char-

acteristics and evolution of both real and holomorphic HF solutions is therefore highly relevant for understanding and improving the performance of post-HF techniques, including NOCI.

The remainder of this chapter is structured as follows. Section 4.2 presents an overview of the essential concepts in algebraic geometry. These concepts are applied in Section 4.3 to enumerate the h-RHF and h-UHF states in two-electron systems. Section 4.4 then explores the topology of real and complex h-HF states in model molecular systems, and the key findings are summarised in Section 4.5.

4.2 Overview of Algebraic Geometry

Algebraic geometry forms a diverse branch of mathematics encompassing the study of roots to systems of polynomial equations in so-called “affine” or “projective” spaces.¹⁷⁶ In particular, the roots to polynomial equations are represented as geometric objects such as curves or surfaces, and the common solutions for a set of multiple polynomials are given by the intersection of these objects. Through this framework, the number of common solutions to a set of polynomials can be counted from only the polynomial structure. While a full exposition of algebraic geometry is well beyond the scope of the current thesis, this section briefly summarises the key concepts required for establishing the number of h-HF states. A more comprehensive introduction can be found in Ref. (176).

4.2.1 Affine Spaces

An affine space is defined as a set of points upon which translations act, providing a generalisation to Euclidean space independent of a specific coordinate origin.¹⁷⁹ An n -dimensional affine space $\mathbb{A}_{\mathbb{C}}^n$ is represented by the set of n -tuples $(a_1, \dots, a_n) \in \mathbb{A}_{\mathbb{C}}^n$, where $a_i \in \mathbb{C}$ are the coordinates of the point.¹⁷⁶ Parallelism and translations are the only Euclidean notions retained in affine spaces, while vector concepts such as distances, angles and orientation are lost. Conventional Euclidean vector spaces are constructed from an affine space by defining an origin point, while two vector spaces with different origins are isomorphic.¹⁸⁰

4.2.2 Projective Spaces

Projective spaces provide an extension to affine spaces by introducing the concept of points-at-infinity.¹⁸⁰ An n -dimensional projective space $\mathbb{P}_{\mathbb{C}}^n$ contains the set of $(n + 1)$ -tuples $(x_0, x_1, \dots, x_n) \in \mathbb{P}_{\mathbb{C}}^n$ where the coordinates $x_i \in \mathbb{C}$ are not all simultaneously zero,

i.e. excluding the point $(0, \dots, 0)$. A point in $\mathbb{P}_{\mathbb{C}}^n$ is defined only up to multiplication by a common scalar, represented by the equivalence relation $(x_0, \dots, x_n) \sim (\lambda x_0, \dots, \lambda x_n)$ for non-zero $\lambda \in \mathbb{C}$. Points-at-infinity arise by noting that the point $(x_0, x_1, \dots, x_n) \in \mathbb{P}_{\mathbb{C}}^n$ maps onto the affine point $(a_1, \dots, a_n) \in \mathbb{A}_{\mathbb{C}}^n$, where $a_i = x_i/x_0$ for $i > 0$.¹⁷⁶ Consequently, the projective space $\mathbb{P}_{\mathbb{C}}^n$ augments $\mathbb{A}_{\mathbb{C}}^n$ with an additional set of points where $x_0 = 0$. Introducing these points-at-infinity is essential for consistently defining geometric intersection rules without exceptions.¹⁸⁰ For example, two lines in $\mathbb{A}_{\mathbb{C}}^2$ must always intersect exactly once unless they are parallel, while all parallel lines in $\mathbb{P}_{\mathbb{C}}^2$ also intersect at a single point-at-infinity.

A projective space can be decomposed into the union of an affine subspace and a projective space of lower dimension $\mathbb{P}_{\mathbb{C}}^n = V_i \cup H_i$, where¹⁷⁶

$$V_i \equiv \{(x_0, \dots, x_n) \in \mathbb{P}_{\mathbb{C}}^n | x_i \neq 0\}, \quad (4.1a)$$

$$H_i \equiv \{(x_0, \dots, x_n) \in \mathbb{P}_{\mathbb{C}}^n | x_i = 0\}. \quad (4.1b)$$

Here, $V_i = \mathbb{A}_{\mathbb{C}}^n$ refers to the 'affine part' of $\mathbb{P}_{\mathbb{C}}^n$, while $H_i = \mathbb{P}_{\mathbb{C}}^{n-1}$ represents the 'hyperplane-at-infinity' containing every point-at-infinity. Notably the affine part can be constructed by restricting any one of the coordinates to non-zero values. Further decomposition in a similar fashion allows a projective space to be constructed as the union of purely affine spaces

$$\mathbb{P}_{\mathbb{C}}^n = V_0 \cup V_1 \cup \dots \cup V_n. \quad (4.2)$$

As an intuitive example, consider an observer in the real flat plane represented by $\mathbb{P}_{\mathbb{R}}^2 = \mathbb{A}_{\mathbb{R}}^2 \cup \mathbb{P}_{\mathbb{R}}^1$. Here, $\mathbb{A}_{\mathbb{R}}^2$ represents the real affine plane, upon which vector spaces can be defined depending on the position, or 'origin', of the observer. The real projective line $\mathbb{P}_{\mathbb{R}}^1$ represents the visual horizon at the infinite limit of the observer's plane. Further compactifying the real projective line through $\mathbb{P}_{\mathbb{R}}^1 = \mathbb{R} \cup \{\infty\} \sim \mathbb{S}_{\mathbb{R}}^1$ represents the visual horizon as a circle $\mathbb{S}_{\mathbb{R}}^1$ around the observer.

4.2.3 Intersection Theory

Identifying the set of common zeros for polynomials defined in $\mathbb{P}_{\mathbb{C}}^n$ is a central objective in algebraic geometry. However, since points in projective space are only defined up to multiplication by a common scalar, only homogeneous polynomials can be considered with the form¹⁷⁶

$$f(\lambda x_0, \dots, \lambda x_n) = \lambda^d f(x_0, \dots, x_n) \quad (4.3)$$

where d defines the order of the polynomial f . The set of zeros of f is then well-defined as

$$Z(f) \equiv \{(x_0, \dots, x_n) \in \mathbb{P}_{\mathbb{C}}^n | f(x_0, \dots, x_n) = 0\} \subset \mathbb{P}_{\mathbb{C}}^n. \quad (4.4)$$

Polynomials defined in $\mathbb{A}_{\mathbb{C}}^n$ can be converted to homogeneous polynomials in $\mathbb{P}_{\mathbb{C}}^n$ by introducing the arbitrary variable x_0 through the mapping $a_i \mapsto x_i/x_0$ for $i \neq 0$.

Combining these concepts leads to Bézout's Theorem for identifying the number of zeros of a set of multiple homogeneous polynomials. A proof of this theorem is mathematically involved but, for the purpose of this chapter, a simple statement of the key result will suffice. In particular, Bézout's Theorem states that the number of common intersections (including multiplicity) between n homogeneous polynomials in $n + 1$ variables is equal to the product of the corresponding polynomial degrees.¹⁷⁵ In other words, if f_1, \dots, f_n define distinct homogeneous polynomials in the projective space $\mathbb{P}_{\mathbb{C}}^n$ with degrees d_1, \dots, d_n respectively, then the number of intersection points between these polynomials is $d_1 \times \dots \times d_n$. As a simple example, a line of degree one intersects a curve of degree d in $\mathbb{P}_{\mathbb{C}}^2$ at exactly d points.

4.3 Enumerating Two-Electron h-RHF States

The closed-shell h-RHF formalism with two-electrons, described by a single spatial orbital $\phi(\mathbf{r})$, provides the simplest case for investigating if the number of h-RHF states is constant across all molecular structures. In what follows, consider the single spatial orbital $\phi(\mathbf{r})$ expanded in a basis of n real orthogonal functions $\{\chi_{\mu}(\mathbf{r})\}$ as

$$\phi(\mathbf{r}) = \sum_{\mu=1}^n C_{\mu} \chi_{\mu}(\mathbf{r}). \quad (4.5)$$

Here, restriction to an orthogonal basis makes the covariant and contravariant tensor notation redundant, and the obvious simplification in indexing has been introduced. The requirement for complex-orthonormalisation of the wave function defines the quadratic constraint equation

$$\sum_{\mu=1}^n C_{\mu}^2 = 1, \quad (4.6)$$

while the h-RHF energy is given by the polynomial

$$\tilde{E}(C_1, \dots, C_n) = h_0 + 2 \sum_{\mu\nu=1}^n h_{\mu\nu} C_{\mu} C_{\nu} + \sum_{\mu,\nu,\sigma,\tau=1}^n h_{\mu\nu\sigma\tau} C_{\mu} C_{\nu} C_{\sigma} C_{\tau}, \quad (4.7)$$

where $h_0 = V_N$ and $h_{\mu\nu\sigma\tau} = 2\langle\mu\nu|\sigma\tau\rangle - \langle\mu\nu|\tau\sigma\rangle$. Points corresponding to h-RHF solutions then exist as stationary points of Eq. (4.7) constrained by Eq. (4.6).

4.3.1 Homogenising the h-RHF Equations

Using the framework of algebraic geometry, the spatial orbital $\phi(\mathbf{r})$ for a two-electron system expanded in an n -dimensional basis can be represented by a point in an affine

space $(C_1, \dots, C_n) \in \mathbb{A}_{\mathbb{C}}^n$. The h-RHF energy (4.7) is then a function $\tilde{E} : \mathbb{A}_{\mathbb{C}}^n \rightarrow \mathbb{C}$ defined by a polynomial of degree four, while the normalisation constraint Eq. (4.6) is a second-order hypersurface $X \subseteq \mathbb{A}_{\mathbb{C}}^n$ defined as

$$X = \left\{ (C_1, \dots, C_n) \in \mathbb{A}_{\mathbb{C}}^n \mid \sum_{\mu=1}^n C_{\mu}^2 = 1 \right\}. \quad (4.8)$$

The roots of the differential $d\tilde{E}$ restricted to X define the h-RHF solutions.

To apply Bézout's Theorem, and enumerate the h-RHF stationary points, Eq. (4.6) and Eq. (4.7) must be expressed as homogeneous polynomials. Homogenisation is achieved by converting to the projective space $\mathbb{P}_{\mathbb{C}}^n$ represented by the points (C_0, \dots, C_n) through the mapping $(C_1, \dots, C_n) \mapsto (C_1/C_0, \dots, C_n/C_0)$. This process leads to the homogeneous constraint equation represented in $\mathbb{P}_{\mathbb{C}}^n$ as

$$\sum_{\mu=1}^n C_{\mu}^2 = C_0^2, \quad (4.9)$$

defining the projective hypersurface

$$\bar{X} = \left\{ (C_0, \dots, C_n) \in \mathbb{P}_{\mathbb{C}}^n \mid \sum_{\mu=1}^n C_{\mu}^2 = C_0^2 \right\}. \quad (4.10)$$

Moreover, the projective h-RHF energy can be written as a rational function $F : \mathbb{P}_{\mathbb{C}}^n \rightarrow \mathbb{C}$ defined by

$$F(C_0, \dots, C_n) = \tilde{E}\left(\frac{C_1}{C_0}, \dots, \frac{C_n}{C_0}\right) = \frac{\bar{E}(C_0, \dots, C_n)}{C_0^4} \quad (4.11)$$

where \bar{E} is the homogeneous version of \tilde{E} defined as

$$\bar{E}(C_0, \dots, C_n) = h_0 C_0^4 + 2 \sum_{\mu, \nu=1}^n h_{\mu\nu} C_{\mu} C_{\nu} C_0^2 + \sum_{\mu, \nu, \sigma, \tau=1}^n h_{\mu\nu\sigma\tau} C_{\mu} C_{\nu} C_{\sigma} C_{\tau}. \quad (4.12)$$

Consequently, h-RHF states exist as vanishing points of the differential

$$dF = \frac{\partial F}{\partial C_0} dC_0 + \sum_{\mu=1}^n \frac{\partial \bar{E}}{\partial C_{\mu}} dC_{\mu} \quad (4.13)$$

restricted to the projective hypersurface \bar{X} , where it is noted that $\frac{\partial F}{\partial C_{\mu}} dC_{\mu} = \frac{\partial \bar{E}}{\partial C_{\mu}} dC_{\mu}$ for $\mu \neq 0$.

4.3.2 Geometrically Decomposing the Constraint

Handling the constraint to the projective hypersurface \bar{X} presents the final hurdle before the two-electron h-RHF states can be enumerated. Although it is tempting to remove

the constraint by simply substituting Eq. (4.9) into Eq. (4.12), this cannot be achieved without either losing information of points-at-infinity or destroying the polynomial form by introducing square-root terms. Instead, the constraint can be handled by combining the homogeneity of the projective h-RHF energy F with a particular decomposition of \bar{X} .

Homogeneity provides the *essential* property of Eq. (4.11) and Eq. (4.12) required for deriving the number of constrained stationary points of \tilde{E} . In particular, homogeneity means that F is invariant to the simultaneous scalar multiplication of all coordinates. Therefore a stationary point of F in $\mathbb{P}_{\mathbb{C}}^n$ is only defined up to this scalar multiplication. To see how this allows the constraint to be decomposed, note that \bar{X} is isomorphic to a complex sphere $\mathcal{S}_{\mathbb{C}}^{n-1}$ of radius C_0 , i.e. $\bar{X} \sim \mathcal{S}_{\mathbb{C}}^{n-1} \subset \mathbb{P}_{\mathbb{C}}^n$. Crucially, homogeneity allows the stationary points of F to be identified on a sphere of *any* radius, although there are two sign-symmetries that must be taken into account. Firstly, since h-RHF states are only defined up to a change of sign for all coordinates in the underlying affine space — i.e. the points (C_0, C_1, \dots, C_n) and $(C_0, -C_1, \dots, -C_n)$ define the same state — only one hemisphere $\tilde{\mathcal{S}}_{\mathbb{C}}^{n-1}$ needs to be considered and antipodal points can be identified as the same state. Secondly, as the full coordinates in the projective space are defined up to multiplication by a scalar value, only positive values of C_0 need to be considered.

The constraint manifold can be further simplified by noting that an $(n-1)$ -dimensional hemisphere defined over a field k is isomorphic to an $(n-1)$ -dimensional projective space

$$\tilde{\mathcal{S}}_k^{n-1} \sim \mathbb{P}_k^{n-1}. \quad (4.14)$$

Following Eq. (4.1a) and Eq. (4.1b), the hemisphere $\tilde{\mathcal{S}}_k^{n-1}$ can therefore be further decomposed into an affine part $V_i = \mathbb{A}_k^{n-1}$ and a hyperplane-at-infinity $H_i = \mathbb{P}_k^{n-2}$ to yield

$$\tilde{\mathcal{S}}_k^{n-1} = V_i \cup H_i = \mathbb{A}_k^{n-1} \cup \mathbb{P}_k^{n-2}. \quad (4.15)$$

Repeatedly applying the isomorphism Eq. (4.14) and decomposition Eq. (4.15) then allows $\tilde{\mathcal{S}}_k^{n-1}$ to be decomposed into the union of disconnected affine spaces as

$$\tilde{\mathcal{S}}_k^{n-1} = \mathbb{A}_k^{n-1} \cup \dots \cup \mathbb{A}_k^0. \quad (4.16)$$

To visualise this decomposition, consider the real hemisphere $\tilde{\mathcal{S}}_{\mathbb{R}}^2 \subset \mathbb{P}_{\mathbb{R}}^3$ using the coordinates $(x_0, x_1, x_2, x_3) \in \mathbb{P}_{\mathbb{R}}^3$ with $x_3 \geq 0$, as illustrated schematically in Fig. 4.1. This hemisphere is isomorphic to the union $\tilde{\mathcal{S}}_{\mathbb{R}}^2 = V_3 \cup H_3$ of the two-dimensional plane defined by $x_3 = 1$,

$$V_3 = \left\{ (x_0, x_1, x_2, 1) \in \mathbb{P}_{\mathbb{R}}^3 \mid x_1^2 + x_2^2 + 1 = x_0^2 \right\} \sim \mathbb{A}_{\mathbb{R}}^2 \quad (4.17)$$

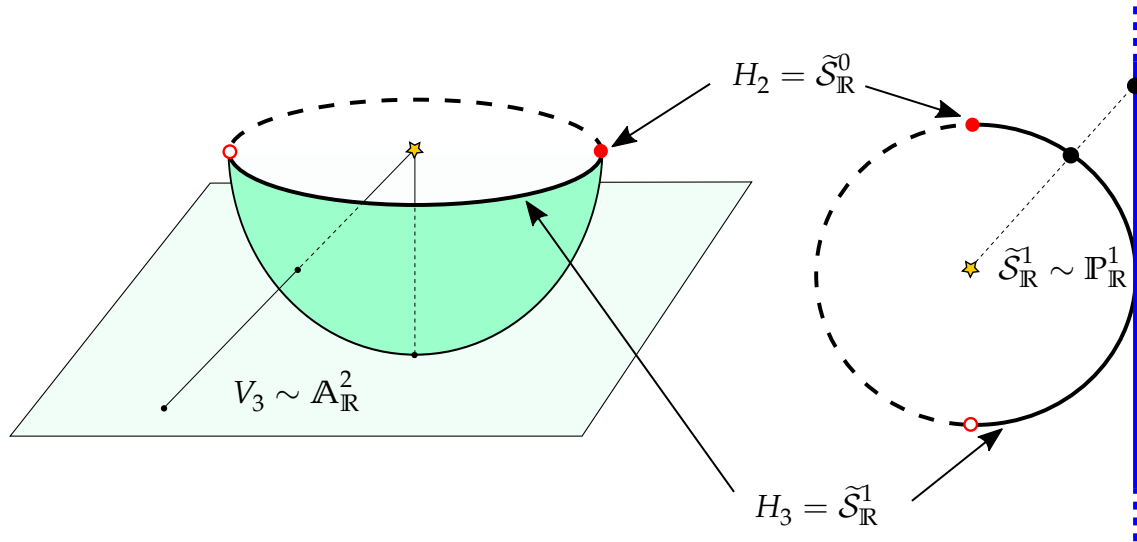


Figure 4.1: Schematic illustration of decomposing a constrained real hemisphere into the union of unconstrained affine subspaces, as given in Eq. (4.21). See main text for details.

and the one-dimensional hemisphere $H_3 = \tilde{\mathcal{S}}_{\mathbb{R}}^1$ representing the ‘semicircle-at-infinity’ where $x_3 = 0$,

$$H_3 = \left\{ (x_0, x_1, x_2, 0) \in \mathbb{P}_{\mathbb{R}}^3 \mid (x_1^2 + x_2^2 = x_0^2) \wedge (x_2 \geq 0) \right\} \sim \mathbb{P}_{\mathbb{R}}^1. \quad (4.18)$$

In turn, the one-dimensional hemisphere can be decomposed into the union $H_3 = V_2 \cup H_2$ of a line

$$V_2 = \left\{ (x_0, x_1, 1) \in \mathbb{P}_{\mathbb{R}}^2 \mid x_1^2 + 1 = x_0^2 \right\} \sim \mathbb{A}_{\mathbb{R}}^1 \quad (4.19)$$

and a zero-dimensional hemisphere $H_2 = \tilde{\mathcal{S}}_{\mathbb{R}}^0$

$$H_2 = \left\{ (x_0, x_1, 0) \in \mathbb{P}_{\mathbb{R}}^2 \mid (x_1^2 = x_0^2) \wedge (x_1 \geq 0) \right\} \sim \mathbb{A}_{\mathbb{R}}^0. \quad (4.20)$$

The antipodal sign-symmetry restricts the remaining constraint H_2 to only one (non-infinite) point $V_1 = \{(1, 1, 0)\}$, allowing $H_2 = V_1$ to be associated with a zero-dimensional affine space. Overall, the original hemisphere has been decomposed into the union of *non-overlapping* affine spaces

$$\tilde{\mathcal{S}}_{\mathbb{R}}^2 = V_3 \cup V_2 \cup V_1 = \mathbb{A}_{\mathbb{R}}^2 \cup \mathbb{A}_{\mathbb{R}}^1 \cup \mathbb{A}_{\mathbb{R}}^0. \quad (4.21)$$

Crucially, this decomposition for a real hemisphere $\tilde{\mathcal{S}}_{\mathbb{R}}^{n-1}$ extends to the complex hemisphere $\tilde{\mathcal{S}}_{\mathbb{C}}^{n-1}$ representing the two-electron h-RHF orbital constraint surface \bar{X} . As a result the h-RHF constraint surface can now be mathematically decomposed into the combination of lower-dimensional unconstrained spaces, avoiding the introduction of square-root terms. In principle, the number of stationary points of Eq. (4.12), given by the set size $|Z_{\text{h-RHF}}|$, can then be counted in each unconstrained affine subspace $|Z_i|$ and,

assuming the coordinates are chosen such that stationary points in each subspace are also stationary points in the overall space, the total number of h-RHF states is simply the sum

$$|Z_{\text{h-RHF}}| = \sum_{i=0}^{n-1} |Z_i|. \quad (4.22)$$

4.3.3 Counting the h-RHF Stationary Points

To count the number of h-RHF solutions using the decomposition in Section 4.3.2, first consider the case of one basis function, $n = 1$. Taking the sign-symmetries into account, there is clearly one trivial solution in the affine space at $(1) \in \mathbb{A}_{\mathbb{C}}^1$. Sign-symmetries of h-RHF states are henceforth implicit.

Now consider the $n = 2$ case, represented by a point $(C_0, C_1, C_2) \in \mathbb{P}_{\mathbb{C}}^2$. The projective h-RHF energy F is then given by

$$F(C_0, C_1, C_2) = h_0 + 2 \sum_{\mu\nu=1}^2 h_{\mu\nu} \frac{C_\mu C_\nu}{C_0^2} + \sum_{\mu\nu\sigma\tau=1}^2 h_{\mu\nu\sigma\tau} \frac{C_\mu C_\nu C_\sigma C_\tau}{C_0^4}. \quad (4.23)$$

Restriction to the hypersurface \bar{X} , in this case defined by $C_0^2 = C_1^2 + C_2^2$, makes F equivalent to the normalised h-RHF energy with C_0 providing the normalisation factor. Consequently, the constrained function $F_{\bar{X}}$ is invariant to global rescaling of the orbital coefficients C_1 and C_2 , and the partial derivative $\frac{\partial F_{\bar{X}}}{\partial C_0}$ is zero for all $C_0 \neq 0$, as illustrated for the hydrogen dimer in Fig. 4.2. Although it is possible for solutions to exist at infinity with $C_0 = 0$, these appear to occur only when electron-electron interactions vanish completely and a more comprehensive investigation is presented in Chapter 6. For the purpose of the current chapter, it is assumed that $C_0 \neq 0$ for all stationary points in real molecular systems.

First take the case $C_2 \neq 0$, where the coordinates are rotated such that

$$\left. \frac{\partial F_{\bar{X}}}{\partial C_2} \right|_{C_2=0} = 0 \quad \forall \quad C_0, C_1. \quad (4.24)$$

Exploiting the invariance of $F_{\bar{X}}$ to C_0 allows the h-RHF solutions to be located as stationary points along either the circle $C_1^2 + C_2^2 = 1$ (black curve in Fig. 4.2) or the line $C_2 = 1$ (blue line in Fig. 4.2). Taking the latter approach enforces $dC_2 = 0$ and leads to an unconstrained affine line $V_2 = \mathbb{A}_{\mathbb{C}}^1$ with coordinates $(C_0, C_1, 1) \in \mathbb{P}_{\mathbb{C}}^2$. When combined with $\frac{\partial F_{\bar{X}}}{\partial C_0} = 0$, the constrained differential becomes

$$dF_{\bar{X}} = \left. \frac{\partial \bar{E}_{\bar{X}}}{\partial C_1} \right|_{C_2=1} dC_1. \quad (4.25)$$

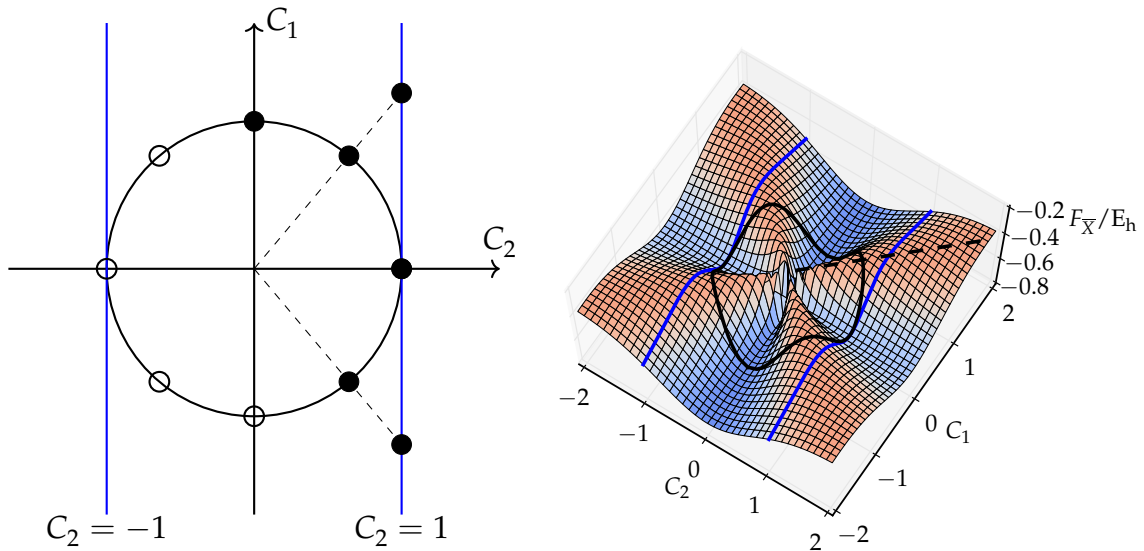


Figure 4.2: Constrained projective h-RHF energy $F_{\bar{X}}$ for the $n = 2$ hydrogen molecule (STO-3G) at a bond length of 2.5 \AA . The coordinate C_0 defines the normalisation constant, representing the distance of a point from the origin, and $\frac{\partial F_{\bar{X}}}{\partial C_0} = 0$ for all $C_0 \neq 0$. Exploiting this invariance, every stationary point constrained to the circle $C_1^2 + C_2^2 = 1$ (black curve) with $C_2 \neq 0$ can alternatively be located as a stationary point constrained to the line $C_2 = 1$ (blue line), where rescaling recovers the normalised h-RHF state (dashed line). Due to the overall sign symmetry, only half the stationary points need to be considered (filled circles vs. open circles).

Since \bar{E} is a fourth degree polynomial in C_1 , the partial derivative $\left. \frac{\partial \bar{E}_{\bar{X}}}{\partial C_1} \right|_{C_2=1}$ is third degree in C_1 and has three roots according to the Fundamental Theorem of Algebra, each defining an h-RHF state.

Next consider the case $C_2 = 0$, representing the constrained points-at-infinity $H_2 = V_1$ and recovering the $n = 1$ system. Since the coordinates have been rotated to satisfy Eq. (4.24), every stationary point in the $n = 1$ subspace $\mathbb{A}_{\mathbb{C}}^0$ must also be a stationary point in the full space, yielding one further solution in the full h-RHF space at the point $(1, 0) \in \mathbb{A}_{\mathbb{C}}^2$. Overall, there are three solutions in the $V_2 = \mathbb{A}_{\mathbb{C}}^1$ subspace and one in the $V_1 = \mathbb{A}_{\mathbb{C}}^0$ subspace, giving a total of $3 + 1 = 4$.

To continue, consider adding a third basis function with orbital coefficients represented by the point $(C_0, C_1, C_2, C_3) \in \mathbb{P}_{\mathbb{C}}^3$. Again, the coordinates corresponding to the orbital coefficients can be rotated such that

$$\left. \frac{\partial F_{\bar{X}}}{\partial C_3} \right|_{C_3=0} = 0 \quad \forall \quad C_0, C_1, C_2. \quad (4.26)$$

Consider first the case $C_3 \neq 0$. Similarly to the $n = 2$ example, the h-RHF states can be located as stationary points on either the sphere $C_1^2 + C_2^2 + C_3^2 = 1$ or the plane $C_3 = 1$, as illustrated for H_3^+ in Fig. 4.3. Taking the latter approach enforces $dC_3 = 0$ and leads to an unconstrained affine plane $V_3 = \mathbb{A}_{\mathbb{C}}^2$ with coordinates $(C_0, C_1, C_2, 1) \in \mathbb{P}_{\mathbb{C}}^3$. The

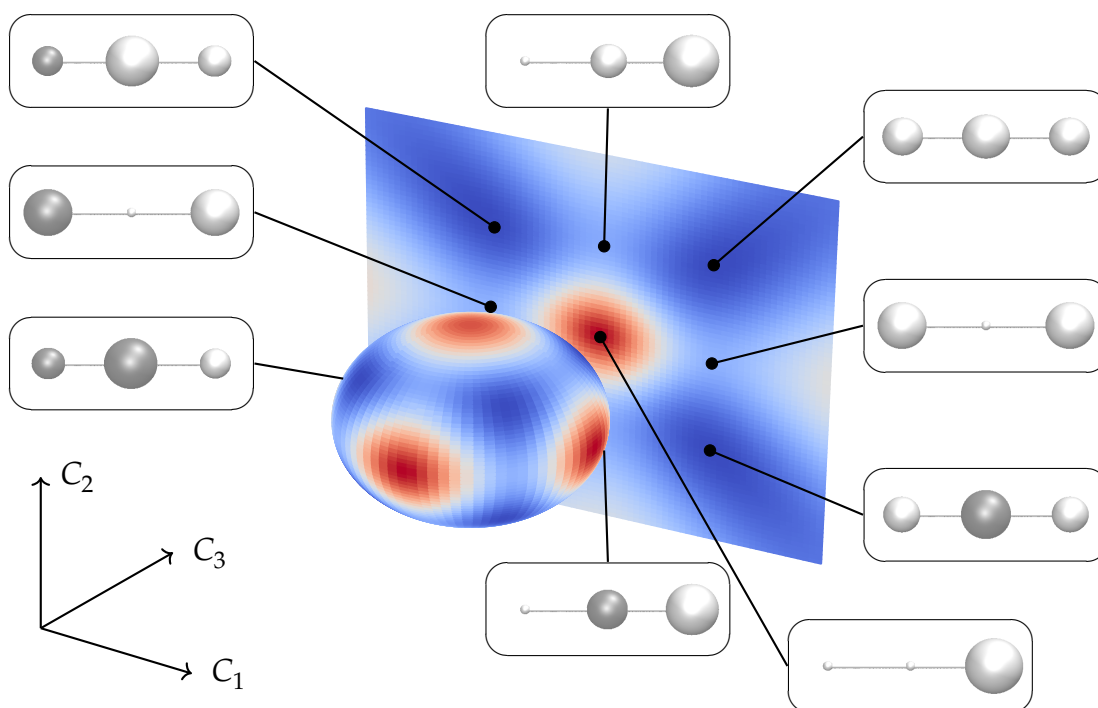


Figure 4.3: Constrained projective h-RHF energy $F_{\bar{X}}$ plotted on the sphere $C_1^2 + C_2^2 + C_3^2 = 1$ and the plane $C_3 = 1$ for linear H_3^+ in a minimal basis (STO-3G) at a bond length of 2.5 \AA . Nine stationary points can be located on the plane $C_3 = 1$, as shown alongside their corresponding orbital plots. The remaining four h-RHF states exist at the infinities of this plane, represented as the grand circle on the sphere corresponding to $C_3 = 0$. Although for illustrative purposes the bond length has been chosen such that all solutions are real, the mathematical framework and results extend to geometries where complex-valued h-RHF states are present.

constrained differential $dF_{\bar{X}}$ then reduces to

$$dF_{\bar{X}} = \left. \frac{\partial \bar{E}_{\bar{X}}}{\partial C_1} \right|_{C_3=1} dC_1 + \left. \frac{\partial \bar{E}_{\bar{X}}}{\partial C_2} \right|_{C_3=1} dC_2. \quad (4.27)$$

The relevant stationary points are now located by finding the common intersections of two third degree homogeneous polynomials

$$\left. \frac{\partial \bar{E}_{\bar{X}}}{\partial C_1} \right|_{C_3=1} = 0 \quad \text{and} \quad \left. \frac{\partial \bar{E}_{\bar{X}}}{\partial C_2} \right|_{C_3=1} = 0. \quad (4.28)$$

Applying Bézout's Theorem, the number of solutions to Eq. (4.28) is given by $3 \times 3 = 9$, yielding nine h-RHF states with $C_3 \neq 0$, shown in Fig. 4.3.

Now consider the remaining subspace $C_3 = 0$, representing the hyperplane-at-infinity H_3 . Since the overall coordinates are chosen to satisfy Eq. (4.26), every stationary

point in this subspace will also correspond to a stationary point in the full space. As a result, the subspace H_3 , represented by the points $(C_0, C_1, C_2, 0) \in \mathbb{P}_{\mathbb{C}}^3$, can be identified with the $n = 2$ case analogous to Fig. 4.2. Moreover, the number of stationary points in the H_3 subspace is the same as the total number of solutions in the $n = 2$ case, giving an additional four solutions. The total number of h-RHF states for $n = 3$ is therefore $9 + 3 + 1 = 13$.

Iteratively repeating the process of identifying the number of solutions in each subspace of the constraint surface, it is possible to extend this argument to a general two-electron system with n basis functions. In particular, the number of stationary points within a subspace of dimension i is given as $|Z_i| = 3^i$. The total number of stationary points, corresponding to the number of h-RHF states, is therefore

$$|Z_{\text{h-RHF}}| = \sum_{i=0}^{n-1} 3^i = \frac{1}{2}(3^n - 1). \quad (4.29)$$

Crucially, the approach taken in this derivation is independent of the nuclear repulsion, one- and two-electron integrals. Therefore, the number of h-RHF solutions depends only on the number of basis functions and every solution *must exist everywhere* as the molecular structure — or any other property — is varied.

Notably, Eq. (4.29) may include solutions with a multiplicity greater than one, for example exactly when states coalesce at the Coulson–Fischer point. Alternatively, solutions with a non-zero dimensionality can occur as continuous lines or planes of stationary points in the orbital coefficient space. In molecular systems, situations of this type will occur when degenerate basis functions are present, for example molecules with π -systems and cylindrical systems. However, an infinite number of solutions can be avoided by forcing the molecular orbitals to transform according to an irreducible representation of the molecular point group, as is widely applied to ensure correct symmetries across electronic structure theory.

4.3.4 Extension to h-UHF and Many-Electron Systems

The derivation of Eq. (4.36) presented in this section is the work of Mark Gross, while the remaining discussion is the contribution of the Author.

Applying more rigorous algebraic geometry provides a related route to deriving Eq. (4.29), although this derivation is well beyond the scope of the current work. This section considers the possibility of extending the algebraic geometry framework to unrestricted or many-electron systems.

In the two-electron h-UHF case, the wave function consists of two spatial orbitals

expanded in the underlying real orthogonal spatial basis as

$$\phi_\alpha(\mathbf{r}) = \sum_{\mu=1}^n {}^\alpha C_\mu \chi_\mu(\mathbf{r}) \quad \text{and} \quad \phi_\beta(\mathbf{r}) = \sum_{\mu=1}^n {}^\beta C_\mu \chi_\mu(\mathbf{r}). \quad (4.30)$$

The α and β molecular orbital coefficients are subject to unconnected complex orthonormalisation constraints

$$\sum_{\mu=1}^n {}^\alpha C_\mu^2 = 1 \quad \text{and} \quad \sum_{\mu=1}^n {}^\beta C_\mu^2 = 1, \quad (4.31)$$

and the h-UHF energy is given by

$$\begin{aligned} \tilde{E}({}^\alpha C_1, \dots, {}^\alpha C_n, {}^\beta C_1, \dots, {}^\beta C_n) = \\ h_0 + \sum_{\mu\nu=1}^n h_{\mu\nu} ({}^\alpha C_\mu {}^\alpha C_\nu + {}^\beta C_\mu {}^\beta C_\nu) + \sum_{\mu\nu\sigma\tau=1}^n h'_{\mu\nu\sigma\tau} {}^\alpha C_\mu {}^\alpha C_\sigma {}^\beta C_\nu {}^\beta C_\tau. \end{aligned} \quad (4.32)$$

Here, the only two-electron terms arise from the Coulomb interaction between the α and β electrons and $h'_{\mu\nu\sigma\tau} = \langle \mu\nu | \sigma\tau \rangle$. A given set of orbital coefficients can now be considered as a point in a $2n$ -dimensional affine space with coordinates

$$({}^\alpha C_1, \dots, {}^\alpha C_n, {}^\beta C_1, \dots, {}^\beta C_n) \in \mathbb{A}_{\mathbb{C}}^{2n}. \quad (4.33)$$

The constraints Eq. (4.31) then define a hypersurface X similar to Eq. (4.8), and the h-UHF states correspond to the stationary points of \tilde{E} constrained to X .

To convert \tilde{E} and X to homogeneous polynomials, switch to a set of bihomogeneous coordinates $(({}^\alpha C_0, {}^\alpha C_1, \dots, {}^\alpha C_n), ({}^\beta C_0, {}^\beta C_1, \dots, {}^\beta C_n)) \in \mathbb{P}_{\mathbb{C}}^n \times \mathbb{P}_{\mathbb{C}}^n$ through the mapping ${}^\alpha C_i \rightarrow {}^\alpha C_i / {}^\alpha C_0$ and ${}^\beta C_i \rightarrow {}^\beta C_i / {}^\beta C_0$ where $i > 0$. This results in the projective hypersurface \bar{X} satisfying the constraint

$$\sum_{\mu=1}^n {}^\alpha C_\mu^2 = {}^\alpha C_0^2 \quad \text{and} \quad \sum_{\mu=1}^n {}^\beta C_\mu^2 = {}^\beta C_0^2, \quad (4.34)$$

and the homogeneous h-UHF energy F

$$\begin{aligned} F(({}^\alpha C_0, {}^\alpha C_1, \dots, {}^\alpha C_n), ({}^\beta C_0, {}^\beta C_1, \dots, {}^\beta C_n)) = \\ h_0 + \sum_{\mu\nu=1}^n h_{\mu\nu} \left(\frac{{}^\alpha C_\mu {}^\alpha C_\nu}{{}^\alpha C_0^2} + \frac{{}^\beta C_\mu {}^\beta C_\nu}{{}^\beta C_0^2} \right) + \sum_{\mu\nu\sigma\tau=1}^n h'_{\mu\nu\sigma\tau} \frac{{}^\alpha C_\mu {}^\alpha C_\sigma {}^\beta C_\nu {}^\beta C_\tau}{{}^\alpha C_0^2 {}^\beta C_0^2}. \end{aligned} \quad (4.35)$$

Solutions to the h-UHF equations can now be identified as stationary points of F constrained to \bar{X} .

The details of the resulting rigorous derivation are well beyond the expertise of *the Author*, however the number of h-UHF solutions in two-electron systems can be identified as a weighted sum of binomial coefficients

$$|Z_{\text{h-UHF}}| = \frac{1}{4} \sum_{i=0}^n \sum_{j=0}^n \sum_{l=0}^n \sum_{k=i+j+1-n-l}^{n-1-l} \binom{n}{i} \binom{n}{j} \binom{i}{l} \binom{j}{k} (-1)^{i+j} 2^{2n+k-l-j}. \quad (4.36)$$

There appears to be no closed form expression for Eq. (4.36). However, for the purposes of h-HF theory, the fact that the number of stationary h-UHF states in two-electron systems can be rigorously computed without *any* dependence on the molecular integrals supports the conjecture that h-HF states exist across all molecular structures.

Extending further to many-electron systems introduces additional challenges as the parametrisation of the h-HF wave function must account for invariance with respect to occupied-occupied orbital rotations. In general, this requires parametrising the complex-orthogonal Grassmannian, representing the set of N -dimensional subspaces of a n -dimensional vector space. However, there is a duality in the complex-orthogonal Grassmannian that allows the $N = n - 1$ case to be equated with a one-electron system, allowing Eq. (4.29) to be applied for systems with one vacant orbital. Alternatively, an extension for general many-electrons may be possible through the Plücker embedding,¹⁸¹ where the Grassmannian is realised as a subset of a projective space. If the h-HF energy can be expressed as a polynomial with this embedding, it is highly likely that algebraic geometry will prove that all h-HF solutions must exist for every molecular structure, and research in this direction is ongoing.

4.3.5 Upper Bound for Real HF States

The principle motivation for deriving the exact number of h-HF solutions was to prove that these solutions exist for all molecular geometries. However, since every real HF state is also a stationary point of the h-HF equations, the total number of h-HF solutions also creates a rigorous upper bound on the number of real RHF and UHF states. In turn, these rigorous upper bounds provide an indication of the complexity of the HF solution set. Notably, Eq. (4.29) has been previously identified as an upper bound on the number of real closed-shell HF solutions for two-electron systems.²¹ However, this previous result was only derived rigorously for two basis functions ($n = 2$), while the derivation for more basis functions was restricted to the zero differential overlap assumption

$$h_{\mu\nu} = \delta_{\mu\nu}h_{\mu\mu} \quad \text{and} \quad \langle \mu\nu | \sigma\tau \rangle = \delta_{\mu\sigma}\delta_{\nu\tau}\langle \mu\nu | \mu\nu \rangle. \quad (4.37)$$

In contrast, employing the algebraic geometry approach presented in section 4.3.3 yields an alternative and entirely generalised geometric proof.

Fukutome presents the only other attempt to compute the complete number of HF states.²² To achieve this, Fukutome expresses the HF optimisation conditions using a density matrix formalism and HF solutions are identified as the intersection of multiple real quadratic hypersurfaces.²² Moreover, the most general c-GHF formalism of HF theory is considered, where molecular orbitals are not restricted to real values or to physical spin values. Lower and upper bounds on the number of c-GHF states for a

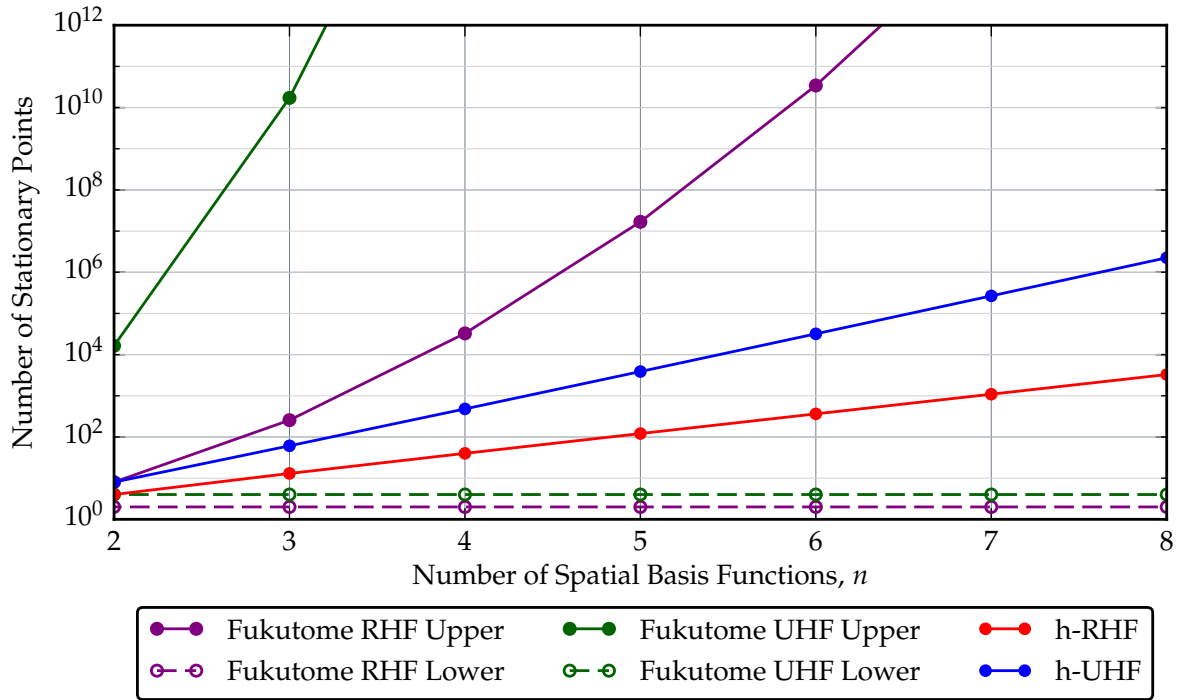


Figure 4.4: Upper bounds on the number of real two-electron RHF and UHF states derived through Eq. (4.29) and Eq. (4.36) are considerably lower than the upper bounds derived in Ref. (22) .

system of N electrons in $2n$ combined spin-spatial basis functions are then identified as

$$\text{Lower} = 2^K \quad \text{Upper} = 2^{(4n^2 - K)}, \quad (4.38)$$

where $K = \min(N, 2n - N)$.

Since all UHF solutions must be stationary points of the GHF equations, and all real HF solutions must be stationary points of the c-HF equations, Eq. (4.38) also provides lower and upper bounds on the number of real UHF states. Moreover, bounds on the number of real RHF states can be identified by taking Eq. (4.38) with n spatial basis functions and $N/2$ closed-shell electron pairs. For the case of two-electron systems, these considerations yield upper bounds on the number of real RHF and real UHF states as 2^{n^2-1} and 4^{2n^2-1} respectively. Comparing these bounds to Eq. (4.29) and Eq. (4.36) demonstrates that the number of h-RHF and h-UHF solutions dramatically reduce the bounds on the number of real RHF and UHF states for two-electron systems, as illustrated in Fig. 4.4. In turn, this reduction indicates that the full HF solution space may be less expansive and complex as previously thought.^{22,23}

4.4 Results and Discussion

Since the number of h-RHF and h-UHF states for two-electron systems depends on only the number of basis functions, the h-HF states for any distinct two-electron systems with

the same number of basis functions can be smoothly interconverted by either moving the basis function centres (i.e. changing structure) or adjusting the atomic charges (i.e. changing the nuclei). Moreover, as the total number of h-RHF and h-UHF states in these systems is known exactly, exhaustively identifying every possible stationary point is now possible. This provides the opportunity to investigate the topology of HF states as molecular structure changes, allowing the coalescence of real HF states at Coulson–Fischer points and the emergence of complex h-HF states to be understood.

The structure of HF coalescence points as the molecular parameters are varied can be classified and generalised through the field of catastrophe theory: a branch of mathematics concerned with the evolution of stationary points on a function as the control parameters are varied.¹⁸² In catastrophe theory, degenerate stationary points, where one or more higher derivatives of the potential become zero, are treated as ‘organising centres’ for non-degenerate stationary points. Expanding the function in terms of small perturbations of the parameters around these degenerate stationary points allows the degeneracy to be lifted in an ‘unfolding’ process. For one-dimensional functions, this allows any degenerate stationary point to be classified as one of only seven ‘elementary catastrophes’, providing a general picture for the evolution of stationary points for different potentials.¹⁸³

For the HF energy potential function, degenerate stationary points refer to Coulson–Fischer points where HF states coalesce. The language of catastrophe theory is therefore ideal for describing and classifying the types of Coulson–Fischer points seen in molecular systems. Previous studies have employed perturbative expansions of the HF energy in the vicinity of instability thresholds to classify the different types of Coulson–Fischer points^{116–118,184} and the intersection of multiple instability thresholds.¹¹⁵ In this section, the full set of h-RHF and h-UHF states in a collection of model systems are identified, allowing the coalescence of real HF states to be investigated and classified using catastrophe theory.

4.4.1 Computational Details

Identification of h-RHF and h-UHF stationary states was performed using an in-house version of the geometric h-HF optimisation algorithm described in Appendix A and implemented using the NUMPY library.¹⁸⁵ The one- and two-electron integrals were computed in Q-CHEM 4.3¹⁸⁶ while all figures were plotted using MATPLOTLIB.¹⁸⁷

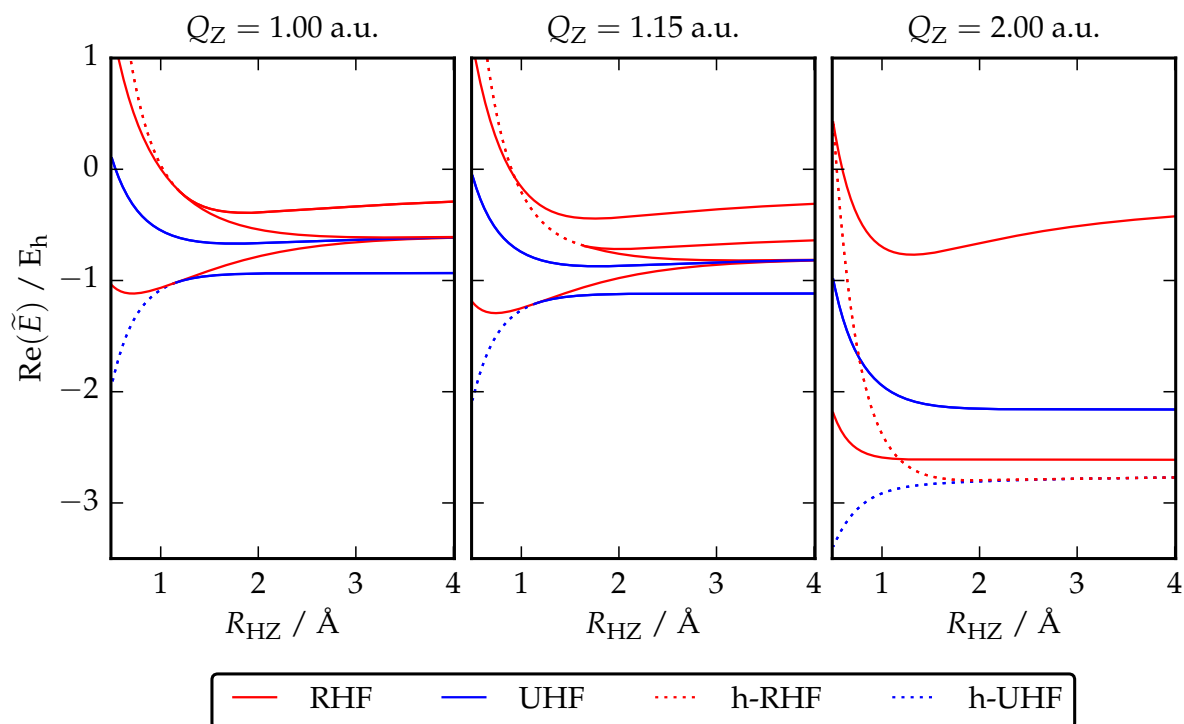


Figure 4.5: Eight h-UHF states (including four h-RHF states) for HZ in the minimal STO-3G basis are located for all bond lengths R_{HZ} and charges Q_Z . Each h-RHF and h-UHF state corresponds to a real RHF (red solid) or real UHF (blue solid) state where the latter exist. h-RHF and h-UHF states with complex-valued orbital coefficients (red dotted and blue dotted respectively) form in pairs with holomorphic energies and orbital coefficients related by complex conjugation. In the case of $Q_Z = 2.00$ a.u., corresponding to HHe^+ , two pairs of h-RHF and h-UHF states exist with complex coefficients across all geometries.

4.4.2 Dihydrogen Isoelectronic Sequence

The HZ molecule provides the first example for understanding how h-RHF and h-UHF states evolve as the molecular structure or atomic charges are varied. Here the molecular geometry is determined by a single parameter: the bond length R_{HZ} . Varying the nuclear charge Q_Z of the hydrogenic Z atom between 0 and 2 enables the smooth interconversion along the isoelectronic sequence $\text{H}^- \rightarrow \text{H}_2 \rightarrow \text{HHe}^+$.¹⁵² Through R_{HZ} and Q_Z , the qualitative behaviour of h-RHF and h-UHF states in symmetric and asymmetric diatomic molecules can be probed and understood.

Consider the molecule represented in the minimal (STO-3G) basis with only two basis functions ($n = 2$). Here, Eq. (4.29) and Eq. (4.36) dictate *exactly* four and eight h-RHF and h-UHF solutions must exist respectively for every set of R_{HZ} and Q_Z . Take first the case $Q_Z = 1.00$ a.u., corresponding to H_2 and for which four h-RHF and eight h-UHF solutions can be identified (Fig. 4.5 left panel). In the dissociation limit each solution has real orbital coefficients and corresponds to a real RHF (red solid)

or UHF (blue solid) stationary state. The RHF solutions represent the σ_g^2 , σ_u^2 and degenerate ionic $H^+ - H^- / H^- - H^+$ configurations (in order of ascending energy) while the additional UHF solutions correspond to the low-energy diradical $^1H-H^\downarrow / ^1H-H^\uparrow$ and the degenerate $\sigma_g\sigma_u$ configurations.

As the molecular bond length shortens, the diradical states coalesce with the σ_g^2 state at the Coulson–Fischer point²⁴ and disappear at shorter bond lengths. Similarly, the ionic states coalesce with the σ_u^2 states, although at a different instability threshold. At both the RHF and UHF coalescence points, two real HF solutions (related by symmetry) simultaneously coalesce with a third real HF state, with the first two appearing to disappear. In contrast, the corresponding h-RHF (red dotted) and h-UHF (blue dotted) solutions continue to exist with complex-valued orbital coefficients, extending across all molecular geometries. Using the classification schemes developed by Mestechkin^{116–118} and Fukutome,^{115,184} these coalescence points can be identified as ‘confluence’ points, where two maxima (minima) converge onto a minimum (maximum).

Reflecting the pairwise disappearance of HF solutions at coalescence points, complex h-RHF and h-UHF solutions always arise in pairs with energies and coefficients related by complex conjugation. Surprisingly, the holomorphic energies of the h-RHF and h-UHF stationary points appear to be real for all geometries in the minimal basis bond stretch of H_2 , despite the complex-valued orbital coefficients of the states. It turns out that hidden symmetries exist in the h-HF formulation which, when conserved, ensure real-valued holomorphic energies. An investigation of these real energies is postponed until Chapter 5.

Breaking the left-right molecular symmetry by moving along the isoelectronic sequence to $Q_Z = 1.15$ a.u. lifts the degeneracy of the ionic states and leads to the coalescence of only the states corresponding to the σ_u^2 and $H^+ - Z^-$ configurations at a ‘pair annihilation’ point (Fig. 4.5 middle panel). Beyond this point, both real RHF solutions disappear while their h-RHF counterparts continue as a complex conjugate pair, this time with complex-valued holomorphic energies. In contrast, since there is no energetic difference between the symmetry-related diradical UHF states, they remain degenerate and still coalesce with the ground RHF state at a triply-degenerate confluence point.

Increasing Q_Z further, the RHF coalescence point occurs at increasingly large bond lengths, ‘unzipping’ until eventually only two real RHF solutions exist across all geometries for $Q_Z = 2.00$ a.u. (Fig. 4.5 right panel). These real states represent the global minima and maxima on the RHF energy and correspond to the σ_g^2 and $H^- - Z^+$ configurations in H_2 . In contrast, the remaining two h-RHF solutions form a complex-conjugate pair with complex orbital coefficients across *all* geometries. Furthermore, the diradical

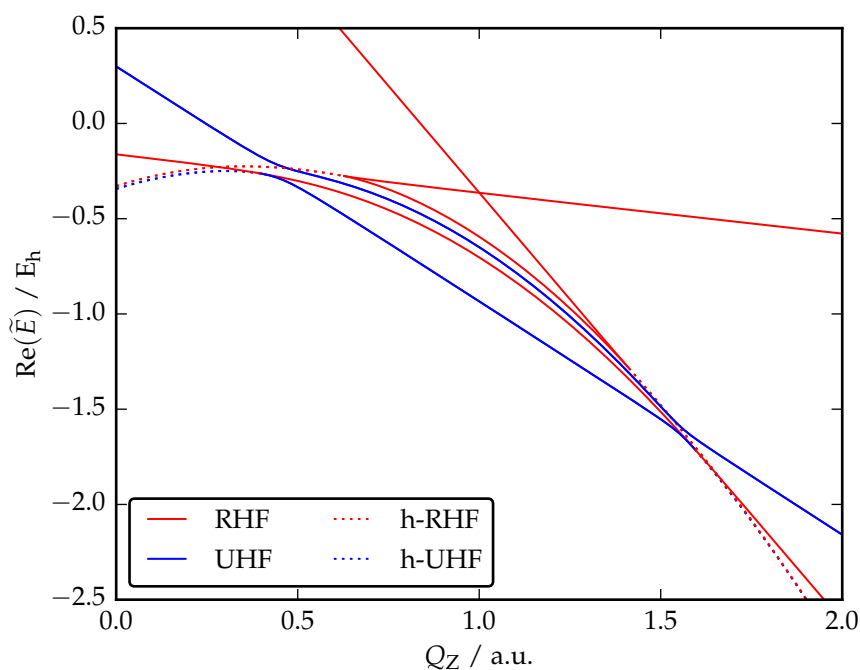


Figure 4.6: All h-RHF and h-UHF solutions of HZ in the minimal STO-3G basis are shown as the nuclear charge Q_Z is varied at the fixed bond length 2.50 \AA , demonstrating the interconversion between the complex h-RHF states of HHe^+ ($Q_Z = 2.00 \text{ a.u.}$) and H_2 ($Q_Z = 1.00 \text{ a.u.}$). The h-RHF and h-UHF states of HHe^+ that exist with complex coefficients for all bond lengths are seen to smoothly evolve into real h-RHF states of H_2 .

h-UHF states no longer coalesce with the ground RHF and also appear to be complex across all geometries, although their holomorphic energies still remain real for all geometries.

It appears unlikely that any ‘physical’ electronic states can be assigned to these solutions with complex-valued orbital coefficients across all bond lengths. Most significantly, the real parts of their holomorphic energies lie below the FCI ground state in this basis, breaking the variational principle. However, they can be smoothly evolved into real states with physical interpretations by varying Q_Z at a fixed bond length, as shown in Fig. 4.6. These states can therefore be considered as ‘dormant’ analytic continuations of real HF states which, when needed, allow connections between the real HF states of chemically distinct isoelectronic systems.

Identifying the full set of h-RHF and h-UHF states in the minimal basis HZ model now allows the coalescence behaviour of the solutions to be fully understood. This behaviour can be further explained and visualised using catastrophe theory by noting that the position of the degenerate Coulson–Fischer points depends solely on the two parameters R_{HZ} and Q_Z . For simplicity, consider the sole occupied RHF spatial orbital $\phi(\mathbf{r})$ expressed in terms of the rotation angle θ describing the degree of mixing between

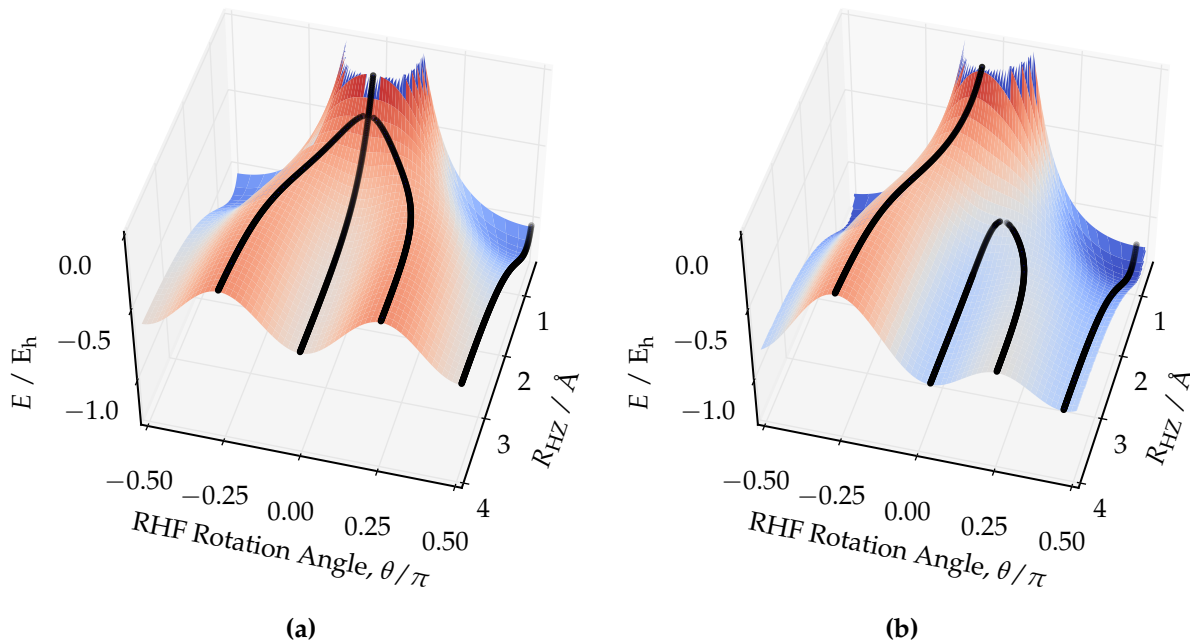


Figure 4.7: Conventional HF energy plotted as a function of the RHF rotation angle θ , see Eq. (4.39), for $Q_Z = 1.00$ a.u. and $Q_Z = 1.15$ a.u. (a) When $Q_Z = 1.00$ a.u. the molecule possesses $D_{\infty h}$ symmetry and the ionic solutions simultaneously converge with the σ_u^2 state, disappearing in a pitchfork bifurcation. (b) For $Q_Z = 1.15$ a.u. the molecular symmetry becomes $C_{\infty v}$, decomposing the pitchfork bifurcation into a primary branch and secondary branch. The two stationary points in the secondary branch coalesce and disappear at a pair-annihilation point.

symmetry-pure (orthogonal) $\sigma_g(\mathbf{r})$ and $\sigma_u(\mathbf{r})$ molecular orbitals

$$\phi(\mathbf{r}) = \sigma_g(\mathbf{r}) \cos \theta + \sigma_u(\mathbf{r}) \sin \theta. \quad (4.39)$$

When $Q_Z = 1.00$ a.u., the confluence point represents a triply-degenerate stationary point and the RHF solutions coalesce in a pitchfork bifurcation¹⁸⁸ (Fig. 4.7a). In contrast, for $Q_Z \neq 1.00$ a.u. the pair annihilation point corresponds to a doubly-degenerate stationary point where the pitchfork bifurcation is broken into a primary branch, existing across all geometries, and two secondary branches that coalesce and disappear (Fig. 4.7b).

Simultaneously considering the stationary points as both R and Q_Z are varied reveals that the structure of these coalescence points can be described more generally as a ‘cusp’ catastrophe.¹⁸² This classification indicates that pair annihilation points (corresponding to ‘fold’ catastrophes) will be significantly more prevalent than confluence points in molecular systems, while the simultaneous convergence of three RHF states in H_2 arises as a direct consequence of the “left-right” symmetry at $Q_Z = 1.00$ a.u. Furthermore, although the diradical UHF states in this model only coalesce at triply-degenerate points, these coalescence points will also form a cusp catastrophe if the degeneracy of the UHF states is broken, e.g. by introducing a magnetic field aligned with the internuclear axis.

4.4.3 Isomorphism of HHeH^{2+} and HHeH :

Consider next the two-electron linear HHeH^{2+} molecule in the minimal (STO-3G) basis. As a system with three basis functions, a total of 13 h-RHF and 61 h-UHF solutions can be identified for all symmetric R_{HHe} bond lengths. For the sake of clarity, only the topology and coalescence points of the h-RHF states will be investigated (Fig. 4.8 left panel).

In the dissociation limit, only five of the h-RHF states correspond to real RHF states, with degeneracies of one, one, one and two in order of ascending energy. Like the dormant states seen in HHe^+ , the remaining eight solutions possess imaginary orbital coefficients across all geometries. However, the fact that over half of h-RHF states appear as dormant complex-valued states in such a simple system suggests that solutions of this type are likely to dominate as systems become larger with more variational degrees of freedom. Shortening the bond length, the three highest energy RHF states coalesce at a triply degenerate confluence point, leaving only one real solution. This type of Coulson–Fischer point is expected since, like H_2 , the HHeH^{2+} molecule possesses $\mathcal{D}_{\infty h}$ spatial symmetry and the doubly degenerate symmetry-broken states are related by left-

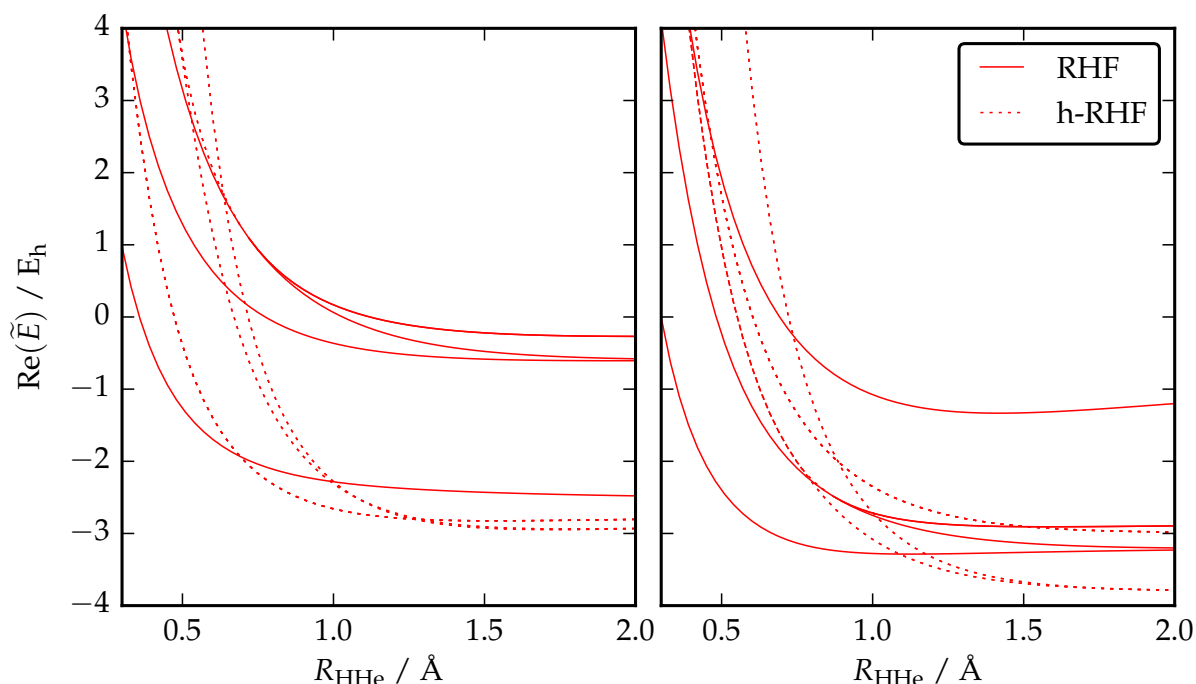


Figure 4.8: The 13 h-RHF states for HHeH^{2+} (left) and HHeH (right) in the minimal STO-3G basis for the symmetric H–He bond stretch. In both cases, six solutions have complex coefficients across all bond lengths, arising in degenerate complex-conjugate pairs. At short bond lengths, two pairs of complex solutions with real holomorphic energies coalesce to form two degenerate pairs with complex-valued holomorphic energies.

right symmetry. Furthermore, this left-right symmetry is preserved by the state these symmetry-broken states coalesce with. Beyond this coalescence point, the corresponding h-RHF states continue as expected with complex-valued orbital coefficients related by complex conjugation although, like in H_2 , they retain real-valued holomorphic energies.

In contrast to H_2 , these real-valued holomorphic energies do not continue for *all* geometries. At approximately $R_{HHe} = 0.5 \text{ \AA}$, the h-RHF states that originally represented the high-energy real RHF state each appear to coalesce with a dormant h-RHF state in the complex plane. Beyond this point, four h-RHF solutions extend with complex-valued holomorphic energies as two double-degenerate pairs related by complex conjugation. This surprising observation demonstrates the potential importance of dormant holomorphic solutions for dictating the coalescence behaviour of states in the complex plane.

Molecular systems with two electrons or two electron holes in n basis functions are mathematically equivalent and Eq. (4.29) applies equally to both. The minimal $HHeH^{2+}$ and $HHeH$ molecules provide a simple example of this isomorphism and a total of 13 h-RHF solutions can also be identified for $HHeH$ (Fig. 4.8 right panel). Significantly, although the real components of the h-RHF energies in $HHeH$ are reversed in order of energy compared to $HHeH^{2+}$, the qualitative behaviour of solutions and the pattern of coalescence points are equivalent. Moreover, as in $HHeH^{2+}$, the coalescence of two pairs of degenerate complex h-RHF states to form a set of four degenerate complex solutions can be observed at $R_{HHe} = 0.7 \text{ \AA}$. This simple particle-hole duality in the h-RHF equations supports the extension of the holomorphic framework from two-electron systems to many-electron molecules.

4.4.4 Double Bond Rotation of Ethene

The concepts discussed in the model systems presented in Section 4.4.2 and Section 4.4.3 can also be extended to molecules containing more than two electrons. In particular, the properties and reactivity of many molecular systems are dominated by a subset of only two electrons which, by freezing the remaining core electrons, can be reduced to two-electron problems. The electronic energy levels in the double bond rotation of ethene provide a chemically intuitive example that depends strongly on the nature of the two-electron, two-centre π bond.^{114,189}

Starting with an orthogonal basis comprising the STO-3G ground state RHF molecular orbitals at a particular planar D_{2h} geometry,* an active orbital space is constructed from the b_{3u} (π) and b_{2g} (π^*) orbitals while the remaining core and virtual orbitals are

* $R_{CC} = 1.255960 \text{ \AA}$; $R_{CH} = 1.082056 \text{ \AA}$; terminal $\angle CH = 115.64 \text{ deg}$

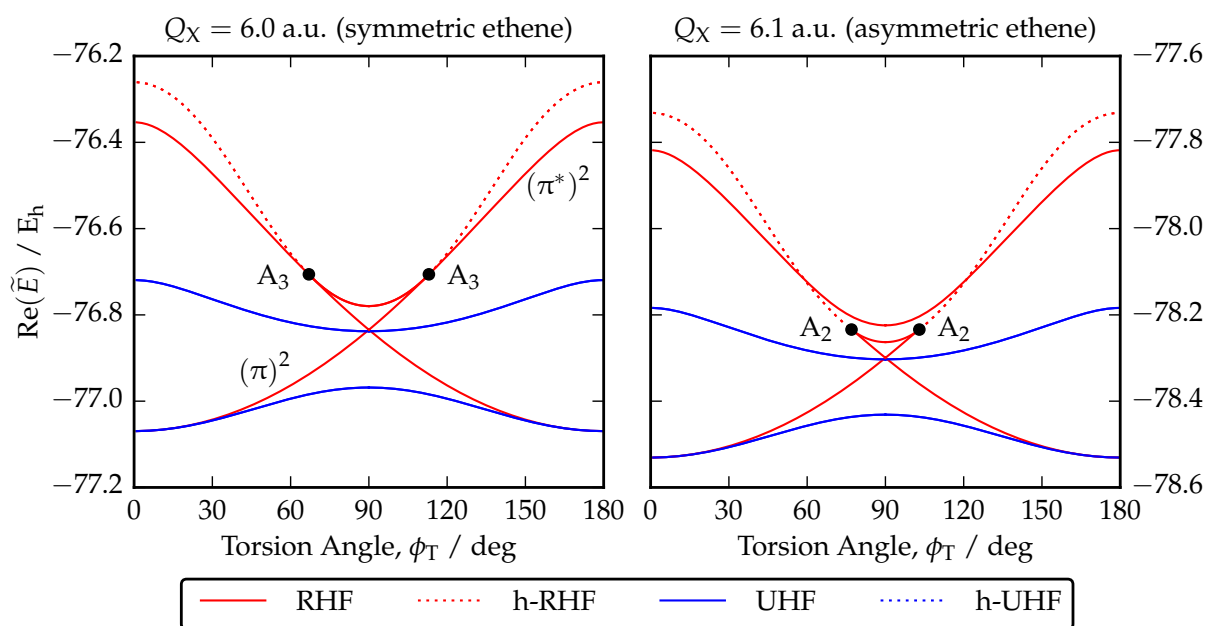


Figure 4.9: h-RHF and h-UHF solutions identified in the two-electron two-orbital active space comprising the π and π^* orbitals of minimal basis CH_2H_2 (STO-3G), where X is a carbon-like atom with nuclear charge Q_X . At $\phi_T = 90^\circ$, every solution corresponds to a real RHF (red solid) or real UHF (blue solid) state. As ϕ_T moves towards 0° or 180° , real RHF states in symmetric ethene (left panel) coalesce at A_3 cusp catastrophes. Breaking the molecular symmetry splits the degeneracy of the ionic RHF states and the coalescence points become doubly degenerate A_2 fold catastrophes (right panel). For this set of bond lengths, the real UHF solutions remain real across all torsion ϕ_T .

frozen. The π electrons in this active space reduce to a two-electron problem in two basis functions, yielding a total of four h-RHF and eight h-UHF stationary points as predicted by Eq. (4.29) and Eq. (4.36) respectively. Relaxing the core and virtual orbitals then allows the corresponding h-RHF and h-UHF states in the full orbital space to be identified (Fig. 4.9 left panel).

From the symmetry equivalence of the carbon centres, the h-RHF and h-UHF states located through this active space resemble those of H_2 . In the C–C dissociation limit, the h-RHF states correspond to the $(\pi)^2$ and $(\pi^*)^2$ configurations and the degenerate symmetry broken $\text{H}_2\text{C}^+ - \text{CH}_2^- / \text{H}_2\text{C}^- - \text{CH}_2^+$ ionic states while the h-UHF solutions represent the $(\pi)(\pi^*)$ and diradical $\text{H}_2\text{C}^\uparrow - \text{CH}_2^\downarrow / \text{H}_2\text{C}^\downarrow - \text{CH}_2^\uparrow$ configurations. As the carbon-carbon bond length R_{CC} is shortened, the ionic states coalesce with the $(\pi^*)^2$ state at approximately $R_{\text{CC}} = 1.29 \text{ \AA}$ in a triply degenerate A_3 cusp catastrophe analogous to Fig. 4.7a.

Of particular interest is the twisted D_{2d} (90 deg) geometry, providing an archetypal model of strongly correlated diradical systems.^{17,144,190} Here the ground RHF state becomes doubly-degenerate, leading to the strong multireference character of the exact wave function. As the torsion angle ϕ_T shifts away from the D_{2d} structure towards the

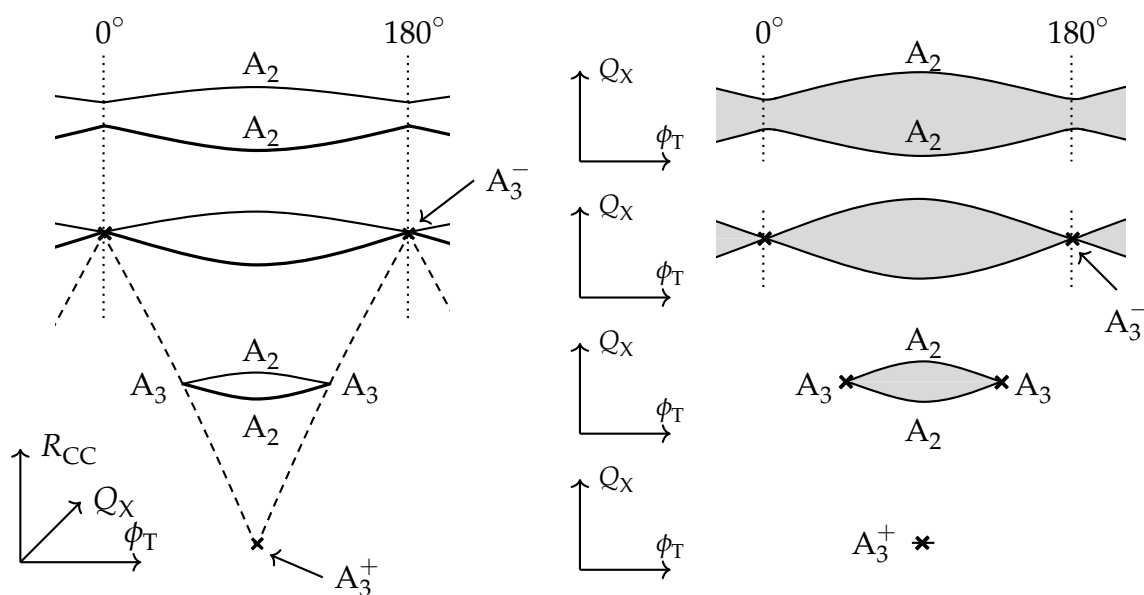


Figure 4.10: Sketch of the conical critical manifold (left) showing the types of coalescence points between real RHF solutions in ethene and their dependence on the molecular structure parameters R_{CC} , ϕ_T and Q_X . Sections through the conical critical manifold (right) demonstrate the dependence of these coalescence points on ϕ_T and Q_X at various values of R_{CC} . Doubly and triply degenerate coalescence points correspond to A_2 fold and A_3 cusp catastrophes respectively. As R_{CC} increases, two cusp catastrophes emerge from an A_3^+ cusp creation catastrophe and recombine at an A_3^- cusp annihilation catastrophe. Within the conoidal ‘shark-tooth’ bifurcation structure (shaded) there exist four real RHF states, while only two remain outside.

planar geometry, this degeneracy is lifted. In the process, the ionic states simultaneously coalesce with the anti-bonding $(\pi^*)^2$ state at two A_3 cusp catastrophes (related by symmetry) located at around $\phi_T = 45$ deg and 135 deg (Fig. 4.9 left panel). The holomorphic counterparts extend with complex-valued orbital coefficients, retaining real-valued holomorphic energies for all torsion angles. Similarly, at certain bond lengths (not shown), the diradical states coalesce with the bonding $(\pi)^2$ state, mirroring a previous study by Fukutome.¹¹⁴

To model the breaking of left-right molecular symmetry, one carbon atom can be replaced with a carbon-like nucleus X containing six electrons and a variable nuclear charge Q_X . Increasing Q_X away from 6.0 a.u. breaks the degeneracy of the ionic states, resulting in the coalescence of only the $(\pi^*)^2$ and $H_2X^- - ^+CH_2$ states at two doubly degenerate A_2 fold catastrophes that shift towards $\phi_T = 90$ deg, as illustrated with $Q_X = 6.1$ a.u. in Fig. 4.9 (right panel). In contrast, the diradical UHF states remain degenerate across all ϕ_T although again, introducing a magnetic field aligned with the X–C axis would break this degeneracy.

The exact position of these coalescence points depends on the other molecular structure parameters, particularly the X–C bond length and the nuclear charge Q_X .

To visualise the global structure of coalescence points between RHF states, a critical manifold can be sketched for all possible variations of R_{CC} , ϕ_T and Q_X (see Fig. 4.10). As R_{CC} increases, two A_3 cusp catastrophes emerge in the plane $Q_X = 6$ a.u. from an A_3^+ cusp ‘creation’ point.¹⁹¹ These symmetry related A_3 catastrophes are connected by two A_2 fold catastrophes when $Q_X \neq 6$ a.u. Further increasing R_{CC} causes the A_3 catastrophes to separate away from $\phi_T = 90$ deg until they recombine at $\phi_T = 0$ deg (or the symmetry related point $\phi_T = 180$ deg) at an A_3^- cusp ‘annihilation’ point.¹⁹¹ At larger bond lengths there are no coalescence points for $Q_X = 6$ a.u., while the two A_2 fold catastrophes remain when $Q_X \neq 6$ a.u. In total, four real RHF states exist for any set of R_{CC} , ϕ_T and Q_X that lie within this ‘shark-tooth’ bifurcation structure, compared to only two outside.

The nature of the multiple h-RHF and h-UHF states for ethene reinforces the principle concepts developed earlier in this chapter. Firstly, the type of coalescence points observed in the symmetric and asymmetric ethene systems illustrates that the relationship between left-right symmetry breaking and confluence or pair annihilation points extends to many-electron HF wave functions. Secondly, the existence of complex h-RHF extensions when the real many-electron RHF states of ethene disappear supports the general applicability of h-HF theory to larger molecules. Finally — and of particular significance for developing NOCI in Chapter 7 — these ethene results illustrate the existence of additional (real) HF solutions at strongly correlated molecular geometries, exactly where multireference approaches are required.

4.5 Concluding Remarks

By formulating the two-electron h-RHF and h-UHF optimisation problem in the framework of algebraic geometry, the exact number of stationary points has been evaluated as Eq. (4.29) and Eq. (4.36) respectively. Crucially, the fact that these expressions only depend on the polynomial form of the h-HF equations and the dimension of the spatial basis set proves that two-electron h-RHF and h-UHF states must exist for all molecular structures or atomic charges. Moreover, the results for the isomorphism of $HHeH^{2+}$ with $HHeH$ and the double bond rotation of ethene strongly support the extension of these results to many-electron molecules. The guarantee that h-HF solutions exist for all molecular structures provides the essential foundation for constructing continuous NOCI basis sets using multiple HF states.

In addition, the number of h-RHF and h-UHF states predicted by Eq. (4.29) and Eq. (4.36) provide upper bounds on the number of two-electron real RHF and real UHF states respectively. These derivations rigorously prove the previous result for

closed-shell systems obtain by Stanton²¹ and dramatically lower the upper bound for two-electron UHF states predicted by Fukutome.²² Moreover, the numerical studies suggest that many h-HF solutions might arise with no correspondence to any real HF state, further reducing the number of real HF solutions in molecular systems. The identification of smaller upper bounds on the number of HF solutions provides an indication that the size and complexity of the HF solution set is lower than previously thought. In turn, this supports the notion that suitable subsets of HF states can be easily identified and exploited through NOCI.

Through in-depth studies of the h-RHF and h-UHF states in two-electron model systems, the behaviour of multiple HF states has been illustrated as the molecular geometry or atomic charges are varied. Applying the framework of catastrophe theory demonstrates the close relationship between the presence of molecular spatial symmetry and the type of coalescence points observed. In particular, the occurrence of triply-degenerate coalescence points arises when two HF states related by symmetry simultaneously coalesce with a third HF state preserving the same symmetry. By breaking the molecular symmetry, triply-degenerate coalescence points decompose into pairwise annihilation points where *both* real HF states disappear, leaving a pair of complex-valued h-HF solutions. Since many molecular systems do not possess any spatial symmetry, this suggests that pair annihilation coalescence points will be more widespread than triply-degenerate coalescence points. Reassuringly, the observation that h-HF solutions extend beyond either type of coalescence point further supports the use of multiple h-HF states for constructing continuous NOCI basis sets.

Finally, in the model systems presented, it can be seen that more real HF solutions exist at geometries that are considered to have multireference character, e.g. the dissociation limit of H₂ or the \mathcal{D}_{2d} twisted geometry of ethene. Away from these geometries, a number of HF states disappear while their corresponding h-HF states extending into the complex-plane. Meanwhile, for systems with no multireference character at any geometry, the lower number of real HF states is compensated for by dormant h-HF solutions with complex-valued orbital coefficients across all geometries. For the purpose of developing a multireference NOCI approach, these observations suggest that the HF states required for the NOCI basis are most likely to exist as real HF states at multireference geometries. Locating real HF states at these geometries and following them as h-HF states across all structures therefore provides a potential route for defining a generalised NOCI approach. This idea is developed further in Chapter 7.

Chapter 5

Real Energies in Holomorphic Hartree–Fock

The work in this chapter has contributed to the publication Ref. (2)

Summary

In previous chapters, it was observed that h-HF states can retain real-valued energies with complex orbital coefficients, occurring in strictly degenerate pairs. These real energies and degeneracies imply the presence of hidden symmetries in the h-HF equations. In this chapter, the conditions and symmetries that lead to these real h-HF energies are explored. It is revealed that the conservation of complex-conjugation, time-reversal, or the combined parity-time symmetry all result in h-HF states with real energies. The presence of real energies for these non-Hermitian Hamiltonians creates new opportunities for developing approximate Hamiltonians and wave function *ansätze* that would previously have been disregarded as unphysical.

5.1 Context and Scope

Although the h-HF energy is a complex-valued function, a number of h-HF solutions are found to retain strictly real-valued energies with complex orbital coefficients. Where h-HF states with complex-orbital coefficients exist, they arise in pairs with coefficients related by complex conjugation. When their energies are complex, they are related by complex conjugation, but the pairs become strictly degenerate when their h-HF energies are real. Degeneracy in quantum mechanics usually indicates hidden symmetries in the Hamiltonian. It is therefore likely that real h-HF energies can be associated with the presence of new symmetries in h-HF theory, and the wider HF approximation. This hypothesis is further supported by the observation that degenerate h-HF states with real energies split into complex-conjugate pairs with complex energies when certain molecular symmetries are broken, as illustrated for HZ in Section 4.4.2. In this chapter, the conditions that lead to complex h-HF solutions with real energies are derived and investigated in detail.

The identification of physical symmetries provides an essential concept in quantum mechanics for describing properties that are invariant under particular transformations. Physical observables must be totally symmetric under the group of symmetry operations corresponding to a quantum system, and exact wave functions must transform according to an irreducible representation of this group. However, occurrences of symmetry-breaking are pervasive in HF theory and appear intimately linked to the breakdown of the single-determinant mean-field approximation in the presence of strong correlation.⁸ Furthermore, when HF wave functions break symmetry, it can be difficult to restore that symmetry using post-HF methods.^{137,192} From a chemical physicist's perspective, the archetypal example is the appearance of spin and spatially symmetry-broken HF solutions for internuclear distances beyond the so-called Coulson–Fischer point in H₂,²⁴ where the two (opposite spin) electrons localise on opposing nuclei with equal probability.

To ensure real energies in quantum theories, the Hamiltonian is usually required to conserve Hermitian symmetry. However, since h-HF theory is explicitly formulated as a non-Hermitian approach, alternative symmetries must account for the real h-HF energies observed. One potential symmetry — known as \mathcal{PT} -symmetry¹⁹³ — provides an alternative condition to Hermiticity that ensures real-valued energies for complex, non-Hermitian Hamiltonians.^{193–202} \mathcal{PT} -symmetry represents invariance with respect to the combined action of space inversion \mathcal{P} and time reversal \mathcal{T} , and has been shown to allow the construction of many new types of Hamiltonians that would previously have been deemed 'unphysical'.¹⁹⁹ A Hermitian Hamiltonian, for example, can be

analytically continued into the complex plane, becoming non-Hermitian in the process and exposing the fundamental topology of eigenstates.²⁰³

Invariance with respect to \mathcal{PT} -symmetry therefore provides the prime candidate for explaining the conditions required for real-valued energies in h-HF theory. However, despite receiving significant attention across theoretical physics,²⁰² \mathcal{PT} -symmetry remains relatively unexplored in electronic structure theory. In this chapter, the presence and conditions for satisfying \mathcal{PT} -symmetry in h-HF are investigated and are shown to provide a sufficient requirement for real-valued h-HF energies. In the process, the gap between \mathcal{PT} -symmetric physics and electronic structure is bridged, paving the way for future developments of \mathcal{PT} -symmetric quantum chemistry such as new wave function *ansätze* or novel approximate Hamiltonians.

In Section 5.2, the essential details of \mathcal{PT} -symmetric quantum mechanics are reviewed. Section 5.3 derives general conditions for real energies in h-HF theory that are then illustrated for the H_2 molecule in Section 5.5. Finally, the key results and potential for future developments are discussed in Section 5.6.

5.2 Review of \mathcal{PT} -Symmetric Hamiltonians

5.2.1 Spin-free \mathcal{PT} -Symmetry

To guarantee a real energy spectrum, it is generally believed that a physically acceptable Hamiltonian \hat{H} must satisfy Hermitian symmetry, i.e. $\hat{H} = \hat{H}^\dagger$. While Hermiticity is a sufficient condition to ensure this property, it is not strictly necessary. In fact, Bender *et al.*¹⁹³ have revealed that the family of \mathcal{PT} -symmetric Hamiltonians^{193,195,199} — satisfying the condition $\hat{H} = \hat{H}^{\mathcal{PT}}$ where $\hat{H}^{\mathcal{PT}} = (\mathcal{PT})\hat{H}(\mathcal{PT})^{-1}$ — provide a more general class of Hamiltonians with a purely real energy spectrum. Notably, $[\mathcal{P}, \mathcal{T}] = 0$ but \mathcal{P} and/or \mathcal{T} may not commute with \hat{H} .²⁰¹ The \mathcal{PT} -symmetric condition for real energies therefore raises the possibility of new non-Hermitian and complex Hamiltonians that retain a physically-acceptable quantum theory.²⁰¹

The textbook \mathcal{PT} -symmetric Hamiltonian

$$\hat{H} = p^2 + ix^3 \quad (5.1)$$

has been extensively studied by the \mathcal{PT} -symmetry community.^{193–202,204–206} From the standard action of \mathcal{P} and \mathcal{T} , where

$$\mathcal{P} : p \rightarrow -p, \quad x \rightarrow -x, \quad (5.2a)$$

$$\mathcal{T} : p \rightarrow -p, \quad x \rightarrow x, \quad i \rightarrow -i, \quad (5.2b)$$

the application of the combined space-time reflection \mathcal{PT} clearly leaves the Hamiltonian (5.1) unchanged. Furthermore, although this Hamiltonian is obviously complex, it has a purely real spectrum of eigenvalues.¹⁹³

Generalising the Hamiltonian (5.1) to the parametric family of \mathcal{PT} -symmetric Hamiltonians¹⁹³

$$\hat{H} = p^2 + x^2(ix)^\epsilon, \quad \epsilon \in \mathbb{R}, \quad (5.3)$$

reveals a more complex and fundamental structure of eigenvalues. It has been observed¹⁹³ and proved²⁰⁷ that for $\epsilon \geq 0$, the Hamiltonian (5.3) has an entirely positive and real spectrum. In contrast, for $\epsilon < 0$, some real eigenvalues coalesce and disappear by forming a pair of complex conjugate eigenvalues. The process of these eigenvalues coalescing and disappearing corresponds to breaking \mathcal{PT} -symmetry in a similar manner to the symmetry breaking and coalescence of HF solutions at Coulson–Fischer points.

Incredibly, \mathcal{PT} -symmetry breaking transitions can be experimentally observed in electronics,^{208,209} microwaves,²¹⁰ acoustics,²¹¹ atomic systems^{212,213} and optics.^{214–219} Furthermore, the points at which this symmetry breaking occurs [$\epsilon = 0$ in the case of Hamiltonian (5.3)] coincide with so-called “exceptional points”^{209,217,220–225} where two (or more) eigenvectors of the Hamiltonian become *identical*. These exceptional points are thought provide the non-Hermitian analogue of conical intersections.²²⁶

5.2.2 Electron \mathcal{PT} -Symmetry

\mathcal{PT} -symmetric systems involving particles with non-zero spin, in the present case spin- $\frac{1}{2}$ electrons, are far less studied than their spin-free counterparts.^{227–229} In what follows, a single-particle state ψ is represented in the two-component spinor basis comprising the states $|\alpha\rangle = (1, 0)^\top$ and $|\beta\rangle = (0, 1)^\top$ by the column vector

$$\psi = \begin{pmatrix} \phi_\alpha \\ \phi_\beta \end{pmatrix}. \quad (5.4)$$

Here, ϕ_α and ϕ_β are spatial functions defining the α and β components of ψ respectively.

The linear parity operator \mathcal{P} acts only on the spatial components and satisfies $\mathcal{P}^2 = \mathcal{I}$, where \mathcal{I} is the identity operator. Its action in the spinor basis can be represented by the block-diagonal matrix

$$\mathcal{P}\psi = \begin{pmatrix} P & 0 \\ 0 & P \end{pmatrix} \begin{pmatrix} \phi_\alpha \\ \phi_\beta \end{pmatrix}, \quad (5.5)$$

where P represents the action of \mathcal{P} on the spatial basis. In contrast, deriving the action of \mathcal{T} is more involved. Fundamentally, \mathcal{T} is required to be an anti-linear operator,

$\mathcal{T}i = -i\mathcal{T}$.^{230,231} However, for systems containing particles with non-zero spin, the reversal of spin-angular momentum under the action of \mathcal{T} must also be included such that, for a given spin operator \hat{s} , one obtains $\mathcal{T}\hat{s} = -\hat{s}\mathcal{T}$. Although a more detailed discussion on the nature of \mathcal{T} for particles of general spin is provided in Appendix B, only the most relevant results are discussed here.

Crucially, in the bosonic case, a basis can always be found in which \mathcal{T} is represented simply as $\mathcal{T} = \mathcal{K}$.²²⁷ Here, \mathcal{K} is the distributive anti-linear complex-conjugation operator which acts only to the right by convention and generally has no matrix representation.²³⁰ Notably, applying \mathcal{K} in algebraic manipulations can lead to non-intuitive results and particular care must be exercised. In contrast, the representation of \mathcal{T} for electrons (i.e. spin- $\frac{1}{2}$ particles) is given by $\mathcal{T} = i\sigma_y\mathcal{K}$,²²⁷ where σ_y is the Pauli spin matrix

$$\sigma_y = \begin{pmatrix} 0 & -i \\ i & 0 \end{pmatrix}. \quad (5.6)$$

This representation leads to a critical difference between the behaviour of \mathcal{T}^2 for the electronic and bosonic representations which, for the electronic case, is given by

$$\mathcal{T}^2 = (i\sigma_y\mathcal{K})(i\sigma_y\mathcal{K}) = \sigma_y\sigma_y i^2 \mathcal{K}^2 = -\sigma_y\sigma_y = -\mathcal{I}. \quad (5.7)$$

Significantly, while \mathcal{T}^2 leaves a bosonic system unchanged, \mathcal{T} must be applied four times to return a fermionic system to its original state. This property leads to the action of time-reversal in fermionic and bosonic systems being classified as “odd” and “even” respectively.²²⁷ Overall, in the two-component spinor basis, the action of \mathcal{T} on ψ can be represented by

$$\mathcal{T}\psi = i\sigma_y\mathcal{K}\psi = \begin{pmatrix} 0 & 1 \\ -1 & 0 \end{pmatrix} \mathcal{K} \begin{pmatrix} \phi_\alpha \\ \phi_\beta \end{pmatrix} = \begin{pmatrix} \phi_\beta^* \\ -\phi_\alpha^* \end{pmatrix}. \quad (5.8)$$

To find the representation of the full \mathcal{PT} operator, the results of Eqs. (5.5) and (5.8) are then simply combined to obtain

$$\begin{aligned} \mathcal{PT}\psi &= \phi^{\mathcal{PT}} = \mathcal{P}i\sigma_y\mathcal{K}\psi \\ &= \begin{pmatrix} 0 & P \\ -P & 0 \end{pmatrix} \mathcal{K} \begin{pmatrix} \phi_\alpha \\ \phi_\beta \end{pmatrix} = \begin{pmatrix} P\phi_\beta^* \\ -P\phi_\alpha^* \end{pmatrix}. \end{aligned} \quad (5.9)$$

5.2.3 \mathcal{PT} -Doublet

As a direct consequence of the odd character of \mathcal{T} , it is impossible to find a single fermionic state ψ that is invariant under the \mathcal{PT} operator. Instead, the closest analogue

is a pair of states assembled into a “ \mathcal{PT} -doublet”²²⁷ of the form

$$\begin{pmatrix} \psi & -\psi^{\mathcal{PT}} \end{pmatrix} = \begin{pmatrix} \phi_\alpha & -P\phi_\beta^* \\ \phi_\beta & P\phi_\alpha^* \end{pmatrix}, \quad (5.10)$$

where ψ and $\psi^{\mathcal{PT}}$ are both eigenvectors of a \mathcal{PT} -symmetric Hamiltonian. The action of \mathcal{PT} on a \mathcal{PT} -doublet is then given by

$$\begin{aligned} \mathcal{PT} \begin{pmatrix} \psi & -\psi^{\mathcal{PT}} \end{pmatrix} &= \begin{pmatrix} 0 & P \\ -P & 0 \end{pmatrix} \mathcal{K} \begin{pmatrix} \phi_\alpha & -P\phi_\beta^* \\ \phi_\beta & P\phi_\alpha^* \end{pmatrix} \\ &= \begin{pmatrix} P\phi_\beta^* & \phi_\alpha \\ -P\phi_\alpha^* & \phi_\beta \end{pmatrix} = \begin{pmatrix} \psi^{\mathcal{PT}} & \psi \end{pmatrix}, \end{aligned} \quad (5.11)$$

where the pair of eigenvectors have been simply swapped along with the introduction of a single minus sign. Invariance under \mathcal{PT} implies that the energies of ψ and $\psi^{\mathcal{PT}}$ are related by complex conjugation, while the additional assumption of unbroken \mathcal{PT} -symmetry implies that ψ and $\psi^{\mathcal{PT}}$ must form strictly degenerate pairs with real energies.²²⁷ Finally, it is useful to note the inverse relationships $\mathcal{P}^{-1} = \mathcal{P}$ and $(i\sigma_y)^{-1} = -i\sigma_y = i\sigma_y^\top$ which combine to give $(\mathcal{PT})^{-1} = -i\sigma_y \mathcal{K} \mathcal{P}$.

5.3 \mathcal{PT} -Symmetry in Holomorphic Hartree–Fock

The h-HF wave function Ψ_{HF} for a system of N electrons is represented by a single Slater determinant constructed from a set of N occupied one-electronic molecular orbitals ψ_i . Each molecular orbital is expanded in a finite-size direct product space of n one-electron spatial basis $\{\chi_1, \dots, \chi_n\}$ and the spin- $\frac{1}{2}$ basis $\{|\alpha\rangle, |\beta\rangle\}$ as

$$\psi_i = \sum_{\mu=1}^n C_{\mu i}^\alpha \chi_\mu |\alpha\rangle + \sum_{\mu=1}^n C_{\mu i}^\beta \chi_\mu |\beta\rangle = \phi_{i\alpha} |\alpha\rangle + \phi_{i\beta} |\beta\rangle, \quad (5.12)$$

where $\phi_{i\alpha}$ and $\phi_{i\beta}$ represent the α and β components of ψ_i respectively. For mathematical convenience, and without loss of generality, the spatial basis functions are assumed to be real and orthogonal. The molecular orbital coefficients $C_{\mu i}^\alpha$ and $C_{\mu i}^\beta$ parameterise and define the Slater determinant. In the spinor column vector representation (5.4), these orbital coefficients can be considered as components of a $(2n \times N)$ matrix \mathbf{C} with the form

$$\mathbf{C} = \begin{pmatrix} \mathbf{C}_\alpha \\ \mathbf{C}_\beta \end{pmatrix}, \quad (5.13)$$

where \mathbf{C}_α and \mathbf{C}_β are $(n \times N)$ sub-matrices representing the expansions of $\phi_{i\alpha}$ and $\phi_{i\beta}$.

As an approximate wave function, Ψ_{HF} does not form an eigenfunction of the true electronic Hamiltonian \hat{H} . Instead, Ψ_{HF} is identified by optimising the HF energy E_{HF} defined by the expectation value for a given inner product $\langle \cdot | \cdot \rangle$ as

$$E_{\text{HF}} = \frac{\langle \Psi_{\text{HF}} | \hat{H} | \Psi_{\text{HF}} \rangle}{\langle \Psi_{\text{HF}} | \Psi_{\text{HF}} \rangle}. \quad (5.14)$$

The particular choice of inner-product leads to either the conventional or holomorphic HF approach. The optimal set of HF molecular orbital coefficients \mathbf{C} are determined using a self-consistent procedure where, on each iteration k , an effective one-electron ‘‘Fock’’ Hamiltonian $F^{(k)}$ is constructed using the current occupied set of orbitals $\mathbf{C}^{(k)}$, such that $F^{(k)} = \mathbf{h} + \mathbf{D}^{(k)} \mathbf{G}$. Here, \mathbf{h} and \mathbf{G} define the (iteration independent) one- and two-electron parts of the Fock matrix and $\mathbf{D}^{(k)}$ is the density matrix at the k th iteration. The new optimal molecular orbitals $\mathbf{C}^{(k+1)}$ are then obtained by diagonalising $F^{(k)}$, i.e. $F^{(k)} \mathbf{C}^{(k+1)} = \mathbf{C}^{(k+1)} \boldsymbol{\epsilon}^{(k+1)}$ where $\boldsymbol{\epsilon}$ is a diagonal matrix of the orbital energies, and the process is repeated until self-consistency is reached.⁸ At convergence one finds $\mathbf{F}\mathbf{D} - \mathbf{D}\mathbf{F} = \mathbf{0}$, demonstrating that the Fock and density matrices only commute when self-consistency is reached. For the current purpose, it is useful to note that F is linear with respect to D .

Crucially, although the true N -electron Hamiltonian \hat{H} is *always* Hermitian, the process of dressing \hat{H} using the molecular orbitals can lead to a non-Hermitian effective one-electron Hamiltonian. In fact, the symmetry of $\mathbf{D}^{(k)}$ and $F^{(k)}$ will depend of the specific choice of the inner product in Eq. (5.14). For example, choosing the Hermitian inner product $\langle \mathbf{x} | \mathbf{y} \rangle_{\text{H}} = \mathbf{x}^\dagger \mathbf{y}$ in conventional HF theory leads to Hermitian density $\mathbf{D}^{(k)} = \mathbf{C}^{(k)} (\mathbf{C}^{(k)})^\dagger$ and Fock matrices $F^{(k)} = (F^{(k)})^\dagger$ that explicitly enforce real energies.⁸ In contrast, the complex-symmetric inner product $\langle \mathbf{x} | \mathbf{y} \rangle_{\text{C}} = \mathbf{x}^\top \mathbf{y}$ used in h-HF requires complex-symmetric density $\mathbf{D}^{(k)} = \mathbf{C}^{(k)} (\mathbf{C}^{(k)})^\top$ and Fock matrices $F^{(k)} = (F^{(k)})^\top$, in general leading to complex-valued energies.

In what follows, the complex-symmetric inner product $\langle \cdot | \cdot \rangle \equiv \langle \cdot | \cdot \rangle_{\text{C}}$ is used exclusively to explore the conditions for \mathcal{PT} -symmetry under the h-HF approximation and to understand under what circumstances E_{HF} is real. It is worth noting that rigorous formulations of \mathcal{PT} -symmetric quantum mechanics introduce an additional linear operator \mathcal{C} and the so-called \mathcal{CPT} inner product to define a positive-definite inner product and ensure conservation of probability, although identifying \mathcal{C} is often non-trivial.^{196,202} However, as an inherently approximate approach with energies given by expectation values rather than formal eigenvalues, h-HF theory requires only a well-defined inner product. Furthermore, since the Fock matrix is explicitly complex-symmetric, its eigenvectors naturally form an orthonormal set under $\langle \cdot | \cdot \rangle_{\text{C}}$ without needing to introduce a \mathcal{CPT} inner product.

5.3.1 One-Electron Picture

It is most instructive to begin by understanding the behaviour of the one-electron density, Fock matrices, and orbital energies under the \mathcal{PT} -operator. First consider the relationship between the complex-symmetric density matrix $D = CC^\top$ and the equivalent density matrix constructed using the \mathcal{PT} -transformed coefficients denoted $C^{\mathcal{PT}} = \mathcal{PT}C$. The combined \mathcal{PT} operator can be represented as the product $\mathcal{PT} = \mathbf{U}\mathcal{K}$, where \mathbf{U} is a $(2n \times 2n)$ real (linear) orthogonal matrix.²²⁷ Remembering that \mathcal{K} only acts on everything to the right yields

$$\underbrace{(C^{\mathcal{PT}})}_{\mathbf{U}\mathcal{K}C} \left(C^{\mathcal{PT}} \right)^\top = (\mathbf{U}C^*) (\mathbf{U}C^*)^\top = \underbrace{\mathbf{U}\mathcal{K}}_{\mathcal{PT}} CC^\top \underbrace{\mathcal{K}\mathbf{U}^\top}_{(\mathcal{PT})^{-1}} = D^{\mathcal{PT}}. \quad (5.15)$$

where $D^{\mathcal{PT}} = (\mathcal{PT})D(\mathcal{PT})^{-1}$. As a result, the density matrix constructed using the \mathcal{PT} -transformed coefficients is a \mathcal{PT} -similarity transformation of the density matrix constructed using the original set of coefficients. Consequently, if a set of coefficients is \mathcal{PT} -symmetric, then the density matrix must be too, and *vice versa*.

Next, consider the symmetry of the Fock matrix $F[D] = \mathbf{h} + D\mathbf{G}$ which, due to its dependence on D , inherits the symmetry of the density used to construct it. Assuming that D is \mathcal{PT} -symmetric, i.e. $D = D^{\mathcal{PT}}$, leads to

$$F[D] = \mathbf{h} + D^{\mathcal{PT}}\mathbf{G} = F[D^{\mathcal{PT}}]. \quad (5.16)$$

This result is trivial since F is linear with respect to D . Moreover, since the one- and two-electron parts of the Fock matrix are \mathcal{PT} -symmetric, i.e. $\mathbf{h} = (\mathcal{PT})\mathbf{h}(\mathcal{PT})^{-1}$ and $\mathbf{G} = (\mathcal{PT})\mathbf{G}(\mathcal{PT})^{-1}$, one finds

$$(\mathcal{PT})F[D](\mathcal{PT})^{-1} = F[D^{\mathcal{PT}}]. \quad (5.17)$$

Equating (5.16) and (5.17) it becomes clear that, if D is \mathcal{PT} -symmetric, then F must also be \mathcal{PT} -symmetric. As a result, the \mathcal{PT} -symmetry of $F^{(k)}$ on a given iteration k is dictated by the \mathcal{PT} -symmetry of the electron density from the current iteration $D^{(k)}$. By extension, the \mathcal{PT} -symmetry of the new molecular orbitals $C^{(k+1)}$ is controlled by the \mathcal{PT} -symmetry of $F^{(k)}$ and, if one starts with a \mathcal{PT} -symmetric guess $D^{(0)}$, then \mathcal{PT} -symmetry can be conserved throughout the self-consistent process. Furthermore, since $C^{(k+1)}$ is \mathcal{PT} -symmetric only if the effective Fock Hamiltonian $F^{(k)}$ is \mathcal{PT} -symmetric (and *vice versa*), the existence of \mathcal{PT} -symmetry in h-HF can be identified by considering only the symmetry of the density itself.

Self-consistency of the h-HF equations requires the eigenvectors which satisfy

$$F[D]C = C\epsilon, \quad (5.18)$$

to be equivalent to the coefficients used to build D itself. In other words, F and D must commute and share the same set of eigenvectors. Acting on the left of Eq. (5.18) with the \mathcal{PT} operator and exploiting the identity $(\mathcal{PT})^{-1}\mathcal{PT} = \mathcal{I}$ therefore yields

$$\begin{aligned} \mathcal{PT}F[D]C &= \mathcal{PT}F[D](\mathcal{PT})^{-1}\mathcal{PT}C = \mathbf{U}\mathcal{K}(C\epsilon) \\ \implies F[D^{\mathcal{PT}}](C^{\mathcal{PT}}) &= \underbrace{(\mathbf{U}C^*)}_{C^{\mathcal{PT}}}\epsilon^*, \end{aligned} \quad (5.19)$$

where the result of Eq. (5.17) and the property that \mathcal{T} is both anti-linear and distributive (such that $\mathcal{K}C\epsilon = C^*\epsilon^*$) have been used. Combining with the result of Eq. (5.15) leads to two key conclusions. Firstly, if a given set of orbital coefficients C represents an optimised self-consistent h-HF solution with eigenvalues ϵ , then its \mathcal{PT} -transformed counterpart $C^{\mathcal{PT}}$ must also be a self-consistent solution with eigenvalues ϵ^* . Secondly, and by extension, if an optimal self-consistent solution is invariant under \mathcal{PT} (i.e. $C = C^{\mathcal{PT}}$), then its eigenvalues must be real.

5.3.2 Many-Electron Picture

Consider now the symmetry of the full Slater determinant Ψ_{HF} and its associated energy E_{HF} . In the many-electron picture, the \mathcal{PT} -operator for an N -electron system is given as a product of one-electron operators,

$$\mathcal{PT} = \bigotimes_{i=1}^N \hat{\pi}(i)\hat{\tau}(i), \quad (5.20)$$

where $\hat{\pi}(i)$ and $\hat{\tau}(i)$ are the parity and time-reversal operators acting only on the single-particle orbital occupied by electron i . From the determinantal form of Ψ_{HF} , its symmetry under \mathcal{PT} can be extracted from the symmetries of its constituent orbitals.

Consider the relationship between the total h-HF energies of two determinants represented by the orbital coefficient matrices C and $C^{\mathcal{PT}}$. Noting that $\mathbf{U}^T\mathbf{U} = \mathbf{U}\mathbf{U}^T = \mathbf{I}$ and exploiting the invariance of the trace to cyclic permutations one finds

$$E_{\text{HF}}[C] = \frac{1}{2} \text{Tr}\{D(\mathbf{h} + F[D])\} = \frac{1}{2} \text{Tr}\{\mathbf{U}D\mathbf{U}^T\mathbf{U}(\mathbf{h} + F[D])\mathbf{U}^T\}. \quad (5.21)$$

Note that $\mathcal{K}^2 = \mathcal{I}$ and, since \mathcal{K} acts only to the right, its application on the far right-hand side will have no effect. Therefore, by applying \mathcal{K} to both sides and inserting $\mathcal{K}^2 = \mathcal{I}$ in the middle, it becomes explicit that

$$E_{\text{HF}}[C]^* = \mathcal{K} \text{Tr}\{\mathbf{U}D\mathbf{U}^T\mathcal{K}^2\mathbf{U}(\mathbf{h} + F[D])\mathbf{U}^T\}\mathcal{K} \quad (5.22)$$

Exploiting the distributive nature of \mathcal{K} over the matrix product within the trace, and since the reality of \mathbf{U} provides $\mathcal{K}\mathbf{U} = \mathbf{U}\mathcal{K}$, the \mathcal{K} operators can be migrated to find

$$\begin{aligned} E_{\text{HF}}[\mathbf{C}]^* &= \text{Tr} \left\{ \underbrace{\mathbf{U}\mathcal{K}}_{\mathcal{PT}} \mathbf{D} \underbrace{\mathcal{K}\mathbf{U}^\text{T}}_{(\mathcal{PT})^{-1}} \underbrace{\mathbf{U}\mathcal{K}}_{\mathcal{PT}} (\mathbf{h} + \mathbf{F}[\mathbf{D}]) \underbrace{\mathcal{K}\mathbf{U}^\text{T}}_{(\mathcal{PT})^{-1}} \right\} \\ &= \text{Tr} \left\{ \mathbf{D}^{\mathcal{PT}} \left(\mathbf{h} + (\mathcal{PT})\mathbf{F}[\mathbf{D}](\mathcal{PT})^{-1} \right) \right\} \\ &= \text{Tr} \left\{ \mathbf{D}^{\mathcal{PT}} \left(\mathbf{h} + \mathbf{F}[\mathbf{D}^{\mathcal{PT}}] \right) \right\} = E_{\text{HF}}[\mathbf{C}^{\mathcal{PT}}], \end{aligned} \quad (5.23)$$

where the result of Eq. (5.17) and the fact that \mathbf{h} is \mathcal{PT} -symmetric are applied. In conclusion, the h-HF energies corresponding to the coefficient matrices \mathbf{C} and $\mathbf{C}^{\mathcal{PT}}$ are related by complex-conjugation. By extension, the h-HF energy of a \mathcal{PT} -symmetric set of orbital coefficients must be real.

5.3.3 Hartree–Fock \mathcal{PT} -Doublet

Constructing a set of occupied orbitals in the structure of a \mathcal{PT} -doublet [see Eq. (5.10)] requires an explicit form of the matrix \mathbf{U} . The linear parity operator \mathcal{P} acts only on the spatial basis and can be represented in the full direct product space by the Kronecker product $\mathbf{I}_2 \otimes \mathbf{P}$, giving

$$\mathcal{P}\mathbf{C} = \begin{pmatrix} \mathbf{P} & \mathbf{0} \\ \mathbf{0} & \mathbf{P} \end{pmatrix} \begin{pmatrix} \mathbf{C}_\alpha \\ \mathbf{C}_\beta \end{pmatrix}, \quad (5.24)$$

where \mathbf{P} is a real $(n \times n)$ matrix representation of \mathcal{P} in the spatial basis, satisfying $\mathbf{P}^2 = \mathbf{I}_n$. As a result, the combined \mathcal{PT} operator can be represented by the $(2n \times 2n)$ matrix constructed from the Kronecker product $\mathbf{U} = (\text{i}\sigma_y) \otimes \mathbf{P}$, such that

$$\mathcal{PT}\mathbf{C} = \mathbf{U}\mathcal{K}\mathbf{C} = \begin{pmatrix} \mathbf{0} & \mathbf{P} \\ -\mathbf{P} & \mathbf{0} \end{pmatrix} \mathcal{K} \begin{pmatrix} \mathbf{C}_\alpha \\ \mathbf{C}_\beta \end{pmatrix} = \begin{pmatrix} \mathbf{P}\mathbf{C}_\beta^* \\ -\mathbf{P}\mathbf{C}_\alpha^* \end{pmatrix}. \quad (5.25)$$

In the coefficient matrix representation [see Eq. (5.13)], a \mathcal{PT} -doublet can then be constructed by pairing each occupied orbital with its \mathcal{PT} -transformed analogue, giving

$$\mathbf{C} = \begin{pmatrix} \mathbf{c} & -\mathcal{PT}\mathbf{c} \end{pmatrix} = \begin{pmatrix} \mathbf{c}_\alpha & -\mathbf{P}\mathbf{c}_\beta^* \\ \mathbf{c}_\beta & \mathbf{P}\mathbf{c}_\alpha^* \end{pmatrix}, \quad (5.26)$$

where \mathbf{c} and $-\mathcal{PT}\mathbf{c}$ form $(2n \times N/2)$ sub-matrices representing the paired orbitals of the \mathcal{PT} -doublet. The action of \mathcal{PT} on a \mathcal{PT} -doublet is then given by

$$\begin{aligned} \mathcal{PT} \begin{pmatrix} \mathbf{c} & -\mathcal{PT}\mathbf{c} \end{pmatrix} &= \mathbf{U}\mathcal{K} \begin{pmatrix} \mathbf{c}_\alpha & -\mathbf{P}\mathbf{c}_\beta^* \\ \mathbf{c}_\beta & \mathbf{P}\mathbf{c}_\alpha^* \end{pmatrix} = \begin{pmatrix} \mathbf{P}\mathbf{c}_\beta^* & \mathbf{c}_\alpha \\ -\mathbf{P}\mathbf{c}_\alpha^* & \mathbf{c}_\beta \end{pmatrix} \\ &= \begin{pmatrix} \mathcal{PT}\mathbf{c} & \mathbf{c} \end{pmatrix} = \begin{pmatrix} \mathbf{c} & -\mathcal{PT}\mathbf{c} \end{pmatrix}, \end{aligned} \quad (5.27)$$

where the last line exploits the anti-symmetry of the determinantal wave function under the permutation of two columns in C .

The behaviour of a \mathcal{PT} -doublet can be illustrated by considering a simple two-electron Slater determinant constructed from the orbitals $(\psi, -\psi^{\mathcal{PT}})$

$$\Psi_{\text{HF}} = \frac{1}{\sqrt{2}} \begin{vmatrix} \psi(1) & -\psi^{\mathcal{PT}}(1) \\ \psi(2) & -\psi^{\mathcal{PT}}(2) \end{vmatrix} = \frac{-\psi(1)\psi^{\mathcal{PT}}(2) + \psi^{\mathcal{PT}}(1)\psi(2)}{\sqrt{2}}. \quad (5.28)$$

Thanks to the linearity and antisymmetry properties of determinants, Eq. (5.27) immediately yields

$$\mathcal{PT}\Psi_{\text{HF}} = \frac{1}{\sqrt{2}} \begin{vmatrix} \psi^{\mathcal{PT}}(1) & \psi(1) \\ \psi^{\mathcal{PT}}(2) & \psi(2) \end{vmatrix} = \Psi_{\text{HF}}. \quad (5.29)$$

5.4 Extension to General Antilinear Operators

Having established that the presence of \mathcal{PT} -symmetry in the density matrix and Fock matrix ensures real-valued HF energies, it is worth considering whether this extends to other symmetries. In particular, consider the general matrix form of an antilinear operator \mathcal{W}

$$\mathcal{W} = \mathbf{W}\mathcal{K}. \quad (5.30)$$

Revisiting the derivations in Section 5.3.1 and Section 5.3.2, where $\mathbf{W} = \mathbf{U}$ for $\mathcal{W} = \mathcal{PT}$, the crucial constraint on the form of \mathcal{PT} (and in particular \mathbf{U}) is that $\mathbf{U}^\top \mathbf{U} = \mathbf{I}$ and the one- and two-electron integrals are \mathcal{PT} -symmetric, i.e.

$$\mathbf{h} = (\mathcal{PT})\mathbf{h}(\mathcal{PT})^{-1} = (\mathbf{U}\mathcal{K})\mathbf{h}(\mathbf{U}^\top \mathcal{K}) \quad (5.31a)$$

$$\mathbf{G} = (\mathcal{PT})\mathbf{G}(\mathcal{PT})^{-1} = (\mathbf{U}\mathcal{K})\mathbf{G}(\mathbf{U}^\top \mathcal{K}). \quad (5.31b)$$

Significantly, this implies that *any* antilinear operator with a matrix representation satisfying these conditions will also guarantee strictly real energies. It is therefore sufficient to consider other symmetries that are preserved by the one- and two-electron integrals and correspond to antilinear operators.

For a real basis, complex conjugation symmetry \mathcal{K} provides the simplest extension with $\mathbf{W} = \mathbf{I}$. Clearly the one- and two-electron integrals (which are also real-valued) must be symmetric with respect to \mathcal{K} . Furthermore, if the density matrix and Fock matrix are symmetric with respect to \mathcal{K} , then they must be real and the h-HF equations reduce to the real HF equations with strictly real energies.

5.4.1 Time-Reversal Symmetry

Time-reversal \mathcal{T} presents another antilinear symmetry conserved by the one- and two-electron integrals. For \mathcal{T} , the matrix representation in the single-particle spinor basis is

given by $\mathcal{T} = i\sigma_y\mathcal{K}$, as discussed in Section 5.2.2. As a result, by simply replacing \mathbf{U} with $i\sigma_y$ throughout the derivations in Section 5.3.2, it is trivial to show that conserving \mathcal{T} -symmetry in the h-HF density matrix and Fock matrix will also ensure real-valued h-HF energies. Furthermore, in contrast to \mathcal{PT} -symmetry, the conditions for \mathcal{T} -symmetry in h-HF do not rely on the presence of parity symmetry in the molecular systems. As a result, \mathcal{T} -symmetry will still ensure real-valued h-HF energies even in molecules with no spatial point-group symmetry.

Similarly to \mathcal{PT} -symmetry, a single electron state ψ cannot by itself be \mathcal{T} -symmetric. Furthermore, it is not possible for a many-electron state with $m_s \neq 0$ to preserve \mathcal{T} -symmetry. Instead, a \mathcal{T} -doublet pair of orbitals analogous to a \mathcal{PT} -doublet must be constructed with a coefficient matrix [see Eq. (5.13)] of the form

$$\mathbf{C} = \begin{pmatrix} \mathbf{c} & -\mathcal{T}\mathbf{c} \end{pmatrix} = \begin{pmatrix} \mathbf{c}_\alpha & -\mathbf{c}_\beta^* \\ \mathbf{c}_\beta & \mathbf{c}_\alpha^* \end{pmatrix}, \quad (5.32)$$

where \mathbf{c} and $-\mathcal{T}\mathbf{c}$ form $(2n \times N/2)$ sub-matrices representing the paired orbitals of the \mathcal{T} -doublet. The action of \mathcal{T} on a \mathcal{T} -doublet is then

$$\begin{aligned} \mathcal{T} \begin{pmatrix} \mathbf{c} & -\mathcal{T}\mathbf{c} \end{pmatrix} &= i\sigma_y\mathcal{K} \begin{pmatrix} \mathbf{c}_\alpha & -\mathbf{c}_\beta^* \\ \mathbf{c}_\beta & \mathbf{c}_\alpha^* \end{pmatrix} = \begin{pmatrix} \mathbf{c}_\beta^* & \mathbf{c}_\alpha \\ -\mathbf{c}_\alpha^* & \mathbf{c}_\beta \end{pmatrix} \\ &= \begin{pmatrix} \mathcal{T}\mathbf{c} & \mathbf{c} \end{pmatrix} = \begin{pmatrix} \mathbf{c} & -\mathcal{T}\mathbf{c} \end{pmatrix}, \end{aligned} \quad (5.33)$$

where, as in Section 5.3.3, the last line exploits the anti-symmetry of the Slater determinantal wave function under the permutation of two columns in \mathbf{C} .

The single-electron orbitals defined by Eq. (5.33) are the h-HF analogue of Kramers' doublets which, through Kramers' theorem, occur in strictly degenerate pairs.²³² Doublets of this form have previously been applied in the (Hermitian) Kramers' RHF^{131,233} and UHF²³⁴ approaches (corresponding to the paired RHF and paired UHF formalisms defined by Stuber and Paldus⁹⁸) to ensure time-reversal symmetry in relativistic Hamiltonians. Crucially, however, the derivation and discussion presented here specifically guarantees real energies using the complex-symmetric (non-Hermitian) inner product.

5.5 Application to Hydrogen Dimer

The hydrogen dimer provides the simplest molecule to illustrate the presence of \mathcal{T} - and \mathcal{PT} -symmetry in h-HF theory. Consider the minimal orbital (real orthogonal) basis

$$\sigma_g = (\chi_L + \chi_R) / \sqrt{2(1 + S)}, \quad (5.34a)$$

$$\sigma_u = (\chi_L - \chi_R) / \sqrt{2(1 - S)}, \quad (5.34b)$$

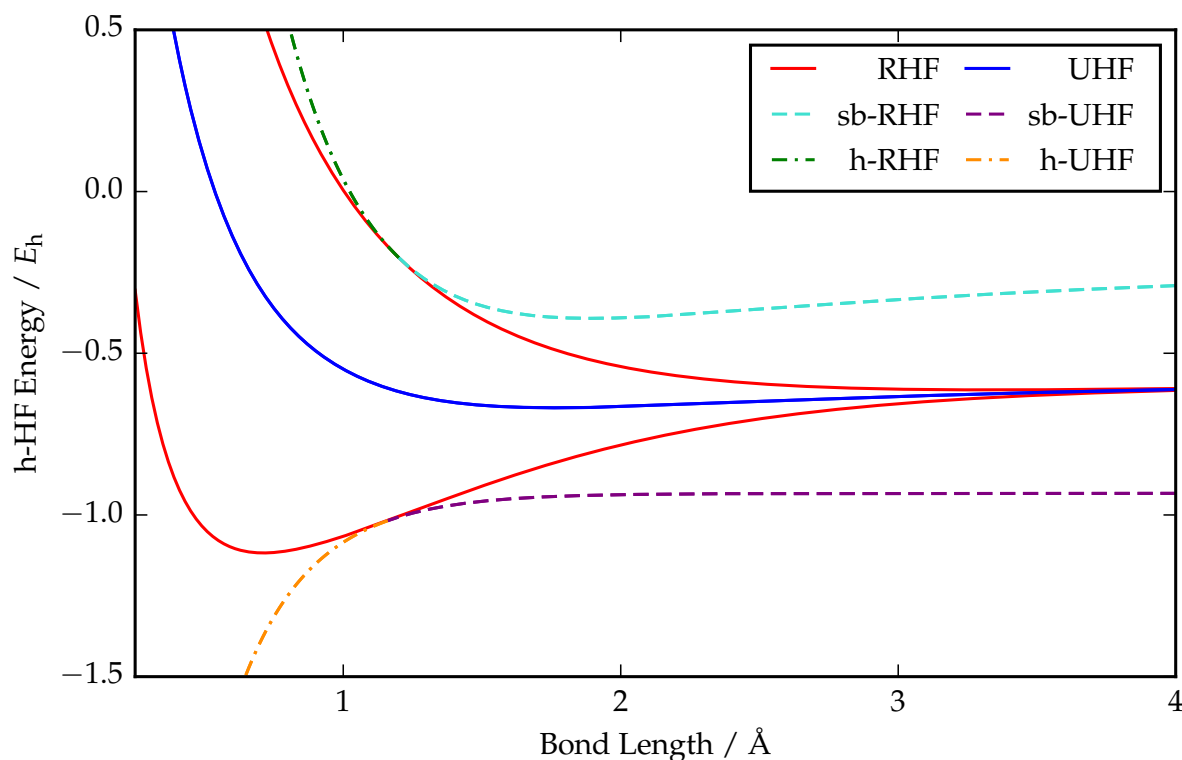


Figure 5.1: The h-HF energy, $\langle \Psi_{\text{HF}} | \hat{H} | \Psi_{\text{HF}} \rangle_{\mathcal{C}}$, for the multiple solutions of H_2 . The spatially symmetry-pure solutions, i.e., the lowest RHF, UHF and highest RHF solutions correspond to the σ_g^2 , $\sigma_g\sigma_u$ and σ_u^2 configurations, respectively. In the dissociation limit, the spatially symmetry-broken UHF (sb-UHF) states and spatially symmetry-broken RHF (sb-RHF) states correspond to diradical configurations (${}^1\text{H}-\text{H}^\dagger$ and ${}^1\text{H}-\text{H}^\ddagger$) and ionic configurations ($\text{H}^+ - \text{H}^-$ and $\text{H}^- - \text{H}^+$) respectively. At shorter bond lengths, the sb-RHF and sb-UHF states coalesce with the spatially symmetry-pure RHF solutions and extend into the complex plane as h-RHF and h-UHF states, respectively. The h-HF energy of the h-RHF and h-UHF solutions, however, remains real.

where χ_L and χ_R are the 1s spatial atomic orbitals on the left and right hydrogen atoms respectively and $S = \langle \chi_L | \chi_R \rangle$ defines their overlap. Without loss of generality, this two-electron system can be considered as a one-dimensional system, and the spatial representation of the parity operator in the (σ_g, σ_u) basis is given by

$$P = \begin{pmatrix} 1 & 0 \\ 0 & -1 \end{pmatrix}. \quad (5.35)$$

From here-on, all calculations are performed with the STO-3G atomic basis. For the sake of simplicity, only the $m_s = 0$ spin manifold is considered.

In addition to the spatially symmetry-pure configurations σ_g^2 , σ_u^2 and $\sigma_g\sigma_u$ (corresponding to two RHF and a doubly degenerate pair of UHF solutions), it is well known that a pair of degenerate spatial symmetry-broken UHF (sb-UHF) solutions develop in the dissociation limit (dashed purple line in Fig. 5.1) in which the electrons localise on

opposite atoms.⁸ These solutions adopt the form given by the parametrisation

$$\Psi_{\text{UHF}}(\mathbf{r}_1, \mathbf{r}_2) = \frac{1}{\sqrt{2}} \begin{vmatrix} \phi_{\text{UHF}}(\mathbf{r}_1)\alpha(1) & \phi_{\text{UHF}}(-\mathbf{r}_1)\beta(1) \\ \phi_{\text{UHF}}(\mathbf{r}_2)\alpha(2) & \phi_{\text{UHF}}(-\mathbf{r}_2)\beta(2) \end{vmatrix}, \quad (5.36)$$

where ϕ_{UHF} represents the optimised spatial orbital corresponding to the UHF solution, and \mathbf{r}_1 and \mathbf{r}_2 are the spatial coordinates of electrons 1 and 2 respectively.

In the dissociation limit, the optimal UHF solutions can be represented schematically as the diradical configurations



However, apart from the chemically intuitive idea of electron correlation, the justification for solutions existing with this particular form is not obvious.

Similarly (although less studied), a pair of degenerate spatial symmetry-broken RHF (sb-RHF) solutions develop (dashed cyan line in Fig. 5.1) with a form given by the parametrisation

$$\Psi_{\text{RHF}}(\mathbf{r}_1, \mathbf{r}_2) = \phi_{\text{RHF}}(\mathbf{r}_1)\phi_{\text{RHF}}(\mathbf{r}_2) \frac{\alpha(1)\beta(2) - \beta(1)\alpha(2)}{\sqrt{2}}. \quad (5.38)$$

Here ϕ_{RHF} represents the optimised spatial orbital corresponding to the RHF solution. In the dissociation limit, the sb-RHF solution corresponds to the localisation of both electrons on the same atom to produce the ionic configurations



Both sb-RHF and sb-UHF solutions are extrema of the HF equations. However, while the sb-UHF solutions are minima, the sb-RHF states correspond to maxima of the HF energy.

5.5.1 Conditions for Real Energies

Rather than using the parametrisations (5.36) and (5.38), consider instead the full UHF space with two spatial molecular orbitals

$$\phi_\alpha = \sigma_g \cos \theta_\alpha + \sigma_u \sin \theta_\alpha, \quad (5.40a)$$

$$\phi_\beta = \sigma_g \cos \theta_\beta + \sigma_u \sin \theta_\beta, \quad (5.40b)$$

where θ_α and θ_β are rotation angles in the range $(-\pi/2, \pi/2]$ controlling the degree of orbital mixing. The occupied orbital coefficient matrix in the combined spatial and

spinor direct product basis is then given by

$$\mathbf{C} = \begin{pmatrix} \mathbf{C}_\alpha \\ \mathbf{C}_\beta \end{pmatrix} = \begin{pmatrix} \cos \theta_\alpha & 0 \\ \sin \theta_\alpha & 0 \\ 0 & \cos \theta_\beta \\ 0 & \sin \theta_\beta \end{pmatrix}, \quad (5.41)$$

and the complex-symmetric density matrix adopts the block form

$$\mathbf{D} = \mathbf{C}\mathbf{C}^\top = \begin{pmatrix} \mathbf{D}_{\alpha\alpha} & \mathbf{0} \\ \mathbf{0} & \mathbf{D}_{\beta\beta} \end{pmatrix}, \quad (5.42)$$

where $\mathbf{D}_{\alpha\alpha} = \mathbf{C}_\alpha \mathbf{C}_\alpha^\top$ and $\mathbf{D}_{\beta\beta} = \mathbf{C}_\beta \mathbf{C}_\beta^\top$.

5.5.1.1 \mathcal{K} -Symmetry

The conditions for conserving complex-conjugation \mathcal{K} -symmetry simply require that $\mathbf{D} = \mathbf{D}^*$. This is trivially satisfied by ensuring that both θ_α and θ_β are real, in which case the h-HF equations reduce to the real HF equations with real energies. Note that this symmetry has already been discussed in Section 3.3.3.1.

5.5.1.2 \mathcal{T} -Symmetry

Next consider the conditions for preserving \mathcal{T} -symmetry in the density matrix. Using the matrix representation $\mathcal{T} = i\sigma_y \mathcal{K}$, the condition for \mathcal{T} -symmetry becomes

$$\begin{pmatrix} \mathbf{D}_{\alpha\alpha} & \mathbf{0} \\ \mathbf{0} & \mathbf{D}_{\beta\beta} \end{pmatrix} = \begin{pmatrix} \mathbf{D}_{\beta\beta}^* & \mathbf{0} \\ \mathbf{0} & \mathbf{D}_{\alpha\alpha}^* \end{pmatrix}. \quad (5.43)$$

Comparing to the parametrisation (5.41), this condition reduces to

$$\begin{pmatrix} \cos^2 \theta_\beta^* & \frac{1}{2} \sin 2\theta_\beta^* \\ \frac{1}{2} \sin 2\theta_\beta^* & \sin^2 \theta_\beta^* \end{pmatrix} = \begin{pmatrix} \cos^2 \theta_\alpha & \frac{1}{2} \sin 2\theta_\alpha \\ \frac{1}{2} \sin 2\theta_\alpha & \sin^2 \theta_\alpha \end{pmatrix}, \quad (5.44)$$

which is satisfied when

$$\tan(\theta_\alpha) = \tan(\theta_\beta^*) \implies \theta_\alpha - \theta_\beta^* = m\pi, \quad (5.45)$$

where $m \in \mathbb{Z}$. Stationary states that satisfy this condition represent holomorphic extensions of the paired UHF formalism.^{98,126}

5.5.1.3 \mathcal{PT} -Symmetry

Finally consider the conditions for \mathcal{PT} -symmetry [see Eq. (5.15)] which, for the density matrix (5.42), becomes

$$\begin{pmatrix} D_{\alpha\alpha} & \mathbf{0} \\ \mathbf{0} & D_{\beta\beta} \end{pmatrix} = \begin{pmatrix} PD_{\beta\beta}^*P & \mathbf{0} \\ \mathbf{0} & PD_{\alpha\alpha}^*P \end{pmatrix}. \quad (5.46)$$

For the parametrisation (5.41), this condition then reduces to

$$\begin{pmatrix} \cos^2 \theta_\beta^* & -\frac{1}{2} \sin 2\theta_\beta^* \\ -\frac{1}{2} \sin 2\theta_\beta^* & \sin^2 \theta_\beta^* \end{pmatrix} = \begin{pmatrix} \cos^2 \theta_\alpha & \frac{1}{2} \sin 2\theta_\alpha \\ \frac{1}{2} \sin 2\theta_\alpha & \sin^2 \theta_\alpha \end{pmatrix}, \quad (5.47)$$

which is satisfied when

$$\tan(\theta_\alpha) = \tan(-\theta_\beta^*) \implies \theta_\alpha + \theta_\beta^* = m\pi, \quad (5.48)$$

where $m \in \mathbb{Z}$. Comparing (5.45) and (5.45) along with the restriction of θ_α and θ_β to the range $(-\pi/2, \pi/2]$ demonstrates that it is impossible for a given density to simultaneously satisfy both \mathcal{PT} - and \mathcal{T} -symmetry.

5.5.2 Real Orbital Coefficients

To visualise these symmetries, first consider the real UHF case, i.e. $(\theta_\alpha, \theta_\beta) \in \mathbb{R}$. Clearly every state in this parametrisation will preserve \mathcal{K} -symmetry and retain real-valued energies. However, it is still possible to observe the presence of \mathcal{T} - and \mathcal{PT} -symmetry by identifying lines of symmetry in the h-HF energy surface. As the h-HF energy is real, the energy of points interconverted by these lines of symmetry will be strictly degenerate.

From Eq. (5.45), \mathcal{T} -symmetry is satisfied when $\theta_\alpha - \theta_\beta = m\pi$ for $m \in \mathbb{Z}$, leading to the constrained molecular orbitals

$$\phi_\alpha = \sigma_g \cos \theta_\alpha + \sigma_u \sin \theta_\alpha, \quad (5.49a)$$

$$\phi_\beta = \sigma_g \cos \theta_\alpha + \sigma_u \sin \theta_\alpha. \quad (5.49b)$$

These constrained orbitals align *exactly* with the real RHF parametrisation (5.38) and create a plane of symmetry demonstrated in Fig. 5.2 (cyan line). Furthermore, it is simple to understand why this symmetry must exist. Since the orbital coefficients (and by extension the density) are all real, the action of \mathcal{T} simply interconverts the two spin states. Since there is no magnetic field, this *spin-flip* operation leaves the h-HF energy unchanged and densities interconverted by this symmetry operation are strictly degenerate.

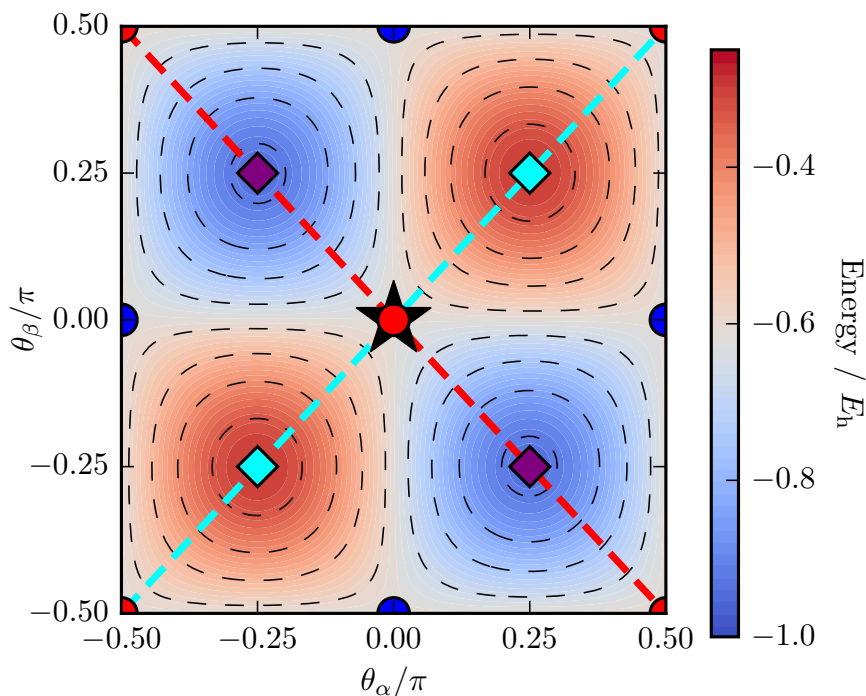


Figure 5.2: The UHF energy of H_2 at 4 Å bond length as a function of θ_α and θ_β showing spin-flip \mathcal{T} -symmetry (dashed cyan line) and \mathcal{PT} -symmetry (dashed red line). The parity (site-flip) operation corresponds to the mapping $(\theta_\alpha, \theta_\beta) \rightarrow (-\theta_\alpha, -\theta_\beta)$, as indicated by inversion through the black star. Spatial symmetry-pure stationary points are indicated by red (RHF) and blue (UHF) circles, while stationary points breaking spatial symmetry are illustrated by cyan (sb-RHF) and purple (sb-UHF) diamonds.

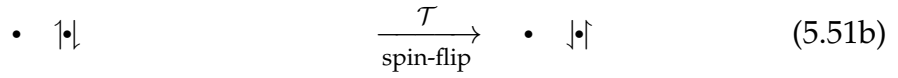
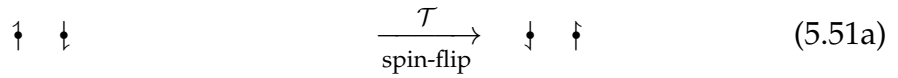
Alternatively, the \mathcal{PT} -symmetry condition (5.48) is satisfied when $\theta_\alpha + \theta_\beta = m\pi$ for $m \in \mathbb{Z}$. This constraint leads to the molecular orbital parametrisation

$$\phi_\alpha = \sigma_g \cos \theta_\alpha + \sigma_u \sin \theta_\alpha, \quad (5.50a)$$

$$\phi_\beta = \sigma_g \cos \theta_\alpha - \sigma_u \sin \theta_\alpha, \quad (5.50b)$$

forming a real-valued \mathcal{PT} -doublet. In fact, these orbitals align *exactly* with the parametrisation provided by Eq. (5.36) and result in an additional line of symmetry in the h-HF energy (red line in Fig. 5.2). This observation justifies the use of the parametrisation (5.36) and the well-known diradical sb-UHF states lie on this line of symmetry. Furthermore, the existence of this symmetry can be understood by noting that the action of the spatial parity operator corresponds to a *site-flip* and thus the overall \mathcal{PT} -symmetry operation for real orbitals corresponds to the combined action of a *spin-* and *site-flip*.

Schematically, the action of \mathcal{T} on the sb-UHF and sb-RHF can be illustrated as



respectively, while \mathcal{PT} operation corresponds to



Therefore, in the minimal basis considered here, the (real) sb-UHF solutions (which correspond to diradical configurations) are \mathcal{PT} -symmetric while the sb-RHF solutions (5.38) (corresponding to ionic configurations) are not \mathcal{PT} -symmetric but do satisfy the spin-flip \mathcal{T} -symmetry. Note also that the spatial symmetry-pure σ_g^2 and σ_u^2 states both also satisfy \mathcal{PT} -symmetry, while the $\sigma_g\sigma_u$ solutions are \mathcal{T} -symmetric.

5.5.3 Complex Orbital Coefficients

Next consider the case of complex orbital coefficients with $(\theta_\alpha, \theta_\beta) \in \mathbb{C}$. The condition for \mathcal{T} -symmetry (5.45) can then be decomposed into real and imaginary parts

$$\text{Re}(\theta_\alpha) - \text{Re}(\theta_\beta) = m\pi, \quad \text{Im}(\theta_\alpha) = -\text{Im}(\theta_\beta), \quad (5.53)$$

while the \mathcal{PT} -symmetry condition (5.48) can be similarly represented as

$$\text{Re}(\theta_\alpha) + \text{Re}(\theta_\beta) = m\pi, \quad \text{Im}(\theta_\alpha) = \text{Im}(\theta_\beta). \quad (5.54)$$

Along these lines of symmetry, the h-HF energy is expected to be real, while the energy of density matrices interconverted by the \mathcal{T} or \mathcal{PT} operators will be related by complex conjugation. Again, a state clearly cannot satisfy \mathcal{PT} - and \mathcal{T} -symmetry simultaneously.

To visualise \mathcal{PT} -symmetry, consider first the h-RHF case where $\theta_\alpha = \theta_\beta = \theta$. For this parametrisation, \mathcal{PT} -symmetric densities are expected when

$$\theta = m\pi/2 + i\vartheta, \quad (5.55)$$

for $\vartheta \in \mathbb{R}$, while no \mathcal{T} -symmetric densities are possible. The h-HF energy is complex in general and so the real and imaginary parts of the energy must be visualised separately as functions of $\text{Re}(\theta)$ and $\text{Im}(\theta)$, shown in Fig. 5.3 for a bond length of 0.75 Å. As expected, lines of \mathcal{PT} -symmetry exist along the values of θ satisfying Eq. (5.55). Here, the energy along the line of symmetry is real-valued, while the energies either side of

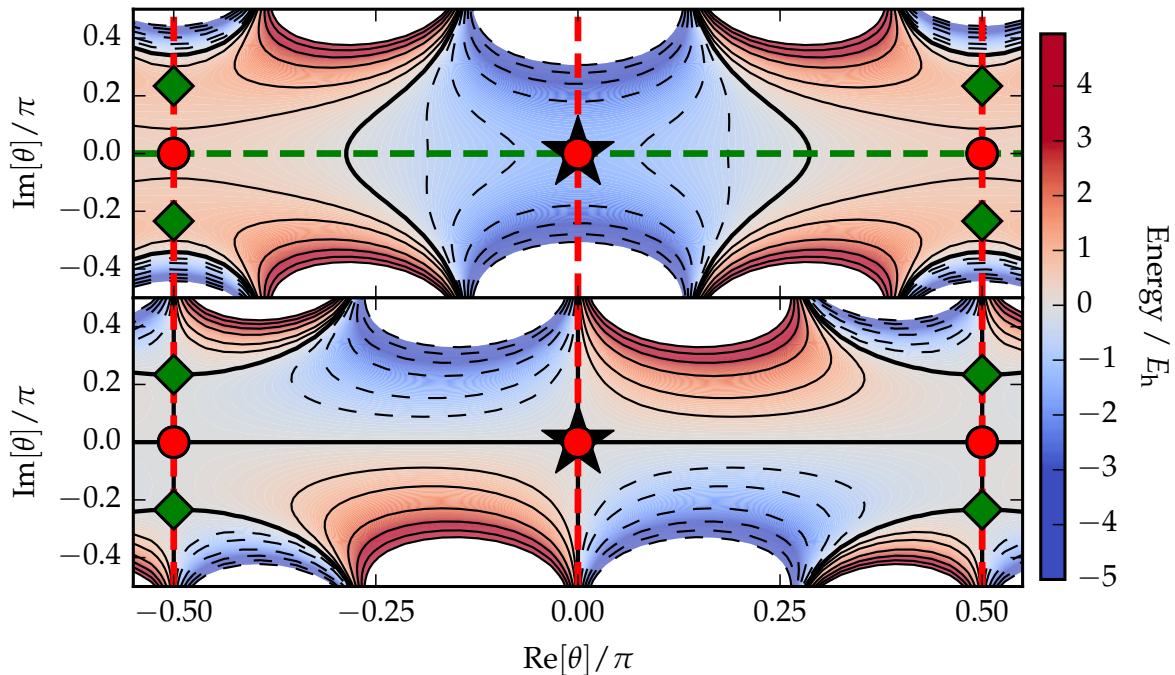


Figure 5.3: Real (top) and imaginary (bottom) components of the h-RHF energy for H_2 at 0.75 \AA bond length as a function of $\text{Re}(\theta)$ and $\text{Im}(\theta)$. The parity (site-flip) operator produces the inversion symmetry $\theta \rightarrow -\theta$, as indicated by inversion through the black star. Vertical lines of symmetry (dashed red lines) along $\text{Re}(\theta) = 0$ and $\text{Re}(\theta) = \pm\pi/2$ coincide with the condition (5.55) for \mathcal{PT} -symmetry, along which the energy is real. Spatial symmetry-pure stationary points are indicated by red (RHF) circles, while complex holomorphic stationary points are illustrated by green (h-RHF) diamonds. Note the energy is also real along the \mathcal{K} -symmetry line $\text{Im}(\theta) = 0$ (dashed green line) along which the orbital coefficients are real.

this line are related by complex conjugation. More explicitly, the (vertical) red lines in Fig. 5.3 along $\text{Re}(\theta) = 0$ and $\text{Re}(\theta) = \pm\pi/2$ coincide with the condition (5.55) for \mathcal{PT} -symmetry and correspond to real h-HF energies. Note that the energy is also real along the line $\text{Im}(\theta) = 0$ (green line) corresponding to \mathcal{K} -symmetry.

As illustrated in Fig. 5.3, the h-RHF stationary solutions (green diamonds) lie on the red \mathcal{PT} -symmetry line and are therefore \mathcal{PT} -symmetric. The complex-conjugate relationship of the two h-RHF states is in fact a manifestation of \mathcal{PT} -symmetry, and the conservation of this hidden symmetry is responsible for their strict degeneracy. Furthermore, since the h-RHF states parametrised by $\theta_\alpha = \theta_\beta = \theta$ are all spin-flip symmetric, the presence of \mathcal{PT} -symmetry in the energy landscape can be justified as the combination of site-flip (centre of inversion at $\theta = 0$) and complex conjugation.

Next consider the complex h-UHF case. As the h-UHF energy is a function of four real variables (real and imaginary parts of θ_α and θ_β), the energy can only be visualised if two variables are set constant. To illustrate the presence of \mathcal{PT} -symmetry, the specific case $\text{Im}(\theta_\alpha) = \text{Im}(\theta_\beta) = \pi/8$ is shown for H_2 at a bond length of 0.75 \AA

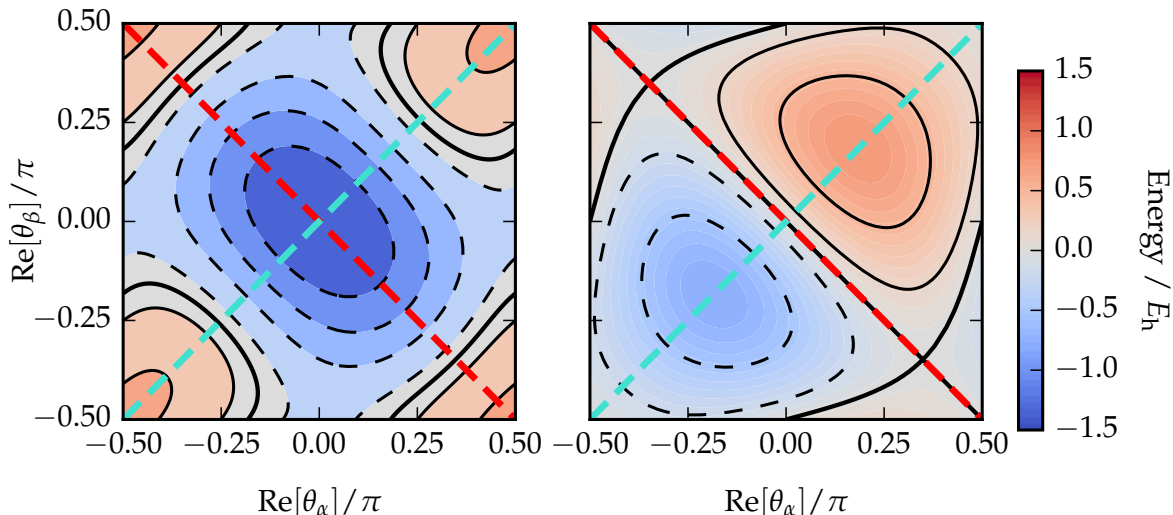


Figure 5.4: Real (left) and imaginary (right) components of the h-UHF energy of H_2 at 0.75 \AA bond length for the illustrative case of fixed imaginary components $\text{Im}(\theta_\alpha) = \text{Im}(\theta_\beta) = \pi/8$. Two lines of symmetry exist along $\text{Re}(\theta_\alpha) = \text{Re}(\theta_\beta)$ and $\text{Re}(\theta_\alpha) + \text{Re}(\theta_\beta) = \pi$, corresponding to spin-flip (dashed cyan line) and \mathcal{PT} -symmetry (dashed red line) respectively. The energy along the \mathcal{PT} -symmetry line is real while the energies related by \mathcal{PT} -symmetry form complex-conjugate pairs. Note that in this particular illustration of the h-UHF energy surface, there are no stationary points.

in Fig. 5.4. Here, the \mathcal{PT} -symmetry line (red dashed) occurs as in Fig. 5.2, although now the complex-conjugation of energies related by the \mathcal{PT} -symmetry line is explicitly observable. Since the orbitals are now complex, spin-flip symmetry (cyan dashed) is no longer equivalent to \mathcal{T} and, although the energies related by spin-flip are degenerate, they are now complex-valued in general. Furthermore, because the site-flip operation takes $(\theta_\alpha, \theta_\beta) \rightarrow (-\theta_\alpha, -\theta_\beta)$, its effect on the h-HF energy landscape cannot be observed under the constraint $\text{Im}(\theta_\alpha) = \text{Im}(\theta_\beta) = \pi/8$.

Notably there are no h-UHF stationary points in Fig. 5.4. In fact, inspection of the stationary points corresponding to the h-UHF solutions in Fig. 5.1 reveals that they follow the form $(\theta_\alpha, \theta_\beta) = (i\vartheta, -i\vartheta)$, for $\vartheta \in \mathbb{R}$, leading to the conclusion that the h-UHF solutions in H_2 are not \mathcal{PT} -symmetric.

In contrast, the presence of \mathcal{T} -symmetry can be visualised using the specific case $\text{Im}(\theta_\alpha) = -\text{Im}(\theta_\beta) = \pi/8$, as shown for the same H_2 geometry in Fig. 5.5. Here, the \mathcal{T} -symmetry line (cyan dashed) occurs along the line $\text{Re}(\theta_\alpha) = \text{Re}(\theta_\beta)$. As with \mathcal{PT} -symmetry, the energy of either side of the \mathcal{T} -symmetry line is related by complex conjugation, while the energy along the line itself remains real. In fact, although they do not appear in Fig. 5.5, the h-UHF stationary states in Fig. 5.1 correspond to stationary points satisfying \mathcal{T} -symmetry and retain real-valued energies. Furthermore, inspecting the orbital coefficients of these h-UHF states reveals that they adopt the expected \mathcal{T} -doublet form (5.32).

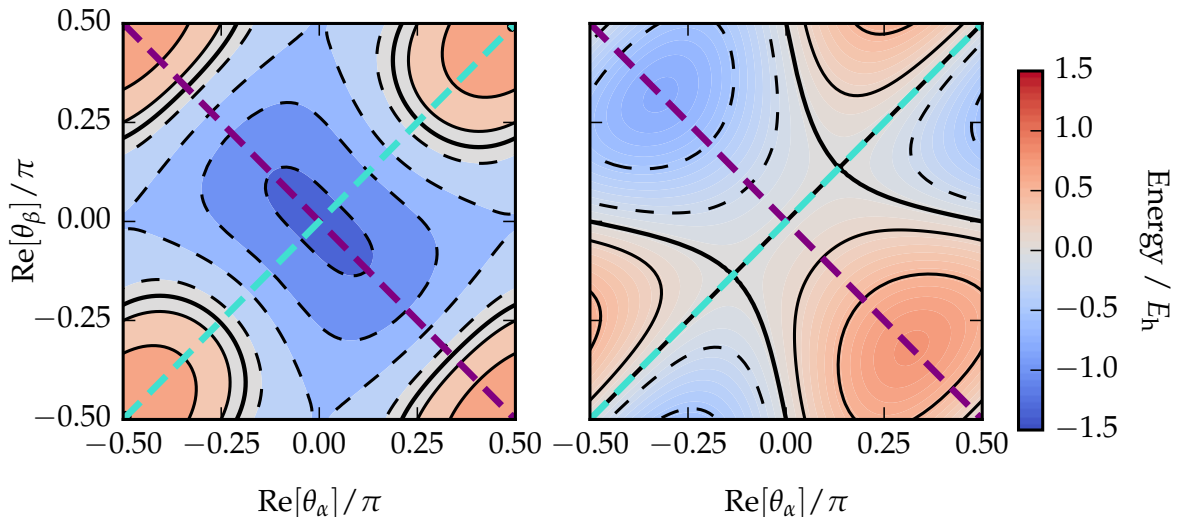


Figure 5.5: The real (left) and imaginary (right) components of the h-UHF energy of H_2 at 0.75 \AA bond length for the illustrative case of fixed imaginary components $\text{Im}(\theta_\alpha) = -\text{Im}(\theta_\beta) = \pi/8$. The line of \mathcal{T} -symmetry exists along $\text{Re}(\theta_\alpha) = \text{Re}(\theta_\beta)$ (dashed cyan line) while the site-flip operation occurs along $\text{Re}(\theta_\alpha) + \text{Re}(\theta_\beta) = 0$ (purple dashed line). The energy along the \mathcal{T} -symmetry line is real, as predicted, while the energies for states related by \mathcal{T} -symmetry form complex-conjugate pairs. We also note that there are no holomorphic HF stationary points on this illustrative landscape representing only a slice of the full holomorphic HF energy surface.

It is no longer possible to visualise the spin-flip operation under the restriction $\text{Im}(\theta_\alpha) = -\text{Im}(\theta_\beta) = \pi/8$, however the site-flip operation can be observed along the line $\text{Re}(\theta_\alpha) = -\text{Re}(\theta_\beta)$ (purple dashed). Similarly to spin-flip symmetry in Fig. 5.4, the site-flip operation leads to the strict degeneracy of states on either side of this line, but does not guarantee real energies along the line itself.

In summary, the \mathcal{PT} -symmetric stationary h-HF solutions for H_2 are the σ_g^2 , σ_u^2 , sb-UHF and h-RHF states, although the effect of \mathcal{PT} -symmetry can be observed throughout the h-HF energy landscape. For these \mathcal{PT} -symmetric solutions, the molecular orbital coefficients possess the \mathcal{PT} -doublet form [see Eq. (5.26)]. In contrast, the sb-RHF and h-UHF solutions satisfy \mathcal{T} -symmetry and also retain real energies. The onset of \mathcal{PT} - or \mathcal{T} -symmetry breaking therefore coincides with the disappearance of the corresponding states at Coulson–Fischer points in a similar manner to other types of symmetry-breaking in HF theory.^{98,125,126}

5.5.4 Breaking Spatial Symmetry

To fully demonstrate how \mathcal{T} - and \mathcal{PT} -symmetry control whether the h-HF energy is real, consider the effect of breaking the left-right symmetry in the HZ molecule [see Section 4.4.2]. Taking the nuclear charge $Q_Z = 1.15 \text{ a.u.}$, it was found in Section 4.4.2 that complex h-RHF states now possess complex energies, while the h-UHF states retain

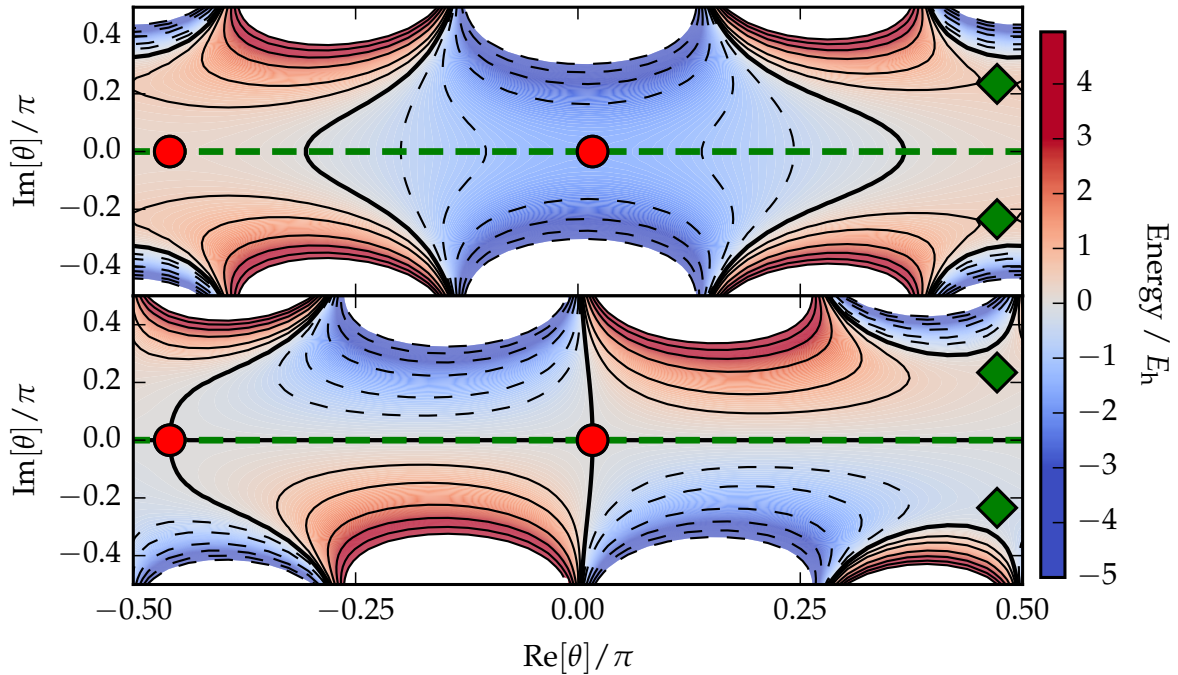


Figure 5.6: Real (top) and imaginary (bottom) components of the h-RHF energy for HZ ($Q_Z = 1.15$ a.u.) at 0.75 \AA bond length as a function of $\text{Re}(\theta)$ and $\text{Im}(\theta)$. The loss of parity symmetry in the molecule means that no states can preserve \mathcal{PT} -symmetry and the only condition for real h-RHF energies is preserving \mathcal{K} -symmetry (dashed green line). Real RHF stationary points (red circles) lie on this line of \mathcal{K} -symmetry. In contrast, the holomorphic stationary points (green diamonds) can no longer satisfy \mathcal{PT} -symmetry and now have complex energies, although they are mutually related by complex conjugation.

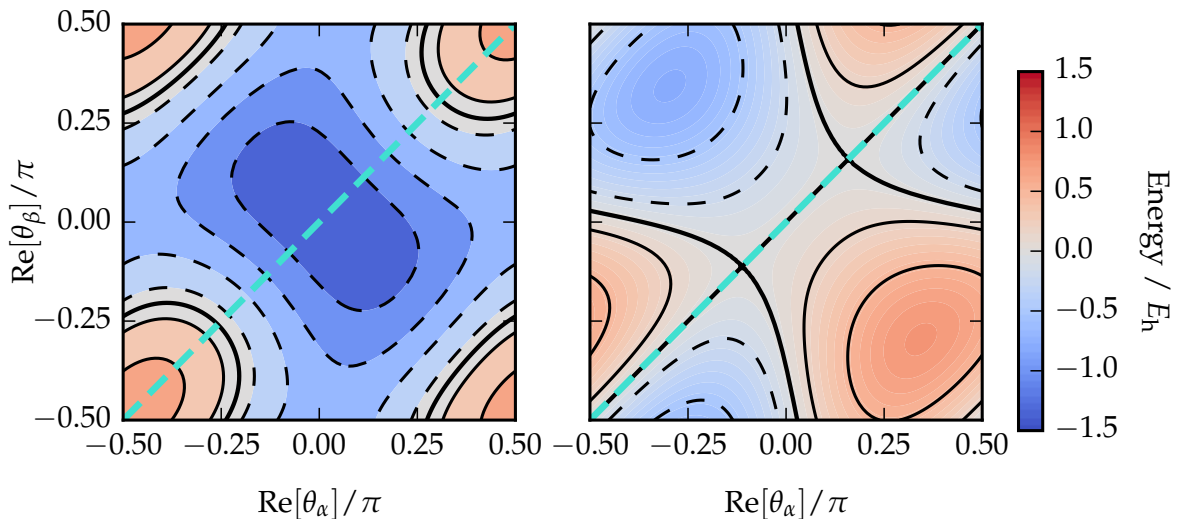


Figure 5.7: Real (top) and imaginary (bottom) components of the h-UHF energy for the HZ molecule ($Q_Z = 1.15$ a.u.) at 0.75 \AA bond length under the constraint $\text{Im}(\theta_\alpha) = -\text{Im}(\theta_\beta) = \pi/8$. The only symmetry evident here is \mathcal{T} -symmetry (cyan dashed) along which the h-UHF energy is strictly real. Energies on either side of this symmetry-line are related by complex conjugation. As the molecule has no left-right symmetry, the degeneracy induced by the site-flip operation in H_2 [see Fig. 5.5] is lost. Note that there are no stationary points on this particular slice of the h-UHF energy surface.

real energies [see Fig. 4.5]. It is now possible to understand why this must be the case. In what follows, the basis Eq. (5.34) is used without loss of generality, although the *gerade* and *ungerade* symmetry labels must be dropped.

Take first the complex energies for the h-RHF states. When the left-right symmetry is broken, there is no longer any parity symmetry in the molecule. It is therefore impossible for the h-RHF states to satisfy \mathcal{PT} -symmetry. Since these stationary states also break \mathcal{K} - and \mathcal{T} -symmetry, there is no rigorous guarantee that their energies are real, as illustrated for a bond length of 0.75 Å in Fig. 5.6. While the h-RHF states in the symmetric H_2 molecule are \mathcal{PT} -symmetric (and possess real h-HF energies), when they are followed onto the corresponding h-RHF states in HZ (green diamonds Fig. 5.6), they lose this symmetry and their energy becomes complex. Note that these two h-RHF states are symmetry related by the \mathcal{K} operator and thus their energies form a complex-conjugate pair.

Finally, consider the real energies for the h-UHF states. Although the loss of parity symmetry in the molecule removes the possibility of satisfying \mathcal{PT} -symmetry, the presence of \mathcal{T} -symmetry in the molecule is left unaffected. This can be illustrated using the $\text{Im}(\theta_\alpha) = -\text{Im}(\theta_\beta) = \pi/8$ slice of the h-UHF energy [see Fig. 5.7], where \mathcal{T} -symmetry (dashed cyan line) continues to ensure real-valued energies. As a result, the h-UHF states that conserved \mathcal{T} -symmetry in H_2 continue to conserve this symmetry in the asymmetric HZ molecule and retain real-valued energies.

5.6 Concluding Remarks

In this chapter, the conditions for real energies in the non-Hermitian h-HF approximation — namely the conservation of \mathcal{K} -, \mathcal{T} - or \mathcal{PT} -symmetry — have been outlined. The key results derived include:

1. A set of molecular orbitals is \mathcal{PT} -symmetric *if and only if* the effective Fock Hamiltonian is \mathcal{PT} -symmetric, and *vice versa*.
2. Starting with a \mathcal{PT} -symmetric guess density matrix, \mathcal{PT} -symmetry can be conserved throughout the self-consistent process.
3. If an optimal self-consistent solution is invariant under \mathcal{PT} , then its eigenvalues and corresponding HF energy must be real.
4. \mathcal{PT} -symmetry can be explicitly satisfied for $m_s = 0$ by constructing the molecular orbitals coefficients in the structure of a so-called \mathcal{PT} -doublet, i.e. pairing each occupied orbital with its \mathcal{PT} -transformed analogue.

5. Slater determinants built from \mathcal{PT} -doublets lead to \mathcal{PT} -symmetric many-electron wave functions.

These conditions explain the observed real energies in previous chapters and provide further insights into the fundamental symmetry and properties of the h-HF energy surface.

The effect of \mathcal{T} - and \mathcal{PT} -symmetry on the h-HF energy landscape has been illustrated using the minimal basis H_2 molecule, and its asymmetric HZ variant. In particular, the sb-UHF and h-RHF wave functions in H_2 are found to be \mathcal{PT} -symmetric, while the sb-RHF and h-UHF wave functions break \mathcal{PT} -symmetry but conserve \mathcal{T} -symmetry. The transitions between broken and unbroken \mathcal{T} - or \mathcal{PT} -symmetry regions coincide with the disappearance of the corresponding solutions at Coulson–Fischer points. Furthermore, when the molecular parity is lost in the asymmetric HZ molecule, the h-RHF state no longer satisfies \mathcal{PT} -symmetry, while the sb-RHF and h-UHF solutions retain \mathcal{T} -symmetry.

5.6.1 Scope for Future Development

By viewing the h-HF framework as a complex-analytic continuation of HF, the results presented in this chapter expose \mathcal{T} - and \mathcal{PT} -symmetry as previously hidden symmetries in HF approximation. These new symmetries can either be conserved or broken in HF wave functions and are of particular interest since the restoration of broken symmetries through Half-Projected^{235–238} or Projected HF^{48,121,192,235} provides a promising route for capturing electron correlation. As a result, it is possible that restoring broken \mathcal{T} - or \mathcal{PT} -symmetry may complement Projected HF approaches, allowing them to be applied in cases where no symmetry-breaking is identified for currently available symmetries.

Demonstrating the existence of \mathcal{PT} -symmetric solutions with real energies in the HF approximation also removes the rigorous condition of Hermiticity that is usually applied in electronic structure theory. This opens the possibility of new wave function *ansätze* or complex non-Hermitian Hamiltonians that would have previously been regarded as unphysical. Of particular note is the similarity between the \mathcal{PT} -doublet form and geminal wave functions built from UHF natural orbitals.^{239,240} The demonstration of \mathcal{PT} -symmetry in HF provides only the first study of \mathcal{PT} -symmetry in electronic structure, and a great deal of further work is required to understand the possible applications of wave functions conserving \mathcal{PT} -symmetry.

Finally, the existence of real energies in non-Hermitian HF formalisms related to h-HF theory raises interesting questions for non-Hermitian approaches that study

metastable resonances [see Section 3.4.3]. In these approaches, complex states represent resonances with a finite lifetime, where the decay rate is given by the imaginary component of the energy.¹⁶⁸ Complex non-Hermitian stationary states that conserve \mathcal{T} - or \mathcal{PT} -symmetry and possess real energies should therefore have infinite lifetimes and correspond to bound states. This makes conceptual sense since these states must be unchanged when time (\mathcal{T}) or space-time (\mathcal{PT}) is reversed, and so they cannot represent either an outgoing or ingoing state. It is therefore possible that, with further work, h-HF states conserving \mathcal{T} - or \mathcal{PT} -symmetry could be assigned to physical bound electronic states while complex h-HF states that break these symmetries may correspond to metastable resonances.¹⁶⁸

Chapter 6

Analytically Continuing the Hamiltonian

The work in this chapter has contributed to the publication Ref. (3)

Summary

Until now, h-HF solutions have only been explored using a real molecular Hamiltonian, where complex states are induced by dressing the Hamiltonian with complex orbital coefficients. In the current chapter, h-HF theory is extended further by constructing complex-analytic continuations of the Hamiltonian itself. By extending to an inherently non-Hermitian Hamiltonian, a fundamental topology of h-HF solutions is revealed in the complex plane where discrete stationary states are unified as one continuous Riemann surface. On this Riemann surface, it is then shown that a ground-state HF wave function can be continuously evolved into an excited-state HF wave function by following a suitable 'complex adiabatic connection'. This conceptual unification of ground and excited states creates new possibilities for understanding quantised molecular energy levels, with the potential to revolutionise excited-state electronic structure theory.

6.1 Context and Scope

Solutions of the h-HF equations have so far only been considered for the real-valued molecular Hamiltonian. The existence of complex h-HF states is therefore induced only by the non-Hermitian dressing of the Hamiltonian by the molecular orbitals to construct the one-electron effective Fock operator. As a result, h-HF states exist as complex-analytic extensions of real HF states and always occur in pairs where both the orbital coefficients and energies are related by complex conjugation. In the current chapter, the behaviour of complex-valued h-HF solutions is investigated when the Hamiltonian operator itself is complex-analytically continued to become an inherently non-Hermitian operator.

The introduction of non-Hermitian Hamiltonians has revolutionised our understanding of multiple eigenstates in quantum systems.¹⁹³ In particular, when a real-symmetric Hamiltonian is analytically continued into the complex plane to become non-Hermitian, a more fundamental topology of eigenstates can be exposed. For example, with non-Hermitian Hamiltonians, quantisation of eigenvalues emerges from different sheets of a continuous Riemann surface.²⁰³ These Riemann surfaces imply that our view of quantised energy levels in Hermitian quantum mechanics arises from restricting energies to real values.

Although Hermitian and non-Hermitian Hamiltonians are closely related, the behaviour of their eigenvalues near degeneracies is starkly different.^{241,242} For example, encircling non-Hermitian degeneracies at “exceptional points” leads to the interconversion of states^{241,243} and can introduce a geometric phase.²²² In contrast, encircling Hermitian degeneracies at “conical intersections”²²⁶ introduces only a geometric phase and leaves the states unchanged.²⁴⁴ More dramatically, while eigenvectors remain orthogonal at conical intersections, the eigenvectors at non-Hermitian exceptional points become *equivalent*. The result is a self-orthogonal (quasi-null) state and a set of eigenvectors that no longer span the full space.¹⁶⁸ Exceptional points are becoming increasingly important in quantum chemistry and are thought to play a role for non-adiabatic decay in metastable systems.²⁴²

In the current chapter, h-HF solutions are explored for a complex-analytically continued Hubbard model, revealing a more fundamental topology where stationary states are connected as a single Riemann surface. As part of this Riemann surface, h-HF states form a continuous manifold of connected sheets that each represent a different state. Coulson–Fischer points then correspond to the intersection of two or more sheets at an exceptional point. Significantly, this suggests that ground and excited HF states can be naturally and smoothly connected across the complex plane.

By introducing a complex-scaled electron–electron interaction, it is shown how the Riemann surface perspective of ground and excited HF states can be generalised to molecular systems. Finally, it is demonstrated that a ground HF state wave function can be continuously evolved into an excited HF state wave function by following a complex adiabatic connection through the complex plane. This conceptual unification of ground and excited states into a single Riemann surface opens new opportunities for developing methods that directly compute approximate excited-state wave functions without relying on ground state information.

6.2 Analytic Continuation of the Hubbard Model

The (symmetric) one-dimensional periodic Hubbard model provides a pedagogical model for the transition between weak and strong electron correlation.²⁴⁵ With a Hamiltonian parametrised by one variable, this model creates the ideal environment for understanding h-HF states as the Hamiltonian itself is analytically continued into the complex plane. In a periodic Hubbard lattice of n sites, the energy is controlled by the kinetic energy term t , representing the ‘hopping’ of electrons between sites, and the on-site electron repulsion U . Taking t as the unit of energy reduces the parametrisation to only one variable: the ratio U/t . By varying this ratio, the Hubbard model provides an archetypal example for the transition between the weak ($U/t \rightarrow 0$) and strong ($U/t \rightarrow \infty$) electron correlation regimes.²⁴⁶

In what follows, the h-HF wave function is expressed using the localised Wannier basis built from a set of orthogonal n spatial orbitals $\{\chi_\mu\}$ each localised on a lattice point of the n -periodic chain.²⁴⁵ Using this basis, the one-electron integrals incorporate only the electronic kinetic energy as

$$h_{\mu\nu} = -t(\delta_{\mu,\nu+1} + \delta_{\mu,\nu-1}), \quad (6.1)$$

where periodic boundary conditions must be respected. The two-electron integrals, containing only the on-site Coulomb repulsion, are given by

$$\langle \mu\nu | \sigma\tau \rangle = U\delta_{\mu\nu}\delta_{\mu\sigma}\delta_{\mu\tau}. \quad (6.2)$$

6.2.1 Hubbard Dimer

Consider first the $n = 2$ periodic Hubbard dimer. In this case, Eq. (4.36) dictates that a total of eight h-UHF states (including four h-RHF) can be expected for all values of U/t , as shown in Fig. 6.1. Mirroring H_2 , these states include a spatially symmetric “ σ_g^2 -like” ground RHF state and a lower energy doubly-degenerate symmetry-broken

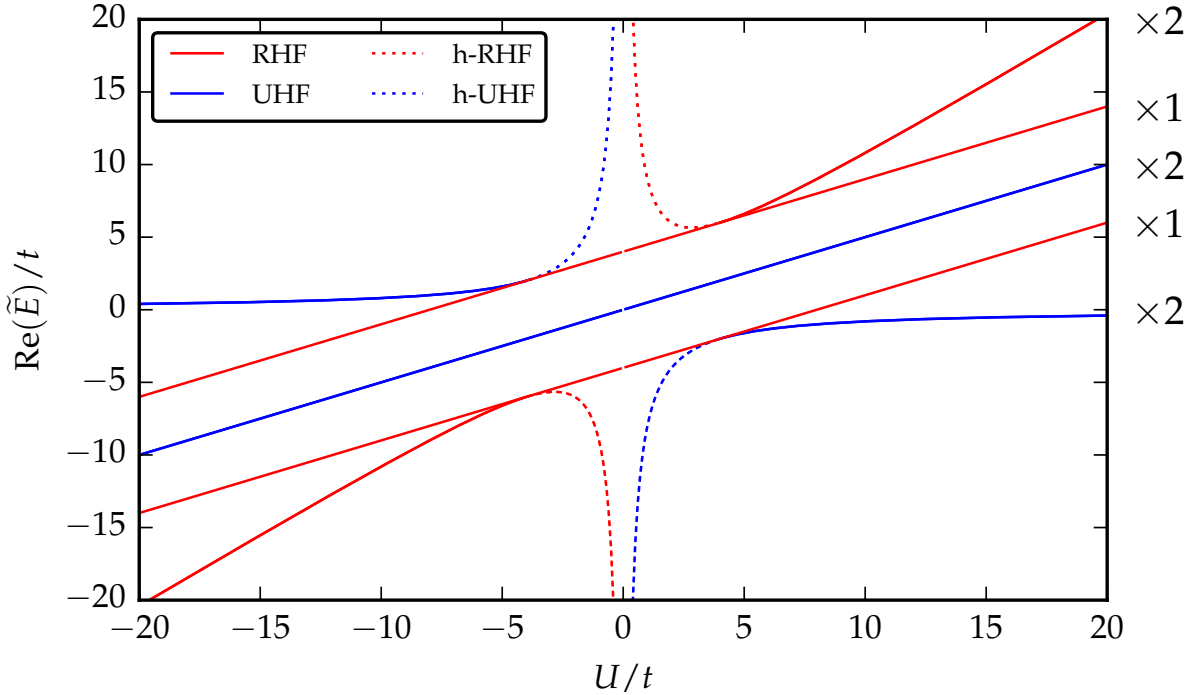


Figure 6.1: Holomorphic energy of the h-HF states in the Hubbard dimer for real U/t . Positive and negative U/t regions correspond to the repulsive and attract regimes respectively. At $U/t = 0$, the h-HF energy of the complex h-RHF (dotted red) and h-UHF (dotted blue) becomes singular as the self-consistency is lost [see main text for more details].

UHF (sb-UHF) state existing in the strong correlation region (large U/t) with ‘diradical’ character. As the correlation weakens towards smaller U/t values, this state coalesces with the ground RHF state at the Coulson–Fischer point, while its h-UHF counterpart continues with complex orbital coefficients. In addition, there exists a doubly degenerate UHF state representing the “ $\sigma_g \sigma_u$ -like” state, a spatially symmetric excited RHF state representing the “ σ_u^2 -like” state, and a degenerate pair of spatially symmetry-broken RHF (sb-RHF) states with ionic character in the strong correlation limit. These ionic states coalesce with the excited RHF state, while their h-RHF counterparts continue with complex orbital coefficients. While all real HF states are also solutions to the h-HF equations, only solutions with complex orbital coefficients will be referred to as h-RHF or h-UHF states.

A similar pattern of HF states can be observed in the attractive regime (negative U/t). However, in this regime the sb-RHF state now represents the overall ground state and coalesces with the “ σ_g^2 -like” as the strength of the correlation is reduced, while the sb-UHF state represents an excited state and coalesces with the “ σ_u^2 -like” state. In both cases, the corresponding h-RHF and h-UHF stationary points continue with complex orbital coefficients towards $U/t \rightarrow 0^-$.

To explicitly understand how the correlation strength controls the existence of sb-

UHF states, consider the sb-UHF states represented by the molecular orbitals

$$\phi_\alpha = \chi_L \cos\left(\frac{\pi}{4} + \theta\right) + \chi_R \sin\left(\frac{\pi}{4} + \theta\right) \quad (6.3a)$$

$$\phi_\beta = \chi_L \cos\left(\frac{\pi}{4} - \theta\right) + \chi_R \sin\left(\frac{\pi}{4} - \theta\right), \quad (6.3b)$$

where χ_L and χ_R are the (real and orthogonal) basis orbitals on the ‘left’ and ‘right’ sites respectively. In this parametrisation, the h-UHF energy can be expressed as

$$\tilde{E}(\theta) = \cos 2\theta \left(-4t + \frac{U}{2} \cos 2\theta \right), \quad (6.4)$$

and the optimal h-UHF states can then be identified as the roots of the differential

$$\frac{d\tilde{E}}{d\theta} = 2 \sin 2\theta (-4t + U \cos 2\theta). \quad (6.5)$$

Upon factorisation, and noting that distinct h-UHF states lie in the domain $\theta \in (-\frac{\pi}{2}, \frac{\pi}{2}]$, this condition yields stationary states at

$$\theta = 0, \quad \frac{\pi}{2} \quad \text{and} \quad \theta = \frac{1}{2} \arccos\left(\frac{4t}{U}\right). \quad (6.6)$$

Here the multi-valued nature of the arccos function leads to the two-fold degeneracy of the sb-UHF states.

Understanding the evolution of the optimal θ values for real U/t is trivial. Firstly, the RHF bonding “ σ_g^2 -like” ($\theta = 0$) and antibonding “ σ_u^2 -like” ($\theta = \pi/2$) states remain constant for all U/t and are fixed by the symmetry of the model. Furthermore, their energies, given by $-t \pm U/2$ respectively, scale linearly with the strength of the correlation.

In contrast, the form of the sb-UHF states depends intimately on the strength of the correlation. Towards the strong-correlation limit ($U/t \rightarrow \infty$), where $\theta \rightarrow 0$ or $\pi/2$, the electrons localise on opposite sites and the energy approaches zero as the relative contribution of the kinetic energy becomes negligible. As the correlation weakens, the sb-UHF states approach the RHF state, eventually coalescing at $U = 4t$. After this Coulson–Fischer point, the h-UHF states continue with pure-imaginary θ and complex orbital coefficients, although their h-UHF energy $-8t^2/U$ remains real. These real h-HF energies are in fact the result of conserving time-reversal \mathcal{T} -symmetry in the h-UHF state, as discussed in Section 5.4.1.

When the electron repulsion vanishes completely in the repulsive regime ($U/t \rightarrow 0^+$), the energy of the h-UHF states approaches a singularity at $-\infty$. Approaching the same loss of electron repulsion from the attractive regime ($U/t \rightarrow 0^-$), the energy of the attractive sb-UHF state also approaches a singularity at $+\infty$. Similar singularities occur for the h-RHF ‘ionic’ solutions and together these points represent the poles on the

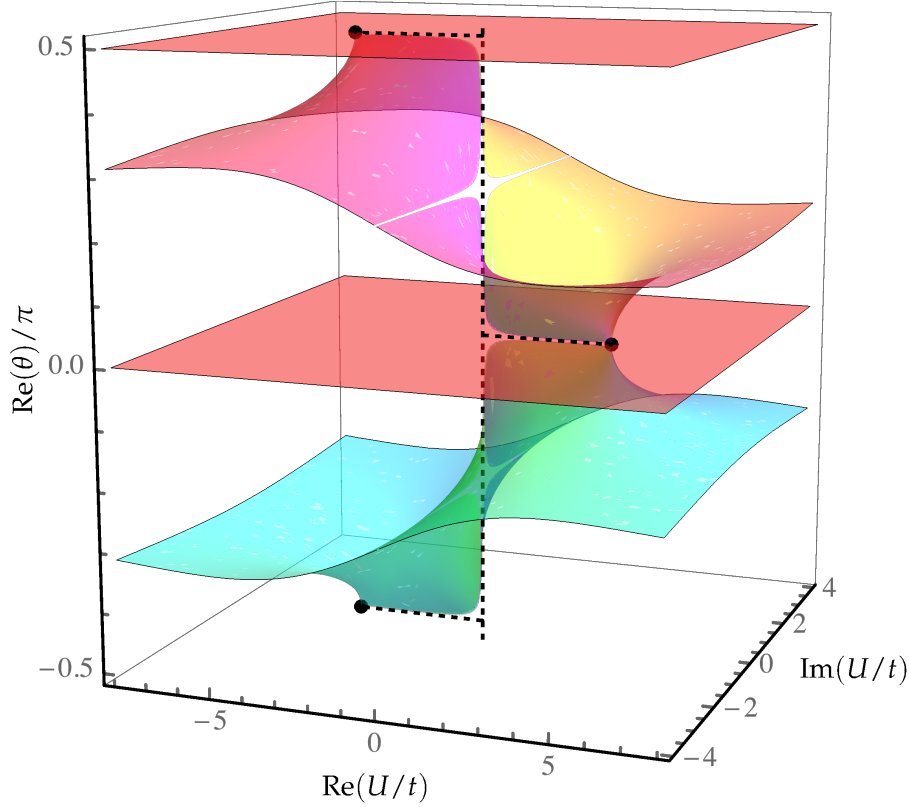


Figure 6.2: Real components of the orbital mixing angle θ for the h-UHF states [Eq. (6.3)] as a function of the real and imaginary parts of U/t . The colouring indicates the phase of θ , and periodic repeats of these surfaces exist with a vertical offset of π . In this representation, h-UHF states become connected as individual sheets of a continuous Riemann surface. The Coulson–Fischer points (black dots) represent branch points on the Riemann surface and are connected by branch cuts (dotted black line).

holomorphic energy function that result from the a non-constant holomorphic function being unbound [see Section 3.3.3.1]. Furthermore, these singularities appear to have physical significance, arising from the complete loss of self-consistency in the model, and a more detailed discussion follows in Section 6.2.3.

Until now, the h-UHF states in the Hubbard model directly mirror those seen in H_2 . However, the full power of this analytic model is harnessed when the correlation strength itself is analytically continued to complex U/t values. Combining the h-HF description with this analytically-continued Hamiltonian reveals a hidden topology of h-UHF states across the complex plane. Extending Eq. (6.6) to complex values of U/t can be achieved by introducing the logarithmic form of arccos as

$$\theta = 0, \quad \frac{\pi}{2} \quad \text{and} \quad \theta = -\frac{i}{2} \ln \left(\frac{1 + \sqrt{1 - z^2}}{z} \right), \quad (6.7)$$

where $z = -U/(4t)$. As a complex multi-valued function, Eq. (6.7) must be visualised using a Riemann surface, illustrated in Fig. 6.2. On this surface, each individual ‘sheet’ represents a different optimal value of θ , defining a different h-UHF stationary state. The

two flat planes represent the symmetry-pure RHF states with $\theta = 0$ or $\pi/2$. Significantly, in this Riemann surface representation, the Coulson–Fischer points (black dots) and the singularity at $U/t = 0$ now appear as *isolated points* on the real U/t axis where multiple sheets intersect. There is no longer any distinction or threshold separating the h-UHF and sb-UHF states or the stationary states in the repulsive and attractive regimes. Instead, the corresponding sb-UHF and h-UHF states become smoothly unified across the complex plane. Furthermore, the degenerate h-UHF states that previously appeared as discretised values of θ now emerge as one continuous manifold of stationary states. Remarkably, this implies that the apparent discrete nature of multiple HF solutions arises as a direct consequence of restricting the conventional description to real U/t values.

Mathematically, the Coulson–Fischer points on this surface represent branch points (black dots) that are required to represent the complex multi-valued function as multiple sheets. Branch cuts (black dashed lines) connect these branch points and represent the joining ‘seams’ between sheets. The observed branch points fall into two classes: ‘square-root’ algebraic branch points at $U = \pm 4t$, and a ‘logarithmic’ transcendental branch point at $U/t = 0$. The existence and classification of these branch points and branch cuts plays an important role in revealing the fundamental nature of both the Coulson–Fischer point and the singularity at $U/t = 0$.

6.2.2 Coulson–Fischer Points as Exceptional Points

The first implication of representing multiple h-HF states using a Riemann surface concerns the nature of the Coulson–Fischer point. On the Riemann surface, the Coulson–Fischer point where the h-UHF and RHF states coalesce is represented by a ‘square-root’ branch point. Therefore, if a h-UHF state is followed along a path around this point and across the branch cut, for example by passing between $U = 0$ and $U = 4t$, then the two symmetry-broken states that coalesce are interconverted (solid red lines in Fig. 6.3). Completing a second rotation restores the solutions to their original states (dashed red lines in Fig. 6.3), although no geometric phase occurs. Remarkably, by extending U/t into the complex plane, the Coulson–Fischer point has been revealed as a non-Hermitian exceptional point^{220,222,241} of the complex Hamiltonian.

Chemically, encircling the Coulson–Fischer point causes the electrons to evolve from a distribution with the α (β) electron on the left (right) site to a distribution with the α (β) electron on the right (left) site. Therefore, by creating a complex effective electron interaction, it is possible to induce a spatial rearrangement of the electrons at the mean-field level. If the Coulson–Fischer point is viewed as a representation of the Mott–Hubbard metal-insulator phase transition,²⁴⁷ then following a path around

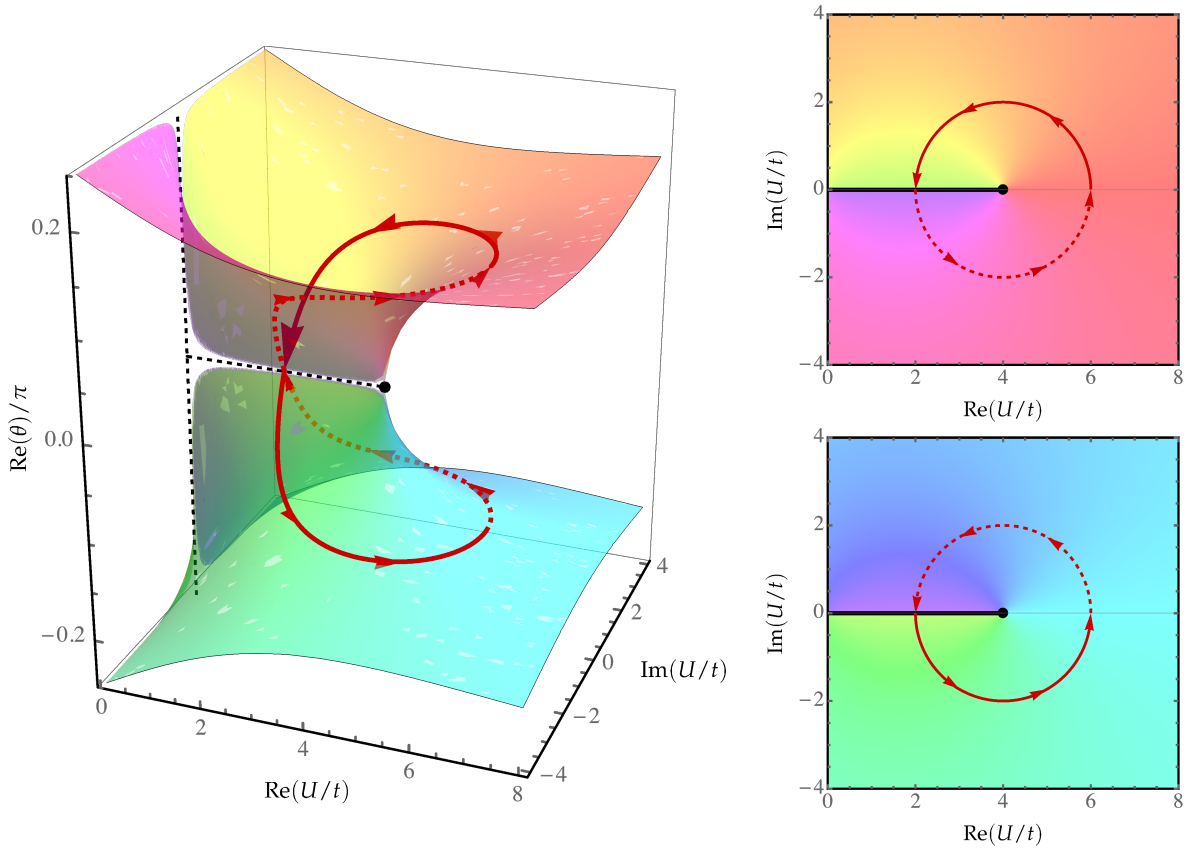


Figure 6.3: Following a path (solid red) around the Coulson–Fischer point (black dot) and across the branch cut (black line) interconverts the symmetry-related h-UHF states, while completing a second rotation returns the solutions to their original state (dashed red). Along this path, the h-UHF state remains stationary with respect to the parametrised Hamiltonian.

this point interconverts the symmetry-related ferromagnetic insulating configurations. It seems plausible that such a transformation might be achieved experimentally if an appropriate complex effective electron interaction could be realised.

From an electronic structure perspective, this interconversion represents a double excitation. Furthermore, if one considers the equivalent Coulson–Fischer point in a larger half-filled Hubbard chain, then the equivalent interconversion would correspond to an N -fold excitation. Therefore, by following a relatively simple pathway in the complex U/t plane, it is possible to evolve a reference configuration to a highly excited configuration, while retaining stationarity with respect to the parametrised Hamiltonian. As a result, this feature of the h-HF Riemann surfaces creates new opportunities for computing direct approximations to excited state configurations that will be explored further in Section 6.3.

6.2.3 Singularity in the Tight-Binding Limit

The second insight into the fundamental nature of HF states lies in the singularity at $U/t = 0$. This point corresponds to a ‘logarithmic’ branch point with a starkly different behaviour to the conventional Coulson–Fischer point. When a solution is followed along a path around this logarithmic branch point and crosses the branch cuts on either side in turn, it will *never* return to its original state. Instead, on the first complete rotation, the solution will become its symmetry-related copy, while the second rotation will take the state to its periodic repeat at $\theta \rightarrow \theta + \pi$.

Furthermore, at $U/t = 0$, both the h-UHF states coalesce at $\theta \rightarrow \pm i\infty$ with an *infinite* negative energy. This singularity can be understood because, in the $U/t \rightarrow 0$ limit, the electron interaction is completely removed from the Hamiltonian and self-consistency is lost. Only the symmetric non-interacting tight-binding Hamiltonian remains which, for $n = 2$, can have only four stationary states. Since symmetry breaking is induced by self-consistency in the effective Fock Hamiltonian, the remaining stationary states must share the symmetry of the kinetic operator. The stationary states in this limit therefore correspond to the symmetry-pure RHF ground and excited state, and the symmetry-pure UHF state with two-fold degeneracy.

In contrast, the h-UHF states still break spatial symmetry when they possess complex orbital coefficients. As a result, they *cannot* be stationary states of the non-interacting Hamiltonian. In fact, as $\theta \rightarrow \pm i\infty$, the h-UHF orbital coefficients become ‘points-at-infinity’ [see Section 4.2.2], representing the quasi-null vectors¹⁵⁴ with non-normalisable orbital coefficients described in Section 3.3.2.1. When the orbital coefficients reach these unphysical quasi-null vectors, the Fock operator becomes ill-defined and a singularity appears in the energy. The existence of these quasi-null vectors with singular energies is the mathematical manifestation of ‘removing’ the unphysical states in the tight-binding limit. Furthermore, the behaviour of approximate HF states as the self-consistency is removed may indicate which HF solutions correspond to ‘physical’ states and which are ‘unphysical’ artefacts of self-consistency.

Similar singularities in the energy occur in a wide-range of self-consistent theories beyond the HF approximation, particularly those that exploit the non-linear self-consistent Dyson equation.^{248,249} In each case, the singularities are associated with a complete loss of self-consistency in the equations and are often used to identify which states should be regarded as ‘unphysical’. It is likely that the mathematical physics behind singularities in the self-consistent Dyson equation is a manifestation of the same effect observed for the complex Hubbard model investigated here.

Finally, visualising the occurrence of h-UHF quasi-null vectors can be achieved using the phase-rigidity Ξ , defined for an orbital ϕ as the ratio between the Hermitian and

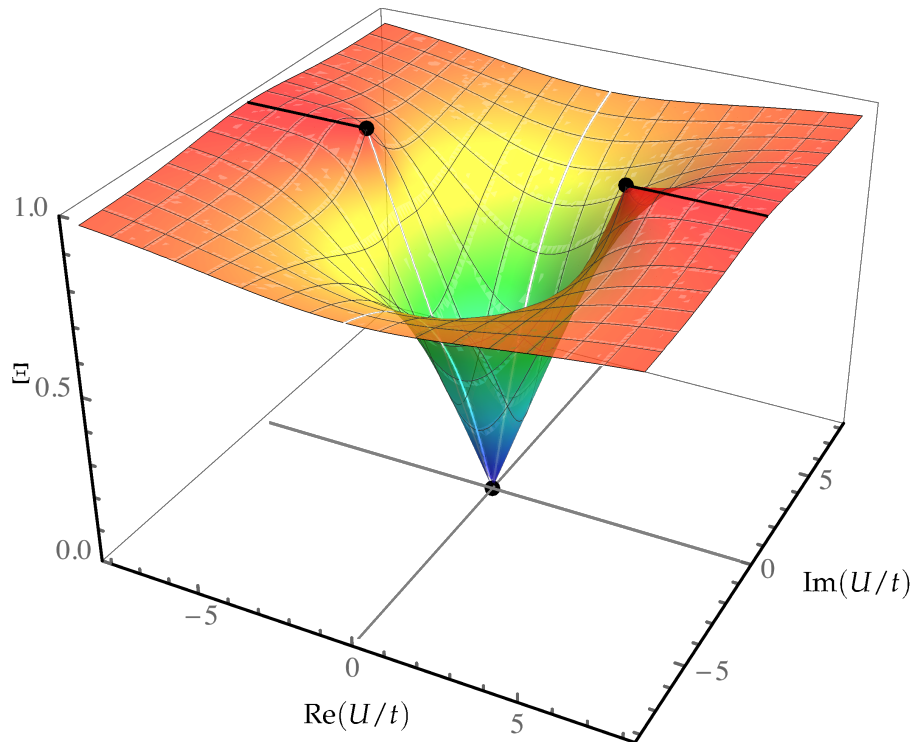


Figure 6.4: Phase rigidity (6.8) of the h-UHF states for complex U/t . Towards the strongly correlated regimes beyond the Coulson–Fischer point (black dots), the h-UHF states for real U/t have real coefficients (black lines) and $\Xi = 1$. Approaching the singularity at the tight-binding limit ($U/t = 0$), the phase rigidity tends to zero and the orbital coefficients become quasi-null, tending to a point-at-infinity.

complex-symmetric inner-product as²⁵⁰

$$\Xi = \frac{\langle \phi^* | \phi \rangle}{\langle \phi | \phi \rangle}. \quad (6.8)$$

For real orbital coefficients, $\Xi = 1$ (solid black line in Fig. 6.4), while when the orbital coefficients become complex, Ξ becomes smaller and eventually vanishes at a point-at-infinity, as shown for the h-UHF states in Fig. 6.4. Quasi-null vectors are also found at exceptional points for linear non-Hermitian Hamiltonians, where the phenomenon is referred to as ‘self-orthogonality’.¹⁶⁸ In contrast, quasi-null vectors are not observed at the conventional Coulson–Fischer point ($U = 4t$) since the presence of self-consistency means that orthogonality is not required between the multiple solutions when they coalesce (black dots in Fig. 6.4). In this sense, the singularity at $U/t = 0$ behaves more like a conventional exceptional point than the Coulson–Fischer point at $U = 4t$. There appear to be few (if any) previously reported cases of exceptional points without self-orthogonality, and so the Coulson–Fischer point at $U = 4t$ represents an important case-study of a potential new class of non-Hermitian degeneracies.

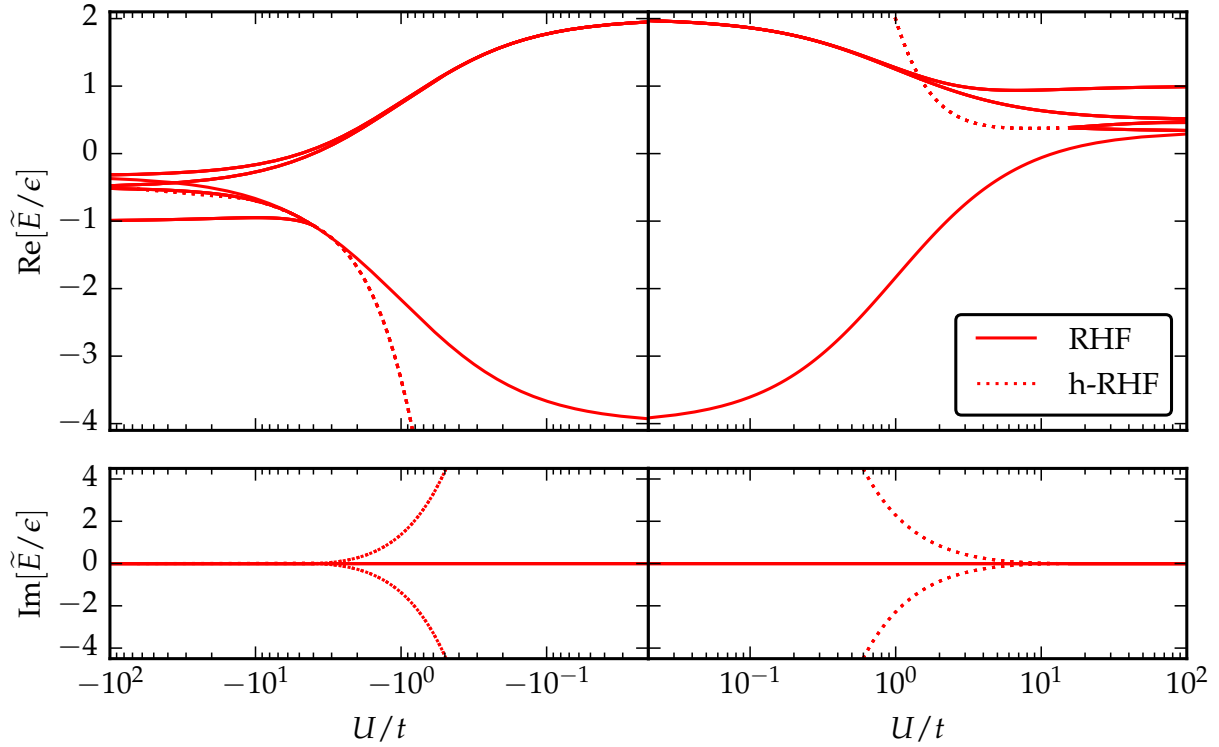


Figure 6.5: Holomorphic energies of the 13 h-RHF stationary states in the two-electron periodic Hubbard trimer using the parametrisation (6.10). Each state corresponds to a real RHF solutions in the $U/t \rightarrow \pm\infty$ limit, with degeneracies in order of ascending $\text{Re}[\tilde{E}/\epsilon]$ of one, three, three, three and three for the repulsive regime.

6.2.4 Hubbard Trimer

To demonstrate that the correspondence between Coulson–Fischer points, exceptional points, and singularities in the tight-binding limit extends beyond the analytically solvable Hubbard dimer, consider the h-HF stationary states of the two-electron periodic Hubbard trimer. For clarity, only the closed-shell h-RHF solutions are considered, for which a total of 13 stationary states exist according to Eq. (4.29). With one occupied and two virtual spatial orbitals, the h-RHF orbital coefficients can be parametrised in terms of two complex orbital rotation angles $\theta_1, \theta_2 \in \mathbb{C}$ using the exponential form of a complex-orthogonal matrix¹⁵⁵

$$\begin{pmatrix} \mathbf{C}_{\text{occ}} & \mathbf{C}_{\text{vir}} \end{pmatrix} = \exp \begin{pmatrix} 0 & -\theta_1 & -\theta_2 \\ \theta_1 & 0 & 0 \\ \theta_2 & 0 & 0 \end{pmatrix}. \quad (6.9)$$

These rotation angles provide a local coordinate system that uniquely defines a h-RHF determinant.

Covering the full range of U/t values can be achieved using the parametrisation

$$(t, U) = (1 - |\epsilon|, \epsilon) \quad \text{for } \epsilon \in [-1, 1], \quad (6.10)$$

$$U/t = (U/t)_{\text{CFP}} + \exp(i\phi)$$

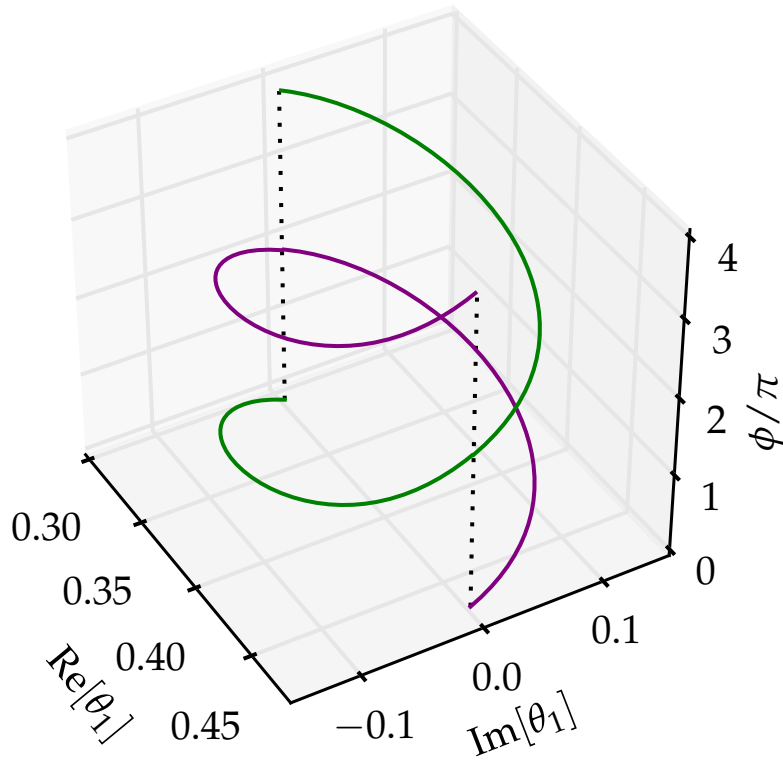


Figure 6.6: Stationary θ_1 values corresponding to the pair of h-RHF states that coalesce in the two-electron periodic Hubbard trimer at $(U/t)_{\text{CFP}} \approx 13.3$ plotted along the path $U/t = (U/t)_{\text{CFP}} + \exp(i\phi)$ around the Coulson–Fischer point. A single rotation interconverts the solutions while a second rotation restores each solutions to their original states, demonstrating the equivalence between general Coulson–Fischer points and non-Hermitian exceptional points.

yielding a total of 13 h-RHF solutions for all non-zero U/t values as shown in Fig. 6.5. In the strongly correlated repulsive and attractive limits ($U/t \rightarrow \pm\infty$), every h-RHF state corresponds to a real RHF stationary state with degeneracies of one, three, three, three and three in ascending order of energy. As the strength of the correlation is reduced in the repulsive regime, the second and third lowest energy states coalesce at a pair annihilation Coulson–Fischer point at $(U/t)_{\text{CFP}} \approx 13.3$. Meanwhile their h-RHF counterparts continue with complex orbital coefficients and energies. Note that there are three symmetry-related copies of this Coulson–Fischer point and, at each point, only two states coalesce.

The equivalence of this Coulson–Fischer point and a non-Hermitian exceptional point can be demonstrated by following a path around the coalescence point in the complex U/t plane, as demonstrated for two coalescing states in Fig. 6.6. After the first rotation, the two states that coalesce at the Coulson–Fischer point are interconverted, while the second rotation restores both solutions to their original state. Note that, contrary to the Coulson–Fischer point in the Hubbard dimer, the two states that are

interconverted in this example are neither related by symmetry nor as excitations of each other. In fact, the relationship between the Coulson–Fischer point and an exceptional point is the only way that these two states can be meaningfully associated.

Continuing towards the tight-binding limit $U/t \rightarrow 0$, the complex-valued h-RHF states tend towards singularities analogous to the two-site Hubbard dimer. However, although only three real RHF can exist when self-consistency is lost with three basis functions, there appears to be seven real RHF states (unique ground state and two three-fold degenerate excited states) tending towards this limit. In fact, the loss of self-consistency at $U/t = 0$, combined with a two-dimensional degenerate subspace in the basis functions, leads to a one-dimensional line of RHF stationary points in the tight-binding limit along which the degenerate basis functions can be arbitrarily mixed. The two sets of three-fold degenerate excited RHF states both reach this line of stationary points as $U/t \rightarrow 0$ rather than tending towards quasi-null vectors, and therefore they still correspond to physically allowed solutions. If the degeneracy of these basis functions is lifted, for example in a non-periodic lattice, then these h-RHF states do indeed become complex-valued and tend to quasi-null singularities.

6.3 Complex Adiabatic Connection

Among the most surprising consequences of representing h-UHF states using a Riemann surface — and the subject for the remainder of this chapter — lies in the observation that the h-UHF state is a *ground state* for the repulsive regime ($U/t > 0$) but becomes an *excited state* in the attractive regime. Therefore, by slowly varying U/t in a suitable manner, a ground-state wave function can be naturally “morphed” into an excited-state wave function along a parametrised pathway of stationary states. Clearly, any such pathway from the repulsive to the attractive regime must avoid the singularity at $U/t = 0$. However, the continuous structure of the Riemann surface enables such a pathway to be built *around* the singularity in the complex plane.³ By allowing complex orbitals and energies, the orderability of states is lost, and the ground and excited states can be readily interchanged along a stationary pathway in the complex plane.

Defining effective methods that reliably provide accurate excited-energies remains a major challenge in theoretical chemistry. Among the most popular approaches include the time-dependent version of density-functional theory^{85,251,252} (TD-DFT), which relies on the linear response formalism, and the equation-of-motion *ansatz* of coupled cluster approach^{253,254} (EOM-CC), where the similarity transformed Hamiltonian (usually truncated) is diagonalised. However, both cases are restricted to only single excitations, and the quality of the computed excited-state energies relies heavily on the similarity

between the single reference ground state and the excited state wave function. As a result, excited states with diffuse wave functions,^{255,256} double excitations,^{257,258} or with charge transfer²⁵⁹ are notoriously difficult to compute using TD-DFT or EOM-CC.

In contrast, direct approximations to excited states that do not rely on the nature of the ground state description are growing in popularity, particularly in the context of the HF,^{20,26,27,29} CASSCF,⁹⁶ and CC^{23,260} approaches. However, identifying and converging direct excited-state approximations often proves difficult as variational collapse onto the ground state must be avoided.^{29,96} Naturally connecting approximate ground and excited states *via* the complex plane — as has been demonstrated using the h-HF approximations — provides a promising alternative for directly identifying excited state energies and wave functions.

In what follows, the Riemann surface perspective of h-HF states in the Hubbard model is extended to molecular Hamiltonians by introducing a complex adiabatic connection where the electron-electron interaction is scaled by a complex value. Using the hydrogen dimer as a proof-of-principle example, it is shown how a ground HF state can be naturally evolved into an excited HF state by following a suitable path in the complex electron-electron plane.

6.3.1 Extension to Molecular Hamiltonians

To generalise the h-HF Riemann surface description beyond the Hubbard model to molecular Hamiltonians, the crucial observation is that the U/t ratio simply rescales the relative contribution of the two-electron component in the Hamiltonian. This relative contribution of the one- and two-electron components is known to induce symmetry-breaking in HF theory and the emergence of multiple solutions to the real HF equations. For molecular Hamiltonians, the equivalent analytic continuation therefore involves introducing an adiabatic scaling parameter λ that explicitly controls the strength of the electron-electron interaction. The λ -scaled Hamiltonian is then given by

$$\hat{H}_\lambda = V_N + \sum_i^N \hat{h}(i) + \lambda \sum_{i<j}^N \frac{1}{r_{ij}}, \quad (6.11)$$

where $\lambda = 0$ for the non-interacting system and $\lambda = 1$ for the physical (i.e. interacting) system.

Optimal h-HF states in molecular systems can now be connected as a continuous Riemann surface in the same manner as the Hubbard dimer, as shown for H_2 in Fig. 6.7. Crucially, by smoothly varying λ through the complex plane, an approximate molecular ground-state can be smoothly transformed into an excited-state wave function in exactly same manner as the Hubbard model. Such a pathway resembles an adiabatic connection

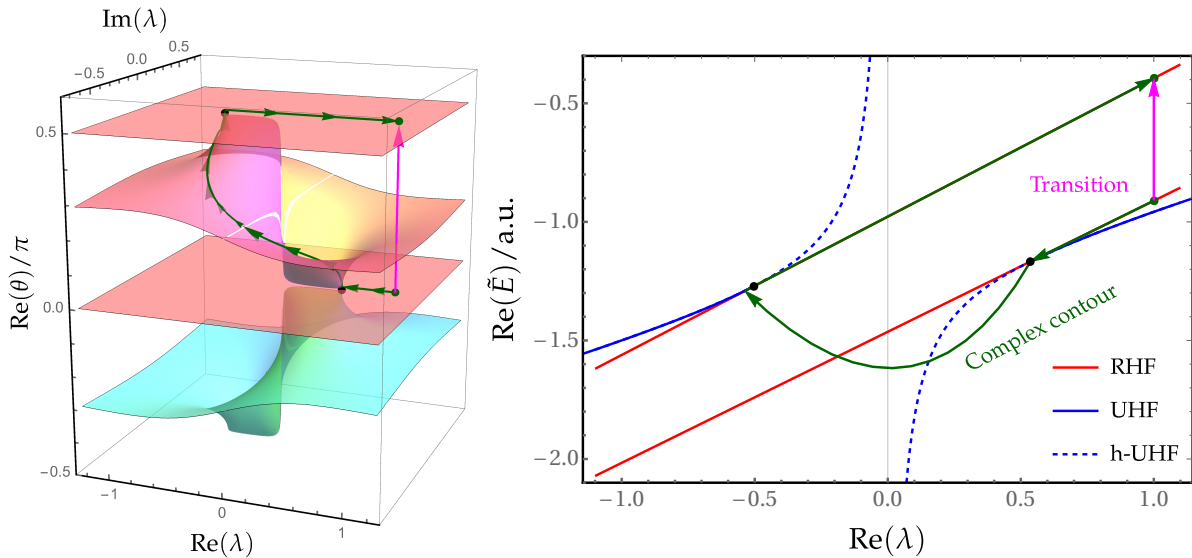


Figure 6.7: An example of a complex adiabatic connection pathway (green) in H_2 enabling the physical transition $\sigma_g^2 \rightarrow \sigma_u^2$ (at $\lambda = 1$) to be obtained. A minimal (STO-3G) basis is used and the bond length is fixed at 1.5 \AA . The real component of θ along the contour (left) illustrates the connecting pathway between the ground and excited state, while the h-HF energy along this contour (right) demonstrates the resulting physical transition.

in DFT^{261,262} although, in contrast to DFT, the molecular wave function is relaxed for each λ along this ‘complex adiabatic connection’. As a result, the h-HF density remains a stationary state at all points along this connecting pathway.

6.3.2 Hydrogen Dimer

To demonstrate the complex adiabatic connection, consider the H_2 model as a direct molecular counterpart to the Hubbard dimer. Using the minimal (STO-3G) basis, the h-UHF orbitals are again parametrised in terms of the orthogonal σ_g and σ_u molecular orbital basis by a single rotation angle θ as

$$\phi_\alpha(\mathbf{r}) = \sigma_g(\mathbf{r}) \cos \theta + \sigma_u(\mathbf{r}) \sin \theta \quad (6.12a)$$

$$\phi_\beta(\mathbf{r}) = \sigma_g(\mathbf{r}) \cos \theta - \sigma_u(\mathbf{r}) \sin \theta. \quad (6.12b)$$

For a given molecular bond length, the optimal h-UHF states under parametrisation (6.12) emerge as a Riemann surface for complex values of the electron-electron scaling λ , illustrated for a bond length of 1.5 \AA in Fig. 6.7 (left panel). The structure of this Riemann surface is directly equivalent to the Hubbard dimer, although the implicit dependence on the one- and two-electron integrals in H_2 makes constructing an analytic form difficult.

One possible complex adiabatic pathway in H_2 that allows the $\sigma_g^2 \rightarrow \sigma_u^2$ physical transition (at $\lambda = 1$) to be obtained along a stationary pathway of h-HF states is

demonstrated in Fig. 6.7 (green curve). Note that the molecular geometry, and one- and two-electron integrals are fixed for all values of λ . Starting on the RHF ground-state wave function at $\lambda = 1$, the scaling parameter λ is decreased to reach the Coulson–Fischer point in the repulsive regime ($\lambda > 0$) at $\lambda \approx 1/2$. At this point, the optimised state can continuously and smoothly transfer onto the h-UHF branch of solutions. The h-UHF can then be followed along the complex contour shown in Fig. 6.7 (left panel), avoiding the singularity at $\lambda = 0$ and the branch cuts running along the real axis. In doing so, the h-UHF state evolves into an excited (real) h-UHF state in the attractive regime ($\lambda < 0$). By increasing λ again, the pathway then reaches the attractive Coulson–Fischer point at $\lambda \approx -1/2$, where one can transfer continuously and smoothly from the h-UHF state to the excited σ_u^2 RHF state. From here, adiabatically following the σ_u^2 RHF state up to $\lambda = 1$ completes the complex adiabatic connection path.

Although the physical transition in the hydrogen dimer provides only a proof-of-principle demonstration of a complex adiabatic connection approach, this new perspective on excited states has the potential to revolutionise how excited-state wave functions are located. By choosing the appropriate complex-scaled parameter, the Riemann surface framework can in principle be extended to any method with multiple solutions, including linear approaches such as CI expansions.

6.4 Concluding Remarks

The behaviour of electronic states for complex non-Hermitian Hamiltonians is only starting to be understood, and this chapter presents a first study in the context of the HF approach. Here, the topology of h-HF stationary states has been explored when the electron-electron interaction is itself analytically-continued into the complex plane. For this inherently non-Hermitian Hamiltonian, it has been shown that discrete h-HF states can be connected as a single, continuous Riemann surface across the complex plane. On this Riemann surface, each h-HF state is represented by an individual sheet, and the Coulson–Fischer points represent exceptional points where multiple sheets intersect.

From the h-HF perspective, there are two key implications from the Riemann surface framework. Firstly, the Coulson–Fischer points are revealed as isolated points on the real axis which, by following a symmetry-broken state around such a point, allow two discrete h-HF states to be interconverted. This isolation of Coulson–Fischer points will play an important role in routinely following h-HF states past the Coulson–Fischer point in Chapter 7. Secondly, the point where self-consistency is completely lost can be shown to correspond to a singularity in the h-HF energy where ‘unphysical’ states become quasi-null. This singularity accounts for the fact that the number of HF states

can be larger than the size of the Hilbert space, and provides an indicator for *which* states correspond to FCI solutions.

Finally, the most surprising feature of the h-HF Riemann surface arises from the observation that a ground HF wave function can be naturally evolved into an excited state wave function by following a suitable pathway in the complex plane. The construction of this ‘complex adiabatic connection’ exploits the fact that ground states in the repulsive regime can be connected to excited states in the attractive regime and, when the energies become complex, the orderability of ground and excited states is lost. Albeit simple, a connection of this type has been demonstrated in the hydrogen dimer to construct the $\sigma_g^2 \rightarrow \sigma_u^2$ transition. Directly connecting ground and excited states through the complex plane in this way has the potential to revolutionise excited state methods, and allow more accurate approximations to wave functions representing double (and higher) excitations.

6.4.1 Scope for Future Development

The use of non-Hermitian Hamiltonians for computing excited state wave functions in electronic structure theory is in its infancy, and many insightful properties remain to be found and understood. For example, this non-Hermitian framework can in principle be extended to compute direct excited states in a wide range of non-linear correlated methods including CC, self-consistent Green’s function methods²⁴⁹ and DFT. In particular, the CC family of methods offers a powerful wave function approach with a range of multiple solutions^{23,177,178,260} that can almost certainly be connected as a single Riemann surface. Furthermore, the nature of singularities and unphysical solutions in self-consistent Green’s function methods^{248,249} could be better understood if the coupling of the self-consistent term were extended to the complex plane.

Alongside non-linear methods, the Riemann surface framework can also be extended to linear approaches including FCI or truncated CI. Although the FCI eigenstates are usually considered as eigenvectors of the FCI Hamiltonian, they also correspond to stationary points of the fully correlated energy function. Therefore, by analytically continuing a suitable parameter in the Hamiltonian, it is possible that ground and excited states could also be connected through the complex plane. Choosing this parameter is less obvious than scaling the self-consistent term in HF theory, although it is possible that the Riemann surface structure of FCI states could be revealed by analytically continuing the molecular structure itself, for example with a complex nuclear position or bond length.

The ability to construct a complex adiabatic connection between CI states opens the possibility of directly computing excited-state wave functions without diagonalising the

full Hamiltonian matrix. At present, solutions to the CI equations are usually obtained using iterative diagonalisation schemes, such as the Davidson algorithm,⁴⁹ and so only the lowest energy states are computationally accessible. Since all the states lower in energy than the target state must be computed simultaneously, the level of excitations that are accessible is greatly restricted. In contrast, if complex adiabatic connections between ground and excited states can be realised in practice, then excited states could be located without needing to compute a large number of intermediate-energy states. To achieve this, a low-energy wave function could be identified using an iterative scheme and then followed along a stationary pathway in the complex plane and evolved into an excited-state wave function.

If the complex adiabatic connection is to be applied as a routine method for locating excited states, then there are a number of practical aspects that must first be addressed. In particular, the topological features of exceptional points in electronic structure methods need to be better understood. For example, what controls the positions of exceptional points in the complex plane? Is every state connected? And how do these exceptional points evolve from approximate to exact methods? Furthermore, computational methods for locating exceptional points need to be developed since these points provide the crucial pathways for connecting ground and excited states. Recent research on locating non-Hermitian degeneracies for metastable resonances provides a promising route in this direction.²⁴²

Finally, introducing Riemann surfaces in electronic structure methods has potential implications beyond identifying excited-state wave functions. In perturbation theory, for example, if a Riemann surface expresses the eigenvalues of the perturbed Hamiltonian

$$\hat{H}_\lambda = \hat{H}_0 + \lambda \hat{V}, \quad (6.13)$$

then the location of exceptional points in the complex λ -plane controls the radius of convergence of the perturbation expansion.^{11,59} Investigating the topology of this type of Riemann surface may therefore provide a new approach to understand the slow convergence of the Møller–Plesset series with particular reference wave functions⁵⁷ or the difference between alternative partitionings of the Hamiltonian.

Overall, by introducing the complex adiabatic connection and Riemann surface frameworks in the HF approximation, this chapter has presented an entirely new perspective on ground and excited states in electronic structure theory, with the potential to revolutionise methods for computing excited states.

Part III

Recapitulation

Chapter 7

General Approach for Multireference Molecules

The work in this chapter has contributed to the publication Ref. (4)

Summary

Combining symmetry-broken HF states in NOCI has been proposed as an effective multireference alternative to the CASSCF approach. Until now, the construction of potential energy surfaces using NOCI has been limited by the disappearance of HF states as the molecular geometry changes. The development of holomorphic Hartree–Fock theory in Part II now allows NOCI to be generalised across all molecular structures. In this chapter, a general NOCI protocol is derived for locating chemically relevant HF states and extending them as h-HF states across all geometries. This protocol captures static correlation to a similar accuracy as CASSCF, while avoiding the simultaneous optimisation of the SCF and CI components of the multireference wave function.

7.1 Context and Scope

A balanced treatment of ground and excited states is essential for the description of a wide range of physical processes, including singlet fission,^{263–265} electron transfer,³³ and primary mechanisms of vision.^{29,266,267} When the exact FCI wave function contains one dominant electronic configuration, single-reference correlation methods such as truncated CI, CC and MP2 approaches can provide accurate ground states.^{11,60} Similarly, excited states can be predicted using single-reference techniques such as CIS⁸⁸ and EOM-CC,^{268,269} although the latter is usually limited to only single and double excitations (EOM-CCSD) by the prohibitive cost of including full triple excitations.⁹⁵ However, when the exact wave function has many dominant configurations in the presence of strong static correlation, the range of available ground- and excited-states methods remains more limited.

Multiconfigurational SCF¹¹ (MCSCF) methods provide the prevailing family of multireference techniques, with CASSCF being the most widely used approach for both ground and excited states.¹⁹ Preventing variational collapse when computing multiple excited states requires a state-averaged formalism (sa-CASSCF), where the weighted energy of states is optimised rather than using a single target state.⁹⁷ However, in MCSCF methods, both the orbital and CI coefficients must be optimised simultaneously. This optimisation can suffer from redundant parameters or convergence issues, and often requires sophisticated second-order minimisation procedures.^{67,68} Furthermore, identifying a suitable set of active orbitals to define the CAS space is difficult to automate and requires a significant amount of expertise.⁷⁰ Finally, CASSCF ultimately scales exponentially with the active space size and remains a challenge for larger systems, despite recent advances using stochastic²⁷⁰ and selected CI⁵³ approaches. Alternative multireference methods are therefore needed to avoid the computational challenges of MCSCF wave functions.

Alongside conventional multireference methods, recent research has focused on building multiconfigurational wave functions by combining multiple HF solutions in NOCI expansions, as described in Section 2.3.^{25,31–34,134} In NOCI, the wave function is constructed as a linear combination of multiple HF states corresponding to the dominant configurations in a molecule.²⁵ Since each determinant is constructed from a bespoke set of orbitals — each optimised individually at the SCF level — NOCI can provide a more balanced treatment of ground and excited states, leading to its application for multi-electron excitations,³¹ core excitations,^{34,35} and charge transfer processes.³³ Furthermore, including symmetry-broken HF solutions representing dominant electron configurations can produce potential energy surfaces for multireference molecules and

provide chemical insight through the diabatic nature of HF states.^{20,25,33}

Previously, applying NOCI using symmetry-broken HF states over a range of molecular geometries has been limited by the disappearance of HF solutions at Coulson–Fischer points,²⁴ leading to unphysical kinks or discontinuities in the NOCI energy.²⁵ However, the development of h-HF theory in Part II now enables analytic continuations of real HF solutions to be constructed for all molecular geometries. The stationary points of the h-HF energy therefore exist across the full potential energy surface and extend with complex orbital coefficients beyond the points where their real counterparts vanish. Furthermore, complex h-HF wave functions are found to smoothly evolve from real HF wave functions. As a result, h-HF stationary states now provide a continuous basis for NOCI calculations with the potential to yield smooth potential energy surfaces across all geometries.

In the current chapter, h-HF theory and NOCI are combined to derive a general approach for constructing smooth and continuous energies across all geometries. First, the modifications of the NOCI approach required to exploit a basis of h-HF states are described. An approach is then developed that easily allows h-HF states to be followed past the Coulson–Fischer point and into the complex orbital coefficient plane. Furthermore, it is shown how a suitable subset of chemically relevant HF states can be identified by applying SCF metadynamics²⁰ in an active orbital space. The combined h-HF and NOCI approach is then applied to the dissociation of F₂, the torsional barrier of ethene, and the pseudo-Jahn–Teller distortion of cyclobutadiene. In each case, NOCI produces qualitatively correct potential energy surfaces free from unphysical cusps or discontinuities while avoiding the challenging optimisation of the MCSCF wave function.

7.2 Theoretical Development

7.2.1 NOCI using h-HF States

Generalising NOCI to handle a basis set comprising h-HF states requires minimal modifications to the computational algorithm. Following Section 2.3.1, the NOCI wave function is constructed as a linear combination of n_{det} mutually non-orthogonal basis states $\{|^x\Psi\rangle\}$ as

$$|\Psi_{\text{NOCI}}\rangle = \sum_x^{n_{\text{det}}} |^x\Psi\rangle c_x. \quad (7.1)$$

Each state $|^x\Psi\rangle$ corresponds to a single Slater determinant constructed from a bespoke set of N occupied molecular orbitals (MOs), $\{|^x\psi_i\rangle\}$, which themselves are formed from

a linear combination of $2n$ (non-orthogonal) atomic spin orbitals (AOs), $\{|\eta_\mu\rangle\}$, as

$$|^x\psi_i\rangle = \sum_{\mu}^n C_{\cdot i}^{\mu\cdot} |^x\eta_\mu\rangle, \quad (7.2)$$

where n is the size of the spatial basis set. These Slater determinants may represent either a real HF solution or a complex h-HF stationary point. The NOCI eigenstates are identified by solving the generalised eigenvalue problem

$$\sum_x^{n_{\text{det}}} (H^{wx} - ES^{wx}) c_x = 0. \quad (7.3)$$

Here $H^{wx} = \langle {}^w\Psi | \hat{H} |^x\Psi \rangle$ and $S^{wx} = \langle {}^w\Psi | ^x\Psi \rangle$ are the Hamiltonian and overlap matrix elements in the non-orthogonal basis and can be evaluated using the approach outlined in Appendix C.

Note that the matrix elements in Eq. (7.3) are always computed using the conventional (Hermitian) inner product. The NOCI energy is therefore always variational, even though the constituent h-HF states may not be. Although the optimised h-HF orbitals are not stationary with respect to the conventional Hermitian HF equations, and do not satisfy Brillouin's theorem,⁸ the application of the generalised Slater–Condon rules for computing matrix elements remains the same. Furthermore, the nonorthonormality of individual h-HF wave functions with respect to the Hermitian inner product is accounted for by the overlap matrix in the generalised eigenvalue equation (7.3). As a result, the only required alteration is the use of complex-valued codensity matrices [see Appendix C] constructed from the h-HF orbital coefficients to compute the Hamiltonian and overlap matrix elements.

7.2.2 Moving Past the Coulson–Fischer Point

The h-HF approach allows real HF states to be analytically continued across all molecular structures. However, identifying the correct complex orbital rotation beyond the Coulson–Fischer point becomes challenging when the number of electrons or basis functions grows. Following h-HF states past the Coulson–Fischer point is particularly difficult for the (real-valued) molecular Hamiltonian since the h-HF energy is symmetric about the real MO coefficient axis. As a result, if an SCF calculation starts from a real guess (for example a real HF solution from a previous geometry), it will show no preference towards any particular complex direction. Furthermore, the coalescence of symmetry-broken HF states often coincides *exactly* with a real symmetry-pure solution at a cusp catastrophe, as discussed in Section 4.4. Consequently, attempts to computationally trace real HF states onto their complex h-HF counterparts often become stuck on a real symmetry-pure HF state instead.

Routinely connecting real-valued HF states and their complex-valued h-HF counterparts is vital for developing a practical NOCI approach using h-HF states. Any method to achieve this must be computationally efficient, ideally incurring no increase in scaling beyond the mean-field $\mathcal{O}(n^4)$ scaling, and must perform reliably for *any* type of Coulson–Fischer point described in Chapter 4. Furthermore, this method should have the potential to be automated without user input, and should require no prior information about the location of any Coulson–Fischer points.

The complex adiabatic connection described in Section 6.3 presents one solution for this problem. By scaling the electron–electron interaction using the complex parameter λ , i.e. creating the perturbed molecular Hamiltonian

$$\hat{H}_\lambda = V_N + \sum_i^N \hat{h}(i) + \lambda \sum_{i < j}^N \frac{1}{r_{ij}}, \quad (7.4)$$

multiple h-HF states emerge as a continuous interconnected manifold in the complex λ -plane with each state represented by an individual sheet of a Riemann surface.³ On this complex manifold, Coulson–Fischer points exist as *isolated* exceptional points along the real λ -axis. Crucially, Coulson–Fischer points can therefore be avoided by simply moving *around* these exceptional points in the complex λ -plane. Stationary h-HF states can then be identified across all molecular structures using a complex-perturbed λ , before being relaxed to the physical case $\lambda = 1$ and combined in a NOCI expansion.

Since the holomorphic SCF optimisation procedure is unchanged for complex λ , this approach retains mean-field scaling and the cost only increases due to the need for additional SCF optimisations at different λ -values. Furthermore, once the HF states at the initial structure have been identified, and the structures of interest have been defined, this approach requires *no further input from the user* or prior knowledge about the location of any Coulson–Fischer points.

To illustrate this idea, consider the symmetry-broken (h-)UHF solutions of H_2 in a minimal basis set (STO-3G) using two spatial orbitals $\phi_\alpha(\mathbf{r})$ and $\phi_\beta(\mathbf{r})$ parameterised by the complex angle θ ,

$$\phi_\alpha(\mathbf{r}) = \sigma_g(\mathbf{r}) \cos \theta + \sigma_u(\mathbf{r}) \sin \theta, \quad (7.5a)$$

$$\phi_\beta(\mathbf{r}) = \sigma_g(\mathbf{r}) \cos \theta - \sigma_u(\mathbf{r}) \sin \theta. \quad (7.5b)$$

Stationary points correspond to the critical values θ_c [see Fig. 7.1]. In the unperturbed case ($\lambda = 1$), the RHF σ_g^2 state (red solid line) and doubly degenerate (h-)UHF states (blue solid line) coalesce at the Coulson–Fischer point (black dot) on the real λ -axis. At shorter bond lengths, the real RHF state remains a stationary point on the real axis while the h-UHF states extend into the complex- θ plane.

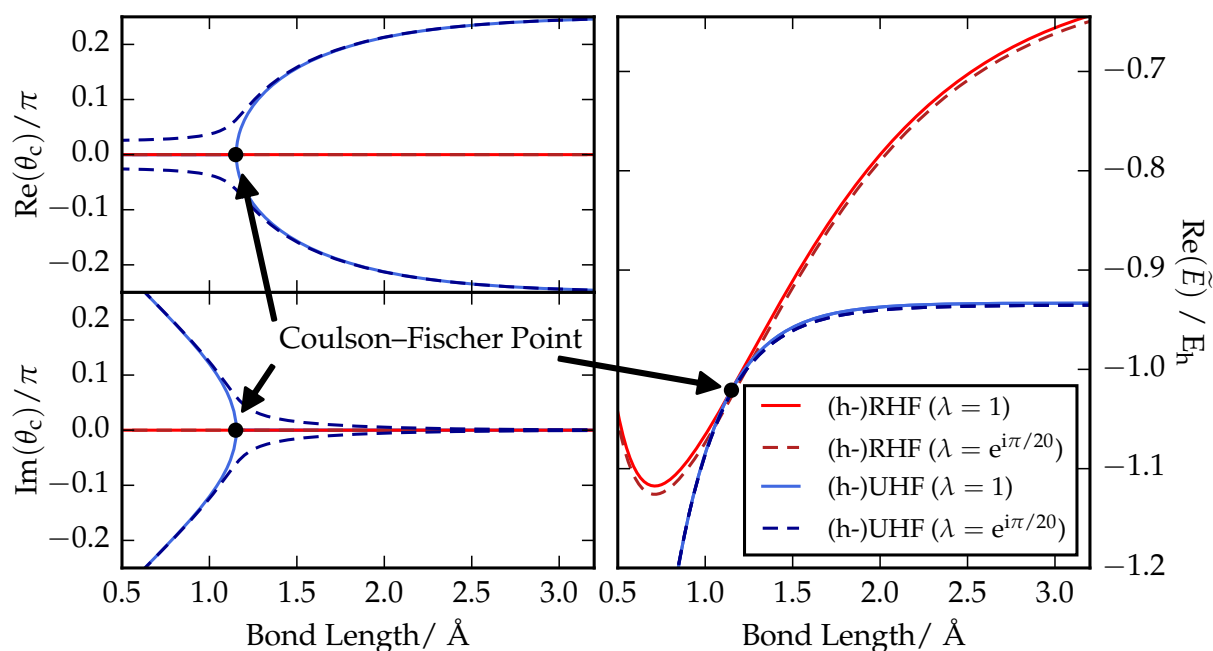


Figure 7.1: The stationary values θ_c (left) for the RHF (red) and h-UHF (blue) states in the unperturbed $\lambda = 1$ (solid) and perturbed $\lambda = e^{i\pi/20}$ (dashed) cases. In the unperturbed case, the three states coalesce simultaneously at the Coulson–Fischer point (black dot), while in the perturbed case the h-UHF solution can be followed smoothly into the complex plane. The h-HF energy (right) is only slightly affected by the perturbation.

To move smoothly from the real symmetry-broken UHF branch, past the Coulson–Fischer point and onto the complex h-UHF branch, the real solutions are first perturbed by taking $\lambda = e^{i\pi/20}$ (dashed lines). Although the critical value θ_c for the RHF state (fixed spatial symmetry) remains unchanged, the corresponding θ_c values for the (h-)UHF state become complex-valued even for long bond lengths. These stationary points now smoothly connect the real symmetry-broken UHF states and the complex h-UHF states *without ever* passing through the Coulson–Fischer point. Relaxing the perturbed stationary points at each bond length back to the physical value $\lambda = 1$ then yields the unperturbed states required for NOCI.

7.2.3 Locating Relevant Hartree–Fock States

With the ability to follow h-HF states across all molecular structures and use them in a NOCI expansion, the final challenge is identifying a manageable subset of relevant HF solutions. Selecting a relevant set of determinants for NOCI is less trivial than in orthogonal CI since the lack of a universal set of MOs removes the concept of excitation levels (i.e. singles, doubles). Furthermore, to capture symmetry-broken determinants, methods must ideally search for stationary states on the HF energy landscape without relying on orbital excitations or a particular set of reference orbitals.

SCF metadynamics provides an effectively black-box approach for locating multiple stationary points.²⁰ Starting from an optimised solution, SCF metadynamics generates new initial guess determinants by randomly mixing occupied and virtual MOs. These determinants are then optimised in the presence of a biasing potential to prevent re-convergence onto a previously known stationary point. However, as shown in Chapter 4, the total number of HF states grows rapidly with the size of the system, often exceeding the dimensions of the full Hilbert space. Furthermore, the solutions identified by SCF metadynamics often include very high-energy determinants with little contribution to the NOCI wave functions. Identifying a suitable set of relevant determinants is therefore both critically important, and surprisingly challenging.

In many cases, a dominant subset of “active” MOs can be identified that strongly influence the characteristics of the HF energy surface. The most relevant HF determinants are usually then related to different active orbital configurations, along with symmetry-broken states formed from mixing these MOs, as illustrated by the eight UHF states for the double-bond rotation of ethene in Section 4.4.4. Exploiting this property, an active space SCF metadynamics approach can be defined that uses these active orbitals to identify a suitable subset of HF states.

Starting from an initial symmetry-pure reference determinant, e.g. the RHF ground state, a metadynamics calculation is run in which only the active MOs are allowed to mix, and where the SCF optimisation proceeds only in this active space — i.e. the inactive orbitals remain frozen throughout. This process leads to a set of determinants that differ only in the composition of their active MOs, but are not themselves fully optimised HF stationary points. Subsequently relaxing the inactive orbitals by optimising each determinant in the full orbital space then yields true HF solutions that form the basis for NOCI. A detailed description of this active space SCF metadynamics procedure is provided in Appendix D.

Crucially, the number of partially optimised HF states with frozen inactive orbitals is controlled by the size of the active orbital space and is generally much smaller than the number of states in the full unfrozen HF space. As a result, active space SCF metadynamics provides a manageable approach to identify a chemically relevant basis of HF states for NOCI, while also retaining the ability to locate symmetry-broken determinants. Finally, it was observed in Section 4.4 that the multiple HF states of interest usually exist as real HF states at molecular structures with strong multireference character, for example in the dissociation limit or at transition states. Since the active space SCF metadynamics approach can only identify real HF stationary points, these are the structures at which relevant HF states should be located.

7.2.4 Combined Protocol

The theoretical tools developed in Sections 7.2.1–7.2.3 now allow a general protocol to be defined that combines active space SCF metadynamics, h-HF and NOCI to compute the ground and excited states of molecular systems. First, initial active space SCF metadynamics calculations are run at the geometries of particular interest (usually those with suspected multireference character) to identify a relevant subset of HF states. These real states are then perturbed away from the real orbital coefficient axis using a complex λ -scaling. The perturbed states can then be followed across all required structures and past any Coulson–Fischer points, extending onto their h-HF extensions when real solutions coalesce and vanish. Finally, the states at each geometry are relaxed back to $\lambda = 1$ and used to construct the NOCI expansion.

The full combined approach can be summarised as follows:

1. Identify real HF solutions at the geometries of interest using active space SCF metadynamics [see Appendix D];
2. Perturb states off the real axis using a complex λ scaling;
3. Trace the perturbed solutions across all geometries, identifying any corresponding complex h-HF solutions required;
4. Relax all states back to $\lambda = 1$;
5. Compute NOCI energies using the resulting basis of multiple h-HF solutions.

In principle, every stage of this combined approach can be automated, except for the initial active space SCF metadynamics calculation. However, a judicious choice of the active orbital space and initial molecular structures is critically important since this will control which HF solutions can be located, in turn influencing the states that can be computed by NOCI. For example, in a diatomic molecule, HF states that are symmetry-broken in the π -symmetry will only be identified if multiple π -orbitals are included in the active space. It is possible that recent developments in locating symmetry-broken SCF solutions^{271,272} or automatically selecting active orbital spaces⁷⁰ may provide routes to remove this element of user input.

7.2.5 Algorithm Implementation

The computational components of the combined approach, including active space SCF metadynamics, h-HF and NOCI, are implemented in a new dedicated LIBNOCI library available in Q-CHEM 5.2.¹⁸⁶ Additional processing in NUMPY¹⁸⁵ is used to manage the process of following states across different molecular structures and complex λ scaling.

First, the lowest energy symmetric RHF state is identified at initial geometries believed to possess multireference character. For diatomics, these geometries lie towards the dissociation limit, while geometries of high symmetry or transition state structures are used for larger molecules. From these ground-state RHF orbitals, an active orbital space is chosen to include the states that intuitively account for the multireference character. Active space SCF metadynamics is then run to identify the low-energy HF states that appear to have the most chemical relevance.

When following states across all molecular structures, a complex value of $\lambda = \exp(i\frac{\pi}{20})$ is usually sufficient to safely navigate past the Coulson–Fischer point. At each structure and complex scaling, h-HF states are optimised using the holomorphic SCF procedure with DIIS extrapolation [see Chapter 3]. A complex-orthogonal variant of the initial maximum overlap method — where orbitals on each iteration are populated according to their overlap with the initial guess orbitals — is found to provide the most stable approach for following particular stationary states across multiple geometries.

Once h-HF solutions are identified across all structures at $\lambda = \exp(i\frac{\pi}{20})$, the states are relaxed to the physical case $\lambda = 1$ by taking the complex-perturbed states as an SCF guess for incremental λ steps. This relaxation can be performed in parallel for every molecular structure and h-HF state of interest. The final stationary h-HF states at $\lambda = 1$ are then used to build the NOCI overlap and Hamiltonian matrix, and the generalised eigenvalue problem is solved to yield the multireference NOCI wave functions. Note that any null space in the NOCI overlap matrix must be accounted for before solving this generalised eigenvalue problem. This is achieved by projecting into the non-null space spanned by the eigenvectors of the NOCI overlap matrix with eigenvalues above a certain threshold value. A null-space threshold of 10^{-6} is found to ensure numerical stability.

7.3 Results and Discussion

The combined active space SCF metadynamics, h-HF and NOCI approach is first illustrated on the hydrogen dimer. NOCI energies for a selection of archetypal molecular systems are then considered including the ground-state dissociation of F_2 , the torsional rotation of ethene, and the ground and excited states in the pseudo-Jahn–Teller distortion of cyclobutadiene. Each system exhibits a challenging electronic structure including multireference character in the ground and excited states. Finally, the performance of combining h-HF and NOCI is assessed by comparing to currently available methods including CIS, CASSCF, EOM-CC and FCI. The cc-pVDZ basis set is used throughout, and all energies are provided in atomic units of Hartrees, E_h .

7.3.1 Computational Details

All h-HF and NOCI energies, along with geometry optimisations (performed at the RHF level) and CIS excitation energies, were calculated using the LIBNOCI implementation in Q-CHEM 5.2.¹⁸⁶ Where h-HF energies become complex, only the real component is plotted. CASSCF energies were computed using the ORCA quantum chemistry package²⁷³ and CC calculations, including EOM-CC,²⁷⁴ were computed using MRCC.* Approximate benchmark comparisons for ethene and cyclobutadiene were obtained using a selected CI (sCI) method^{51,52,275,276} shown to provide near FCI accuracy for both ground and excited states.^{257,277-279} In particular, the CIPSI (CI using a perturbative selection made iteratively) algorithm^{51,275,276} implemented in QUANTUM PACKAGE 2.0²⁸⁰ was used with the frozen core approximation. Further information on sCI calculations, including detailed results, is available in Appendix E.

7.3.2 Hydrogen Dimer

To demonstrate the combined h-HF and NOCI approach, first consider the hydrogen dimer. At short bond lengths close to equilibrium, H₂ has single reference character and the correlation energy is predominantly dynamic in nature. In contrast, the $1\sigma_g$ and $1\sigma_u$ orbitals become degenerate in the dissociation limit, leading to multireference character and the breakdown of the RHF approximation. However, a symmetry-broken UHF state with diradical character emerges for large bond lengths with the correct energy in the dissociation limit.⁸ Correcting the dissociation behaviour of the ground-state requires the combination of at least the $1\sigma_g^2$ and $1\sigma_u^2$ configurations.

To identify the lowest eight HF states that correspond to the minimal basis solutions [see Section 4.4.2], an SCF metadynamics active space can be defined using the $1\sigma_g$ and $1\sigma_u$ orbitals from the RHF ground-state. In this active space, eight h-HF states can be identified which, once relaxed in the full orbital space, correspond to the symmetry-broken UHF diradical states, RHF σ_g^2 state, doubly degenerate $\sigma_g\sigma_u$ UHF states, RHF σ_u^2 state and symmetry-broken ionic RHF states (in order of increasing energy). Although the symmetry-broken UHF state dissociates to the correct energy, it suffers from spin contamination and represents a superposition of a singlet and triplet state.⁸

By perturbing these states off the real axis using $\lambda = \exp(i\frac{\pi}{20})$ and then relaxing the stationary points at each bond length to $\lambda = 1$, each HF state (and their complex

*MRCC, a quantum chemical program suite written by M. Kállay, P. R. Nagy, Z. Rolik, D. Mester, G. Samu, J. Csontos, J. Csóka, B. P. Szabó, L. Gyevi-Nagy, I. Ladjánszki, L. Szegedy, B. Ladóczki, K. Petrov, M. Farkas, P. D. Mezei, and B. Hégyely. See also Z. Rolik, L. Szegedy, I. Ladjánszki, B. Ladóczki, and M. Kállay, *J. Chem. Phys.* **139**, 094105 (2013), as well as: www.mrcc.hu

h-HF counterparts) can be identified across the full binding curve, as shown in Fig. 7.2. Combining these eight h-HF states in NOCI yields the four lowest energy states $1^1\Sigma_g^+$, $1^3\Sigma_u^-$, $1^1\Sigma_u^+$ and $2^1\Sigma_g^+$, in order of ascending energy (solid green). The lowest singlet and triplet states dissociate to the exact FCI limit (black stars) while the broken spin-symmetry of the symmetry-broken UHF state is restored. This demonstrates that NOCI is able to capture the static correlation required to correctly describe the multireference character in the dissociation limit.

In contrast, the quality of the ground-state energy deteriorates at shorter bond lengths, indicating that the NOCI expansion lacks the dynamic correlation which dominates in this region. Furthermore, although the NOCI excited $1^1\Sigma_u^+$ and $2^1\Sigma_g^+$ states correspond qualitatively to FCI, they are both variationally higher than the exact result. This offset error further indicates that this NOCI formalism struggles to capture the dynamic correlation present in these excited state wave functions.

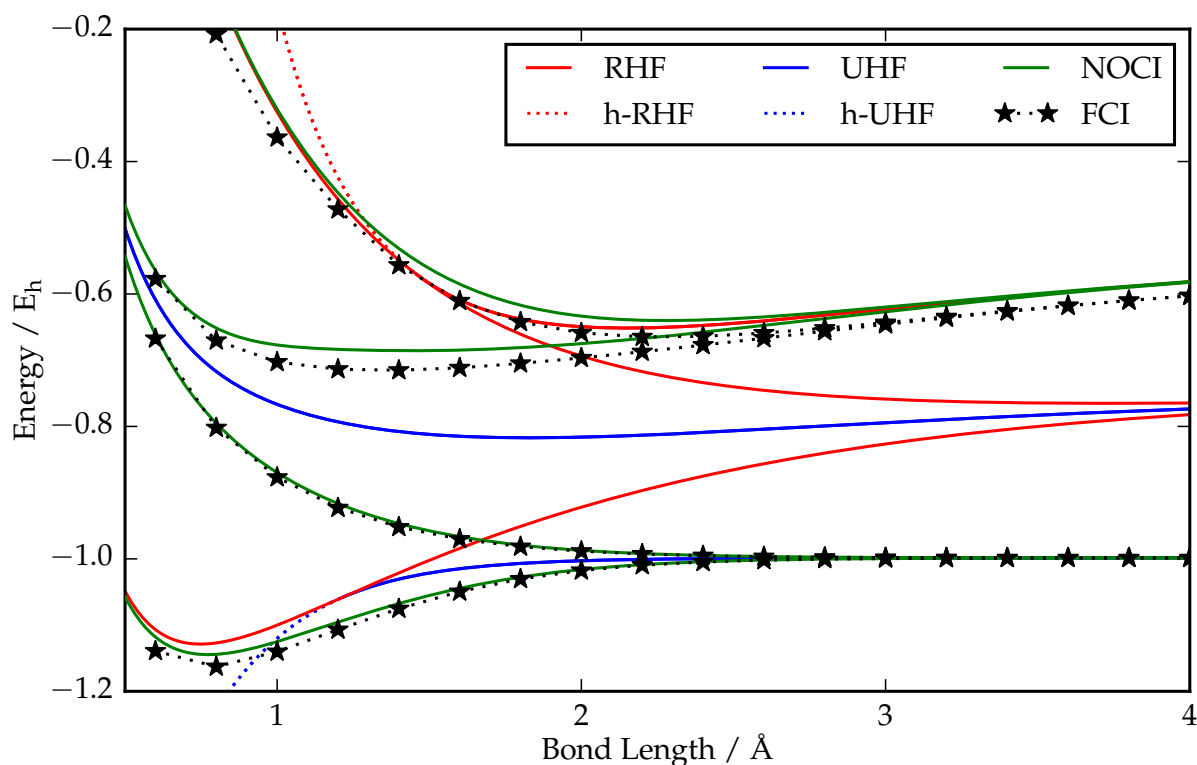


Figure 7.2: Real RHF (solid red) and UHF (solid blue) energies identified using SCF metadynamics with the (σ_g, σ_u) active space for the hydrogen dimer (cc-pVDZ). Complex h-RHF (dotted red) and h-UHF (dotted blue) states exist when real HF states coalesce. NOCI energies (solid green) using this set of HF states are compared to their exact FCI counterparts (black stars).

7.3.3 Dissociation of the Fluorine Dimer

Due to the combination of strong static and dynamic correlation effects, the ground-state binding curve for the fluorine is notoriously difficult to compute.^{17,64,103,281–284} The particularly challenging electronic structure is present even at the HF level, where RHF vastly overestimates the binding energy⁶⁴ (as found with most single bonds) and UHF predicts a completely unbound potential.^{103,284} Moreover, the RHF ground state provides a poor reference wave function at both equilibrium and dissociation geometries,²⁸² posing further difficulties for post-HF methods. For example, CCSD overbinds the molecule by almost a factor of two,⁶⁴ while the “gold standard” CCSD(T) fails completely at large bond lengths.⁶⁴ Even conventional multireference methods struggle to describe the dissociation energy correctly, with full valence CASSCF(14, 8) underestimating the potential well depth by around a factor of a half.¹⁰³ In contrast, CCSDT — known to describe single bond breaking well⁶⁴ — provides a remarkably close approximation to the exact FCI potential energy surface computed by Bytautas and Ruedenberg²⁸⁵

Taking an active space for SCF metadynamics comprising the valence $3\sigma_g$ bonding and $3\sigma_u$ antibonding molecular orbitals (leaving the π orbitals frozen), eight real UHF states can be identified in the dissociation limit that directly mirror those of H_2 . After relaxation in the full orbital space, these correspond to two spatially symmetry-broken UHF states with diradical character ($^1F\cdots F^{\uparrow}$ and $^1F\cdots F^{\downarrow}$), the bonding σ_g^2 and antibonding σ_u^2 RHF states, two non-bonding $\sigma_g\sigma_u/\sigma_u\sigma_g$ UHF solutions, and two spatially symmetry-broken RHF states resembling the ionic configurations $F^+\cdots F^-$ and $F^-\cdots F^+$, as shown in Fig. 7.3. As the bond length is shortened, two distinct Coulson–Fischer points arise, involving the coalescence of the diradical UHF and ionic RHF solutions with the σ_g^2 and σ_u^2 states respectively. The pattern of these coalescence points mirrors the Coulson-Fischer points in H_2 . Furthermore, for shorter bond lengths, the corresponding h-RHF (dotted red) and h-UHF (dotted blue) solutions continue to exist with complex orbital coefficients.

First, consider a minimal NOCI basis containing only the “ σ_g^2 -like” RHF ground state and the two radical UHF states along with their h-UHF counterparts, denoted from here-on as “NOCI(3)”. The resulting binding curve closely matches the CASSCF(14, 8) result, as shown in Fig. 7.3, suggesting that NOCI(3) can capture the static correlation that is accounted for by CASSCF(14, 8). Furthermore, the variational flexibility offered by these three determinants appears sufficient to overcome the deficiency of the unbound UHF approximation, leading to a qualitatively correct bound potential. However, like CASSCF(14, 8), the NOCI(3) result underestimates the binding energy and overestimates the equilibrium bond length, implying that NOCI(3) fails to capture

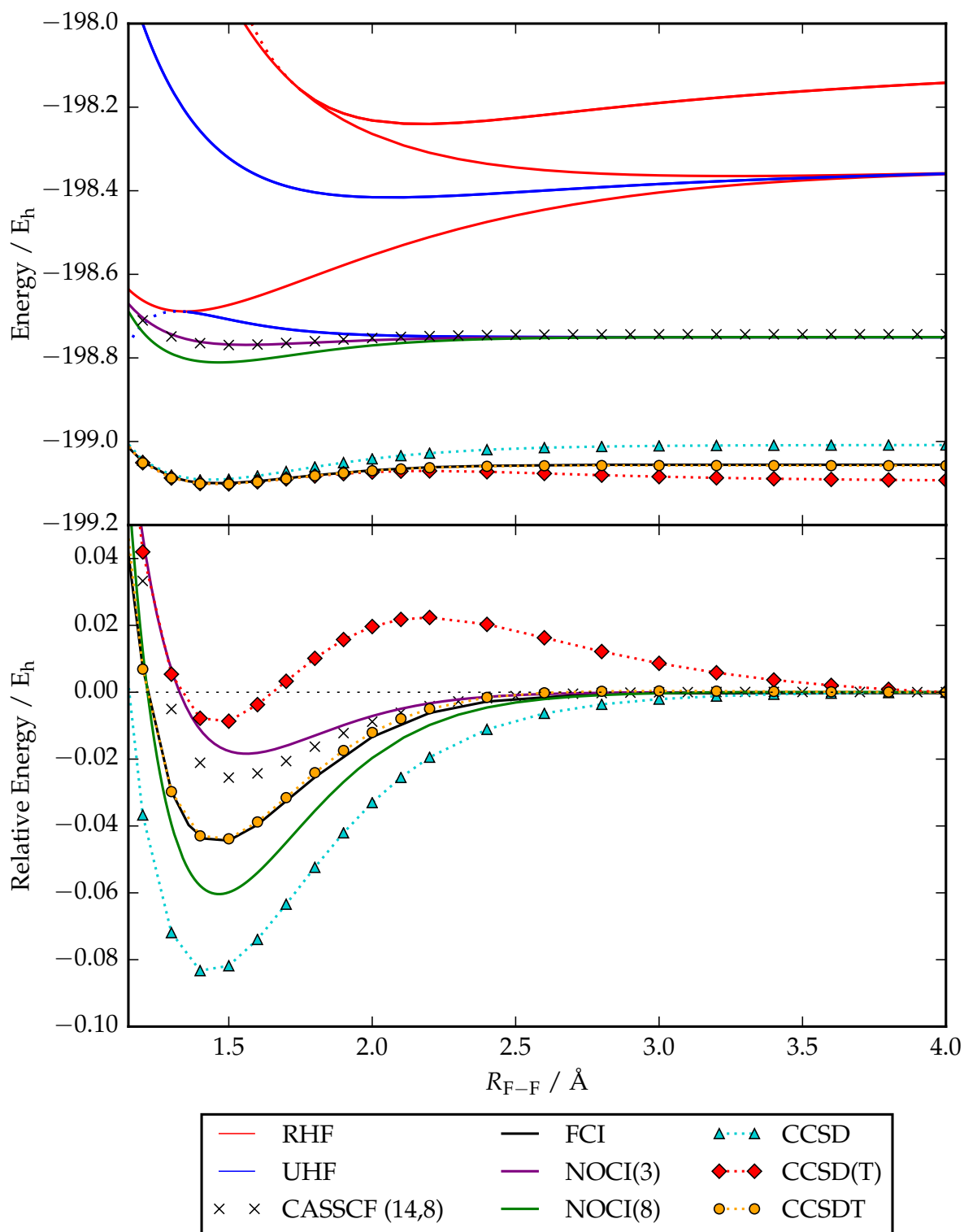


Figure 7.3: Absolute (top) energies for the eight multiple h-HF solutions of F_2 (cc-pVDZ), along with NOCI(3) and NOCI(8) ground state energies computed using only the three lowest and all eight h-HF states respectively. Binding curves (bottom) are computed relative to the value of each method at $R_{F-F} = 4.0$ Å and compared to FCI energies from Ref. (285).

the dynamic correlation that dominates at shorter bond lengths.

In contrast, including all eight h-HF solutions in the NOCI basis, denoted NOCI(8), lowers the ground state energy further relative to CASSCF(14, 8), particularly in the equilibrium region. Introducing these extra HF solutions in the NOCI expansion appears to allow some dynamic correlation to be computed at shorter bond lengths. Although NOCI(8) now overestimates the molecular binding energy, the absolute error is reduced in comparison to both NOCI(3) and CCSD. Furthermore, the equilibrium bond length predicted by NOCI(8) shows a promising correspondence to both FCI and CCSDT (bottom panel in Fig. 7.3).

Overall, even with only eight HF determinants from a Hilbert space of dimension 4.7×10^{13} , NOCI provides a good representation of the relative binding curve across the full range of geometries. However, a large error remains in the absolute energy due to the lack of dynamic correlation between the electrons on the same fluorine atom. This error further illustrates that NOCI primarily accounts for static correlation, in a similar manner to CASSCF with an active space of an equivalent size.

	$R_{F-F} = 2\text{\AA}$	$R_{F-F} = 8\text{\AA}$
RHF	-198.55412	-198.32475
CASCI(2, 2)	-0.18046	-0.39945
CASSCF(2, 2)	-0.19724	-0.41897
CASSCF(14, 8)	-0.19834	-0.41897
Unrelaxed NOCI(8)	-0.18046	-0.39945
NOCI(8)	-0.21596	-0.42576
FCI	-0.51470	-0.73070

Table 7.1: Total ground-state RHF energy and the correlation energy captured by the multi-reference methods considered for fluorine dimer (cc-pVDZ). The CASCI(2,2) and CASSCF(2,2) energies are computed using the same active space ($3\sigma_g$ and $3\sigma_u$) as the SCF metadynamics. FCI energies are taken from Ref. (285).

To emphasise the importance of orbital relaxation outside the SCF metadynamics active space, the NOCI correlation energies before and after the final relaxation step in the full orbital space are compared with CASSCF(2,2) and CASCI(2,2) using the equivalent active space [see Table 7.1]. Firstly, although the number of HF states identified by SCF metadynamics in the (2,2) active space is larger than the number of CASCI(2,2) states, the “unrelaxed” NOCI energy using partially optimised HF states (i.e. with frozen inactive orbitals) is identical to the CASCI(2,2) ground-state energy. This indicates that the CASCI(2,2) space is completely spanned by the multiple partially optimised HF states, and these HF states must contain redundancies. In contrast, once the multiple HF states are relaxed in the full orbital space, the NOCI energy is lowered by a further 20–40 mE_h , falling below the CASSCF(2,2) and CASSCF(14,8) results.

The final relaxation step is therefore essential to the performance of NOCI, providing a similar effect to the orbital relaxation that distinguishes CASSCF from CASCI.

7.3.4 Torsional Rotation of Ethene

The ethene molecule is the simplest example of an unsaturated polyene and possesses a rich electronic structure. In particular, the torsional isomerisation of ethene provides a prototype for photo-induced processes, including the isomerisation of retinal in mechanisms of vision.^{286,287} Moreover, the twisted \mathcal{D}_{2d} structure of ethene is a prime example of diradical systems that provide promising targets for singlet-fission^{288,289} and arise as reactive intermediates.²⁹⁰ However, describing the torsional rotation of ethene is challenging because the single-reference character of the planar \mathcal{D}_{2h} must be balanced with an even treatment of the $(\pi)^2$ and $(\pi^*)^2$ configurations that become degenerate at the twisted \mathcal{D}_{2d} structure.¹⁷ As a result, single-reference methods such as CCSD and CCSD(T) suffer from unphysical cusps in the rotational barrier.

	x	y	z
C	0.6603068	0.0000000	0.0000000
C	-0.6603068	0.0000000	0.0000000
H	1.2293090	0.9225699	0.0000000
H	1.2293090	-0.9225699	0.0000000
H	-1.2293090	0.9225699	0.0000000
H	-1.2293090	-0.9225699	0.0000000

Table 7.2: Initial geometry for ethene optimised at the RHF (cc-pVDZ) level in Angstroms.

To compute the NOCI energies of ethene, the initial planar \mathcal{D}_{2h} equilibrium geometry is first identified as the RHF minimum energy structure [see Table 7.2]. From this geometry the molecule is twisted around the central C–C double bond by the torsional angle ϕ_T to reach the multireference \mathcal{D}_{2d} structure ($\phi_T = 90$ deg), as illustrated schematically in Fig. 7.4. At the \mathcal{D}_{2h} geometry, the out-of-plane π and π^* ground state RHF orbitals have symmetries b_{1u} and b_{2g} respectively, while at the twisted \mathcal{D}_{2d} geometry, these

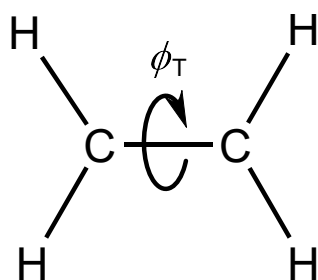


Figure 7.4: Schematic demonstrating the rotational torsion of ethene. Bond lengths and angles are held constant for all torsion angles ϕ_T .

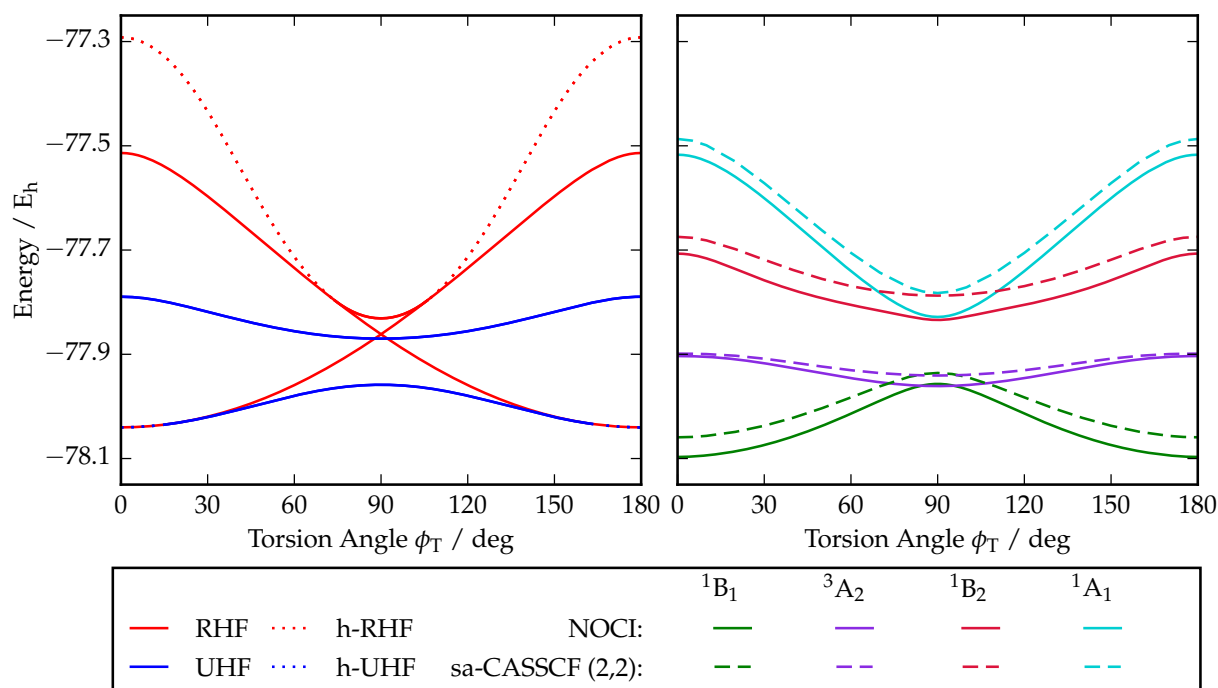


Figure 7.5: *Left:* Real RHF (solid red) and UHF (solid blue) states for the torsional rotation of ethene. When real states disappear, their holomorphic counterparts continue as complex h-RHF (dotted red) and h-UHF (dotted blue) solutions. *Right:* The four lowest energy NOCI states computed using these multiple HF solutions, compared to the sa-CASSCF(2,2) energies for the lowest four states (including three singlets and one triplet). Term symbols are given relative to the twisted D_{2d} geometry.

orbitals become a degenerate e pair. As a result, the low-lying 1A_g , $^3B_{3u}$, $^1B_{1u}$ and 1A_g states of planar ethene correlate with the 1B_1 , 3A_2 , 1B_2 and 1A_1 states at the twisted D_{2d} geometry respectively.

Using an active space for SCF metadynamics containing the π and π^* orbitals from the symmetric RHF ground state, eight real HF solutions can be identified at the multireference D_{2d} geometry, mirroring those found in Section 4.4.4. After relaxation in the full orbital space, these states (in ascending order of energy) correspond to a pair of diradical UHF states with one electron occupying a p-orbital on each carbon, two UHF ($\pi\pi^*$) states, the doubly degenerate RHF states with $(\pi)^2$ and $(\pi^*)^2$ configurations, and a pair of symmetry-broken RHF solutions with ionic configurations. Following each state away from $\phi_T = 90$ deg, towards the planar structure, the degeneracy of the lowest energy RHF solution breaks and the system becomes predominantly single-reference [left panel in Fig. 7.5]. Furthermore, as observed in Section 4.4.4, the symmetry-broken UHF states coalesce with the lower energy $(\pi)^2$ state, while the ionic RHF states coalesce with the higher energy $(\pi^*)^2$ solution. Beyond these coalescence points the corresponding h-UHF and h-RHF states continue to exist with complex orbital coefficients.

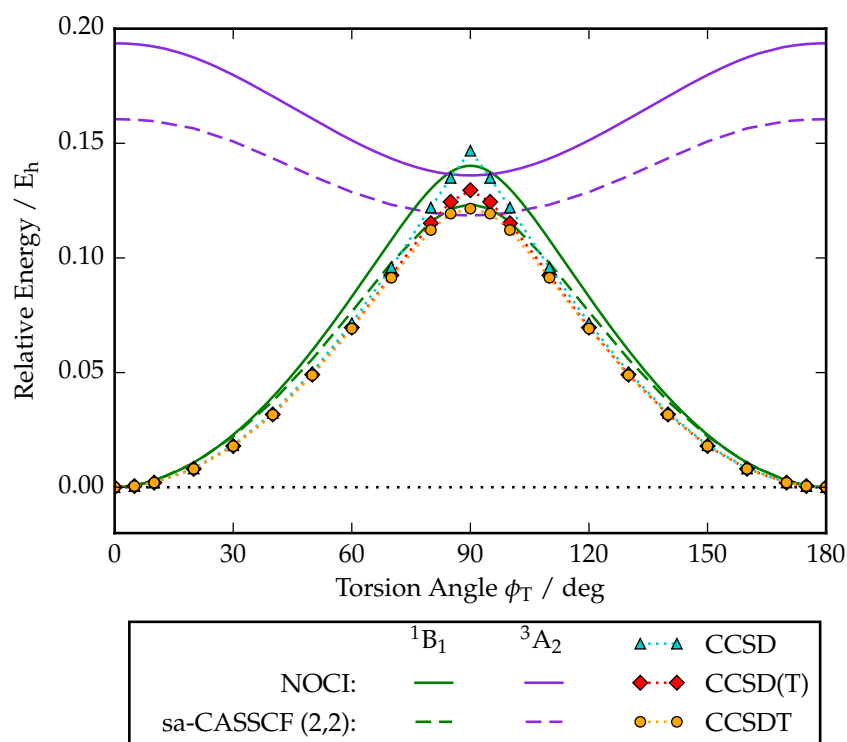


Figure 7.6: Comparison of methods for the torsional barrier of ethene. Each curve is plotted relative to the minimum ground-state energy for the corresponding method. Single-reference CCSD and CCSD(T) calculations fail to describe the multireference twisted geometry ($\phi_T = 90$ deg), resulting in unphysical cusps. In contrast NOCI and state-averaged sa-CASSCF(2,2) produce smooth torsional barriers. Term symbols are given relative to the twisted \mathcal{D}_{2d} geometry.

When a basis for NOCI is built using these eight HF states (and their complex h-HF counterparts), smooth ground- and excited-state energies can be computed across all torsional angles (solid lines in Fig. 7.5). Each NOCI state corresponds qualitatively to the equivalent sa-CASSCF(2,2) result (dashed lines in Fig. 7.5) using the same active space, demonstrating that the NOCI wave function is able to capture the static correlation. Moreover, the relative NOCI energy remains smooth for all angles along the torsional barrier (see Fig. 7.6), in contrast to the unphysical cusps that are present in the single-reference CCSD and CCSD(T) energies at $\phi_T = 90$ deg.

However, for the torsional isomerisation, NOCI overestimates the barrier height compared to all other methods considered. One possible cause of this error is the relative contributions of the symmetry-broken HF states to the singlet and triplet NOCI states. At the \mathcal{D}_{2d} structure, only the ground state RHF and lower energy diradical UHF states have the correct symmetry to contribute to the 1B_1 state, while only the diradical and ($\pi\pi^*$) UHF states contribute to the 3A_2 state. Each state is therefore constructed from a basis of four HF states, leading to a similar degree of variational flexibility in both cases. In contrast, at the planar \mathcal{D}_{2d} structure, the h-RHF state corresponding to the ionic RHF

	$E_{\text{tot}}(1^1A_g)$	${}^3B_{3u}$	${}^1B_{1u}$	2^1A_g
NOCI	-78.09715	0.19374	0.39026	0.58006
CASSCF(2,2)	-78.06744	0.16520	—	—
sa-CASSCF(2,2)	-78.05927	0.16052	0.38460	0.57237
CIS	-78.04017	0.14166	0.31308	0.33712
EOM-CCSD	-78.34912	0.17119	0.33010	0.33854
EOM-CCSDT	-78.35947	0.17331	0.32584	0.33629
ex-FCI	-78.36025(5)	0.17323(8)	0.3246(2)	0.33604(7)

Table 7.3: Total energy E_{tot} of the ground singlet state, and first three vertical excitation energies for planar D_{2h} ethene ($\phi_T = 0$ deg).

	$E_{\text{tot}}(1^1B_1)$	3A_2	1B_2	1A_1
NOCI	-77.95681	-0.00422	0.12262	0.12847
CASSCF(2,2)	-77.94419	-0.00356	—	—
sa-CASSCF(2,2)	-77.93581	-0.00494	0.14838	0.15331
CIS	-77.86163	-0.83382	0.03888	0.22485
EOM-CCSD	-78.20237	-0.02913	0.08789	0.12639
EOM-CCSDT	-78.23797	0.00032	0.08985	0.10300
ex-FCI	-78.2389(4)	0.00134(7)	0.0950(3)	0.0992(5)

Table 7.4: Total energy E_{tot} of the ground singlet state, and first three vertical excitation energies for twisted D_{2d} ethene ($\phi_T = 90$ deg).

state can also contribute to the ground-state singlet, and thus the ground-state singlet is now constructed from a total of six states, in contrast to four states for the ground-state triplet. As a result, the relative variational freedom of the singlet and triplet NOCI states is not constant across the torsional barrier, leading to the observed non-parallelity error.

Finally, the vertical excitation energies at the D_{2h} and D_{2d} structures provide an important testing ground for electronic structure methods.^{257,291–297} Predicting the singlet ($1^1A_g \rightarrow 2^1A_g$) excitation at the D_{2h} geometry is particularly challenging due to the diffuse Rydberg nature of the 2^1A_g state.^{291–295} Moreover, at the twisted D_{2d} geometry, dynamic correlation is known to lower the singlet state below the triplet state,^{293,298,299} resulting in a violation of Hund’s rules through the dynamic spin-polarisation effect.²⁹⁰

In Table 7.3 and Table 7.4, the NOCI excitation energies are compared to EOM-CCSD, EOM-CCSDT, CASSCF(2,2) and ex-FCI for the D_{2h} and D_{2d} structures respectively. At each geometry, state-specific CASSCF(2,2) energies are included for the ground-state singlet and triplet states, along with state-averaged energies targeting the four lowest states simultaneously. For the D_{2h} structure, the dominant single-reference character leads to accurate EOM-CCSD and EOM-CCSDT results relative to ex-FCI. However, the uneven treatment of the singlet and triplet states in NOCI is evident as the ($1^1A_g \rightarrow {}^3B_{3u}$) transition is overestimated. In contrast, the singlet–singlet

NOCI excitation energies are of comparable accuracy to sa-CASSCF(2,2), while both approaches lack the dynamic correlation required to correctly predict the challenging ($1^1A_g \rightarrow 2^1A_g$) transition. The accuracy of the singlet–singlet NOCI excitation energy further indicates the uneven characterisation of singlet and triplet states using this NOCI basis.

At the multireference D_{2d} geometry, only EOM-CCSDT predicts the correct ordering of the 1^1B_1 and 3^1A_2 states. In contrast, both NOCI and CASSCF(2,2) fail to capture the dynamic correlation required to account for the dynamic spin polarisation effect. For higher singlet–singlet excitations, NOCI reduces the error in the sa-CASSCF(2,2) by a factor of about a half, in particular predicting the ($1^1B_1 \rightarrow 1^1A_1$) transition to a similar degree of accuracy as the EOM-CCSD. The accuracy of NOCI for these higher singlet–singlet excitations demonstrates the superior representation of the excited state wave function by using multiple (excited) HF stationary states.

7.3.5 Distortion of Cyclobutadiene

Finally, consider the cyclobutadiene molecule. Correctly describing the ground and excited states of cyclobutadiene has long been of interest as an archetypal anti-aromatic and highly reactive system.^{282,300–309,309–321} In particular, methods must balance the multireference nature of the square D_{4h} geometry with the single-configurational character of the rectangular D_{2h} energy minimum.

At the D_{4h} geometry, the highest occupied molecular orbital (HOMO) comprises a doubly-degenerate pair of singly occupied orbitals, leading to the π -configuration $(a_{2u})^2(e_g)^2$. This configuration results in a 1^1B_{1g} ground state and a low-lying 3^1A_{2g} first excited state, followed by two higher energy states of 1^1A_{1g} and 1^1B_{2g} symmetry. As the molecule distorts towards the rectangular geometry, the symmetry drops from D_{4h} to D_{2h} and the π -configuration becomes $(b_{1u})^2(b_{2g})^2$. The associated descent in symmetry of the ground state ($1^1B_{1g} \rightarrow 1^1A_g$) and excited singlet state ($1^1B_{2g} \rightarrow 1^1A_g$) leads to a second-order pseudo-Jahn–Teller effect that favours a distortion towards the rectangular geometry.^{302–305}

Starting from the rectangular geometry optimised at the RHF level [see Table 7.5], the pseudo-Jahn–Teller distortion through the square geometry is modelled by simultaneously rotating two opposite corners around the central C_4 rotation axis with the distortion angle ϕ_D , as illustrated in Fig. 7.7. The C–H and diagonal C–C distances are held constant for each distortion angle.

While the ground-state RHF solution provides a suitable reference for the D_{2h} geometry, it becomes doubly-degenerate at the D_{4h} transition state. In each degenerate RHF solution (sketched as RHF 1 in Fig. 7.8), only one of the degenerate HOMO or-

	x	y	z
C	-0.6615206	-0.7841690	0.0000000
C	0.6615206	-0.7841690	0.0000000
C	-0.6615206	0.7841690	0.0000000
C	0.6615206	0.7841690	0.0000000
H	-1.4260054	-1.5465327	0.0000000
H	1.4260054	-1.5465327	0.0000000
H	-1.4260054	1.5465327	0.0000000
H	1.4260054	1.5465327	0.0000000

Table 7.5: Initial geometry for cyclobutadiene optimised at the RHF (cc-pVDZ) level in Angstroms.

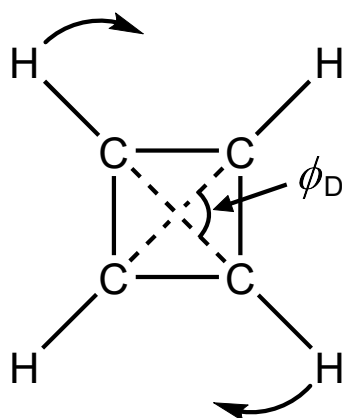


Figure 7.7: Schematic demonstrating the modelled distortion of cyclobutadiene, where two opposite corners of the square are rotated by the distortion angle ϕ_D around the central C_4 rotation axis. For all distortion angles ϕ_D , the C–H and diagonal C–C distances are held constant.

bitals is doubly-occupied. As a result, single reference methods such as CCSD and CCSD(T) fail to provide even a qualitatively correct description of the energy surface, with unphysical cusps propagated from the RHF description occurring at the square geometry. Removing these cusps requires either the full inclusion of triple excitations (i.e. CCSDT),^{310–312} or multireference approaches such as multi-configurational SCF,^{304,320} generalised valence-bond theory,^{316,321} or multireference CC.^{306,307,309,315,322}

At the square \mathcal{D}_{4h} transition state geometry, an active space for SCF metadynamics is defined with the four π orbitals (a_{2u} , e_g and b_{2u}) from the ground state RHF solution. In this active space, a total of twelve low-energy real HF states are then located which, after relaxation in the full orbital space, have degeneracies of two, four, two, two and two (in order of ascending energy). In what follows, the n^{th} -lowest RHF and UHF state at the square geometry are denoted “RHF n ” and “UHF n ” respectively.

Inspecting the π orbitals for each solution — sketched for one state of each degenerate set at the square geometry in Fig. 7.8 — spatially symmetry-broken orbitals are found in the UHF 1, UHF 2 and RHF 2 solutions. In contrast, the orbitals of the UHF 3 states

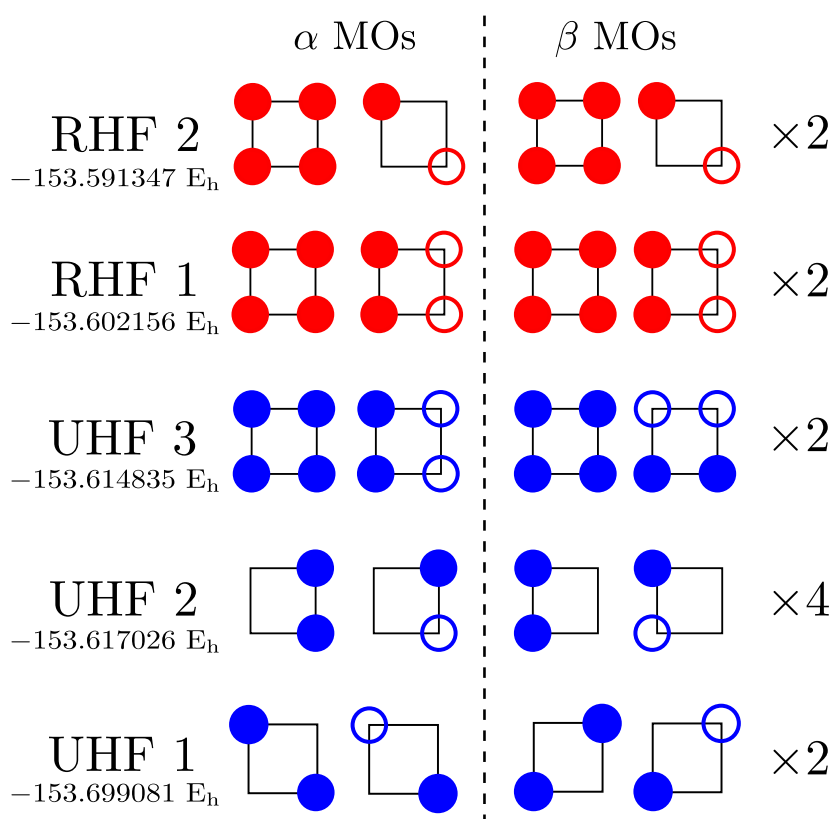


Figure 7.8: Sketch of the α (left) and β (right) occupied π molecular orbitals for the multiple RHF (red) and UHF (blue) states of cyclobutadiene, along with the HF energy and degeneracy of each state at the \mathcal{D}_{4h} geometry. Empty/filled circles (not to scale) indicate significant negative/positive contributions to the orbitals from the out-of-plane carbon p-orbitals. See main text for more details.

preserve spatial symmetry, representing the $(a_{2u})^2(e_g)^2$ configuration in which both orbitals in the degenerate e_g pair are singly occupied. The RHF 1 orbitals represent the same valence configuration but with only one of the degenerate e_g orbitals holding both electrons. Degeneracies for each state can be deduced by considering the spatial and spin symmetries of the system. The (h)-HF energies of each states across the potential energy surface are shown in the left panel of Fig. 7.9.

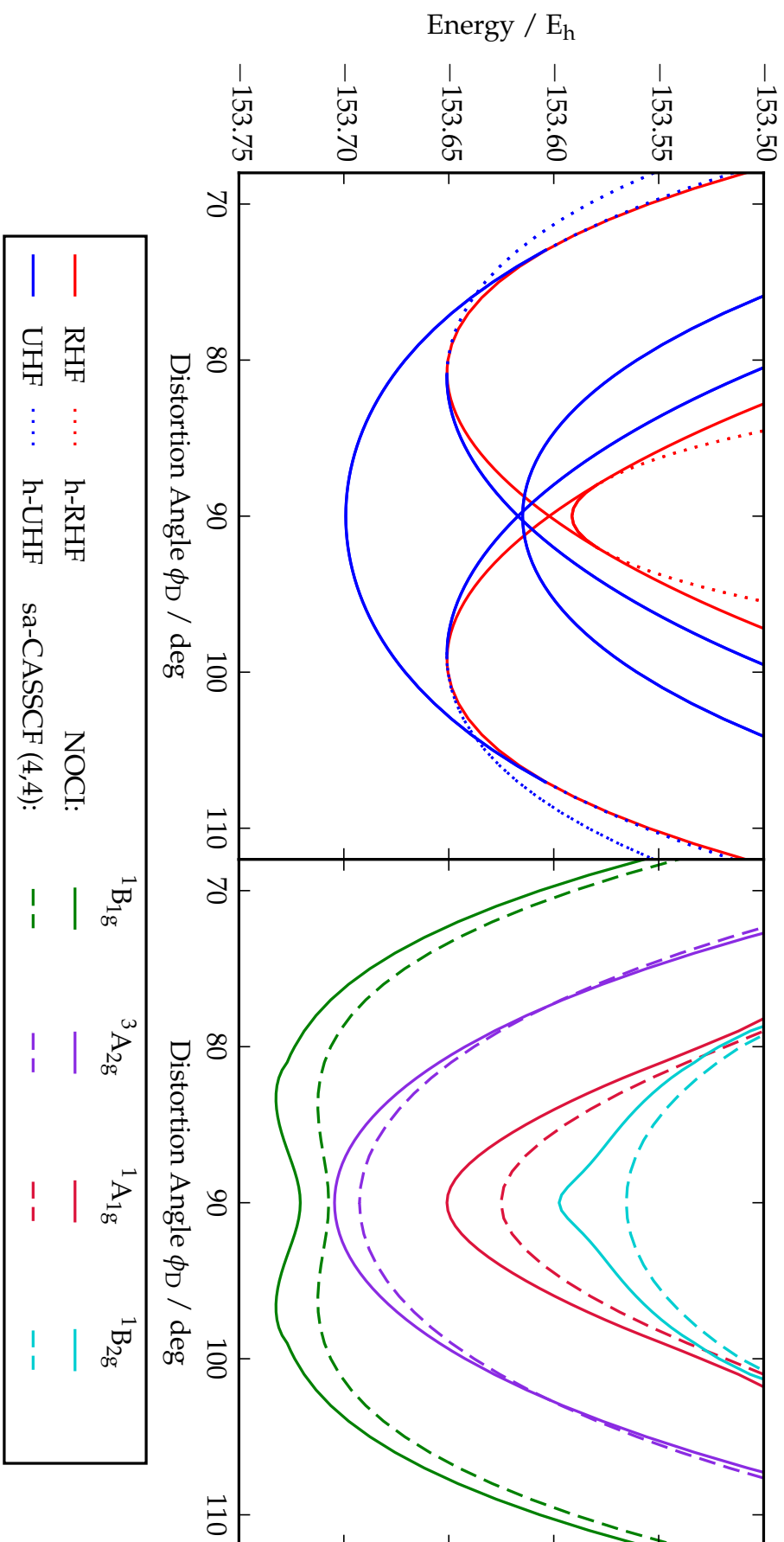


Figure 7.9: *Left:* Real RHF (solid red) and UHF (solid blue) states for the distortion of cyclobutadiene. When real states disappear, their h-HF counterparts continue as complex h-RHF (dotted red) and h-UHF (dotted blue) solutions. Only the real part of any complex h-HF energies is plotted.

Right: The four lowest energy NOCI states computed using these multiple h-HF solutions, compared to the sa-CASSCF(4,4) energies for the lowest four states. Term symbols are given relative to the square D_{4h} geometry.

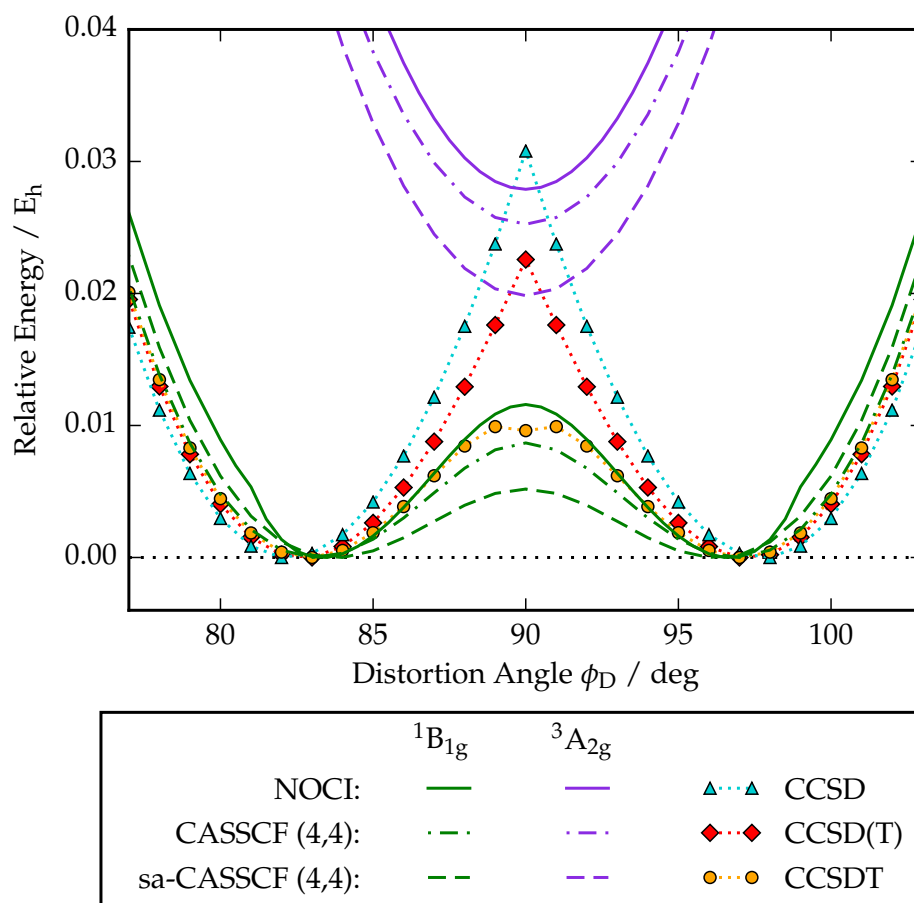


Figure 7.10: Comparison of NOCI and other methods for the relative autoisomerisation barrier and first excited state of cyclobutadiene. Each curve is plotted relative to the ground state minimum energy for the corresponding method. Term symbols are given relative to the square \mathcal{D}_{4h} geometry.

Moving away from the square geometry, the RHF 1 and UHF 2 states split into lower (higher) energy states RHF 1a (RHF 1b) and UHF 2a (UHF 2b) with one- and two-fold degeneracies respectively. The single degeneracy of the RHF 1a ground state leads to the dominant single-reference character at the rectangular geometry. In addition, each of the symmetry-broken solutions coalesces with the symmetry-pure RHF 1a state at a different Coulson–Fischer point shown in Fig. 7.9. For distortion angles further away from 90 deg, the h-HF counterparts of the vanishing states continue to exist with complex orbital coefficients (dotted lines in Fig. 7.9).

Using these HF solutions as a basis for NOCI recovers continuous and smooth energies that are all variationally lower than their sa-CASSCF(4,4) counterparts (right panel in Fig. 7.9). Again, NOCI recovers the static correlation required to provide a qualitatively correct description of the ground and excited states, while the use of individually optimised HF states quantitatively improves the energy relative to sa-CASSCF. Furthermore, NOCI yields a smooth relative ground-state autoisomerisation

	$E_{\text{tot}}(^1\text{B}_{1g})$	$^3\text{A}_{2g}$	$^1\text{A}_{1g}$	$^1\text{B}_{2g}$
NOCI	-153.72075	0.01630	0.06987	0.12331
CIS	-153.60216	-0.06703	0.01840	0.22862
CASSCF(4,4)	-153.70956	0.01657	—	—
sa-CASSCF(4,4)	-153.70721	0.01465	0.08204	0.14176
EOM-CCSD	-154.18974	-0.02062	0.24389	0.25355
EOM-CCSDT	-154.23741	0.00271	—	—
ex-FCI	-154.234(1)	0.013(3)	0.058(2)	0.078(1)

Table 7.6: Total energy E_{tot} of the singlet ground state, and the first three vertical excitation energies for square cyclobutadiene.

barrier [see Fig. 7.10] with a close agreement to CCSDT. In fact, even a state-specific CASSCF(4,4) ground-state calculation fails to reproduce the relative accuracy of NOCI.

Notably, however, the NOCI ground state exhibits a bump at around $\phi_D = 99$ deg. This feature appears to result from a complicated “avoided crossing” between the h-HF extension of the RHF 2 state and another solution (complex for all geometries and not shown) in the complex orbital coefficient plane. Exploring the topology of these states for complex λ in the vicinity of this bump reveals a Coulson–Fischer point away from the real axis, although a detailed investigation is beyond the scope of the current work. Instead, it suffices to note that the h-HF states used for NOCI are consistent across all distortion angles without any coalescence, and thus the NOCI energies remain both smooth and continuous.

Finally, consider the vertical excitation energies for \mathcal{D}_{4h} cyclobutadiene. At this geometry, dynamic correlation lowers the singlet below the triplet state,^{301,304,314} leading to a violation of Hund’s rules through the dynamic spin-polarisation effect.²⁹⁰ In Table 7.6 the excitation energies calculated using NOCI are compared to those computed using CIS, EOM-CCSD, EOM-CCSDT, both state-specific CASSCF(4,4) and sa-CASSCF(4,4), and ex-FCI. In sa-CASSCF(4,4), the four lowest energy states are simultaneously optimised, while the state-specific variant focuses on only the lowest energy singlet and triplet states in separate calculations.

For the ($^1\text{B}_{1g} \rightarrow ^3\text{A}_{2g}$) transition, NOCI matches the state-specific CASSCF(4,4) result, although both overestimate the excitation energy. In contrast, the uncorrelated CIS leads to an incorrect ordering of the singlet and triplet states, as does the absence of static correlation in EOM-CCSD. For the higher energy singlet-singlet transitions, NOCI gives the closest estimate to the ex-FCI result in comparison to all the methods considered. In contrast, EOM-CCSD significantly overpredicts the excitation energies, while the EOM-CCSDT calculations failed to converge for these transitions. Overall, NOCI appears to match the performance of state-specific CASSCF(4,4) and outperforms

EOM-CCSD to provide accurate estimates of multireference excitation energies at a significantly lower cost.

7.4 Concluding Remarks

This chapter has presented a general protocol that uses h-HF stationary states to construct NOCI wave functions with smooth and continuous energies for all molecular structures along a particular trajectory. Firstly, it was shown that minimal modifications are required to solve the generalised NOCI eigenvalue problem constructed using complex h-HF solutions. Secondly, to identify a relevant subset of real HF solutions that contribute towards capturing the multireference character along the trajectory, an active space SCF metadynamics approach has been defined. In this approach, the HF orbitals are first mixed and optimised in the active space while the inactive orbitals are kept frozen. Each state is then relaxed in the full orbital space to identify a ‘true’ HF stationary state. Finally, introducing a complex-perturbed electron-electron interaction λ allows real HF solutions to be extended onto their corresponding complex h-HF states by going *around* the Coulson–Fischer point in the complex λ -plane. A h-HF solution can then be easily followed across all geometries using a complex-valued λ and then relaxed back to $\lambda = 1$ to use in the NOCI expansion.

The application of the combined h-HF and NOCI approach has been demonstrated by considering the ground and low-lying excited states in the dissociation of H_2 and F_2 , the double-bond rotation in ethene, and the pseudo-Jahn–Teller distortion of cyclobutadiene. NOCI appears to capture correlation to a similar, if not better, accuracy than CASSCF using an equivalent active space, and can provide multireference excitation energies with remarkably small NOCI expansions. Moreover, the final orbital relaxation of each HF state in the full orbital space provides a similar effect to the orbital optimisation in CASSCF. As a result, NOCI presents a promising alternative to CASSCF while avoiding the difficulties of simultaneously optimising the orbital and CI expansion coefficients. Furthermore, this NOCI approach is systematically improvable by increasing the number of HF states included, and scales favourably with the system size.

7.4.1 Scope for Future Development

The applications of using fully optimised multiple HF solutions as a basis for NOCI still remain relatively unexplored, and this approach holds great potential for larger systems that are out of reach for conventional multireference techniques. In particular, the inclusion of symmetry-broken solutions that qualitatively represent physical states can

provide chemical insight into complicated processes such as electron transfer.³³ Moreover, there are a range of possible opportunities for further developing and improving this NOCI approach to create a fully fledged, black-box method.

Firstly, using a complex-perturbed Hamiltonian to follow HF states across all molecular structures can in principle be applied for *any* set of HF states. In particular, this means that the use of active space SCF metadynamics could be replaced by any other method for locating HF states, for example SF-NOCI or NOCIS. Identifying the relevant HF states is currently the limiting factor of this NOCI approach and it is possible that future computational developments may alleviate this bottleneck. For example, recent advances in selecting active orbital spaces⁷⁰ or identifying HF states using algebraic approaches^{271,272} may provide effective alternatives.

Secondly, developing optimised computational implementations of this NOCI approach could increase the size of the molecular systems that can be computed. In particular, the most computationally intensive component of the algorithm is performing the large number of SCF optimisations that are needed to locate multiple HF states and follow them across all molecular structures. Improved methods for more intelligently locating multiple HF states (as described above) would help reduce this cost. Furthermore, since many of the SCF optimisations are independent of each other (for example following one state across all geometries), performing these optimisations in parallel would reduce the total time required.

Thirdly, in this work and others, NOCI has been found to predominantly account for static rather than dynamic correlation. In this sense, the NOCI wave function performs a similar role to the CASSCF wave function. A perturbative correction to NOCI should therefore provide improved quantitative energies that include dynamic correlation. However, defining perturbative corrections to the NOCI wave function is challenging because there are no common reference orbitals or single-particle energies, and the NOCI wave function can have a non-zero overlap with the entire Hilbert space. The NOCI-MP2 approach provides one possible ‘perturb-then-diagonalise’ route where each HF state is individually perturbed and the resulting states are combined in the NOCI expansion.^{134,146} In contrast, developing a NOCI perturbation theory through a similar approach to CASPT2^{75,76} or NEVPT2⁸² has the potential to provide a more rigorous and direct perturbative correction to the NOCI energy. Developing this type of perturbation correction for NOCI forms the focus of Chapter 8.

Finally, to construct a fully self-contained theoretical framework, the derivation of nuclear gradients for NOCI should be considered. With nuclear gradients, it would then be possible to energetically optimise the molecular structure and reaction pathways to identify ground and excited state energies that are fully consistent within the NOCI

approximation. Furthermore, molecular gradients would allow the NOCI potential energy surface to be used for efficient *ab initio* molecular dynamics simulations without relying on finite difference approximations. Using fully optimised real HF states should simplify the derivation of NOCI molecular gradients through the application of the Hellmann–Feynman theorem.³²³ However, since complex h-HF solutions are not stationary states on the conventional (Hermitian) HF energy surface, explicit molecular gradients for these states must be developed.

Ultimately, by developing a systematic and routine NOCI approach, this chapter has laid the foundations for using NOCI to describe multireference ground and excited states in general. This approach provides a similar accuracy to CASSCF for both ground and excited states, presenting a viable multireference approach that avoids the computational challenges of CASSCF.

Chapter 8

Second-Order NOCI Perturbation Theory

The work in this chapter has contributed to the publication Ref. (5)

Summary

In Chapter 7, and in previous work, NOCI was found to mainly capture static electron correlation to provide similar accuracy to CASSCF with a comparable active space size. For CASSCF wave functions, the remaining dynamic correlation is often captured using the highly successful diagonalise-then-perturb CASPT2 approach, allowing quantitative energies to be computed. While a perturbative correction to NOCI has previously been introduced through the NOCI-MP2 approach, this uses the alternative perturb-then-diagonalise philosophy and relies on a series of approximations. Instead, this chapter develops a rigorous diagonalise-then-perturb correction to NOCI that directly mirrors CASPT2. The resulting “NOCI-PT2” theory is found to provide similar accuracy to CASPT2, allowing quantitative energy surfaces to be computed through the NOCI framework.

8.1 Context and Scope

Electron correlation in molecules is often partitioned into so-called static effects, describing large spatial rearrangements of electron density, or dynamic effects arising from the detailed relative motion of electrons. Static correlation can be accounted for using multireference methods such as the CASSCF approach,¹⁸ and Chapter 7 shows that NOCI captures static correlation with a similar accuracy to CASSCF. In contrast, strong dynamic correlation is most successfully addressed through single-reference many-body perturbation theory such as the MP2 method,¹² or the closely related coupled-cluster approach.⁶³

Handling systems where both static and dynamic correlation effects become important presents a more difficult challenge for electronic structure theory. Methods such as CASSCF fail to efficiently capture dynamic correlation, while single-reference perturbation theory and coupled-cluster break down in the presence of strong static correlation.¹¹ The most popular solution is to add perturbative corrections on top of multireference wave functions, leading to methods such as CASPT2,^{75,76} or NEVPT2.⁸² In this way, static correlation is handled by the multiconfigurational reference wave function while dynamic correlation is captured “in the presence of” static correlation through so-called “diagonalise-then-perturb” corrections. However, these methods suffer from the same limitations as the reference CASSCF approach, including the need for specialised experience in selecting the active orbitals and issues associated with variations in the active space as the molecular geometry change.⁷⁷

Since NOCI captures mainly static correlation with a similar accuracy to CASSCF, adding a rigorous perturbative correction to NOCI is the obvious next step towards a quantitative theory. Any NOCI-based perturbation theory should ideally reduce to either MP2 for a single determinant NOCI wave function, or a multireference approach such as CASPT2 if a suitable set of orthogonal reference determinants is chosen. The only previous attempt to add a perturbative correction to NOCI was NOCI-MP2 theory,^{134,146,147} where the NOCI basis determinants are perturbed using MP2 theory in a perturb-then-diagonalise approach. However, the original NOCI-MP2 approach was found to suffer from size-consistency issues that required *ad hoc* alterations to the working equations.¹⁴⁶ Furthermore, while NOCI-MP2 reduces to MP2 theory for a single reference determinant, it does not recover either CASPT2 or NEVPT2 when a suitable orthogonal set of NOCI determinants is chosen.

Instead, this chapter considers building a rigorous diagonalise-then-perturb correction to the reference NOCI wave function. This is achieved by identifying a suitable zeroth-order Hamiltonian and first-order interacting space in a similar manner to

CASPT2. The resulting theory — referred to as “NOCI-PT2” — is a closer analogue to conventional multireference perturbation theory than the NOCI-MP2 approach, and is found to provide a similar level of accuracy to CASPT2. By defining this rigorous NOCI-PT2 correction, the combined NOCI and NOCI-PT2 framework becomes a direct mirror of CASSCF and CASPT2. This finally establishes NOCI-based methods as a fully fledged alternative to the conventional orthogonal CASSCF framework.

The remainder of this chapter is structured as follows. Section 8.2 describes the challenges of NOCI-based perturbation theory and the development of the NOCI-PT2 approach. In Section 8.3, NOCI-PT2 is applied to a series of molecular examples and its performance is compared to currently available methods. Finally, Section 8.4 summarises the key conclusions and highlights potential directions for future research.

8.2 Theoretical Development

8.2.1 Prerequisites to NOCI Perturbation Theory

Constructing a rigorous diagonalise-then-perturb NOCI correction starts by defining the reference wave function

$$|\Psi^{(0)}\rangle = |\Psi_{\text{NOCI}}\rangle = \sum_x^{n_{\text{det}}} |^x\Psi\rangle c_x, \quad (8.1)$$

where each basis state $|^x\Psi\rangle$ corresponds to a single Slater determinant constructed from a bespoke set of N occupied MOs $\{|^x\psi_i\rangle\}$. Following the NOCI approach outlined in Chapter 7, this set of determinants may correspond to real HF solutions or complex-valued h-HF stationary states.⁴ It will be assumed that the basis determinants are normalised but not necessarily stationary states of the real HF energy and do not satisfy Brillouin’s condition.⁸ For complex h-HF stationary states, normalisation can be achieved by orthonormalising the occupied orbitals with respect to the unitary condition and then constructing the virtual orbitals from the corresponding orthogonal subspace.

Formally defining a second-order perturbative correction requires three key components:

- (i) Constructing a well-defined and simple reference Hamiltonian \hat{H}_0 ;
- (ii) Identification of the first-order interacting space;
- (iii) Avoiding intruder states and quasi-degeneracies.

However, the nonorthogonal structure of the NOCI reference wave function makes each of these components more challenging than single-reference approaches such as MP2, or orthogonal multireference perturbation theories including CASPT2.

8.2.2 Defining the Reference Hamiltonian

The reference Hamiltonian \hat{H}_0 lies at the heart of all perturbation theories and should have a simple form with eigenfunctions corresponding to the zeroth-order wave functions. For the single-reference case, \hat{H}_0 is almost universally defined using the one-electron Fock operator,

$$\hat{H}_0 = \hat{F} = \sum_i^N \hat{f}(i) \quad (8.2)$$

leading to Møller–Plesset partitioning.¹² However, when a multireference reference wave function is used, there is no longer a common set of occupied one-electron orbitals and the Fock operator definition becomes ambiguous. The most common solution is to introduce a generalised Fock operator \hat{F} defined in the atomic spin-orbital basis as^{75,76}

$$F[\mathbf{P}_\Psi]_{\mu\nu} = h_{\mu\nu} + \sum_{\sigma\tau}^{2n} \langle \mu\sigma | | \nu\tau \rangle (P_\Psi)^{\tau\sigma}, \quad (8.3)$$

where \mathbf{P}_Ψ is the one-electron reduced density matrix of the multireference wave function Ψ [see Appendix C]. For a single determinant reference wave function, this generalised Fock operator reduces to the Møller–Plesset zeroth-order Hamiltonian since the molecular orbitals become eigenfunctions of the Fock operator. However, to ensure that a multireference wave function remains an eigenfunction of \hat{H}_0 , the generalised Fock operator must be further modified using projectors onto the subspaces corresponding to the reference wave function and external interacting space. For example, including these projectors for a CASSCF wave function leads to the CASPT2 zeroth-order Hamiltonian defined in Eq. (1.66).

Like all multireference approaches, the NOCI wave function $|\Psi_{\text{NOCI}}\rangle$ also suffers from the lack of well-defined occupied orbitals. Furthermore, each NOCI basis state is an independently optimised Slater determinant. There is therefore no common set of MOs to build any model reference Hamiltonian and the perturbing determinants cannot be split into subspaces corresponding to those used in the CASPT2 reference Hamiltonian. Instead, the most unambiguous choice of zeroth-order Hamiltonian is to use a generalised Fock operator built from the NOCI one-particle density matrix \mathbf{P}_{NOCI} and split it using projectors onto the reference wave function and external space to give

$$\hat{H}_0 = \mathcal{M} \hat{F}_G \mathcal{M} + \mathcal{Q} \hat{F}_G \mathcal{Q}, \quad (8.4)$$

where $\hat{F}_G = \hat{F}[\mathbf{P}_{\text{NOCI}}]$ and the model- and external-space projectors are defined as

$$\mathcal{M} = |\Psi_{\text{NOCI}}\rangle \langle \Psi_{\text{NOCI}}| \quad \text{and} \quad \mathcal{Q} = \mathcal{I} - |\Psi_{\text{NOCI}}\rangle \langle \Psi_{\text{NOCI}}|. \quad (8.5)$$

Crucially, this reference Hamiltonian reduces to the Møller–Plesset zeroth-order Hamiltonian for a single determinant wave function and is closely related to the CASPT2

zeroth-order Hamiltonian if the NOCI basis states span an orthogonal complete active space.

8.2.3 Identifying the First-Order Interacting Space

Deriving a second-order energy correction requires the identification of the first-order wave function. Usually an *ansatz* for the first-order wave function is built from the set of external-space determinants that can couple to the reference wave function, defining the ‘first-order interacting space’. However, partitioning the Hilbert space determinants into model and external spaces is impossible for NOCI as every determinant can have a component in the reference wave function. The absence of well-defined Hilbert space partitioning is shared with other reference wave functions such as matrix product states used in the density matrix renormalisation group approach.^{324–326}

Despite the lack of a well-defined Hilbert space partitioning, the model space projector \mathcal{M} can be easily defined in terms of the NOCI expansion determinants as

$$\mathcal{M} = \sum_{wx}^{n_{\text{det}}} |{}^w\Psi\rangle S_{wx} \langle {}^x\Psi|, \quad (8.6)$$

where $S^{wx} = \langle {}^w\Psi|{}^x\Psi\rangle$ is the metric tensor in the multiple HF solution basis. In contrast, the external space projector \mathcal{Q} cannot be constructed explicitly as there is no well-defined resolution of the identity since each reference NOCI determinant is built from a different set of orbitals. Instead, it is possible to proceed with the representation $\mathcal{Q} = \mathcal{I} - \mathcal{M}$ and identify the first-order wave function by solving

$$\left(\mathcal{Q}(\hat{H}_0 - E^{(0)})\mathcal{Q} \right) |\Psi^{(1)}\rangle = -\mathcal{Q}\hat{V}\mathcal{M}|\Psi^{(0)}\rangle, \quad (8.7)$$

where $E^{(0)} = \langle \Psi_{\text{NOCI}} | \hat{H}_0 | \Psi_{\text{NOCI}} \rangle$.

Note that this first-order wave function equation also corresponds to minimising the Hylleraas functional⁴⁰

$$\mathcal{L}[\Psi^{(1)}] = \langle \Psi^{(1)} | \mathcal{Q}(\hat{H}_0 - E^{(0)})\mathcal{Q} | \Psi^{(1)} \rangle + \langle \Psi^{(1)} | \mathcal{Q}\hat{V}\mathcal{M} | \Psi^{(0)} \rangle + \langle \Psi^{(0)} | \mathcal{M}\hat{V}\mathcal{Q} | \Psi^{(1)} \rangle. \quad (8.8)$$

For a given approximate first-order wave function, the value of this Hylleraas functional also provides a variational estimate of the true second-order energy.¹¹

In orthogonal perturbation theory, $|\Psi^{(1)}\rangle$ can be expanded in terms of the single and double replacement determinants from each reference determinant in the multi-determinantal reference wave function.^{75,76} However, since the NOCI wave function can span the whole Hilbert space, expanding the first-order wave function in terms of excited determinants built from a *single* orthogonal set of MOs requires excitations

of all orders. Instead, the first-order wave function *ansatz* can be built by considering the set of determinants in the combined Hilbert spaces constructed from every reference determinant in the NOCI wave function. While this approach requires multiple representations of the full Hilbert space, it will be shown that only single and double excitations from each reference determinant are required.

Considering the zeroth-order Hamiltonian (8.4) and the expansion

$$\begin{aligned} \mathcal{Q}\hat{V}|\Psi^{(0)}\rangle &= (\mathcal{I} - \mathcal{M})(\hat{H} - \hat{H}_0)|\Psi^{(0)}\rangle \\ &= (\hat{H} - \hat{H}_0 - \mathcal{M}\hat{H} + \mathcal{M}\hat{H}_0)|\Psi^{(0)}\rangle \\ &= (\hat{H} - E_{\text{ref}})|\Psi^{(0)}\rangle, \end{aligned} \quad (8.9)$$

the second-order energy (1.47c) is then given by

$$E^{(2)} = \langle \Psi^{(1)} | \mathcal{Q}\hat{V} | \Psi^{(0)} \rangle = \langle \Psi^{(1)} | \hat{H} - E_{\text{ref}} | \Psi^{(0)} \rangle, \quad (8.10)$$

where $E_{\text{ref}} = \langle \Psi^{(0)} | \hat{H} | \Psi^{(0)} \rangle = E^{(0)} + E^{(1)}$ and $|\Psi^{(1)}\rangle$ may not be orthogonal to $|\Psi^{(0)}\rangle$. Inserting the NOCI wave function (8.1) and expanding the action of the Hamiltonian on each determinant then gives

$$\begin{aligned} E^{(2)} &= \sum_w^{n_{\text{ref}}} \langle \Psi^{(1)} | \hat{H} - E_{\text{ref}} | {}^w\Psi \rangle c_w \\ &= \sum_w^{n_{\text{ref}}} \left[\sum_{I \in \mathcal{W}}^{SD} \langle \Psi^{(1)} | {}^wI\Psi \rangle \langle {}^wI\Psi | \hat{H} | {}^w\Psi \rangle + \langle \Psi^{(1)} | {}^w\Psi \rangle \left(\langle {}^w\Psi | \hat{H} | {}^w\Psi \rangle - E_{\text{ref}} \right) \right] c_w, \end{aligned} \quad (8.11)$$

where ${}^wI\Psi$ denotes an excitation from the reference determinant, ${}^w\Psi \equiv |{}^w\Psi\rangle$ and $\sum_{I \in \mathcal{W}}^{SD}$ indicates the sum over single and double excitations in the Hilbert space \mathcal{W} built from determinant w . Crucially, any triple (or higher) replacement determinant in one Hilbert space representation can only couple to the reference wave function if it corresponds to a linear combination of single and double excitations from other reference wave functions. The first-order interacting space can therefore be represented using only single and double excitations from *each* reference determinant in the NOCI expansion. Note that the reference determinants $\{|{}^w\Psi\rangle\}$ are not included in the first-order interacting space as they satisfy the NOCI eigenvalue problem and do not contribute to the second-order energy.

8.2.4 Computing the Second-Order Energy

Using the first-order interacting space allows an *ansatz* for the first-order wave function to be constructed as

$$|\Psi^{(1)}\rangle = \sum_w^{n_{\text{ref}}} \sum_{I \in \mathcal{W}}^{SD} |{}^wI\Psi\rangle a_{wI}, \quad (8.12)$$

where a_{wI} represents coefficients that remain to be identified. The first-order wave function equation can now be fully expanded as

$$\sum_w^{n_{\text{ref}}} \sum_{I \in \mathcal{W}}^{SD} (\mathcal{Q}(\hat{H}_0 - E^{(0)})\mathcal{Q})|^{wI}\Psi\rangle a_{wI} = -(\hat{H} - E_{\text{ref}})|\Psi^{(0)}\rangle. \quad (8.13)$$

The variable coefficients a_{wI} can be solved by projecting Eq. (8.13) onto the first-order interacting space to give the simultaneous equations

$$\sum_w^{n_{\text{ref}}} \sum_{I \in \mathcal{W}}^{SD} \langle x^J\Psi | (\mathcal{Q}(\hat{H}_0 - E^{(0)})\mathcal{Q})|^{wI}\Psi\rangle a_{wI} = -\langle x^J\Psi | \hat{H} - E_{\text{ref}} | \Psi^{(0)}\rangle, \quad (8.14)$$

defining the rigorous diagonalise-then-perturb ‘‘NOCI-PT2’’ equations. Higher excitations can in principle couple to the single and double excitations through $(\mathcal{Q}(\hat{H}_0 - E^{(0)})\mathcal{Q})$. However, the approximate first-order wave function obtained from Eq. (8.14) provides a variational estimate of the second-order energy to be computed through the Hylleraas functional (8.8).

Introducing the matrix elements

$$F^{xJ,wI} = \langle x^J\Psi | \mathcal{Q}\hat{H}_0\mathcal{Q}|^{wI}\Psi\rangle, \quad (8.15a)$$

$$S^{xJ,wI} = \langle x^J\Psi | \mathcal{Q}|^{wI}\Psi\rangle, \quad (8.15b)$$

$$V^{xJ} = \langle x^J\Psi | \hat{H} - E_{\text{ref}} | \Psi^{(0)}\rangle, \quad (8.15c)$$

allows the NOCI-PT2 equations to be expressed as the linear equation

$$\left(F - E^{(0)}S \right) \mathbf{a} = -\mathbf{V}, \quad (8.16)$$

with the corresponding second-order energy given by $E^{(2)} = \mathbf{a}^\dagger \mathbf{V}$. Explicitly expanding $\mathcal{Q} = \mathcal{I} - |\Psi^{(0)}\rangle\langle\Psi^{(0)}|$ and noting that $\mathcal{Q}\hat{H}_0\mathcal{Q} = \mathcal{Q}\hat{F}_G\mathcal{Q}$ allows (8.15a) and (8.15b) to be expressed as

$$\begin{aligned} F^{xJ,wI} &= \langle x^J\Psi | \hat{F}_G |^{wI}\Psi\rangle + E^{(0)} \langle x^J\Psi | \Psi^{(0)}\rangle \langle \Psi^{(0)} |^{wI}\Psi\rangle \\ &\quad - \langle x^J\Psi | \hat{F}_G | \Psi^{(0)}\rangle \langle \Psi^{(0)} |^{wI}\Psi\rangle - \langle x^J\Psi | \Psi^{(0)}\rangle \langle \Psi^{(0)} | \hat{F}_G |^{wI}\Psi\rangle \end{aligned} \quad (8.17)$$

and

$$S^{xJ,wI} = \langle x^J\Psi |^{wI}\Psi\rangle - \langle x^J\Psi | \Psi^{(0)}\rangle \langle \Psi^{(0)} |^{wI}\Psi\rangle, \quad (8.18)$$

respectively. In these expansions, terms containing $\Psi^{(0)}$ account for any components of the first-order interacting space that are already present in the reference wave function.

The matrix form of the NOCI-PT2 equations highlights the relationship to the CASPT2 approach.⁷⁸ Furthermore, the recently derived Spin-Symmetry-Projected HF Perturbation Theory (SUPT2) provides a closely related nonorthogonal first-order wave function equation.³²⁷ However, the first-order wave function in SUPT2 is expanded

using symmetry-projections of the single and double replacement determinants through a “projection-after-excitation” style. In contrast, NOCI-PT2 considers excitations from each reference determinant individually, allowing the perturbative contribution from each Hilbert space representation to be explicitly captured.

Solving the NOCI-PT2 equations can be achieved using the same approach as solving the most general form of the CASPT2 equations [for more details, see Ref. (78)]. Like CASPT2, it is possible for redundancies to exist among the perturbing determinants, particularly since single and double excitations built from different NOCI reference determinants are likely to be linearly dependent. The presence of these redundancies leads to a null space in the overlap matrix (8.15b) and must be taken into account by first diagonalising the overlap matrix to identify the non-null eigenvectors. Constructing the projection matrix into the non-null space X , where

$$X^\dagger S X = I, \quad (8.19)$$

allows the first-order wave function to be transformed into

$$(\tilde{F} - E^{(0)} I) \tilde{a} = -\tilde{V}, \quad (8.20)$$

where $\tilde{F} = X^\dagger F X$, $\tilde{a} = X^\dagger S a$ and $\tilde{V} = X^\dagger V$. Identifying the diagonal matrix

$$\Delta = Y^\dagger \tilde{F} Y - E^{(0)} I \quad (8.21)$$

then allows the the first-order wave function coefficients to be evaluated as

$$\tilde{\tilde{a}} = -\Delta^{-1} \tilde{\tilde{V}}, \quad (8.22)$$

where $\tilde{\tilde{a}} = Y^\dagger \tilde{a}$ and $\tilde{\tilde{V}} = Y^\dagger \tilde{V}$. The second-order energy correction can then be computed as

$$E^{(2)} = \tilde{\tilde{a}}^\dagger \tilde{\tilde{V}} = -\tilde{\tilde{V}}^\dagger \Delta^{-1} \tilde{\tilde{V}}. \quad (8.23)$$

In practice, since all single and double excitations from each reference determinant are included in the first-order wave function, the dimensions of the NOCI-PT2 matrices will scale as $\mathcal{O}(n_{\text{ref}} N^2 n^2)$ and exact diagonalisation will generally be intractable. Furthermore, in contrast to CASPT2, the NOCI-PT2 matrices do not possess any block-diagonal form that would reduce the cost of exact diagonalisation. Instead, the NOCI-PT2 equations can be evaluated using an iterative linear solver such as DIIS^{150,151} or MINRES³²⁸ by casting Eq. (8.16) into the form

$$M a = -V \quad (8.24)$$

where $M = F - E^{(0)}S$. Using Eqs. (8.17) and (8.18) allows the matrix elements of M to be explicitly expanded as

$$\begin{aligned} M^{xJ,wI} = & \langle x^J \Psi | \hat{F}_G | w^I \Psi \rangle \\ & - \langle x^J \Psi | \hat{F}_G | \Psi^{(0)} \rangle \langle \Psi^{(0)} | w^I \Psi \rangle - \langle x^J \Psi | \Psi^{(0)} \rangle \langle \Psi^{(0)} | \hat{F}_G | w^I \Psi \rangle \\ & - E^{(0)} \left[\langle x^J \Psi | w^I \Psi \rangle - 2 \langle x^J \Psi | \Psi^{(0)} \rangle \langle \Psi^{(0)} | w^I \Psi \rangle \right]. \end{aligned} \quad (8.25)$$

The consistency of the linear problem (8.24) is ensured since the redundancy in the perturbing determinants appears in both M and V in exactly the same way, ensuring that a unique solution exists. However, the likely presence of a null-space in M can lead to slow iterative convergence, although this effect can be alleviated using a suitable preconditioning scheme.

8.2.5 Intruder States and Imaginary Shifts

Like all perturbation theories, and in particular multireference approaches, NOCI-PT2 is susceptible to the effects of intruder states from singularities in the second-order perturbation equations. In the full NOCI-PT2 approach, intruder states arise when the eigenvalues of \tilde{F} (diagonal elements of Δ) are close to zero, creating poles in Δ^{-1} that cause the first-order wave function coefficients to blow-up. While the presence of intruder states often indicates a bad choice of Hamiltonian partitioning or reference wave function, their effects can be mitigated using either a real⁷⁹ or imaginary shift⁸⁰ in the reference energy. Real energy shifts only move the poles in Δ^{-1} along the real axis, often causing the divergences to simply occur at a different molecular geometry. In contrast, imaginary shifts move the poles into the complex plane and provide a more robust way of removing intruder state divergences. Both real and imaginary shifts also introduce a small distortion into the potential energy landscape, although this effect is smaller using imaginary shifts.⁸⁰ For these reasons, only the imaginary shift philosophy will be considered for removing singularities in the NOCI-PT2 approach.

In orthogonal multireference perturbation approaches, the imaginary shift is introduced using the transformation $\hat{H}_0 \rightarrow \hat{H}_0 + i\epsilon$.⁸⁰ However, identifying the first-order wave function using this shifted reference Hamiltonian requires both F and S to be considered separately, rather than the combined matrix M . This approach is easy when the perturbing wave functions are mutually orthogonal, but becomes more challenging for the nonorthogonal first-order interacting space in NOCI-PT2. Instead, it is easier to introduce an imaginary shift $i\epsilon$ by following an alternative approach described for the related SUPT2 method in Ref. (327).

The derivation for this alternative approach starts by noting that the exact (non-null)

eigenvalues of M are given by³²⁷

$$\sum_{wI,xJ} Z_{p,xJ}^* M^{xJ,wI} Z_{wI,q} = \Delta_p \delta_{pq}, \quad (8.26)$$

where the transformations X and Y defined in Eqs. (8.19) and (8.21) are combined to construct the unitary transformation $Z = XY$. Note that the orthogonal non-null space (indexed by p, q, \dots) will have a lower dimensionality than the full first-order interacting space (indexed by wI, xJ, yK, \dots) when there are redundancies in the NOCI-PT2 equations. In this orthogonal non-null space, the exact first-order wave function coefficients with an imaginary shift are given by

$$\tilde{a}_p = -\frac{\tilde{V}_p}{\Delta_p + i\epsilon}. \quad (8.27)$$

While the first-order wave function coefficients may be complex when the reference NOCI wave function is complex-valued, the second-order energy must always be real. To ensure a real-valued second-order correction using an imaginary shift, the coefficients can be defined as

$$\tilde{a}_p = -\frac{\Delta_p \tilde{V}_p}{\Delta_p^2 + \epsilon^2}, \quad (8.28)$$

where the additional contribution that would lead to a complex-valued energy is neglected.

Using Eq. (8.26) and the relations

$$\Delta^2 = Z^\dagger M S^{-1} M Z \quad (8.29a)$$

$$\tilde{a} = Z^\dagger S a \quad (8.29b)$$

$$\tilde{V} = Z^\dagger V \quad (8.29c)$$

allows Eq. (8.28) to be back-transformed to give a new linear problem for the shifted first-order wave function coefficients as

$$(M S^{-1} M + \epsilon^2 S) a = -M S^{-1} V. \quad (8.30)$$

Crucially, while this new linear problem requires the construction of a modified input matrix and vector, it can still be solved with a conventional linear solver. However, it is generally not possible to exactly diagonalise S to compute the required inverse S^{-1} . Instead, since only an approximate first-order wave function is needed to account for the imaginary shift, it can be assumed that this additional overlap matrix is diagonal, giving the simpler linear problem

$$(M^2 + \epsilon^2 I) a = -M V. \quad (8.31)$$

Once the approximate imaginary-shifted coefficients have been identified, a variational estimate of the second-order energy can then be obtained through the unshifted Hylleraas functional (8.8),⁸⁰ given in matrix form as

$$E^{(2)} = \mathbf{a}^\dagger \mathbf{M} \mathbf{a} + \mathbf{a}^\dagger \mathbf{V} + \mathbf{V}^\dagger \mathbf{a}. \quad (8.32)$$

8.2.6 Algorithm Implementation

The current NOCI-PT2 implementation begins by assuming a suitable set of (h)-HF states $\{|\Psi^x\rangle\}$ have been provided. The combined NOCI and NOCI-PT2 approach then proceeds as follows:

1. Orthogonalise the occupied orbitals for each reference state $|\Psi^x\rangle$ with respect to the unitary constraint and construct the corresponding virtual orbitals.
2. Solve the reference NOCI problem (7.3) to identify the reference wave function $|\Psi^{(0)}\rangle = |\Psi_{\text{NOCI}}\rangle$.
3. Construct the generalised Fock operator (8.3) and zeroth-order Hamiltonian (8.4) using the NOCI density matrix defined in Eq. (C.20).
4. Build the $M^{xJ,wI}$ [Eq. (8.25)] and V^{xJ} [Eq. (8.15c)] matrix elements using the generalised Slater–Condon rules outlined in Appendix C.
5. Define the linear problem $\mathbf{A}\mathbf{x} = \mathbf{B}$ depending on whether an imaginary shift is used:
 - *Unshifted approach*: $\mathbf{A} = \mathbf{M}$ and $\mathbf{B} = -\mathbf{V}$;
 - *Imaginary shift of $i\epsilon$* : $\mathbf{A} = \mathbf{M}^2 + \epsilon^2 \mathbf{I}$ and $\mathbf{B} = -\mathbf{M}\mathbf{V}$,
6. Iteratively solve the linear problem using the MINRES algorithm to identify the first-order wave function coefficients \mathbf{x} .
7. Compute $E^{(2)}$ from the Hylleraas functional using (8.32).

Iteratively solving the NOCI-PT2 linear problem in Step 6 can be accelerated by introducing a simple symmetric diagonal preconditioner $D_{ij} = |A_{ii}|\delta_{ij}$ to give the modified matrices $\mathbf{A}' = \mathbf{D}^{-1/2}\mathbf{A}\mathbf{D}^{-1/2}$ and $\mathbf{B}' = \mathbf{D}^{-1/2}\mathbf{B}$. The optimal first-order wave function coefficients are then given in the un-preconditioned space as $\mathbf{x} = \mathbf{D}^{-1/2}\mathbf{x}'$, where $\mathbf{A}'\mathbf{x}' = \mathbf{B}'$. Convergence of the MINRES algorithm is judged using the length of the residual vector $\mathbf{r}' = \mathbf{A}'\mathbf{x}' - \mathbf{B}'$, with a threshold value of $|\mathbf{r}'| < 10^{-7}$.

This algorithm has been implemented in a developmental version of Q-CHEM 5.2 using the LIBNOCI library. Although it is primitive and far from optimal, it is sufficient for a first investigation into NOCI-PT2. In the longer term, the algorithm may be

accelerated by using the nonorthogonal Wick's theorem to compute matrix elements without repeatedly performing Löwdin pairing for the excited determinants.³²⁹ This acceleration may then allow matrix elements to be computed on-the-fly, removing the high memory requirements of explicitly storing the M matrix and V vectors.

8.3 Results and Discussion

The NOCI-PT2 approach is first illustrated on the hydrogen dimer. Its application to strongly correlated wave functions is assessed using the symmetric stretch of the square H_4 molecule, which possesses a degenerate HOMO and LUMO across the full binding curve. The ground-state dissociation of the fluorine dimer is then considered as a molecular example exhibiting strong static and dynamic correlation. In each case, NOCI-PT2 is compared to the CASPT2 approach using an equivalent active space and NOCI-MP2 computed with the same NOCI reference wave function. All NOCI-MP2 calculations use the size-consistent "version 2" approach described in Refs. (146) and (147). Energies are provided in atomic units of Hartrees, E_h .

8.3.1 Computational Details

All h-HF and NOCI energies were calculated using the LIBNOCI library in Q-CHEM 5.2.¹⁸⁶ Where h-HF energies become complex, only the real component is plotted. NOCI-PT2 energies were calculated using the algorithm described in Section 8.2.6 and implemented in a developmental version of the LIBNOCI library in Q-CHEM 5.2. All NOCI-MP2 energies were computed using an in-house implementation in a developmental version of the LIBNOCI library in Q-CHEM 5.2. CASSCF and CASPT2 energies were computed using the OPENMOLCAS package.³³⁰ Exact FCI energies for H_2 and H_4 were computed using ORCA.²⁷³ Near-exact energies for F_2 were computed using the CIPSI method implemented in QUANTUM PACKAGE 2.0²⁸⁰ and were converged to an extrapolated error less than 0.01 mE_h .

8.3.2 Hydrogen Dimer

The hydrogen dimer is the simplest molecular system that exhibits a transition between dominant static and dynamic correlation. At large bond lengths, the strong static correlation arises from the near-degeneracy of the bonding σ_g and antibonding σ_u molecular orbitals and is associated with the physical dissociation of the closed-shell H_2 molecule into an open-shell singlet comprising two H radicals. Since this open-shell singlet cannot be faithfully described by a single HF determinant, the true wave

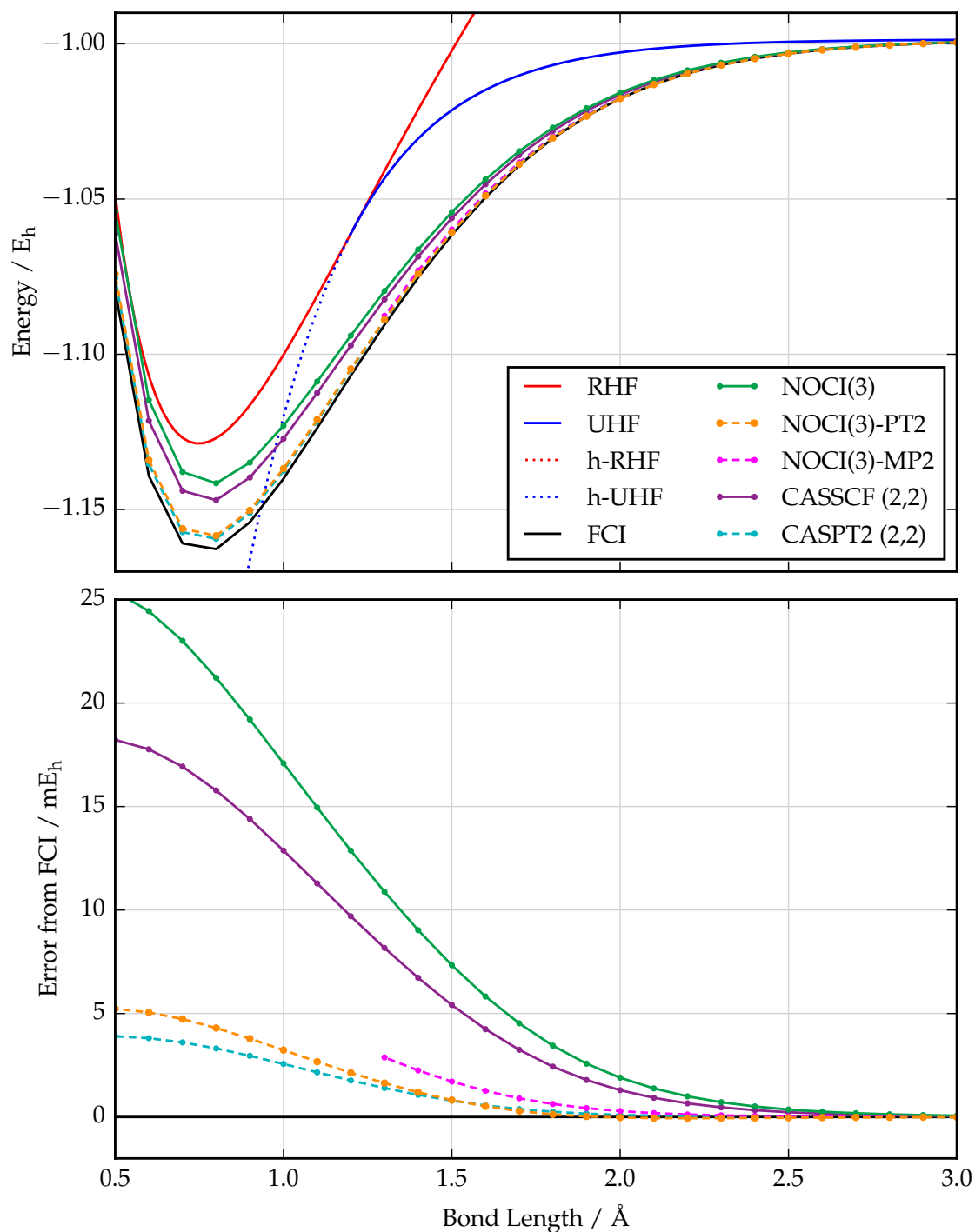


Figure 8.1: *Top:* Absolute NOCI(3) and NOCI(3)-PT2 energies for the hydrogen dimer (cc-pVDZ) computed using the lowest RHF and degenerate UHF states with their h-UHF counterparts. *Bottom:* Error in the NOCI(3)-PT2 energy with respect to the exact FCI energy compared to CASPT2(2,2) with an equivalent number of configuration state functions and NOCI(3)-MP2 using the same reference NOCI wave function.

function adopts predominantly multireference character. At the HF level, this strong static correlation causes the breakdown of the closed-shell RHF approximation and the emergence of a lower energy symmetry-broken UHF (sb-UHF) state. In contrast, the

single determinant RHF state provides a qualitatively correct description of the energy near the equilibrium geometry and the remaining error arises from dynamic correlation.

Taking the cc-pVDZ basis set, the lowest-energy RHF state (σ_g^2) and the two degenerate sb-UHF states along with their h-UHF counterparts can be used to construct a symmetry-restored NOCI wave function (top panel in Fig. 8.1). The corresponding NOCI(3) energy becomes exact in the dissociation limit since here the sb-UHF states tend towards the FCI energy. Using the same number of configuration state functions in the CASSCF(2,2) approach also allows the dissociation limit to be described exactly. However, NOCI(3) and CASSCF(2,2) only effectively account for static correlation and fail to capture the dynamic correlation that becomes significant for short bond lengths. For example, the error in the NOCI(3) and CASSCF(2,2) energies close to the equilibrium structure range between around 20–25 mE_h and 15–25 mE_h respectively (bottom panel in Fig. 8.1).

Adding the NOCI-PT2 correction on top of the NOCI(3) wave function significantly improves the energy, providing an error of $< 5 mE_h$ close to the equilibrium structure. Across all geometries, the NOCI-PT2 energy matches the CASPT2(2,2) result to within 1 mE_h , demonstrating that the CASPT2 and NOCI-PT2 approaches provide a closely related perturbative correction for the CASSCF and NOCI reference wave functions respectively (bottom panel in Fig. 8.1). Furthermore, the NOCI-MP2 energy can also be computed using the same reference NOCI(3) wave function when the real sb-UHF states exist. While NOCI-MP2 also improves the NOCI(3) energy, it provides a worse perturbative correction in comparison to NOCI-PT2. When the h-UHF states becomes complex for bond lengths shorter than the Coulson–Fischer point, the NOCI-MP2 correction fails completely as unphysical negative eigenvalues appear in the perturbed overlap matrix (2.14b).

Ideally the quality of the NOCI-PT2 perturbative correction should not deteriorate as the size of the basis set and corresponding Hilbert space increases. The dependence of NOCI-PT2 on the basis set can be tested by considering the hydrogen dimer using the larger cc-pVTZ basis. The equivalent NOCI(3) reference wave function built using the RHF and sb-UHF states and the corresponding CASSCF(2,2) wave function still capture the static correlation in the dissociation limit. Since the quality of the NOCI energy varies across the binding curve, a fair assessment of NOCI-PT2 can be introduced by defining the percentage correction of a perturbation theory compared to the error in the reference wave function energy, given by

$$\text{Percentage Correction} = \frac{E_{\text{PT2}} - E_{\text{ref}}}{E_{\text{FCI}} - E_{\text{ref}}} \times 100\%. \quad (8.33)$$

This perturbative correction is compared for NOCI-PT2, CASPT2 and NOCI-MP2 using

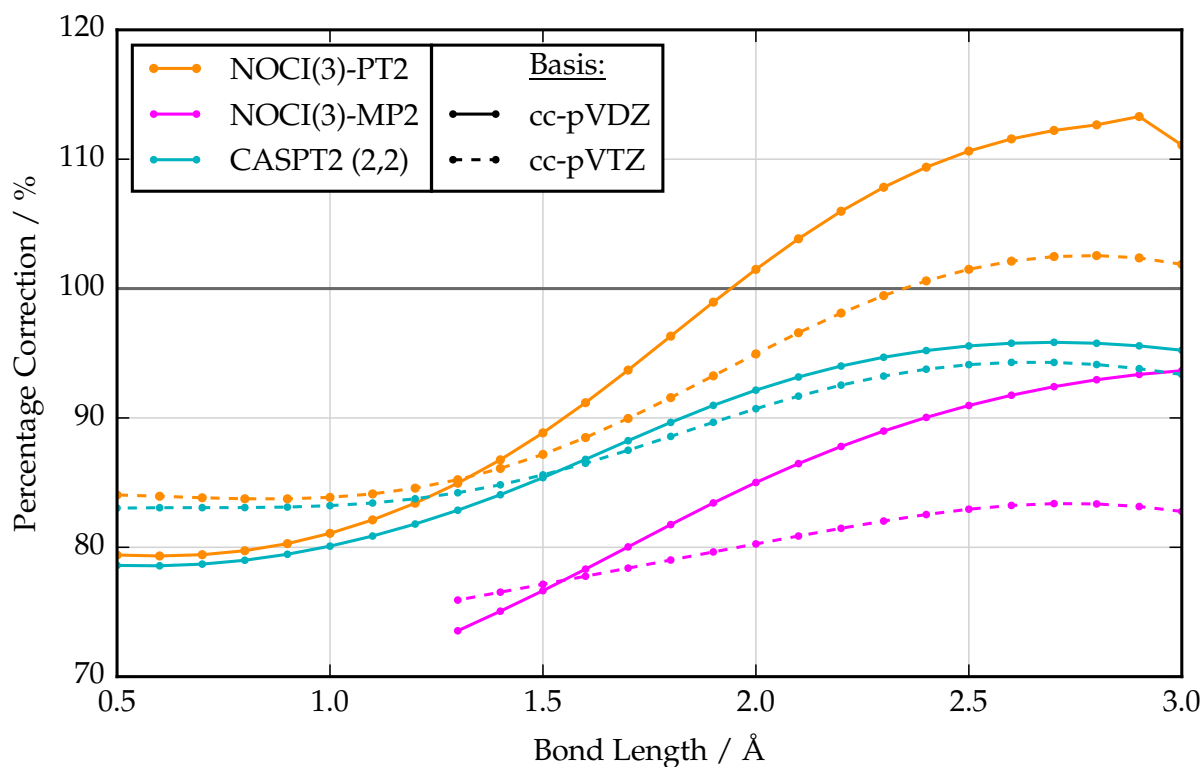


Figure 8.2: Comparing the percentage correction [see Eq. (8.33)] for NOCI-PT2, CASPT2 and NOCI-MP2 using the cc-pVDZ and cc-pVTZ illustrates that the NOCI-PT2 correction does not deteriorate for larger basis sets. The kink in the NOCI(3)-PT2 percentage correction at large bond lengths is likely to be a numerical result of the small error in the reference NOCI(3) energy.

the cc-pVDZ (solid lines) and cc-pVTZ (dashed lines) basis sets in Fig. 8.2. Significantly, no deterioration in the NOCI-PT2 correction occurs on moving from the cc-pVDZ basis to the cc-pVTZ basis; in fact the NOCI-PT2 correction is often more effective in the larger basis. Furthermore, NOCI-PT2 appears to provide a similar percentage correction to CASPT2 in the equilibrium regime, while NOCI-MP2 is clearly the least efficient approach. Finally, NOCI-PT2 yields non-variational energies for large bond lengths where the percentage correction rises over 100%.

8.3.3 Square H_4 Symmetric Stretch

Next consider the square H_4 molecule as an example of a molecule with a degenerate HOMO and LUMO across the full symmetric stretch. With the cc-pVDZ basis, one can locate ten low lying HF states that provide a dominant contribution to a NOCI wave function, with degeneracies of two, four, two and two in order of ascending energy in the dissociation limit. Using these states along with their h-UHF counterparts as a basis for a NOCI(10) calculation allows the ground-state singlet state (top panel in Fig. 8.3) and triplet state (top panel in Fig. 8.4) to be computed with a similar accuracy to

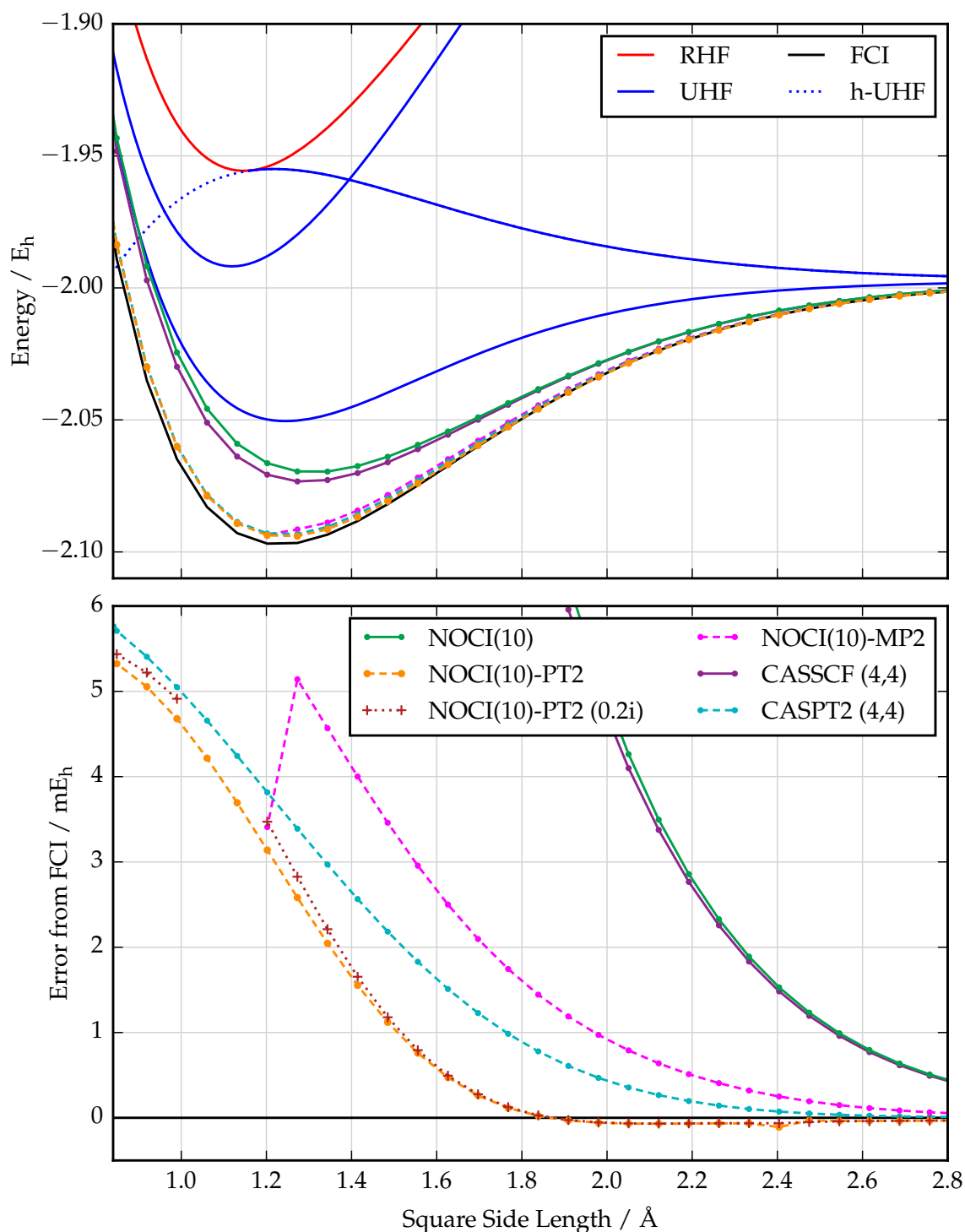


Figure 8.3: *Top:* Absolute NOCI(10) and NOCI(10)-PT2 energies for the ground-state singlet along the symmetric stretch of square H_4 (cc-pVDZ). The NOCI basis comprises the two degenerate ground RHF states and eight (h-)UHF solutions with degeneracies of two, four, and two in order of ascending energy at the dissociation limit. *Bottom:* Error in the singlet NOCI(10)-PT2 energy with respect to the exact FCI energy compared to NOCI(10)-MP2 using the same reference NOCI wave function and CASPT2(4,4).

CASSCF(4,4). Here the CASSCF active space contains the four lowest energy molecular orbitals. Like the hydrogen dimer, both approaches become exact in the dissociation

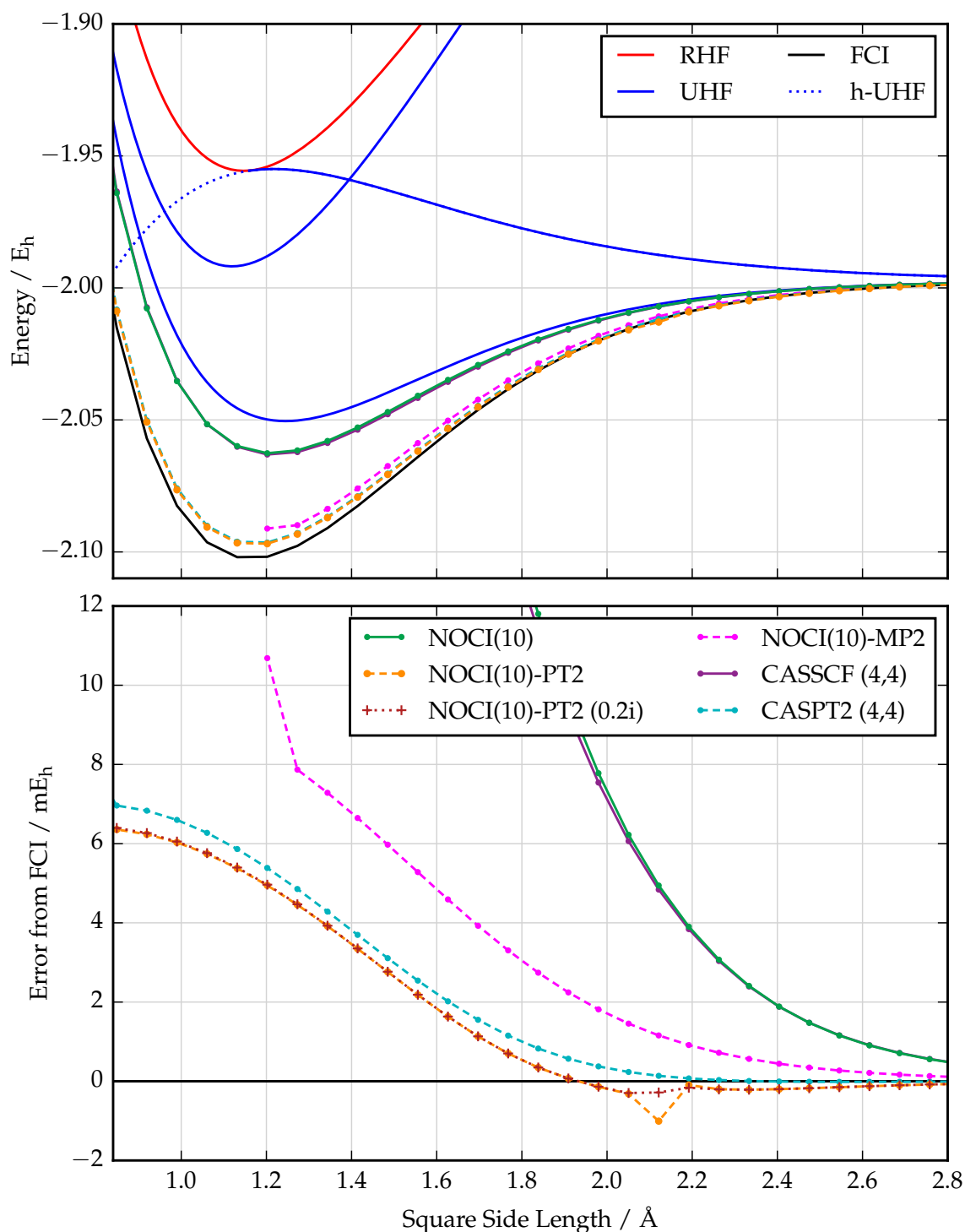


Figure 8.4: *Top:* Absolute NOCI(10) and NOCI(10)-PT2 energies for the ground-state triplet along the symmetric stretch of square H_4 (cc-pVDZ). The NOCI basis comprises the two degenerate ground RHF states and eight (h-)UHF solutions with degeneracies of two, four, and two in order of ascending energy at the dissociation limit. *Bottom:* Error in the triplet NOCI(10)-PT2 energy with respect to the exact FCI energy compared to NOCI(10)-MP2 using the same reference NOCI wave function and CASPT2(4,4).

limit but fail to capture the dynamic correlation that dominates near the equilibrium geometry.

Adding the NOCI-PT2 correction to the NOCI(10) wave function provides a significant improvement to both the singlet and triplet energies. For example, the error in the NOCI-PT2 energy in the equilibrium region falls to around 6 mE_h or less, providing a marginally better estimate than CASPT2 even though the CASSCF reference wave function has a lower energy than NOCI(10) in both cases (bottom panels in Figs. 8.3 and 8.4). Furthermore, NOCI-PT2 provides a significantly improved estimate of the equilibrium geometry compared to the reference NOCI energy for both the singlet and triplet binding curves. In contrast, adding the NOCI-MP2 correction to the same NOCI(10) reference wave function provides the worst perturbative correction across all geometries, and breaks down completely in the vicinity of the Coulson–Fischer point and at shorter bond lengths.

While the CASPT2 energy is smooth across all geometries, both the singlet and triplet NOCI-PT2 energies exhibit a small “kink” in the binding curve corresponding to a singularity in the NOCI-PT2 equations. Adding a small imaginary shift of $\epsilon = 0.2 \text{ E}_h$ as described in Section 8.2.5 allows the effect of these singularities to be successfully mitigated. For the triplet state, the imaginary shift leaves the NOCI-PT2 energy virtually unchanged away from the position of the unshifted singularities. However, near the Coulson–Fischer point in the singlet binding curve (square side length $\approx 1.15 \text{ \AA}$), the imaginary-shifted NOCI-PT2 equations fails to converge. Since the modified linear problem (8.31) also fails to converge with $\epsilon = 0.0 \text{ E}_h$, this failure can be attributed to the use of Eq. (8.31) rather than introduction of an imaginary shift. Furthermore, the degree of redundancy in the M matrix will be greatest in the vicinity of a Coulson–Fischer point, and taking M^2 amplifies the effect of these redundancies in any iterative approach.

8.3.4 Fluorine Dimer

Finally, the fluorine dimer provides an example of a system where both static and dynamic electron correlation are present across all geometries, making it a challenging test case for electronic structure methods.^{17,284} For example, the UHF approximation fails completely in F_2 and predicts an unbound potential.²⁸⁴ In Section 7.3.3, it was shown that a NOCI(3) wave function built from the RHF ground state and the two degenerate sb-UHF ground states allows a bound potential to be recovered that closely matches the full valence CASSCF(14,8) energy. However, both full valence CASSCF(14,8) and NOCI only capture static correlation and have a remaining error of approximately 300 mE_h relative to the exact FCI energy (see Fig. 7.3). The fluorine dimer therefore presents an ideal test for assessing the performance of NOCI-PT2 when both static and dynamic correlation effect become significant.

Given the additional electrons in F_2 compared to H_4 or H_2 , the cc-pVDZ basis set

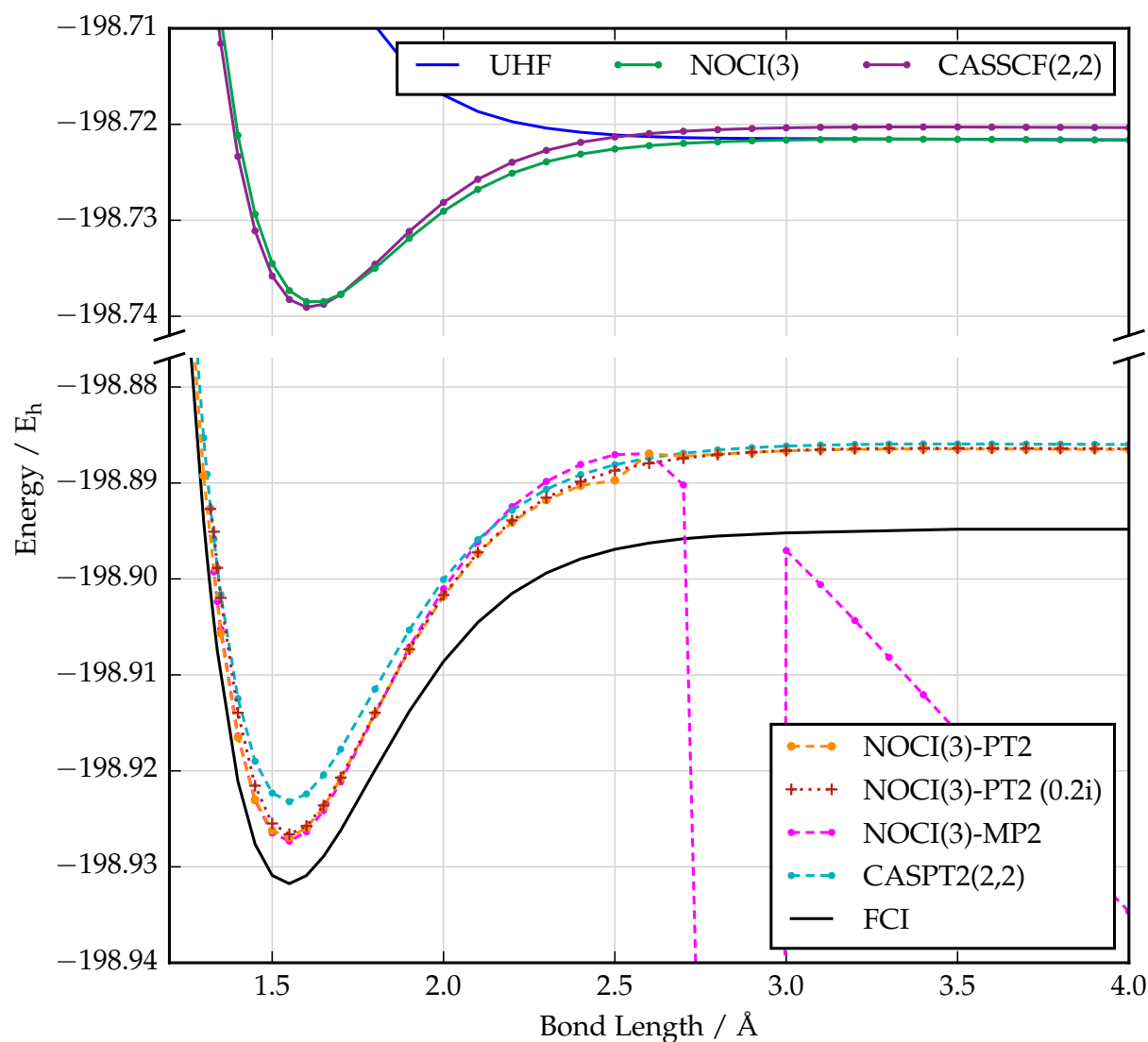


Figure 8.5: Absolute NOCI(3) and NOCI(3)-PT2 energies for the F_2 binding curve (6-31g) using the symmetric RHF state and low-lying diradical UHF states as the NOCI basis. The NOCI(3)-PT2 energy shows a close correspondence to an equivalent CASPT2 calculation and reduces the energy error to within 10 mE_h of the exact FCI result across all bond lengths.

is beyond the capabilities of the current NOCI-PT2 implementation. Instead, the 6-31G basis set can be used and HF solutions corresponding to those in Fig. 7.3 can be identified. The simplest NOCI(3) reference wave function can then be constructed from the RHF ground state and two degenerate symmetry-broken (h-)UHF states. This NOCI(3) expansion recovers a bound potential that closely mirrors the CASSCF(2,2) result, where the active space contains the valence σ_g and σ_u molecular orbitals (see Fig. 8.5). Note that the NOCI(3) energy is variationally lower than CASSCF(2,2) in the dissociation limit. However, the NOCI(3) binding curve is only qualitatively correct and misses between $170\text{--}190 \text{ mE}_h$ of the exact energy. Furthermore, NOCI(3) underestimates the binding energy by over 50% and overestimates the bond length by around 0.1 \AA .

Adding the NOCI-PT2 correction to the NOCI(3) reference wave function significantly improves the energy, reducing the error to within 10 mE_h of the FCI energy across the full binding curve and only 4.8 mE_h in the equilibrium region. The NOCI-PT2 energy also shows a remarkable similarity to the CASPT2 energy across the majority of the binding curve. Furthermore, the NOCI-PT2 correction significantly improves the shape of the potential energy surface, with a better estimate of the equilibrium bond length and a reduction in the error of the dissociation energy to only 10 %. These improvements occur even though the properties of the reference NOCI(3) potential energy were comparatively poor. Given the improvement of NOCI gained by adding the non-bonding $\sigma_g\sigma_u$, antibonding σ_u^2 and ionic HF states in Section 7.3.3, it is likely that using the NOCI(8) reference wave function will provide an even more accurate NOCI-PT2 energy. The NOCI-MP2 energy can also be computed using the same NOCI(3) reference wave function. While NOCI-MP2 closely matches NOCI-PT2 in the equilibrium regime, it fails catastrophically for larger bond lengths when the MP2 correction to the reference RHF state breaks down.²⁸⁴

Finally, NOCI-PT2 again suffers from the presence of intruder-state singularities along the F_2 binding curve, demonstrated by the kink at around 2.5 \AA in Fig. 8.5. Adding an imaginary shift of 0.2 E_h again recovers a smooth potential energy with only a minor distortion of the binding curve away from the singularity. However, like H_4 , the modified imaginary shift equations (8.31) are significantly more ill-conditioned than the real linear problem (8.24). This ill-conditioning causes a much slower iterative convergence that fails completely in the vicinity of the Coulson–Fischer point (around 1.32 \AA) where there is the greatest redundancy in the NOCI-PT2 first-order interacting space.

8.4 Concluding Remarks

This chapter has derived a rigorous diagonalise-then-perturb correction to NOCI that captures the remaining dynamic correlation to provide quantitative accuracy. The resulting NOCI-PT2 theory uses a generalised Fock operator to define the reference Hamiltonian and is conceptually related to the CASPT2 extension for CASSCF wave functions.^{75,76} Despite the lack of any convenient Hilbert space partitioning when using a NOCI reference wave function, it has been shown that a first-order interacting space can be constructed using the combined set of single and double excitations built from each reference determinant in the NOCI wave function. This first-order interacting space allows the first-order wave function and second-order energy correction to be defined in terms of a polynomially-scaling number of perturbing determinants. The

resulting NOCI-PT2 equations are closely related to CASPT2 theory⁷⁸ and the recently developed SUPT2 approach,³²⁷ and can be solved using any iterative linear method.

The performance of NOCI-PT2 has been demonstrated by considering a series of small but challenging molecular systems where both static and dynamic correlation effects are important. In each case, NOCI-PT2 provides a similar level of accuracy to CASPT2 computed with a comparable CASSCF reference wave function, highlighting the close relationship between the two theories. Furthermore, NOCI-PT2 has been found to consistently outperform the previous NOCI-MP2 approach,^{134,146,147} particularly in the challenging F_2 molecule where NOCI-MP2 fails completely for large bond lengths. However, like many multireference perturbation theories, NOCI-PT2 suffers from the effects of intruder states that create singularities in the perturbative correction. It has been shown how these singularities can be mitigated by introducing an imaginary shift into the NOCI-PT2 equations in a similar way to the SUPT2 approach.³²⁷

Introducing NOCI-PT2 represents a major theoretical step forward for the NOCI framework. While NOCI provides a similar accuracy to CASSCF wave functions with a similar size, neither are able to capture the dynamic correlation that is required for quantitative energy predictions. In contrast, adding the NOCI-PT2 correction performs an equivalent role to CASPT2 and now brings the combined NOCI/NOCI-PT2 framework level in accuracy to the CASSCF/CASPT2 framework. Furthermore, NOCI-PT2 has similar advantages to NOCI that make both methods conceptually simpler than the CASSCF family of approaches. For example, once a suitable set of reference HF states have been identified, they can simply be followed across a reaction trajectory to compute a smooth energy surface. In this way, NOCI avoids any issues associated with defining an active space or changes in the active orbitals along a reaction trajectory that plague the application of CASSCF. Note that the NOCI-PT2 approach has been derived with sufficient generality that h-HF states can be easily included to ensure smooth energies when real HF states disappear, and complex h-HF solutions have been used extensively throughout this chapter.

8.4.1 Scope for Future Development

While this chapter presents a promising first study on NOCI-PT2, there are several areas that must be addressed to construct an efficient computational approach.

Firstly, the current NOCI-PT2 implementation has been found to suffer from numerical instabilities and slow convergence of the linear perturbation problem, particularly when an imaginary shift is used. This slow convergence is associated with the presence of redundancies in the first-order interacting space that arise by using the combined set of single and double excitations from different nonorthogonal determinants. Further-

more, these effects are most severe in the vicinity of the Coulson–Fischer point where two (or more) reference states and their corresponding excited determinants become equivalent. Approximations to the NOCI-PT2 equations may be required to remove these redundancies by construction, allowing a reliable and efficient computational procedure to be developed. For example, contraction schemes may allow a NOCI-PT2 correction to be solved in the space of non-redundant single and double excitations from each reference. These contracted first-order wave functions could then be interacted through a smaller nonorthogonal expansion.

Secondly, the current NOCI-PT2 implementation involves explicitly building the perturbation matrices and solving them using an iterative linear approach. However, the number of determinants in the first-order interacting space has relatively steep polynomial scaling of $\mathcal{O}(n_{\text{ref}}N^2n^2)$ and the perturbation matrices rapidly develop prohibitive memory costs. Extending the applications of NOCI-PT2 to larger molecular systems or basis sets will therefore require direct iterative approaches where the relevant matrix elements are computed on-the-fly. Furthermore, the matrix elements themselves will then need to be computed using a more efficient approach than the generalised Slater–Condon rules described in Appendix C. The nonorthogonal Wick’s theorem, where matrix elements are described in terms of the corresponding reference determinants, provides a promising alternative to achieve this acceleration.³²⁹

Once a more computationally stable and efficient implementation has been developed, it will be possible to explore how the NOCI-PT2 approach performs in different chemical scenarios. For example, it will be important to establish how the quality of the NOCI-PT2 energy depends on the choice of determinants in the reference NOCI wave function. Only the simplest NOCI wave functions have been considered in this chapter, and the improvement found in Chapter 7 when certain HF states were added to the NOCI basis suggests that the current NOCI-PT2 results can be improved in a similar manner. Furthermore, the performance of NOCI-PT2 for predicting properties beyond the energy must be also be assessed, while a complete theoretical framework will require the development of nuclear gradients of the NOCI-PT2 energy.

Finally, the NOCI-PT2 framework must be generalised and tested for excited state problems. Taking a suitable set of higher energy HF stationary points allows excited states to be considered in the NOCI framework without the state-averaging procedures that are required in excited-state CASSCF. Furthermore, the individual orbital relaxation of high-energy HF solutions can provide a more accurate foundation for constructing the excited-state NOCI energies. The addition of NOCI-PT2 to these reference NOCI wave functions could then present a highly accurate and conceptually simple approach for predicting excited-state properties. While these excited-state NOCI-PT2 calculations

are likely to suffer from intruder-state effects, the imaginary shift developed in this chapter should allow any singularities to be removed.

Ultimately, this chapter has developed a rigorous perturbative correction that now allows quantitative energies to be computed from the NOCI framework. This NOCI-PT2 method provides a similar accuracy as CASPT2, developing the combined NOCI/NOCI-PT2 approach into a viable quantitative alternative to the combined CASSCF/CASPT2 framework.

Chapter 9

Concluding Remarks

Predicting potential energy surfaces for molecules with competing electronic structures is essential for describing dissociating bonds and reactive transition states. However, such cases present major challenges for electronic structure methods that build a correlated wave function from a single reference HF state. The most common solution is to use the multireference CASSCF approach,^{18,19} but optimising the CASSCF wave function is computationally challenging and the cost scales exponentially with the number of correlated electrons. Instead, combining several HF states in a NOCI expansion has been proposed to exploit the natural description of strong correlation provided by multiple HF solutions.^{20,25} However, until now the development of NOCI has stalled because the disappearance of HF states as the molecular structure changes causes unphysical kinks and discontinuities in the NOCI energy.²⁵

This thesis has introduced a new theory — holomorphic Hartree–Fock (h-HF) — to construct a continuous basis for NOCI across all molecular geometries. In h-HF theory, the real HF equations are analytically continued into the complex plane by removing the complex-conjugation of orbital coefficients in the HF energy function. Crucially, every real HF state remains a stationary point of this modified energy function and, when a real HF state coalesces and disappears, its h-HF counterpart continues to exist with complex orbital coefficients. As a result, h-HF states provide complex-analytic continuations of real HF states across all molecular geometries and can be used to define a consistent basis set for NOCI expansions.

The theoretical foundations and understanding that underpin the h-HF approach have been derived in Part II. From a mathematical perspective, the framework of algebraic geometry has allowed the numbers of h-RHF and h-UHF states for two-electron systems to be rigorously derived. These numbers only depend on the size of the spatial basis set, proving that all two-electron h-RHF and h-UHF solutions must exist across all molecular structures. It is highly likely that this rigorous approach could be extended to many-electron systems, supporting the belief that *all* h-HF states must exist across every geometry. Moreover, since real HF states are also h-HF solutions, the

exact number of two-electron h-RHF and h-UHF states provides a rigorous upper bound on the number of real RHF and UHF states respectively. Surprisingly few mathematical properties are known about the HF approach,^{22,23} and the h-HF framework therefore provides incredibly valuable insights into the wider HF approximation.

By forming the complex-analytic continuation of the real HF equations, this thesis has shown that h-HF theory also reveals profound insights into the general nature of molecular electronic states.

Firstly, enforcing certain conditions on the non-Hermitian h-HF equations — in particular symmetry with respect to combined parity-time inversion \mathcal{PT} — has been shown to guarantee real-valued h-HF energies. \mathcal{PT} -symmetry therefore provides an alternative condition to Hermiticity for ensuring real electronic energies, representing a major departure from conventional quantum chemistry. Although this condition has only been demonstrated in the h-HF approach, it is exciting to imagine where \mathcal{PT} -symmetry could be applied elsewhere in electronic structure theory. For example, \mathcal{PT} -symmetric Hamiltonians have previously been found to transform highly non-local systems into localised forms in quantum physics.²⁰² Deriving similar transformations for molecular Hamiltonians could present a powerful tool for developing local descriptions of electron correlation that may lead to linear-scaling methods.³³¹ Furthermore, the addition of real energies through \mathcal{PT} -symmetry introduces a new aspect to non-Hermitian Hamiltonians that describe metastable resonances.¹⁶⁸

Secondly, introducing a complex-scaled electron-electron interaction has revealed that discrete ground and excited h-HF states form a continuous Riemann surface in the complex plane. Each h-HF solution corresponds to an individual sheet on this surface and Coulson–Fischer points form exceptional points where the sheets intersect. This conceptual unification of ground and excited states into one mathematical structure challenges the current perspective of discretised electronic states. In particular, it appears that discrete electronic states only emerge by restricting energies to real values. Furthermore, it has been shown how a ground-state wave function can be naturally evolved into an excited-state wave function by following a complex adiabatic connection on a Riemann surface. Interconverting ground and excited states in this way creates new opportunities for directly computing approximate excited-state wave functions, with the potential for more accurate excitation energies than conventional methods such as CIS²⁵⁹ or EOM-CC.⁶³

In Part III, the development of h-HF theory has been combined with NOCI to construct smooth potential energy surfaces across all geometries. Using an active space SCF metadynamics approach and a complex-scaled electron-electron interaction, it has been shown how h-HF states can be routinely computed across all molecular structures.

The combined h-HF and NOCI approach is found to capture static correlation to a similar extent as CASSCF, while avoiding the coupled optimisation of CASSCF orbital and CI coefficients. Furthermore, using multiple h-HF states to build the multireference expansion avoids issues associated with changes in the CASSCF active orbitals as the molecular structure changes. This thesis has therefore established a viable and much-needed alternative to CASSCF for constructing accurate multireference wave functions.

Finally, a rigorous diagonalise-then-perturb correction to the NOCI reference wave function has been defined, allowing the remaining dynamic correlation to be captured. The resulting NOCI-PT2 theory provides the nonorthogonal analogue to the CASPT2 correction for CASSCF wave functions, and reduces to CASPT2 for a suitable set of orthogonal configurations in the reference wave function. NOCI-PT2 has been shown to provide similar accuracy to CASPT2 energies computed with a multiconfigurational expansion of an equivalent length. Introducing NOCI-PT2 now allows quantitative energy surfaces to be predicted through the multireference NOCI framework.

By deriving h-HF theory, this thesis has developed a general multireference NOCI framework that can be applied across the full potential energy surface. Static correlation is accounted for by the reference NOCI wave function, and dynamic correlation can then be captured through the rigorous NOCI-PT2 correction. Moving forwards, this NOCI framework must be tested across a wider range of molecular systems to understand its applicability and refine these computational approaches. Deriving nuclear gradients for the NOCI energy will enable the optimisation of molecular structures and the use of NOCI potential energy surfaces in *ab initio* molecular dynamics simulations. Ultimately, further exploring these directions will turn NOCI into a self-contained theory with the potential to revolutionise predictions of multireference electronic wave functions.

Appendices

Appendix A

Geometric Holomorphic HF Optimisation

The analytic holomorphic orbital energy gradients energy derived in Section 3.3.3 define the rigorous derivatives required for a direct optimisation of the h-HF energy. Direct optimisation methods including the quasi-Newton approach are widely used to locate stationary points of high-dimensional functions³³² and can provide a useful alternative to the conventional DIIS approach for solving the SCF equations.^{159,161,162,164–167,333} In this appendix, a direct quasi-Newton approach to optimising the h-HF energy is developed that explicitly satisfies the holomorphic complex-orthogonal Grassmannian orbital constraint manifold (see Section 3.3.2.3).

A.1 Quasi-Newton Methods

Quasi-Newton methods are a family of optimisation algorithms that accumulate information about the gradient and approximate Hessian of a function to improve convergence onto local and global minima.³³² Given a vector \mathbf{X}_k on iteration k , quasi-Newton methods attempt to locate stationary points of the function $f(\mathbf{X})$ by taking steps to minimise the Taylor expansion of the gradient as

$$\mathbf{X}_{k+1} = \mathbf{X}_k - \mathbf{B}_k \nabla f(\mathbf{X}_k), \quad (\text{A.1})$$

where the approximate inverse Hessian \mathbf{B}_k is updated iteratively. These algorithms require gradient information but yield quadratic convergence for smooth functions.

The most popular quasi-Newton optimisation routine is the BFGS method,³³² where an approximate inverse Hessian matrix is updated on each step as

$$\mathbf{B}_{k+1} = \left(\mathbf{I} - \frac{\mathbf{p}_k \mathbf{y}_k^\dagger}{\mathbf{y}_k^\dagger \mathbf{p}_k} \right) \mathbf{B}_k \left(\mathbf{I} - \frac{\mathbf{p}_k \mathbf{y}_k^\dagger}{\mathbf{y}_k^\dagger \mathbf{p}_k} \right) + \frac{\mathbf{p}_k \mathbf{p}_k^\dagger}{\mathbf{y}_k^\dagger \mathbf{p}_k}. \quad (\text{A.2})$$

Here $\mathbf{y}_k = \nabla f(\mathbf{X}_{k+1}) - \nabla f(\mathbf{X}_k)$ defines the change in the gradient and $\mathbf{p}_k = \mathbf{X}_{k+1} - \mathbf{X}_k$ is the step taken. Using the BFGS algorithm, the exact minimum for a quadratic form in N dimensions can be located in N iterations.³³⁴ For unconstrained optimisation of a function $f(\mathbf{X})$, where $\mathbf{X} \in \mathbb{C}^N$, the BFGS algorithm proceeds as follows:³³⁴

1. Take an initial guess \mathbf{X}_0 and approximate inverse Hessian $\mathbf{B}_0 = \mathbf{I}$;
2. Obtain the Newton–Raphson step direction $\mathbf{p}_k = -\mathbf{B}_k \nabla f(\mathbf{X}_k)$;
3. Minimise $f(\mathbf{X})$ along a line search in direction \mathbf{p}_k to find the step size α_k ;
4. Update the position, $\mathbf{X}_{k+1} = \mathbf{X}_k + \alpha_k \mathbf{p}_k$;
5. Compute the change in the gradient, $\mathbf{y}_k = \nabla f(\mathbf{X}_{k+1}) - \nabla f(\mathbf{X}_k)$;
6. Update the approximate inverse Hessian using Eq. (A.2);
7. Repeat steps 2–6 until the magnitude of the gradient falls below a certain threshold.

For the case of functions subject to an orthogonality constraint, the required modifications to the quasi-Newton approach have been described in detail by Edelman *et al.*¹⁵⁶ and Lim and Savas.¹⁵⁷ In particular, all gradients and steps must lie in the tangent space to the constraint manifold at a given position. Furthermore, on each quasi-Newton iteration, the previous steps, gradients, and approximate Hessians must be transformed into the new tangent space at the updated position through a process known as ‘parallel transport’.¹⁵⁶ The line search in Step 3 is then restricted to the constraint surface, requiring the use of ‘geodesic’ line searches.

For real-valued Grassmann manifolds, the process of parallel transport can be simplified by exploiting a local representation of the tangent space.¹⁵⁷ At a given point \mathbf{X} , the basis for the tangent space \mathbf{X}_\perp can be used to construct the constrained gradient into a local representation as

$$\nabla f(\mathbf{X}) = \mathbf{X}_\perp^\top \frac{df(\mathbf{X})}{d\mathbf{X}}. \quad (\text{A.3})$$

Significantly, gradients, steps, and approximate inverse Hessians remain constant under the effect of parallel transport. Instead, the tangent basis itself must be parallel-transported along the geodesic in the direction of the step \mathbf{p} with length α as¹⁵⁷

$$\mathbf{X}_\perp(\alpha) = \mathbf{X}_\perp(\mathbf{U} \cos(\boldsymbol{\Sigma}\alpha) \mathbf{U}^\top + \mathbf{I} - \mathbf{U}\mathbf{U}^\top) - \mathbf{X}\mathbf{V} \sin(\boldsymbol{\Sigma}\alpha) \mathbf{U}^\top, \quad (\text{A.4})$$

where $\mathbf{p} = \mathbf{U}\boldsymbol{\Sigma}\mathbf{V}^\top$ is a real singular-value decomposition.

A.2 Optimising the h-HF Energy

Deriving a constrained quasi-Newton method to optimise the h-HF energy can be achieved in a similar manner to the Geometric Direct Minimisation approach¹⁶⁴ for optimising the conventional HF energy, with only a few modifications.

Since the h-HF energy is a complex-valued function, it is not possible to consider the quasi-Newton method as a minimisation approach. Instead, it is tempting to optimise

the real-valued square-magnitude of the h-HF energy gradient $|\nabla\tilde{E}_{\text{HF}}|^2$. However, these modified landscapes are known to suffer from a large number of non-stationary points where $|\nabla E|^2$ becomes a non-zero minimum, causing convergence issues for quasi-Newton optimisation.³³⁵ Despite losing the concept of minimisation, the Newton step of a complex-valued function will still point towards locations where the gradient vanishes. Therefore, the gradient and approximate inverse Hessian of the h-HF energy can still be used to construct search directions for the quasi-Newton algorithm, avoiding any issues associated with $|\nabla\tilde{E}_{\text{HF}}|^2$. The optimal step length can be identified by minimising the magnitude of the gradient or DIIS error during the line-search phase of each iteration.

In the case of h-HF, the constraint surface corresponds to the complex-orthogonal Grassmannian, as described in Section 3.3.2.3. For a given set of orbital coefficients $\mathbf{C} = \begin{pmatrix} \mathbf{C}_{\text{occ}} & \mathbf{C}_{\text{vir}} \end{pmatrix}$, the virtual orbitals represent the basis for the tangent space. Gradients and steps in this tangent space basis can be represented using the block form of a complex-orthogonal transformation defined in Eqs. 3.37 and 3.38. Significantly, the constrained orbital gradient $\mathbf{g}_k = \nabla\tilde{E}_{\text{HF}}(\mathbf{C}_k)$ defined in Eq. (3.46) is already represented in this tangent basis. Furthermore, once an optimal step $\alpha_k \mathbf{p}_k$ has been identified in the tangent basis, the updated occupied and virtual orbitals can be computed using the exponential transformation

$$\mathbf{C}^{(k+1)} = \mathbf{C}^{(k)} \exp \begin{pmatrix} \mathbf{0} & -\alpha_k \mathbf{p}_k^\top \\ \alpha_k \mathbf{p}_k & \mathbf{0} \end{pmatrix}. \quad (\text{A.5})$$

This transformation also parallel-transport the tangent basis represented by the virtual orbitals.

The popular BFGS Hessian update is not necessarily the optimal choice for optimising the h-HF energy. In general, the approximate inverse Hessian should be designed to mirror the properties of the exact Hessian. For example, the BFGS update is designed to maintain Hermiticity and positive-definiteness of the inverse Hessian to encourage global minimisation of a function.

However, for the h-HF energy surface, the exact Hessian forms a complex-symmetric matrix rather than a Hermitian matrix. The complex-conjugation in the Hermitian BFGS update step (A.2) must therefore be replaced with the transpose operator to define a complex-symmetric update. Furthermore, since the concept of minimisation is lost on the complex-valued h-HF energy surface, attempting to maintain positive-definiteness of the inverse Hessian is no longer desirable. Instead, a complex-symmetric variant of the symmetric rank-one (SR1) inverse Hessian update³³² provides a more suitable option for optimising the h-HF energy. The SR1 approach iterates the inverse Hessian

using the update

$$\mathbf{B}_{k+1} = \mathbf{B}_k + \frac{(\mathbf{y}_k - \mathbf{B}_k \mathbf{s}_k)(\mathbf{y}_k - \mathbf{B}_k \mathbf{s}_k)^\top}{(\mathbf{y}_k - \mathbf{B}_k \mathbf{s}_k)^\top \mathbf{s}_k} \quad (\text{A.6})$$

and preserves the complex-symmetry of \mathbf{B} without maintaining positive-definiteness.

Finally, the holomorphic orbital rotation space can become very high dimensional and many iterations may be required to obtain a good approximation of the inverse Hessian. However, the rate of convergence can be accelerated by applying similar coordinate transformations to the conventional Geometric Direct Minimisation approach.¹⁶⁴ In particular, the molecular orbitals on each iteration can be transformed into pseudo-canonical orbitals by diagonalising the occupied-occupied and virtual-virtual blocks of the holomorphic Fock matrix $\tilde{\mathbf{F}}$. The orbital gradients can then be transformed to energy-weighted coordinates using the transformation

$$\bar{g}_{ai} = \frac{g_{ai}}{\sqrt{\tilde{F}_{aa} - \tilde{F}_{ii}}}, \quad (\text{A.7})$$

where $g_{ai} = (\nabla \tilde{E}_{\text{HF}})_{ai}$ corresponds to the h-HF energy gradient in the local basis of occupied-virtual rotations (see Section 3.3.3.2). These energy-weighted coordinates are designed to transform the approximate Hessian $B_{ia,jb} = 2(\tilde{F}_{aa} - \tilde{F}_{ii})\delta_{ij}\delta_{ab}$ into the identity matrix.¹⁶⁷

It is now possible to define a quasi-Newton optimisation scheme for the h-HF energy as follows:

1. Start with an initial set of orbitals $\mathbf{C}^{(0)}$;
2. Pseudo-canonicalise the orbitals using the holomorphic Fock matrix;
3. Transform gradients $\{\mathbf{g}_0, \dots, \mathbf{g}_{k-1}\}$ and steps $\{\mathbf{p}_0, \dots, \mathbf{p}_{k-1}\}$ from previous iterations into the current energy-weighted pseudo-canonical orbitals;
4. Compute the new constrained gradient \mathbf{g}_k using Eq. (3.46) and convert into energy-weighted coordinates using Eq. (A.7);
5. Build the SR1 inverse Hessian \mathbf{B}_k from previous gradients and steps;
6. Compute the approximate Newton–Raphson step $\bar{\mathbf{p}}_k = -\mathbf{B}_k \bar{\mathbf{g}}_k$ and convert back to an occupied-virtual rotation $p_{ai} = \bar{p}_{ai} \sqrt{\tilde{F}_{aa} - \tilde{F}_{ii}}$;
7. Identify the optimal step length α_k by minimising the magnitude of the gradient along a geodesic line search in the direction of \mathbf{p}_k ;
8. Update the orbitals through the complex-orthogonal transformation

$$\mathbf{C}^{(k+1)} = \mathbf{C}^{(k)} \exp \begin{pmatrix} \mathbf{0} & -\alpha_k \mathbf{p}_k^\top \\ \alpha_k \mathbf{p}_k & \mathbf{0} \end{pmatrix}, \quad (\text{A.8})$$

using the expansion (3.39).

9. Repeat Steps 2–8 until convergence is reached.

This second-order approach has been implemented using the LIBGSCF library in the Q-CHEM 5.2 quantum chemistry software package.

Appendix B

\mathcal{T} -Symmetry for General Spins

The derivation presented here loosely follows Weinberg's discussion on the nature of \mathcal{T} in Ref. (231), although notation more familiar to electronic structure is used. Since the action of \mathcal{T} reverses angular momentum, spin-angular momentum operators \hat{s} are required to satisfy

$$\hat{s}\mathcal{T} = -\mathcal{T}\hat{s}, \quad \hat{s}^2\mathcal{T} = \mathcal{T}\hat{s}^2. \quad (\text{B.1})$$

Considering a general spin state $|s, m_s\rangle$ then yields

$$\hat{s}_z[\mathcal{T}|s, m_s\rangle] = -\mathcal{T}\hat{s}_z|s, m_s\rangle = -m_s[\mathcal{T}|s, m_s\rangle], \quad (\text{B.2})$$

$$\hat{s}^2[\mathcal{T}|s, m_s\rangle] = \mathcal{T}\hat{s}^2|s, m_s\rangle = s(s+1)[\mathcal{T}|s, m_s\rangle]. \quad (\text{B.3})$$

In combination, these results imply

$$\mathcal{T}|s, m_s\rangle = \gamma(s, m_s)|s, -m_s\rangle, \quad (\text{B.4})$$

for some complex value $\gamma(s, m_s)$.

To identify the functional form of $\gamma(s, m_s)$, the ladder operators $\hat{s}_\pm = \hat{s}_x \pm i\hat{s}_y$ can be used which, due to the anti-linear character of \mathcal{T} , satisfy

$$\hat{s}_\pm\mathcal{T} = -\mathcal{T}\hat{s}_\mp. \quad (\text{B.5})$$

From the standard ladder operator relationship

$$\hat{s}_\pm = \zeta_\pm(s, m_s)|s, m_s \pm 1\rangle, \quad (\text{B.6})$$

where $\zeta_\pm(s, m_s) = \sqrt{s(s+1) - m_s(m_s \pm 1)}$, one finds

$$\begin{aligned} \hat{s}_\pm\mathcal{T}|s, m_s\rangle &= -\mathcal{T}\hat{s}_\mp|s, m_s\rangle \\ &= -\zeta_\mp(s, m_s)\mathcal{T}|s, m_s \mp 1\rangle. \end{aligned} \quad (\text{B.7})$$

Alternatively, the result of Eq. (B.4) leads to

$$\hat{s}_\pm\mathcal{T}|s, m_s\rangle = \gamma(s, m_s)\zeta_\pm(s, -m_s)|s, -m_s \pm 1\rangle, \quad (\text{B.8})$$

and

$$\mathcal{T}|s, m_s \mp 1\rangle = \gamma(s, m_s \mp 1)|s, -m_s \pm 1\rangle. \quad (\text{B.9})$$

Inserting Eq. (B.8) and Eq. (B.9) into the LHS and RHS of Eq. (B.7) respectively, and noting that $\xi_{\pm}(s, -m_s) = \xi_{\mp}(s, m_s)$, one finds

$$\gamma(s, m_s) = -\gamma(s, m_s \mp 1) = (-1)^{s-m_s}\gamma(s, s). \quad (\text{B.10})$$

Here $\gamma(s, s)$ is an arbitrary complex value that is conventionally set to unity. As a result, the action of \mathcal{T} on a function ϕ , expressed in the basis $\{|s, m_s\rangle\}$ with dimension $n_s = (2s + 1)$, is given by

$$\mathcal{T}\phi = \mathbf{Z}\mathcal{K}\phi, \quad (\text{B.11})$$

where \mathbf{Z} is an $(n_s \times n_s)$ orthogonal matrix representing the action of \mathcal{T} on the spin eigenfunctions, given explicitly as

$$Z_{ij} = \begin{cases} (-1)^{2s+1-i}, & \text{if } i + j = 2(s + 1), \\ 0, & \text{otherwise.} \end{cases} \quad (\text{B.12})$$

Next, consider the specific \mathbf{Z} matrices for various spin cases:

$$\begin{aligned} s = 0 : \mathbf{Z} &= \begin{pmatrix} 1 \end{pmatrix}, \\ s = \frac{1}{2} : \mathbf{Z} &= \begin{pmatrix} 0 & 1 \\ -1 & 0 \end{pmatrix}, \\ s = 1 : \mathbf{Z} &= \begin{pmatrix} 0 & 0 & 1 \\ 0 & -1 & 0 \\ 1 & 0 & 0 \end{pmatrix}, \\ s = \frac{3}{2} : \mathbf{Z} &= \begin{pmatrix} 0 & 0 & 0 & 1 \\ 0 & 0 & -1 & 0 \\ 0 & 1 & 0 & 0 \\ -1 & 0 & 0 & 0 \end{pmatrix}, \\ s = 2 : \mathbf{Z} &= \begin{pmatrix} 0 & 0 & 0 & 0 & 1 \\ 0 & 0 & 0 & -1 & 0 \\ 0 & 0 & 1 & 0 & 0 \\ 0 & -1 & 0 & 0 & 0 \\ 1 & 0 & 0 & 0 & 0 \end{pmatrix}. \\ &\vdots \end{aligned}$$

Significantly, for the bosonic (integer s) case, \mathbf{Z} is symmetric, i.e. $\mathbf{Z} = \mathbf{Z}^T$, while in the fermionic (half-integer s) case, \mathbf{Z} becomes skew-symmetric, i.e. $\mathbf{Z} = -\mathbf{Z}^T$. This

observation leads to two key results. First, considering the operation $\mathcal{T}^2\phi = \mathbf{Z}^2\mathcal{K}^2\phi$ yields $\mathbf{Z}^2 = \mathbf{Z}^\top\mathbf{Z} = \mathbf{I}$ in the bosonic case and $\mathbf{Z}^2 = -\mathbf{Z}^\top\mathbf{Z} = -\mathbf{I}$ for the fermionic case. When combined with the relationship $\mathcal{K}^2 = \mathcal{I}$, this result leads directly to the even and odd character of \mathcal{T} for bosons and fermions respectively. Secondly, since \mathbf{Z} is symmetric and orthogonal in the bosonic case, it can be decomposed into the form $\mathbf{Z} = \mathbf{V}\mathbf{\Sigma}\mathbf{V}^\top$, where \mathbf{V} is orthogonal and $\mathbf{\Sigma}$ is a diagonal matrix containing the eigenvalues of \mathbf{Z} , each equal to -1 or $+1$. Taking $\mathbf{\Sigma} = \boldsymbol{\lambda}\boldsymbol{\lambda}^\top$ gives

$$\mathcal{T}\phi = \mathbf{Z}\mathcal{K}\phi = \mathbf{V}\boldsymbol{\lambda}\boldsymbol{\lambda}^\top\mathbf{V}^\top\mathcal{K}\phi = (\mathbf{V}\boldsymbol{\lambda})\mathcal{K}(\mathbf{V}\boldsymbol{\lambda})^\dagger\phi. \quad (\text{B.13})$$

Consequently, for the bosonic case, one can always find a transformation $(\mathbf{V}\boldsymbol{\lambda})$ into a basis under which the action of time-reversal reduces to $\mathcal{T} = \mathcal{K}$, described in Ref. (227) as a ‘‘canonical’’ bosonic basis. Similarly, in the fermionic case, the properties of skew-symmetric orthogonal matrices allow \mathbf{Z} to be decomposed into the form $\mathbf{Z} = \mathbf{Q}\boldsymbol{\Lambda}\mathbf{Q}^\top$,³³⁶ where \mathbf{Q} is orthogonal and $\boldsymbol{\Lambda}$ takes the form

$$\boldsymbol{\Lambda} = \begin{pmatrix} i\sigma_y & & \\ & \ddots & \\ & & i\sigma_y \end{pmatrix}. \quad (\text{B.14})$$

As a result, the action of \mathcal{T} can be expressed as

$$\mathcal{T}\phi = \mathbf{Z}\mathcal{K}\phi = \mathbf{Q}\boldsymbol{\Lambda}\mathbf{Q}^\top\mathcal{K}\phi = (\mathbf{Q})\boldsymbol{\Lambda}\mathcal{K}(\mathbf{Q})^\dagger\phi, \quad (\text{B.15})$$

and thus, for fermionic systems, it is always possible to find a transformation \mathbf{Q} into a canonical fermionic basis in which the action of time-reversal reduces to $\mathcal{T} = \boldsymbol{\Lambda}\mathcal{K}$.²²⁷

Appendix C

Computing NOCI Matrix Elements

Matrix elements between nonorthogonal determinants built from different sets of molecular determinants can be evaluated using the generalised Slater–Condon rules as described in Ref. (40). In this appendix, general forms for the matrix elements used in this thesis are derived. Only one-particle and two-particle operators are considered, which can be represented in their most general form as

$$\hat{O}_1 = \sum_i^N \hat{o}_1(i) \quad \text{and} \quad \hat{O}_2 = \sum_{i<j}^N \hat{o}_2(i, j) \quad (\text{C.1})$$

respectively. A general Slater determinant $|^x\Psi\rangle$ is built from N occupied molecular orbitals (MOs), $\{|^x\psi_i\rangle\}$, which themselves are formed from a linear combination of $2n$ (non-orthogonal) atomic spin orbitals (AOs), $\{|\eta_\mu\rangle\}$, as

$$|^x\psi_i\rangle = \sum_\mu^{2n} |\eta_\mu\rangle {}^xC_{.i}^\mu, \quad (\text{C.2})$$

where n is the size of the spatial basis set.

Evaluating the matrix elements between two nonorthogonal determinants $|^x\Psi\rangle$ and $|^w\Psi\rangle$ is greatly simplified if the orbitals are converted into a biorthogonal basis using Löwdin’s pairing approach.^{137,138} First, the overlap matrix between the two sets of occupied orbitals is constructed as

$${}^{wx}S_{ij} = \langle {}^w\psi_i | {}^x\psi_j \rangle = \sum_{\mu\nu}^{2n} ({}^wC^*)_{i.\mu} S_{\mu\nu} ({}^xC)_{.j\nu}. \quad (\text{C.3})$$

The singular-value decomposition ${}^{wx}S = \mathbf{U}\tilde{\mathbf{S}}\mathbf{V}^\dagger$ then allows each set of occupied orbitals to be transformed as

$$|^x\tilde{\psi}_j\rangle = \sum_\mu^{2n} |\eta_\mu\rangle {}^xC_{.j}^{\tilde{\mu}} \quad \text{and} \quad |^w\tilde{\psi}_j\rangle = \sum_\mu^{2n} |\eta_\mu\rangle {}^wC_{.j}^{\tilde{\mu}} \quad (\text{C.4})$$

such that their overlap is diagonal

$${}^{wx}\tilde{S}_{ij} = \langle {}^w\tilde{\psi}_i | {}^x\tilde{\psi}_j \rangle = s_i \delta_{ij}. \quad (\text{C.5})$$

Here the transformed molecular orbital coefficients are given by ${}^x\tilde{C}_{.j}^{\mu\cdot} = {}^xC_{.i}^{\mu\cdot} V_{ij}$ and ${}^w\tilde{C}_{.j}^{\mu\cdot} = {}^wC_{.i}^{\mu\cdot} U_{ij}$. Note that when holomorphic orbitals satisfying the complex-orthogonality constraint are used in the NOCI expansion, this transformation restores unitarity of the occupied orbitals. The unitary \mathbf{U} and \mathbf{V} transformations can introduce phase factors into the Slater determinants that must be removed by ensuring $\det(\mathbf{U}) = 1$ and $\det(\mathbf{V}) = 1$.

Although the transformed overlap matrix is diagonal, these biorthogonal orbitals are not mutually orthonormal and the diagonal elements fall in the range $0 \leq s_i \leq 1$. The overlap matrix element between two determinants can then be trivially computed from the diagonal elements as

$${}^{wx}\mathcal{S} = \langle {}^w\Psi | {}^x\Psi \rangle = \prod_i^N s_i. \quad (\text{C.6})$$

In what follows, it will be useful to follow Ref. (25) and define a ‘‘reduced overlap’’ ${}^{wx}\tilde{\mathcal{S}}$ as the product of non-zero single-orbital overlaps

$${}^{wx}\tilde{\mathcal{S}} = \prod_{\substack{i \\ s_i \neq 0}}^N s_i. \quad (\text{C.7})$$

Furthermore, introducing the co-density matrix

$${}^{wx}P_i^{\mu\nu} = ({}^x\tilde{C})_{.i}^{\mu\cdot} ({}^w\tilde{C}^*)_{.i}^{\nu\cdot} \quad (\text{C.8})$$

and the weighted co-density matrix

$${}^{wx}W^{\mu\nu} = \sum_i^N ({}^x\tilde{C})_{.i}^{\mu\cdot} \frac{1}{s_i} ({}^w\tilde{C}^*)_{.i}^{\nu\cdot} \quad (\text{C.9})$$

will allow matrix forms to be derived for each relevant integral.

For a one-electron operator \hat{O}_1 the generalised Slater–Condon rules⁴⁰ lead to

$$\langle {}^w\Psi | \hat{O}_1 | {}^x\Psi \rangle = \sum_i^N \langle {}^w\tilde{\psi}_i | \hat{O}_1 | {}^x\tilde{\psi}_i \rangle \prod_{k \neq i}^N \langle {}^w\tilde{\psi}_k | {}^x\tilde{\psi}_k \rangle. \quad (\text{C.10})$$

Depending on the number of zero-overlap elements between the biorthogonal orbitals, the integral $\langle {}^w\Psi | \hat{O}_1 | {}^x\Psi \rangle$ can be represented in matrix form as

$$\text{None:} \quad {}^{wx}\tilde{\mathcal{S}} \sum_{\mu\nu}^{2n} {}^{wx}W^{\nu\mu} \langle \mu | \hat{O}_1 | \nu \rangle, \quad (\text{C.11a})$$

$$s_i = 0 : \quad {}^{wx}\tilde{\mathcal{S}} \sum_{\mu\nu}^{2n} {}^{wx}P_i^{\nu\mu} \langle \mu | \hat{O}_1 | \nu \rangle, \quad (\text{C.11b})$$

$$> 2 : \quad 0. \quad (\text{C.11c})$$

Here, $\langle \mu | \hat{o}_1 | \nu \rangle = \langle \eta_\mu | \hat{o}_1 | \eta_\nu \rangle$ define the one-electron integrals in the spin-orbital basis. Similarly, for a two-electron operator \hat{O}_2 the generalised Slater–Condon rules⁴⁰ lead to

$$\langle {}^w\Psi | \hat{O}_2 | {}^x\Psi \rangle = \sum_{i < j}^N \left[\langle {}^w\tilde{\psi}_i {}^w\tilde{\psi}_j | \hat{O}_2 | {}^x\tilde{\psi}_i {}^x\tilde{\psi}_j \rangle - \langle {}^w\tilde{\psi}_i {}^w\tilde{\psi}_j | \hat{O}_2 | {}^x\tilde{\psi}_j {}^x\tilde{\psi}_i \rangle \right] \prod_{k \neq i,j}^N \langle {}^w\tilde{\psi}_k | {}^x\tilde{\psi}_k \rangle. \quad (\text{C.12})$$

Again, the (weighted) co-density matrices can be used to define matrix forms for the integral $\langle {}^w\Psi | \hat{O}_2 | {}^x\Psi \rangle$ depending on the number of zero-overlap elements between the biorthogonal orbitals to give

$$\text{None:} \quad \frac{1}{2} {}^{wx}\tilde{S} \sum_{\mu\nu\sigma\tau}^{2n} {}^{wx}W^{\nu\mu} [\langle \mu\sigma | \hat{o}_2 | \nu\tau \rangle - \langle \mu\sigma | \hat{o}_2 | \tau\nu \rangle] {}^{wx}W^{\tau\sigma}, \quad (\text{C.13a})$$

$$s_i = 0: \quad {}^{wx}\tilde{S} \sum_{\mu\nu\sigma\tau}^{2n} {}^{wx}P_i^{\nu\mu} [\langle \mu\sigma | \hat{o}_2 | \nu\tau \rangle - \langle \mu\sigma | \hat{o}_2 | \tau\nu \rangle] {}^{wx}W^{\tau\sigma}, \quad (\text{C.13b})$$

$$s_i, s_j = 0: \quad {}^{wx}\tilde{S} \sum_{\mu\nu\sigma\tau}^{2n} {}^{wx}P_i^{\nu\mu} [\langle \mu\sigma | \hat{o}_2 | \nu\tau \rangle - \langle \mu\sigma | \hat{o}_2 | \tau\nu \rangle] {}^{wx}P_j^{\tau\sigma}, \quad (\text{C.13c})$$

$$> 2: \quad 0, \quad (\text{C.13d})$$

where $\langle \mu\sigma | \hat{o}_2 | \nu\tau \rangle = \langle \eta_\mu \eta_\sigma | \hat{o}_2 | \eta_\nu \eta_\tau \rangle$ defines the two-electron integral in the spin-orbital basis. These general forms for one- and two-electron integrals now make it possible to explicitly define the Hamiltonian and Fock matrix elements used within this thesis, as given in Table C.1 and Table C.2.

Finally, in Chapter 8 the one-particle NOCI density matrix is used to construct a generalised Fock operator for a given NOCI wave function

$$|\Psi\rangle = \sum_w^{n_{\text{ref}}} |{}^w\Psi\rangle c_w. \quad (\text{C.14})$$

Following Ref. (139), the one-particle density operator

$$\hat{\rho}(x) = \sum_{i=1}^N \delta(x_i - x) \quad (\text{C.15})$$

can be used to define the corresponding NOCI density as

$$\rho_\Psi(x) = \sum_{i=1}^N \langle \Psi | \delta(x_i - x) | \Psi \rangle = \sum_{wx}^{n_{\text{ref}}} c_w^* {}^{wx}\rho(r) c_x, \quad (\text{C.16})$$

where ${}^{wx}\rho(x)$ is the co-density operator given by

$${}^{wx}\rho(x) = \sum_{i=1}^N \langle {}^w\Psi | \delta(x_i - x) | {}^x\Psi \rangle. \quad (\text{C.17})$$

Using biorthogonal molecular orbitals, the co-density can be represented as

$${}^{wx}\rho(r) = \sum_{\mu\nu}^{2n} |\eta_\mu(x)\rangle {}^{wx}\rho^{\mu\nu} \langle \eta_\nu(x)|, \quad (\text{C.18})$$

where the matrix elements ${}^{wx}\rho^{\mu\nu}$ can be computed using the generalised Slater–Condon rules as given Table C.3. The combined one-particle density matrix corresponding to the NOCI wave function is then given in the spin-orbital basis as

$$\rho_{\Psi}(\mathbf{x}) = \sum_{\mu\nu}^{2n} |\eta_{\mu}(\mathbf{x})\rangle (P_{\Psi})^{\mu\nu} \langle \eta_{\nu}(\mathbf{x})|, \quad (\text{C.19})$$

where

$$(P_{\Psi})^{\mu\nu} = \sum_{wx}^{n_{\text{ref}}} c_w^* {}^{wx}\rho^{\mu\nu} c_x. \quad (\text{C.20})$$

Zeros in $\{s_i\}$	H^{wx}
None	$\left(V_N + \sum_{\mu\nu}^{2n} {}^{wx}W^{\nu\mu} h_{\mu\nu} + \frac{1}{2} \sum_{\mu\nu\sigma\tau}^{2n} {}^{wx}W^{\nu\mu} \langle \mu\sigma \nu\tau \rangle {}^{wx}W^{\tau\sigma} \right) {}^{wx}\tilde{\mathcal{S}}$
s_i	$\left(\sum_{\mu\nu}^{2n} {}^{wx}P_i^{\nu\mu} h_{\mu\nu} + \sum_{\mu\nu\sigma\tau}^{2n} {}^{wx}P_i^{\nu\mu} \langle \mu\sigma \nu\tau \rangle {}^{wx}W^{\tau\sigma} \right) {}^{wx}\tilde{\mathcal{S}}$
s_i, s_j	$\left(\sum_{\mu\nu\sigma\tau}^{2n} {}^{wx}P_i^{\nu\mu} \langle \mu\sigma \nu\tau \rangle {}^{wx}P_j^{\tau\sigma} \right) {}^{wx}\tilde{\mathcal{S}}$
> 2	0

Table C.1: Hamiltonian matrix elements $H^{wx} = \langle {}^w\Psi | \hat{H} | {}^x\Psi \rangle$ between two nonorthogonal states $|{}^w\Psi\rangle$ and $|{}^x\Psi\rangle$ with biorthogonal orbitals $|{}^w\tilde{\psi}_i\rangle$ and $|{}^x\tilde{\psi}_i\rangle$ respectively. $h_{\mu\nu}$ and $\langle \mu\sigma || \nu\tau \rangle$ define the one- and antisymmetrised two-electron integrals in the atomic spin-orbital basis, while V_N is the nuclear repulsion.

Zeros in $\{s_i\}$	F^{wx}
None	$\left(\sum_{\mu\nu}^{2n} {}^{wx}W^{\nu\mu} F_{\mu\nu} \right) {}^{wx}\tilde{\mathcal{S}}$
s_i	$\left(\sum_{\mu\nu}^{2n} {}^{wx}P_i^{\nu\mu} F_{\mu\nu} \right) {}^{wx}\tilde{\mathcal{S}}$
> 1	0

Table C.2: Fock matrix elements $F^{wx} = \langle {}^w\Psi | \hat{F} | {}^x\Psi \rangle$ between two nonorthogonal states $|{}^w\Psi\rangle$ and $|{}^x\Psi\rangle$ with biorthogonal orbitals $|{}^w\tilde{\psi}_i\rangle$ and $|{}^x\tilde{\psi}_i\rangle$ respectively. $F_{\mu\nu}$ defines the Fock matrix element in the atomic spin-orbital basis.

Zeros in $\{s_i\}$	${}^{wx}\rho^{\mu\nu}$
None	${}^{wx}\tilde{\mathcal{S}} {}^{wx}W^{\mu\nu}$
s_i	${}^{wx}\tilde{\mathcal{S}} {}^{wx}P_i^{\mu\nu}$
> 1	0

Table C.3: Density matrix elements ${}^{wx}\rho^{\mu\nu}$ between two nonorthogonal states $|{}^w\Psi\rangle$ and $|{}^x\Psi\rangle$ with biorthogonal orbitals $|{}^w\tilde{\psi}_i\rangle$ and $|{}^x\tilde{\psi}_i\rangle$ respectively.

Appendix D

Active-Space Metadynamics

Chapter 7 proposes an active space variant of SCF metadynamics²⁰ to assist the identification of chemically relevant real HF states. Computationally implementing active space SCF metadynamics requires only minimal modifications to the conventional approach and involves:

- (i) Optimising HF wave functions with frozen orbitals;
- (ii) Applying the SCF metadynamics search within active orbitals.

This appendix provides a detailed description of these two components.

D.1 Hartree–Fock Optimisation using Frozen Orbitals

The HF wave function, represented by a single Slater determinant, can be parameterised in terms of molecular orbitals expanded in the $2n$ -dimensional spin-orbital basis $\{\eta(\mathbf{x})\} = \{\chi(\mathbf{r})\} \otimes \{\alpha(\sigma), \beta(\sigma)\}$ as

$$\psi_i(\mathbf{x}) = \sum_{\mu}^{2n} \eta_{\mu}(\mathbf{x}) C_{\cdot i}^{\mu}, \quad (\text{D.1})$$

where $\{C_{\cdot i}^{\mu}\}$ define the molecular orbital coefficients. Consider optimising a determinant of this form with inactive occupied orbitals (i, j, k, \dots), frozen virtual orbitals (a, b, c, \dots), and n_{act} active orbitals (p, q, r, \dots). The SCF procedure with DIIS extrapolation^{150,151} can be applied using only two major modifications. In what follows, the conventional HF approach is applied using Hermitian Fock matrices and unitary orbitals.

Firstly, the Fock matrix on the k -th iteration $F^{(k)}$ is diagonalised by projecting the full Fock matrix into the subspace spanned by the active orbitals to give

$$f_{pq}^{(k)} = \sum_{\mu\nu}^{2n} (C^{(k)*})_{p\cdot}^{\mu} F_{\mu\nu}^{(k)} (C^{(k)})_{\cdot q}^{\nu}. \quad (\text{D.2})$$

where $(C^{(k)})_{\cdot q}^{\nu}$ defines the molecular orbital coefficients on iteration k . Note that the Fock matrix $F^{(k)}$ is built using the density of *all* occupied molecular orbitals, and the active-space Fock matrix $f^{(k)}$ corresponds to the active-active block of the full Fock matrix $F^{(k)}$ in the molecular orbital basis. This active-space Fock matrix can be diagonalised to give the $n_{\text{act}} \times n_{\text{act}}$ transformation Q among the active orbitals

$$\sum_q^{n_{\text{act}}} f_{pq}^{(k)} Q_{qr}^{(k)} = Q_{pr}^{(k)} \epsilon_r. \quad (\text{D.3})$$

New active orbitals in the full space can then be computed as

$$(C^{(k+1)})_{\cdot r}^{\mu} = \sum_p^{n_{\text{act}}} (C^{(k)})_{\cdot p}^{\mu} Q_{pr}^{(k)} \quad (\text{D.4})$$

with corresponding orbital eigenvalues ϵ_r . The occupied orbitals chosen from these new active orbitals can be determined using either the *aufbau* principle⁸ or projection-based schemes such as MOM.²⁶ In this process, the remaining inactive occupied orbitals and frozen virtual orbitals are unchanged.

Secondly, the DIIS extrapolation scheme must be modified by projecting the full error matrix

$$e_{\mu\nu} = \sum_{\sigma\tau}^{2n} [F_{\mu\sigma} P^{\sigma\tau} S_{\tau\nu} - S_{\mu\sigma} P^{\sigma\tau} F_{\tau\nu}] \quad (\text{D.5})$$

into the active orbital space to give

$$\bar{e}_{\mu\nu} = \sum_{\sigma\tau\lambda\gamma}^{2n} S_{\mu\sigma} (P_{\text{act}})^{\sigma\tau} e_{\tau\lambda} (P_{\text{act}})^{\lambda\gamma} S_{\gamma\nu}, \quad (\text{D.6})$$

where P_{act} is the projector onto the active orbital space, defined as

$$(P_{\text{act}})^{\mu\nu} = \sum_p^{n_{\text{act}}} C_{\cdot p}^{\mu} (C^*)_{p\cdot}^{\nu}. \quad (\text{D.7})$$

Representing the active-space error matrix in the full space in this way means that DIIS extrapolation is still defined in the full orbital space but only changes the active-active block of the Fock matrix. Furthermore, the magnitude of the active-space error vector $\bar{e}_{\mu\nu}$ provides a metric for convergence.

An active-space SCF optimisation can be summarised as follows:

1. Take an initial set of coefficients C_i^{μ} and active orbital indices $\{p, q, r, \dots\}$;
2. Form the one-particle density matrix (1.29) and Fock matrix (1.28);
3. Project the DIIS error matrix (D.5) into the active orbital space using Eq. (D.6);
4. Perform the DIIS extrapolation using the projected error matrices and full Fock matrices from the current and previous iterations;

5. Project the extrapolated Fock matrix into the active orbital space using Eq. (D.2);
6. Diagonalise the active-space Fock matrix to identify the transformation (D.3);
7. Update the active orbitals using Eq. (D.4) and select new occupied orbitals;
8. Repeat steps 2–7 until convergence is reached.

D.2 SCF Metadynamics with Active Orbitals

Several partially-optimised HF states can be identified using the active-space SCF approach by introducing an active-space variant on the SCF metadynamics method described in Section 2.2.3.2. In SCF metadynamics, the conventional SCF procedure is modified by adding a Gaussian potential to the Fock matrix to bias the optimisation away from previously located HF solutions.²⁰ This bias is introduced computationally by defining a modified Fock matrix

$$F'_{\mu\nu} = F_{\mu\nu} + \sum_w {}^w P_{\mu\nu} N_w \lambda_w e^{-\lambda_w d_{0w}^2}, \quad (\text{D.8})$$

where ${}^w P_{\mu\nu}$ is the density matrix of the previous state w , N_w and λ_w correspond to the height and width of the bias potential, and d_{0w}^2 is the distance between state w and the density currently undergoing optimisation. The biasing potential is removed for a DIIS error below 10^{-5} to allow a true stationary point to be identified. Crucially this biased Fock matrix can be directly used in Step 2 of the active-space SCF optimisation described in Section D.1. This work uses initial values of $N_w = \lambda_w = 1$ and scales the height and width of the Gaussian by a factor of 1.01 each time the biased optimisation re-converges to a previously found solution.

With the biased optimisation procedure largely unchanged using an active-orbital space, only the generation of random guesses needs to be altered. In the original SCF metadynamics algorithm, random initial guesses are generated by mixing two occupied and virtual orbitals, selected either randomly or depending on how close their energies lie to the Fermi level.²⁰ Using active orbitals, the selection criteria is modified to only involve rotations between an occupied or virtual orbital in the active space. In this work, each initial guess is generated by repeatedly selecting an active orbital pair p, q and introducing an orbital rotation selected from a uniform random number in the range $\theta \in [0, 3\pi]$ to give the modified orbitals

$$\begin{aligned} \tilde{\phi}_p &= \phi_p \cos(\theta) - \phi_q \sin(\theta) \\ \tilde{\phi}_q &= \phi_p \sin(\theta) + \phi_q \cos(\theta). \end{aligned} \quad (\text{D.9})$$

This selection and rotation process is repeated ten times for each initial guess, and an occupied orbital may therefore undergo repeated mixing with different virtual orbitals.

Once a set of partially-optimised HF wave functions have been identified using active-space SCF metadynamics, they can be individually optimised in the full orbital space to yield fully stationary HF states. There is no guarantee that each partially-optimised HF state corresponds to a fully stationary HF solution.

Appendix E

Benchmark Selected CI Calculations

E.1 Computational Details

To obtain an estimate of the exact FCI excitation energies in ethene and cyclobutadiene, the CI expansion is iteratively grown using the CIPSI (CI using a perturbative selection made iteratively) approach^{51,275,276} implemented in QUANTUM PACKAGE 2.0.²⁸⁰ Starting from the CIS wave function, and using the frozen core approximation, the truncated CI space is grown as large as computationally feasible. At each iteration, the variational energy E_{var} of the truncated CI wave function and a second-order perturbative correction E_{PT2} are computed. In the FCI limit, one expects $E_{\text{var}} \rightarrow E_{\text{FCI}}$ and $E_{\text{PT2}} \rightarrow 0$.

Following previous work,^{257,277,278,337} E_{var} is extrapolated against E_{PT2} to obtain the extrapolated FCI (ex-FCI) estimate $E_{\text{ex-FCI}}$ corresponding to $E_{\text{PT2}} = 0$. Similarly to the approach described by Loos *et al.*,²⁵⁷ the average of a two- and three-point linear fit is taken to estimate the value of $E_{\text{ex-FCI}}$, while the spread of these fits is used to assess the error associated with this extrapolation. Using the algorithm implemented in QUANTUM PACKAGE 2.0, the E_{PT2} correction is evaluated through a hybrid stochastic-deterministic algorithm.³³⁸ To ensure spin-purity and treat ground and excited states as evenly as possible, all the singlet states are determined using a common set of n_{det} determinants while the triplet state is computed in a separate calculation with a similar number of determinants.

E.2 Results

E.2.1 D_{2h} Ethene

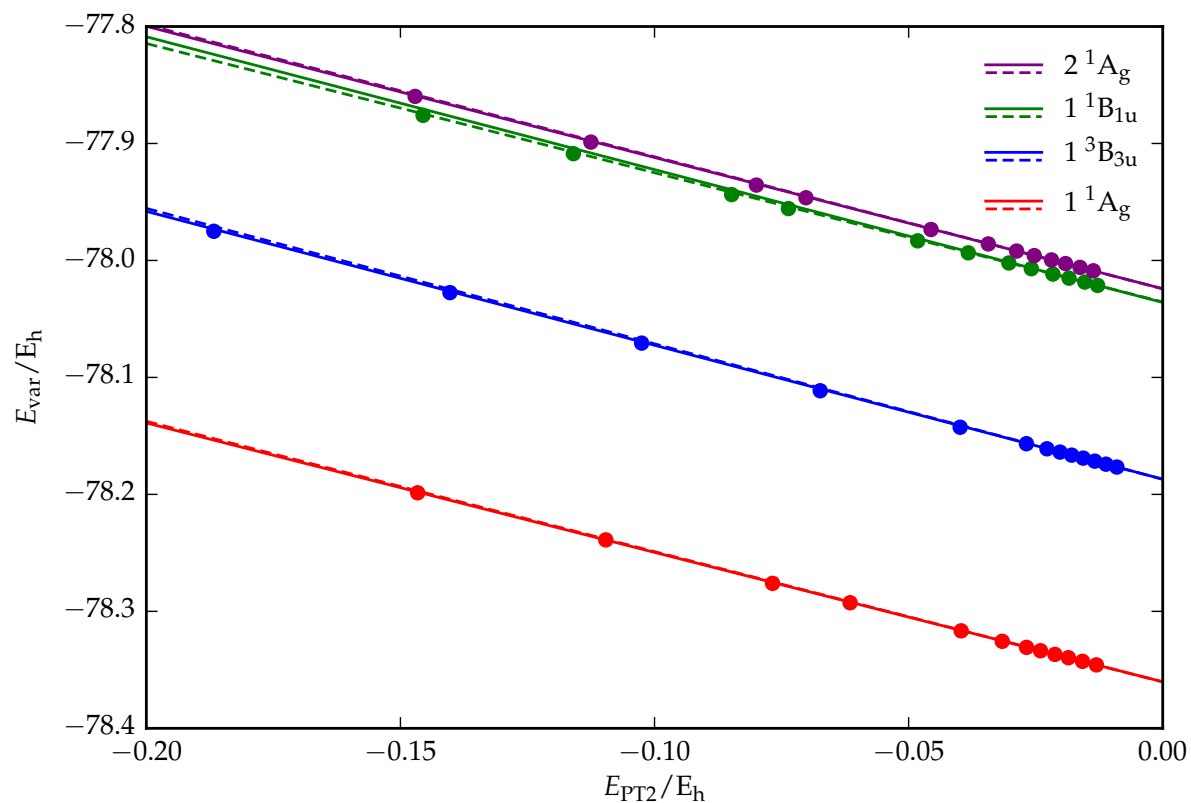


Figure E.1: Extrapolation of the variational energy E_{var} against the perturbative correction $E_{\text{PT}2}$ for the ground and excited states of D_{2h} ethene (cc-pVDZ) using two-point (solid lines) and three-point (dashed lines) linear fits.

n_{det}	$E_{\text{var}}(1^1A_{1g})$	$E_{\text{PT2}}(1^1A_{1g})$	$E_{\text{var}}(1^1B_{1u})$	$E_{\text{PT2}}(1^1B_{1u})$	$E_{\text{var}}(2^1A_{1g})$	$E_{\text{PT2}}(2^1A_{1g})$
641	-78.04016520	-0.35961126	-77.72708282	-0.34408610	-77.70304874	-0.35307349
1286	-78.11007858	-0.25428215	-77.79873070	-0.23959741	-77.78362563	-0.23649222
2590	-78.15098648	-0.20523323	-77.84064224	-0.19000712	-77.82048528	-0.19411060
5196	-78.19864538	-0.14660770	-77.87596631	-0.14554883	-77.85974925	-0.14711380
10397	-78.23890542	-0.10959129	-77.90871078	-0.11597205	-77.89882301	-0.11251691
20809	-78.27604203	-0.07677185	-77.94371771	-0.08482635	-77.93556822	-0.07995609
27202	-78.29263936	-0.06151420	-77.95566217	-0.07365331	-77.94642385	-0.07020143
54410	-78.31666712	-0.03966251	-77.98325491	-0.04821394	-77.97353010	-0.04559195
89526	-78.32558311	-0.03158065	-77.99350189	-0.03826005	-77.98588643	-0.03432285
179063	-78.33079370	-0.02679558	-78.00215985	-0.03027616	-77.99196659	-0.02874947
322139	-78.33367828	-0.02404678	-78.00704649	-0.02585648	-77.99584369	-0.02528330
644283	-78.33678722	-0.02120961	-78.01162647	-0.02161513	-77.99956402	-0.02188181
1195632	-78.33961768	-0.01856781	-78.01512548	-0.01843841	-78.00267343	-0.01911907
2390986	-78.34273852	-0.01578328	-78.01848654	-0.01533082	-78.00590328	-0.01627439
4651445	-78.34576640	-0.01304674	-78.02135100	-0.01280843	-78.00884348	-0.01365302

Table E.1: Variational energy E_{var} and perturbative correction E_{PT2} for the singlet states of \mathcal{D}_{2h} ethene. All energies are given in Hartrees using the cc-pVDZ basis set.

n_{det}	$E_{\text{var}}(^3\text{B}_{3u})$	$E_{\text{PT2}}(^3\text{B}_{3u})$
641	-77.89850575	-0.26131582
1287	-77.97506643	-0.18672418
2577	-78.02749474	-0.14025758
5163	-78.07067841	-0.10253654
10333	-78.11141429	-0.06739522
20673	-78.14259214	-0.03985883
41359	-78.15668333	-0.02681712
82723	-78.16102585	-0.02277490
165455	-78.16383991	-0.02020561
330927	-78.16643860	-0.01790732
661843	-78.16898308	-0.01564041
1323661	-78.17159575	-0.01336839
2646843	-78.17416444	-0.01117394
5291845	-78.17662492	-0.00902446

Table E.2: Variational energy E_{var} and perturbative correction E_{PT2} for the triplet ground state of \mathcal{D}_{2h} ethene. All energies are given in Hartrees using the cc-pVDZ basis set.

	$E_{\text{ex-FCI}}(1^1\text{A}_g)$	$E_{\text{ex-FCI}}(^3\text{B}_{3u})$	$E_{\text{ex-FCI}}(^1\text{B}_{1u})$	$E_{\text{ex-FCI}}(2^1\text{A}_g)$
Two-Point	-78.36020210	-78.18695516	-78.03589640	-78.02415704
Three-Point	-78.36030323	-78.18708283	-78.03547488	-78.02426268

Table E.3: Extrapolated FCI energy $E_{\text{ex-FCI}}$ for the ground and excited states of \mathcal{D}_{2h} ethene using two- and three-point linear fits. All energies are given in Hartrees using the cc-pVDZ basis set.

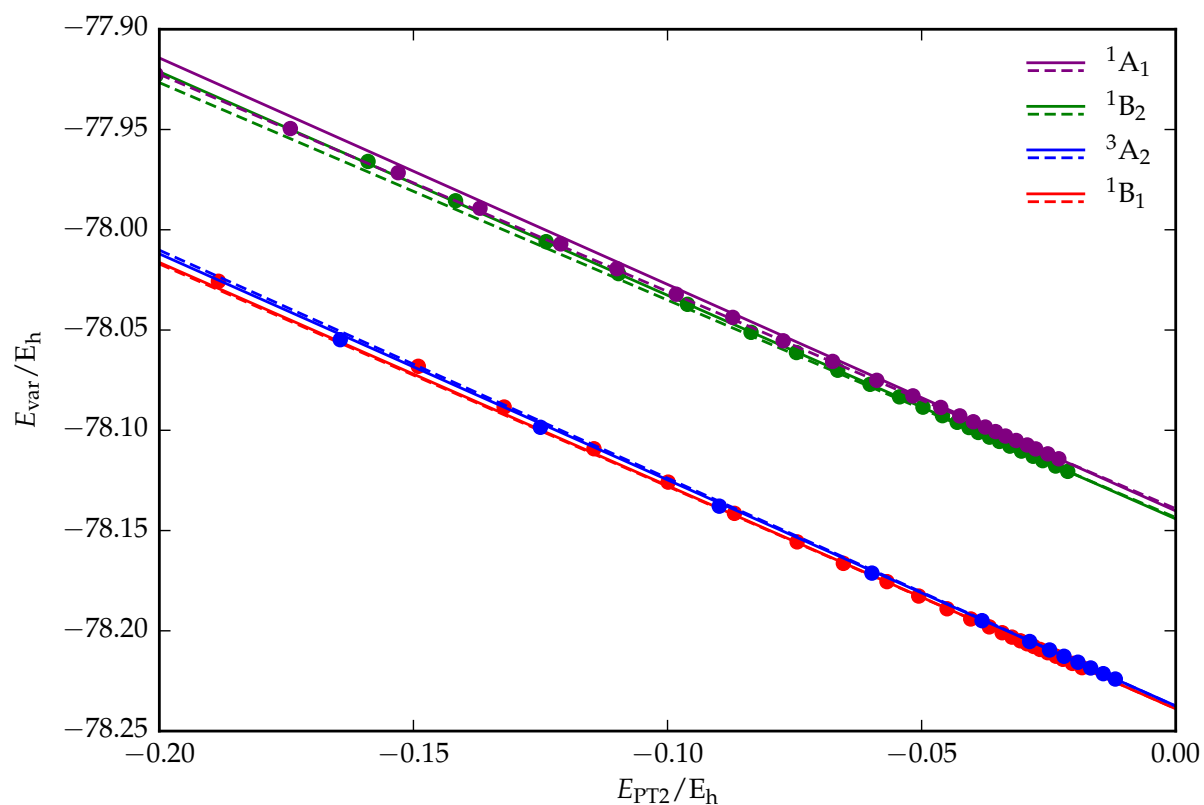
E.2.2 \mathcal{D}_{2d} Ethene

Figure E.2: Extrapolation of the variational energy E_{var} against the perturbative correction $E_{\text{PT}2}$ for the ground and excited states of \mathcal{D}_{2d} ethene (cc-pVDZ) using two-point (solid lines) and three-point (dashed lines) linear fits.

n_{det}	$E_{\text{var}}(^1B_1)$	$E_{\text{pr}2}(^1B_1)$	$E_{\text{var}}(^1B_2)$	$E_{\text{pr}2}(^1B_2)$	$E_{\text{var}}(^1A_1)$	$E_{\text{pr}2}(^1A_1)$
641	-77.86163319	-0.28058332	-77.82275364	-0.23525159	-77.63678258	-0.24818157
1280	-77.96915781	-0.24213624	-77.87936731	-0.23879623	-77.85967742	-0.26735992
2143	-78.02567067	-0.18838027	-77.92304866	-0.20065332	-77.89711762	-0.22507747
3647	-78.06808356	-0.14904371	-77.96592259	-0.15893355	-77.92241363	-0.20068114
5368	-78.08840001	-0.13215279	-77.98554108	-0.14171706	-77.94951884	-0.17422036
7641	-78.10920682	-0.11447785	-78.00593360	-0.12389257	-77.97153433	-0.15300443
10192	-78.12584490	-0.09988340	-78.02186691	-0.10964351	-77.98925151	-0.13690414
13621	-78.14142232	-0.08683403	-78.03717441	-0.09607693	-78.00704783	-0.12101311
17598	-78.15564929	-0.07450096	-78.05114543	-0.08356889	-78.01940045	-0.10997108
21975	-78.16636353	-0.06540159	-78.06122331	-0.07463370	-78.03213012	-0.09829029
27159	-78.17547829	-0.05681703	-78.07004494	-0.06651097	-78.04369216	-0.08716036
33202	-78.18266637	-0.05057198	-78.07707576	-0.06014337	-78.05537414	-0.07724336
40567	-78.18901227	-0.04499262	-78.08332700	-0.05434780	-78.06564979	-0.06751135
49204	-78.19409194	-0.04033848	-78.08845747	-0.04973922	-78.07507986	-0.05882486
59533	-78.19803804	-0.03668129	-78.09271101	-0.04589727	-78.08283622	-0.05171392
70887	-78.20095988	-0.03415348	-78.09601671	-0.04299891	-78.08859912	-0.04623654
83807	-78.20313994	-0.03222775	-78.09862321	-0.04068182	-78.09282298	-0.04249203
99984	-78.20498363	-0.03057054	-78.10108076	-0.03884852	-78.09574695	-0.03983214
121508	-78.20647364	-0.02923054	-78.10341357	-0.03664020	-78.09838088	-0.03747423
149508	-78.20779708	-0.02794807	-78.10555369	-0.03469343	-78.10064898	-0.03544901
192977	-78.20929401	-0.02668568	-78.10789631	-0.03263385	-78.10286925	-0.03348302
260900	-78.21092236	-0.02519284	-78.11037885	-0.03036509	-78.10508238	-0.03139155
369812	-78.21266855	-0.02356205	-78.11295389	-0.02806273	-78.10732531	-0.02922391
513016	-78.21420654	-0.02219699	-78.11514458	-0.02616862	-78.10928738	-0.02755041
792082	-78.21625136	-0.02034602	-78.11782858	-0.02362807	-78.11175774	-0.02518033
1246877	-78.21836863	-0.01844352	-78.12047989	-0.02125020	-78.11420932	-0.02300960

Table E.4: Variational energy E_{var} and perturbative correction $E_{\text{pr}2}$ for the singlet states of D_{2d} ethene. All energies are given in Hartrees using the cc-pVDZ basis set.

n_{det}	$E_{\text{var}}(^3A_{2g})$	$E_{\text{PT2}}(^3A_{2g})$
641	-77.94501556	-0.26939335
1295	-78.01187689	-0.20460888
2595	-78.05481541	-0.16440303
5201	-78.09849809	-0.12501541
10407	-78.13783478	-0.08981761
20815	-78.17121793	-0.05978235
41633	-78.19493467	-0.03811539
83267	-78.20533610	-0.02874323
166549	-78.20955766	-0.02482827
333163	-78.21269998	-0.02198502
666343	-78.21565460	-0.01924503
1332567	-78.21853469	-0.01673550
2664535	-78.22137491	-0.01425775
5326435	-78.22404603	-0.01188806

Table E.5: Variational energy E_{var} and perturbative correction E_{PT2} for the triplet ground state of \mathcal{D}_{2d} ethene. All energies are given in Hartrees using the cc-pVDZ basis set.

	$E_{\text{ex-FCI}}(^1B_1)$	$E_{\text{ex-FCI}}(^3A_2)$	$E_{\text{ex-FCI}}(^1B_2)$	$E_{\text{ex-FCI}}(^1A_1)$
Two-Point	-78.23889427	-78.23744631	-78.14417374	-78.14019599
Three-Point	-78.23881785	-78.23757101	-78.14349967	-78.13910134

Table E.6: Extrapolated FCI energy $E_{\text{ex-FCI}}$ for the ground and excited states of \mathcal{D}_{2d} ethene using two- and three-point linear fits. All energies are given in Hartrees using the cc-pVDZ basis set.

E.2.3 Cyclobutadiene

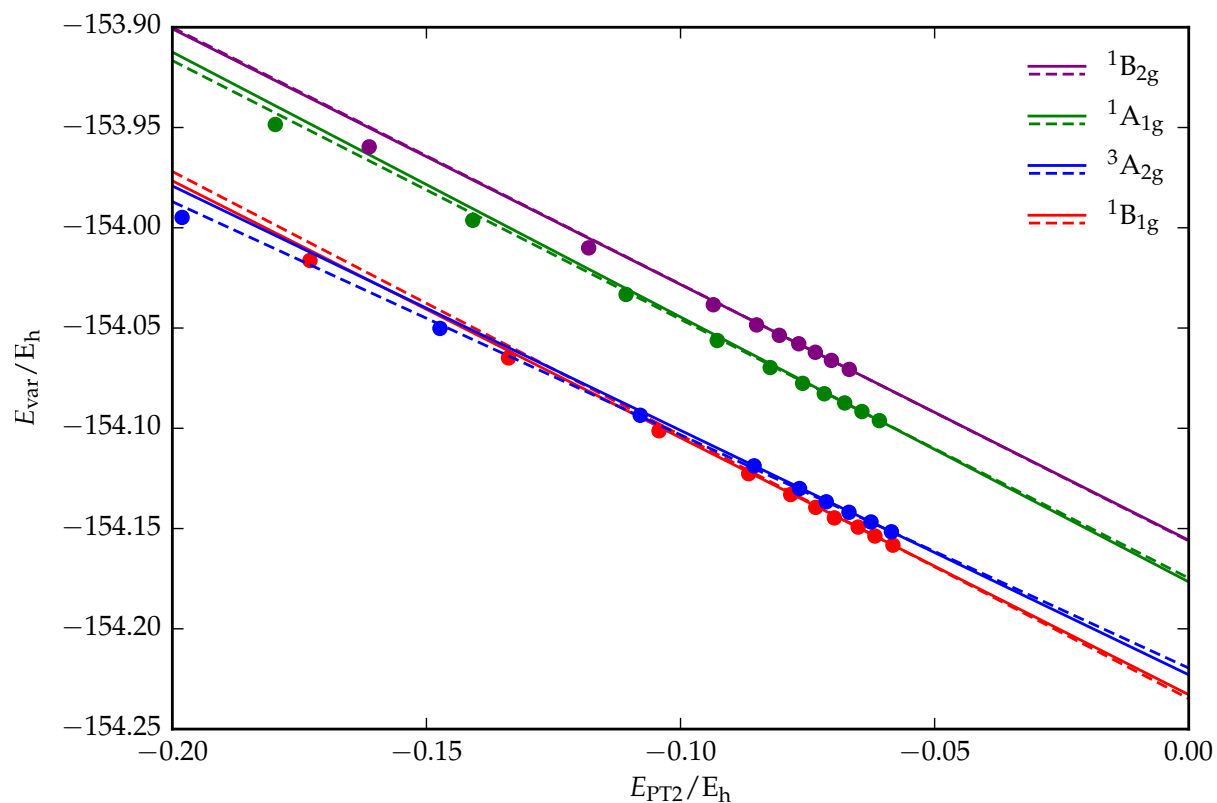


Figure E.3: Extrapolation of the variational energy E_{var} against the perturbative correction E_{PT2} for the ground and excited states of square D_{4h} cyclobutadiene (cc-pVDZ) using two-point (solid lines) and three-point (dashed lines) linear fits.

n_{det}	$E_{\text{var}}(^1B_{1g})$	$E_{\text{PT2}}(^1B_{1g})$	$E_{\text{var}}(^1A_{1g})$	$E_{\text{PT2}}(^1A_{1g})$	$E_{\text{var}}(^1B_{2g})$	$E_{\text{PT2}}(^1B_{2g})$
1241	-153.60215631	-0.41582548	-153.58374982	-0.36628188	-153.37352818	-0.39798242
2486	-153.72114173	-0.40923866	-153.65884637	-0.40727047	-153.64331676	-0.44311396
4179	-153.78292275	-0.36338945	-153.72042110	-0.37272386	-153.69156830	-0.38857297
7598	-153.84584472	-0.30630096	-153.78051331	-0.31579950	-153.71998575	-0.36292551
14866	-153.89773366	-0.26699290	-153.83163547	-0.27564084	-153.77850587	-0.31269202
29096	-153.95957322	-0.21736905	-153.89259743	-0.22559148	-153.83355773	-0.26629524
56974	-154.01631334	-0.17291535	-153.94849719	-0.17973631	-153.89698987	-0.21363023
110609	-154.06489067	-0.13384841	-153.99626494	-0.14087948	-153.95965493	-0.16126604
210289	-154.10123808	-0.10423209	-154.03325006	-0.11072002	-154.01003710	-0.11807994
391967	-154.12263640	-0.08659362	-154.05621615	-0.09277286	-154.03838970	-0.09354860
705809	-154.13304090	-0.07832084	-154.06969917	-0.08235484	-154.04844848	-0.08503701
1225595	-154.13943225	-0.07338737	-154.07758731	-0.07597806	-154.05363701	-0.08056273
2082476	-154.14468977	-0.06973087	-154.08278397	-0.07171463	-154.05784823	-0.07673966
3609921	-154.14926746	-0.06505198	-154.08737151	-0.06769769	-154.06208160	-0.07347382
6112945	-154.15372843	-0.06174878	-154.09164123	-0.06430723	-154.06614770	-0.07031188
10374047	-154.15827081	-0.05820367	-154.09617470	-0.06087538	-154.07063171	-0.06679552

Table E.7: Variational energy E_{var} and perturbative correction E_{PT2} for the singlet states of square D_{4h} cyclobutadiene. All energies are given in Hartrees using the cc-pVDZ basis set.

n_{det}	$E_{\text{var}}(^3A_{2g})$	$E_{\text{PT2}}(^3A_{2g})$
1241	-153.66917033	-0.59769686
2485	-153.76478516	-0.44651819
4971	-153.81636535	-0.38268097
9947	-153.87340848	-0.31894004
19903	-153.93385178	-0.25651560
39825	-153.99483965	-0.19808227
79655	-154.05018720	-0.14733932
159313	-154.09350370	-0.10793298
318639	-154.11873101	-0.08552676
637337	-154.13004376	-0.07657975
1274669	-154.13665132	-0.07131522
2549261	-154.14189252	-0.06685546
5098453	-154.14671816	-0.06251834
10195851	-154.15161226	-0.05850315

Table E.8: Variational energy E_{var} and perturbative correction E_{PT2} for the triplet ground state of square \mathcal{D}_{4h} cyclobutadiene. All energies are given in Hartrees using the cc-pVDZ basis set.

	$E_{\text{ex-FCI}}(^1B_{1g})$	$E_{\text{ex-FCI}}(^3A_{2g})$	$E_{\text{ex-FCI}}(^1A_{1g})$	$E_{\text{ex-FCI}}(^1B_{2g})$
Two-Point	-154.23284756	-154.22292153	-154.17659082	-154.15580827
Three-Point	-154.23480445	-154.21957696	-154.17469425	-154.15614823

Table E.9: Extrapolated FCI energy $E_{\text{ex-FCI}}$ for the ground and excited states of square \mathcal{D}_{4h} cyclobutadiene using two- and three-point linear fits. All energies are given in Hartrees using the cc-pVDZ basis set.

References

1. Burton, H. G. A.; Gross, M.; Thom, A. J. W. *J. Chem. Theory Comput.* **2018**, *14*, 607.
2. Burton, H. G. A.; Thom, A. J. W.; Loos, P.-F. *J. Chem. Theory Comput.* **2019**, *15*, 4374.
3. Burton, H. G. A.; Thom, A. J. W.; Loos, P.-F. *J. Chem. Phys.* **2019**, *150*, 041103.
4. Burton, H. G. A.; Thom, A. J. W. *J. Chem. Theory Comput.* **2019**, *15*, 4851.
5. Burton, H. G. A.; Thom, A. J. W. *Reaching Full Correlation through Nonorthogonal Configuration Interaction: A Second-Order Perturbative Approach*, **2020**, arXiv:2005.03962.
6. Atkins, P.; Friedman, R. *Molecular Quantum Mechanics*; Oxford University Press, 2005.
7. Heitler, W.; London, F. *Z. Phys.* **1927**, *44*, 455.
8. Szabo, A.; Ostlund, N. S. *Modern Quantum Chemistry*; Dover Publications Inc., 1989.
9. Born, M.; Oppenheimer, R. *Ann. Phys.* **1927**, *389*, 457.
10. Hartree, D. R.; Hartree, W. *Proc. R. Soc. London Ser. A. Math. Phys. Sci.* **1935**, *150*, 9.
11. Helgaker, T.; Jørgensen, P.; Olsen, J. *Molecular Electronic-Structure Theory*; John Wiley & Sons, 2000.
12. Møller, C.; Plesset, M. S. *Phys. Rev.* **1934**, *46*, 618.
13. Nesbet, R. K. *Proc. Royal Soc. A* **1955**, *230*, 312.
14. Čížek, J. *J. Chem. Phys.* **1966**, *45*, 4256.
15. Čížek, J. *Adv. Quantum Chem.* **1969**, *14*, 35.
16. Bartlett, R. J.; Musiał, M. *Rev. Mod. Phys.* **2007**, *79*, 291.
17. Krylov, A. I. *J. Chem. Phys.* **2000**, *113*, 6052.
18. Roos, B. O.; Taylor, P. R.; Sigbahn, P. E. M. *J. Chem. Phys.* **1980**, *48*, 157.

19. Malmqvist, P.-A.; Roos, B. O. *Chem. Phys. Lett.* **1989**, 189.
20. Thom, A. J. W.; Head-Gordon, M. *Phys. Rev. Lett.* **2008**, 101, 193001.
21. Stanton, R. E. *J. Chem. Phys.* **1968**, 48, 257.
22. Fukutome, H. *Prog. Theor. Phys.* **1971**, 45, 1382.
23. Kowalski, K.; Jankowski, K. *Phys. Rev. Lett.* **1998**, 81, 1195.
24. Coulson, C. A.; Fischer, I. *Philos. Mag.* **1949**, 40, 386.
25. Thom, A. J. W.; Head-Gordon, M. *J. Chem. Phys.* **2009**, 131, 124113.
26. Gilbert, A. T. B.; Besley, N. A.; Gill, P. M. W. *J. Phys. Chem. A* **2008**, 112, 13164.
27. Besley, N. A.; Gilbert, A. T. B.; Gill, P. M. W. *J. Chem. Phys.* **2009**, 130, 124308.
28. Barca, G. M. J.; Gilbert, A. T. B.; Gill, P. M. W. *J. Chem. Phys.* **2014**, 141, 111104.
29. Barca, G. M. J.; Gilbert, A. T. B.; Gill, P. M. W. *J. Chem. Theory Comput.* **2018**, 14, 1501.
30. Barca, G. M. J.; Gilbert, A. T. B.; Gill, P. M. W. *J. Chem. Theory Comput.* **2018**, 14, 19.
31. Sundstrom, E. J.; Head-Gordon, M. *J. Chem. Phys.* **2014**, 140, 114103.
32. Mayhall, N. J.; Horn, P. R.; Sundstrom, E. J.; Head-Gordon, M. *Phys. Chem. Chem. Phys.* **2014**, 16, 22694.
33. Jensen, K. T.; Benson, R. L.; Cardamone, S.; Thom, A. J. W. *J. Chem. Theory Comput.* **2018**, 14, 4629.
34. Oosterbaan, K. J.; White, A. F.; Head-Gordon, M. *J. Chem. Phys.* **2018**, 149, 044116.
35. Oosterbaan, K. J.; White, A. F.; Head-Gordon, M. *J. Chem. Theory Comput.* **2019**, 2966, 15.
36. Pople, J. *Int. J. Quantum Chem.* **1971**, 5, 175.
37. Small, D.; Sundstrom, E.; Head-Gordon, M. *J. Chem. Phys.* **2015**, 142, 024104.
38. Hiscock, H. G.; Thom, A. J. W. *J. Chem. Theory Comput.* **2014**, 10, 4795.
39. Burton, H. G. A.; Thom, A. J. W. *J. Chem. Theory Comput.* **2016**, 12, 167.
40. Mayer, I. *Simple Theorems, Proofs, and Derivations in Quantum Chemistry*; Springer, 2003.

41. Head-Gordon, M.; Maslen, P. E.; White, C. A. *J. Chem. Phys.* **1998**, *108*, 616.
42. McQuarrie, D. A. *Quantum Chemistry*, 2nd ed.; University Science Books, 2007.
43. Hehre, W. J.; Stewart, R. F.; Pople, J. A. *J. Chem. Phys.* **1969**, *51*, 2657.
44. Ditchfield, R.; Hehre, W. J.; Pople, J. A. *J. Chem. Phys.* **1971**, *54*, 724.
45. Dunning Jr., T. H. *J. Chem. Phys.* **1989**, *90*, 1007.
46. Roothaan, C. C. J. *Rev. Mod. Phys.* **1951**, *23*, 69.
47. Hall, G. G. *Proc. Royal Soc. A* **1951**, *205*, 541.
48. Löwdin, P.-O. *Phys. Rev.* **1955**, *97*, 1509.
49. Davidson, E. R. *J. Comput. Phys.* **1975**, *17*, 87.
50. Booth, G. H.; Thom, A. J. W.; Alavi, A. *J. Chem. Phys.* **2009**, *131*, 054106.
51. Evangelisti, S.; Daudey, J. P.; Malrieu, J. P. *Chem. Phys.* **1983**, *75*, 91.
52. Holmes, A. A.; Tubman, N. M.; Umrigar, C. J. *J. Chem. Theory Comput.* **2016**, *12*, 3674.
53. Smith, J. E. T.; Mussard, B.; Holmes, A. A.; Sharma, S. J. *Chem. Theory Comput.* **2017**, *13*, 5468.
54. Fulde, P. *Electron Correlations in Molecules and Solids*, 3rd ed.; Springer-Verlag, 1995.
55. Christiansen, O.; Olsen, J.; Jørgensen, P.; Koch, H.; Malmqvist, P.-Å. *Chem. Phys. Lett.* **1996**, *261*, 369.
56. Olsen, J.; Jørgensen, P.; Helgaker, T.; Christiansen, O. *J. Chem. Phys.* **2000**, *112*, 9735.
57. Gill, P. M. W.; Pople, J. A.; Radom, L.; Nobes, R. H. *J. Chem. Phys.* **1988**, *89*, 7307.
58. Sergeev, A. V.; Goodson, D. Z.; Wheeler, S. E.; Allen, W. D. *J. Chem. Phys.* **2005**, *123*, 064105.
59. Sergeev, A. V.; Goodson, D. Z. *J. Chem. Phys.* **2006**, *124*, 094111.
60. Shavitt, I.; Bartlett, R. *Many-Body Methods in Chemistry and Physics*; Cambridge University Press, 2009.
61. Purvis III, G. D.; Bartlett, R. J. *J. Chem. Phys.* **1982**, *76*, 1910.

62. Raghavachari, K.; Trucks, G. W.; Pople, J. A.; Head-Gordon, M. *Chem. Phys. Lett.* **1989**, *157*, 479.
63. Bartlett, R. J. *WIREs Comput. Mol. Sci.* **2012**, *2*, 126.
64. Kowalski, K.; Piecuch, P. *Chem. Phys. Lett.* **2001**, *344*, 165.
65. Evangelista, F. A. *J. Chem. Phys.* **2018**, *149*, 030901.
66. Olsen, J. *Int. J. Quantum Chem.* **2011**, *111*, 3267.
67. Kreplin, D. A.; Knowles, P. J.; Werner, H.-J. *J. Chem. Phys.* **2019**, *150*, 194106.
68. Kreplin, D. A.; Knowles, P. J.; Werner, H.-J. *J. Chem. Phys.* **2020**, *152*, 074102.
69. Keller, S.; Boguslawski, K.; Janowski, T.; Reiher, M.; Pulay, P. *J. Chem. Phys.* **2015**, *142*, 244104.
70. Stein, C. J.; Reiher, M. *J. Chem. Theory Comput.* **2016**, *12*, 1760.
71. Szalay, P. G.; Müller, T.; Gidofalvi, G.; Lischka, H.; Shepard, R. *Chem. Rev.* **2012**, *112*, 108.
72. Buenker, R. J.; Peyerimhoff, S. D.; Butscher, W. *Mol. Phys.* **1978**, *35*, 771.
73. Werner, H.-J.; Knowles, P. J. *J. Chem. Phys.* **1988**, *89*, 5803.
74. Jeziorski, B.; Monkhorst, H. J. *Phys. Rev. A* **1981**, *24*, 1668.
75. Andersson, K.; Malmqvist, P.-Å.; Roos, B. O.; Sadlej, A. J.; Wolinski, K. *J. Phys. Chem.* **1990**, *93*, 5483.
76. Andersson, K.; Malmqvist, P.-Å.; Roos, B. O. *J. Chem. Phys.* **1992**, *96*, 1218.
77. Pulay, P. *Int. J. Quantum Chem.* **2011**, *111*, 3273.
78. Andersson, K.; Roos, B. O. In *Modern Electronic Structure Theory*; Yarkony, D. R., Ed.; World Scientific: Singapore, 1995; Vol. 2; Chapter Multiconfigurational Second-Order Perturbation Theory, p 55.
79. Roos, B. O.; Andersson, K. *Chem. Phys. Lett.* **1995**, *245*, 215.
80. N. Forsberg and P.-A. Malmqvist, *Chem. Phys. Lett.* **1997**, *274*, 196.
81. Ghigo, G.; Roos, B. O.; Malmqvist, P.-Å. *Chem. Phys. Lett.* **2004**, *396*, 142.

82. Angeli, C.; Cimiraglia, R.; Evangelisti, S.; Leininger, T.; Malrieu, J.-P. *J. Chem. Phys.* **2001**, *114*, 10252.
83. Angeli, C.; Cimiraglia, R.; Malrieu, J.-P. *J. Chem. Phys.* **2002**, *117*, 9138.
84. Dylla, K. G. *J. Chem. Phys.* **1995**, *102*, 4909.
85. Dreuw, A.; Head-Gordon, M. *Chem. Rev.* **2005**, *105*, 4009.
86. González, L.; Escudero, D.; Serrano-Andrés, L. *Chem. Phys. Chem.* **2011**, *13*, 28.
87. Bene, J. E. D.; Ditchfield, R.; Pople, J. A. *J. Chem. Phys.* **1971**, *55*, 2236.
88. Foresman, J. B.; Head-Gordon, M.; Pople, J. A.; Frisch, M. J. *J. Phys. Chem.* **1992**, *96*, 135.
89. Head-Gordon, M.; Rico, R. J.; Oumi, M.; Lee, T. J. *Chem. Phys. Lett.* **1994**, *219*, 21.
90. Subotnik, J. E. *J. Chem. Phys.* **2011**, *135*, 071104.
91. Liu, X.; Fatehi, S.; an Brad S. Veldkamp, Y. S.; Subotnik, J. E. *J. Chem. Phys.* **2012**, *136*, 161101.
92. Liu, X.; Subotnik, J. E. *J. Chem. Theory Comput.* **2014**, *10*, 1004.
93. Monkhorst, H. J. *Int. J. Quantum Chem.* **1977**, *12*, 421.
94. Lischka, H.; Nachtigallová, D.; Aquino, A. J. A.; Szalay, P. G.; Plasser, F.; Machado, F. B. C.; Barbatti, M. *Chem. Rev.* **2018**, *118*, 7293.
95. Bartlett, R. J.; Watts, J. D. *Chem. Phys. Lett.* **1995**, *223*, 81.
96. Tran, L. N.; Shea, J. A. R.; Neuscamman, E. J. *Chem. Theory Comput.* **2019**, *15*, 4790.
97. Werner, H.-J.; Meyer, W. J. *Chem. Phys.* **1981**, *74*, 5794.
98. Stuber, J. L.; Paldus, J. In *Fundamental World of Quantum Chemistry: A Tribute Volume to the Memory of Per-Olov Löwdin*; Brändas, E. K., Kryachko, E. S., Eds.; Kluwer Academic Publishers: Dordrecht, The Netherlands, 2003; Vol. 1; Chapter Symmetry Breaking in the Independent Particle Model, p 67.
99. Slater, J. C. *Phys. Rev.* **1951**, *82*, 538.
100. Overhauser, A. W. *Phys. Rev. Lett.* **1960**, *4*, 462.
101. Kohn, W. *Phys. Rev. Lett.* **1967**, *19*, 789.

102. Purwanto, W.; Al-Saidi, W. A.; Krakauer, H.; Zhang, S. *J. Chem. Phys.* **2008**, *128*, 114309.
103. Gordon, M. S.; Truhlar, D. G. *Theor. Chim. Acta* **1987**, *71*, 1.
104. Nobes, R. H.; Moncrieff, D.; Wong, M. W.; Radom, L.; Gill, P. M. W.; Pople, J. A. *Chem. Phys. Lett.* **1991**, *182*, 216.
105. Mori-Sánchez, P.; Cohen, A. *J. Chem. Phys.* **2014**, *141*, 164124.
106. Lykos, P.; Pratt, G. W. *Rev. Mod. Phys.* **1963**, *35*, 496.
107. Thouless, D. J. *Nucl. Phys.* **1960**, *21*, 225.
108. Sawada, K.; Fukuda, N. *Prog. Theor. Phys.* **1961**, *25*, 653.
109. Adams, W. H. *Phys. Rev.* **1962**, *127*, 1650.
110. Čížek, J.; Paldus, J. *J. Chem. Phys.* **1967**, *47*, 3976.
111. Paldus, J.; Čížek, J. *J. Chem. Phys.* **1970**, *52*, 2919.
112. Čížek, J.; Paldus, J. *J. Chem. Phys.* **1970**, *53*, 821.
113. Seeger, R.; Pople, J. A. *J. Chem. Phys.* **1977**, *66*, 3045.
114. Fukutome, H. *Prog. Theor. Phys.* **1973**, *50*, 1433.
115. Fukutome, H. *Prog. Theor. Phys.* **1975**, *53*, 1320.
116. Mestechkin, M. M. *Int. J. Quantum Chem.* **1978**, *13*, 469.
117. Mestechkin, M. *Int. J. Quantum Chem.* **1979**, *15*, 601.
118. Mestechkin, M. *J. Mol. Struct.: THEOCHEM* **1988**, *181*, 231.
119. Vaucher, A. C.; Reiher, M. *J. Chem. Theory Comput.* **2017**, *13*, 1219.
120. Li, X.; Paldus, J. *J. Chem. Phys.* **2009**, *131*, 084110.
121. Jiménez-Hoyos, C. A.; Henderson, T. M.; Tsuchimochi, T.; Scuseria, G. E. *J. Chem. Phys.* **2012**, *136*, 164109.
122. Cui, Y.; Bulik, I. W.; Jiménez-Hoyos, C. A.; Henderson, T. M.; Scuseria, G. E. *J. Chem. Phys.* **2013**, *139*, 154107.
123. Qiu, Y.; Henderson, T. M.; Zhao, J.; Scuseria, G. E. *J. Chem. Phys.* **2017**, *147*, 064111.

124. Jake, L. C.; Henderson, T. M.; Scuseria, G. E. *J. Chem. Phys.* **2018**, *148*, 024109.
125. Fukutome, H. *Int. J. Quantum Chem.* **1981**, *20*, 955.
126. Jiménez-Hoyos, C. A.; Henderson, T. M.; Scuseria, G. E. *J. Chem. Theory Comput.* **2011**, *7*, 2667.
127. Roothaan, C. C. J. *Rev. Mod. Phys.* **1960**, *32*, 179.
128. Tsuchimochi, T.; Scuseria, G. E. *J. Chem. Phys.* **2010**, *133*, 141102.
129. Coulson, C. A.; White, R. J. *Mol. Phys.* **1970**, *18*, 577.
130. Ostlund, N. S. *J. Chem. Phys.* **1972**, *57*, 2994.
131. Hafner, P. *J. Phys. B: At. Mol. Phys.* **1980**, *13*, 3297.
132. Curtiss, L. A.; Raghavachari, K.; Redfern, P. C.; Pople, J. A. *J. Chem. Phys.* **1997**, *106*, 1063.
133. Tran, H. K.; Van Voorhis, T.; Thom, A. J. W. *J. Chem. Phys.* **2019**, *151*, 034112.
134. Yost, S. R.; Kowalczyk, T.; Van Voorhis, T. *J. Chem. Phys.* **2013**, *139*, 174104.
135. Nite, J.; Jiménez-Hoyos, C. A. *J. Chem. Theory Comput.* **2019**, *15*, 5343.
136. Broer, R.; Nieuwpoort, W. C. *Theor. Chim. Acta* **1988**, *73*, 405.
137. Löwdin, P. O. *J. Appl. Phys.* **1962**, *33*, 251.
138. Amos, A. T.; Hall, G. G. *Proc. R. Soc. London Ser. A. Math. Phys. Sci.* **1961**, *263*, 483–493.
139. Huynh, B. C.; Thom, A. J. W. Symmetry in Multiple Self-Consistent-Field Solutions of Transition-Metal Complexes. 2020.
140. Wibowo, M.; Broer, R.; Remco W. A, H. *Comput. Theor. Chem* **2017**, *1116*, 190.
141. Krausbeck, F.; Mendive-Tapia, D.; Thom, A. J.; Bearpark, M. J. *Comput. Theor. Chem* **2014**, *1040-1041*, 14.
142. Pathak, S.; Wagner, L. K. *J. Chem. Phys.* **2018**, *149*, 234104.
143. Landinez Borda, E. J.; Gomez, J.; Morales, M. A. *J. Chem. Phys.* **2019**, *150*, 074105.
144. Krylov, A. I. *Chem. Phys. Lett.* **2001**, *338*, 375.
145. Mayhall, N. J.; Goldey, M.; Head-Gordon, M. *J. Chem. Theory Comput.* **2014**, *10*, 589.

146. Yost, S. R.; Head-Gordon, M. J. *Chem. Phys.* **2016**, *145*, 054105.
147. Yost, S. R.; Head-Gordon, M. J. *Chem. Theory Comput.* **2019**, *14*, 4791.
148. Nite, J.; Jiménez-Hoyos, C. A. *Efficient Multi-Configurational Wavefunction Method with Dynamical Correlation Using Non-Orthogonal Configuration Interaction Singles and Doubles (NOCISD)*, **2019**, (Preprint).
149. Fischer, W.; Lieb, I. *A Course in Complex Analysis*, 1st ed.; Vieweg+Teubner Verlag, 2012.
150. Pulay, P. *Chem. Phys. Lett.* **1980**, *73*, 393.
151. Pulay, P. *J. Comput. Chem.* **1982**, *3*, 556.
152. King, H. F.; Stanton, R. E. *J. Chem. Phys.* **1969**, *50*, 3789.
153. Arfken, G. B.; Weber, H. J. *Mathematical Methods for Physicists*; Elsevier Academic Press, 2005.
154. Craven, B. D. *J. Aust. Math. Soc.* **1969**, *10*, 341.
155. Gantmacher, F. R. *The Theory of Matrices*; American Mathematical Society, 1987; Vol. 2.
156. Edelman, A.; Tomás, A. A.; Smith, S. T. *SIAM J. Matrix Anal. Appl.* **1998**, *20*, 303.
157. Savas, B.; Lim, L.-H. *SIAM J. Sci. Comput.* **2010**, *32*, 3352.
158. Chiumiento, E.; Melgaard, M. J. *Geom. Phys.* **2012**, *62*, 1866.
159. Hutter, J.; Parrinello, M.; Vogel, S. J. *Chem. Phys.* **1994**, *101*, 3862.
160. Choudhury, D.; Horn, R. A. *Linear Multilinear Algebra* **1987**, *21*, 149.
161. Douady, J.; Ellinger, Y.; Subra, R.; Levy, B. J. *Chem. Phys.* **1980**, *72*, 1452.
162. Chaban, G.; Schmidt, M. W.; Gordon, M. S. *Theor. Chim. Acta* **1997**, *97*, 88.
163. Daniels, A. D.; Scuseria, G. E. *Phys. Chem. Chem. Phys.* **2000**, *2*, 2173.
164. Van Voorhis, T.; Head-Gordon, M. *Mol. Phys.* **2002**, *100*, 1713.
165. Backsay, G. B. *Chem. Phys.* **1981**, *61*, 385.
166. Backsay, G. B. *Chem. Phys.* **1982**, *65*, 383.
167. Head-Gordon, M.; Pople, J. A. *J. Phys. Chem.* **1987**, *92*, 3063.

168. Moiseyev, N. *Non-Hermitian Quantum Mechanics*; Cambridge University Press, 2011.
169. White, A. F.; Head-Gordon, M.; McCurdy, C. W. *J. Chem. Phys.* **2015**, *142*, 054103.
170. Frya, D.; Armstrong Jr., L. *Phys. Rev. A* **1986**, *34*, 1682.
171. Reinhardt, W. P. *Annu. Rev. Phys. Chem.* **1982**, *33*, 223.
172. Aguilar, J.; Combes, J. M. *Commun. math. Phys.* **1971**, *22*, 269.
173. Balslev, E.; Combes, J. M. *Commun. math. Phys.* **1971**, *22*, 280.
174. Riss, U. V.; Meyer, H.-D. *J. Phys. B: At. Mol. Phys.* **1993**, *26*, 4503.
175. Hartshorne, R. *Algebraic Geometry*, 1st ed.; Springer-Verlag, 1977.
176. Hulek, K. *Elementary Algebraic Geometry*, 1st ed.; American Mathematical Society, 2003.
177. Jankowski, K.; Kowalski, K.; Jankowski, P. *Chem. Phys. Lett.* **1994**, *222*, 608.
178. Jankowski, K.; Kowalski, K.; Jankowski, P. *Int. J. Quantum Chem.* **1994**, *53*, 501.
179. Snapper, E.; Troyer, R. J. *Metric Affine Geometry*; American Mathematical Society, 1971.
180. Semple, J. G.; Kneebone, G. T. *Algebraic Projective Geometry*; Oxford University Press, 1998.
181. Griffiths, P.; Harris, J. *Principles of Algebraic Geometry*, 2nd ed.; John Wiley and Sons, 1994.
182. Gilmore, R. *Catastrophe Theory for Scientists and Engineers*, 1st ed.; Dover Publications Inc., 1993.
183. Thom, R. *Structural Stability and Morphogenesis*, 1st ed.; Westview Press, 1994.
184. Fukutome, H. *Prog. Theor. Phys.* **1974**, *52*, 1766.
185. Oliphant, T. E. *A guide to NumPy*; Trelgol Publishing USA, 2006; Vol. 1.
186. Shao, Y. et al. *Mol. Phys.* **2015**, *113*, 184.
187. Hunter, J. D. *Comput. Sci. Eng.* **2007**, *9*, 90.

188. Strogatz, S. H. *Nonlinear Dynamics and Chaos: With Applications to Physics, Biology, Chemistry, and Engineering*; Perseus Books, 1994.
189. Schmidt, M. W.; Truong, P. N.; Gordon, M. S. *J. Am. Chem. Soc.* **1987**, *109*, 5217.
190. Barbatti, M.; Paier, J.; Lischka, H. *J. Chem. Phys.* **2004**, *121*, 11614.
191. Hidding, J.; Shandarin, S. F.; van de Weygaert, R. *Mon. Not. R. Astron. Soc.* **2014**, *437*, 3442.
192. Scuseria, G. E.; Jiménez-Hoyos, C. A.; Henderson, T. M.; Samanta, K.; Ellis, J. K. *J. Chem. Phys.* **2011**, *135*, 124108.
193. Bender, C. M.; Boettcher, S. *Phys. Rev. Lett.* **1998**, *80*, 5243.
194. Bender, C. M.; Boettcher, S.; Meisinger, P. N. *J. Math. Phys.* **1999**, *40*, 2201.
195. Bender, C. M.; Berry, M. V.; Mandilara, A. *J. Phys. A: Math. Gen.* **2002**, *35*, L467.
196. Bender, C. M.; Brody, D. C.; Jones, H. F. *Phys. Rev. Lett.* **2002**, *89*, 270401.
197. Bender, C. M.; Brody, D. C.; Jones, H. F. *Am. J. Phys.* **2003**, *71*, 1095.
198. Bender, C. M.; Brod, J.; Refid, A.; Reuter, M. E. *J. Phys. A: Math. Gen.* **2004**, *37*, 10139.
199. Bender, C. M. *Contemp. Phys.* **2005**, *46*, 277.
200. Bender, C. M.; Chen, J.; Milton, K. A. *J. Phys. A: Math. Gen.* **2006**, *39*, 1657.
201. Bender, C. M. *Rep. Prog. Phys.* **2007**, *70*, 947.
202. Bender, C. M. *PT-Symmetry in Quantum and Classical Physics*; World Scientific, 2019.
203. Bender, C. M.; Brody, D. C.; Hook, D. W. *J. Phys. A: Math. Gen.* **2008**, *41*, 352003.
204. Bender, C. M.; Brody, D. C.; Jones, H. F.; Meister, B. K. *Phys. Rev. Lett.* **2007**, *98*, 040403.
205. Bender, C. M. *J. Phys.: Conf. Ser.* **2015**, *631*, 012002.
206. Bender, C. M.; Hassanpour, N.; Hook, D. W.; Klevansky, S. P.; Sünderhauf, C.; Wen, Z. *Phys. Rev. A* **2017**, *95*, 052113.
207. Dorey, P.; Dunning, C.; Tateo, R. *J. Phys. A: Math. Gen.* **2001**, *34*, 5679.
208. Schindler, J.; Li, A.; Zheng, M. C.; Ellis, F. M.; Kottos, T. *Phys. Rev. A* **2011**, *84*, 040101(R).

209. Choi, Y.; Hahn, C.; Yoon, J. W.; Song, S. H. *Nat. Comm.* **2018**, *9*, 2182.
210. Bittner, S.; Dietz, B.; Günther, U.; Harney, H. L.; Miski-Oglu, M.; Richter, A.; Schäfer, F. *Phys. Rev. Lett.* **2012**, *108*, 024101.
211. Peng, B.; Özdemir, Ş. K.; Lei, F.; Monifi, F.; Gianfreda, M.; Long, G. L.; Fan, S.; Nori, F.; Bender, C. M.; Yang, L. *Nat. Phys.* **2014**, *10*, 394.
212. Hang, C.; Huang, G.; Konotop, V. V. *Phys. Rev. Lett.* **2013**, *110*, 083604.
213. Zhao, K. F.; Schaden, M.; Wu, Z. *Phys. Rev. A* **2010**, *81*, 042903.
214. Chong, Y. D.; Ge, L.; Stone, A. D. *Phys. Rev. Lett.* **2011**, *106*, 093902.
215. Dopfer, J.; Mailybaev, A. A.; Böhm, J.; Kuhl, U.; Girschik, A.; Libisch, F.; Milburn, T. J.; Rabl, P.; Moiseyev, N.; Rotter, S. *Nature* **2016**, *537*, 76.
216. Guo, A.; Salamo, G. J.; Duchesne, D.; Morandotti, R.; Volatier-Ravat, M.; V. Aimez, G. A. S.; Christodoulides, D. N. *Phys. Rev. Lett.* **2009**, *103*, 093902.
217. Liertzer, M.; Li Ge, A. C.; Stone, A. D.; Türeci, H. E.; Rotter, S. *Phys. Rev. Lett.* **2012**, *108*, 173901.
218. Rüter, C. E.; Makris, K. G.; El-Ganainy, R.; Christodoulides, D. N.; Segev, M.; Kip, D. *Nat. Phys.* **2010**, *6*, 192.
219. Longhi, S. *Phys. Rev. Lett.* **2010**, *105*, 013903.
220. Heiss, W. D.; Sannino, A. L. *J. Phys. A: Math. Gen.* **1990**, *23*, 1167.
221. Heiss, W. D.; Sannino, A. L. *Phys. Rev. A* **1991**, *43*, 4159.
222. Heiss, W. D. *Eur. Phys. J. D* **1999**, *7*, 1.
223. Dorey, P.; Dunning, C.; Lishman, A.; Tateo, R. *J. Phys. A: Math. Gen.* **2009**, *42*, 465302.
224. Heiss, W. D. *J. Phys. A: Math. Gen.* **2012**, *45*, 444016.
225. Heiss, W. D. *Nat. Phys.* **2016**, *12*, 823.
226. Yarkony, D. R. *Rev. Mod. Phys.* **1996**, *68*, 985.
227. Jones-Smith, K.; Mathur, H. *Phys. Rev. A* **2010**, *82*, 042101.
228. Cherbal, O.; Trifonov, D. A. *Phys. Rev. A* **2012**, *85*, 052123.
229. Beygi, A.; Klevansky, S. P.; Bender, C. M. *Phys. Rev. A* **2018**, *97*, 032128.

230. Ballentine, L. E. *Quantum Mechanics: A Modern Development*; World Scientific, 1998.
231. Weinberg, S. *The Quantum Theory of Fields*; Cambridge University Press: Cambridge, 1995; Vol. 1.
232. Kramers, H. A. *Proc. R. Acad. Arts Sci.* **1930**, *33*, 959.
233. Lee, S. Y.; Lee, Y. S. *J. Comput. Chem.* **1992**, *13*, 595.
234. Kim, Y. S.; Lee, S. Y.; Oh, W. S.; Park, B. H.; Han, Y. K.; Park, S. J.; Lee, Y. S. *Int. J. Quantum Chem.* **1998**, *66*, 91.
235. Smeyers, Y. G.; Doreste-Suarez, L. *Int. J. Quantum Chem.* **1973**, *7*, 687.
236. Smeyers, Y. G.; Delgado-Barrio, G. *Int. J. Quantum Chem.* **1974**, *8*, 733.
237. Cox, P. A.; Wood, M. H. *Theor. Chim. Acta* **1976**, *41*, 269.
238. Smeyers, Y. G.; Delgado-Barrio, G. *Int. J. Quantum Chem.* **1976**, *10*, 461.
239. Ellis, J. K.; Martin, R. L.; Scuseria, G. E. *J. Chem. Theory Comput.* **2013**, *9*, 2857.
240. Födvári, D.; Tóth, Z.; Surján, P.; Szabados, Á. *J. Chem. Phys.* **2019**, *150*, 034103.
241. Feuerbacher, S.; Sommerfeld, T.; Cederbaum, L. S. *J. Chem. Phys.* **2004**, *120*, 3201.
242. Benda, Z.; Jagau, T. *J. Phys. Chem. Lett.* **2018**, *9*, 6978.
243. Hernández, E.; Jáuregui, A.; Mondragán, A. *J. Phys. A: Math. Gen.* **2006**, *39*, 10087.
244. Berry, M. V. *Proc. Royal Soc. A* **1984**, *392*, 45.
245. Essler, F.; Frahm, H.; Gohmann, G.; Klumper, A.; Korepin, V. *The One-Dimensional Hubbard Model*; Cambridge University Press, 2005.
246. Carrascal, D. J.; Ferrer, J.; Smith, J. C.; Burke, K. *J. Phys.: Condens. Matter* **2015**, *27*, 393001.
247. Mott, N. F. *Rev. Mod. Phys.* **1968**, *40*, 677.
248. Stan, A.; Romaniello, P.; Rigamonti, S.; Reining, L.; Berger, J. A. *New J. Phys.* **2015**, *17*, 093045.
249. Tarantino, W.; Romaniello, P.; Berger, J. A.; Reining, L. *Phys. Rev. B* **2017**, *96*, 045124.
250. Bulgakov, E. N.; Rotter, I.; Sadreev, A. F. *Phys. Rev. E* **74**, 056204.
251. Runge, E.; Gross, E. K. U. *Phys. Rev. Lett.* **1984**, *52*, 997.

252. Gross, E. K. U.; Kohn, W. *Adv. Quantum Chem.* **1990**, *21*, 255.
253. Emrich, K. *Nucl. Phys. A* **1981**, *351*, 379.
254. Krylov, A. I. *Annu. Rev. Phys. Chem.* **2008**, *59*, 433.
255. Grimme, S.; Parac, M. *Chem. Phys. Chem.* **2003**, *4*, 292.
256. Cai, Z.-L.; Sendt, K.; Reimers, J. R. *J. Chem. Phys.* **2002**, *117*, 5543.
257. Loos, P.-F.; Boggio-Pasqua, M.; Scemama, A.; Caffarel, M.; Jacquemin, D. *J. Chem. Theory Comput.* **2019**, *15*, 1939.
258. Maitra, N. T.; Zhang, F.; Cave, R. J.; Burke, K. *J. Chem. Phys.* **2004**, *120*, 5932.
259. Dreuw, A.; Head-Gordon, M. *J. Am. Chem. Soc.* **2004**, *126*, 4007.
260. Piecuch, P.; Kowalski, K. In *Computational Chemistry: Reviews of Current Trends*; Leszczynski, J., Ed.; World Scientific, 2000; Vol. 5; Chapter 1. In Search of the Relationship between Multiple Solutions Characterizing Coupled-Cluster Theories, p 1.
261. Langreth, D. C.; Perdew, J. P. *Solid State Commun.* **1975**, *17*, 1425.
262. Gunnarsson, O.; Lundqvist, B. I. *Phys. Rev. B* **1976**, *13*, 4274.
263. Coto, P. B.; Sharifzadeh, S.; Neaton, J. B.; Thoss, M. *J. Chem. Theory Comput.* **2015**, *11*, 147.
264. Mayhall, N. J. *J. Chem. Theory Comput.* **2016**, *12*, 4263.
265. Zimmerman, P. M.; Zhang, Z.; Musgrave, C. B. *Nat. Comm.* **2010**, *2*, 648.
266. Gozem, S. et al. *J. Chem. Theory Comput.* **2014**, 3074.
267. Gozem, S.; Huntress, M.; Schapiro, I.; Lindh, R.; Granovsky, A. A.; Angeli, C.; Olivucci, M. *J. Chem. Theory Comput.* **2012**, *8*, 4069.
268. Stanton, J. F.; Bartlett, R. J. *J. Chem. Phys.* **1993**, *98*, 7029.
269. Watts, J. D.; Bartlett, R. J. *J. Chem. Phys.* **1994**, *101*, 3073.
270. Manni, G. L.; Smart, S. D.; Alavi, A. *J. Chem. Theory Comput.* **2016**, *12*, 1245.
271. Tóth, Z.; Pulay, P. *J. Chem. Phys.* **2016**, *145*, 164102.
272. Thompson, L. M. *J. Chem. Phys.* **2018**, *149*, 194106.

273. Neese, F. *WIREs Comput. Mol. Sci.* **2012**, *2*, 73.
274. Kállay, M.; Gauss, J. *J. Chem. Phys.* **2004**, *121*, 9257.
275. Huron, B.; Malrieu, J. P.; Rancurel, P. *J. Chem. Phys.* **1973**, *58*, 5745.
276. Giner, E.; Scemama, A.; Caffarel, M. *Can. J. Chem.* **2013**, *91*, 879.
277. Holmes, A. A.; Umrigar, C. J.; Sharma, S. *J. Chem. Phys.* **2017**, *147*, 164111.
278. Loos, P.-F.; Scemama, A.; Blondel, A.; Garniron, Y.; Caffarel, M.; Jacquemin, D. *J. Chem. Theory Comput.* **2018**, *14*, 4360.
279. Scemama, A.; Benali, A.; Jacquemin, D.; Caffarel, M.; Loos, P. F. *J. Chem. Phys.* **2018**, *149*, 034108.
280. Garniron, Y. et al. *J. Chem. Theory Comput.* **2019**, *15*, 3591.
281. Sears, J. S.; Sherrill, C. D.; Krylov, A. I. *J. Chem. Phys.* **2003**, *118*, 9084.
282. Yang, K. R.; Jalan, A.; Green, W. H.; Truhlar, D. G. *J. Chem. Theory Comput.* **2013**, *9*, 418.
283. Krylov, A. I.; Sherrill, C. D. *J. Chem. Phys.* **2002**, *116*, 3194.
284. Laidig, W. D.; Saxe, P.; Bartlett, R. J. *J. Chem. Phys.* **1987**, *86*, 887.
285. Bytautas, L.; Nagata, T.; Gordon, M. S.; Ruedenberg, K. *J. Chem. Phys.* **2007**, *127*, 164317.
286. Gai, F.; Hasson, K. C.; Cooper McDonald, J.; Anfinrud, P. A. *Science* **1998**, *279*, 1886.
287. Hasson, K. C.; Gai, F.; Anfinrud, P. A. *Proc. Natl. Acad. Sci.* **1996**, *93*, 15124.
288. Minami, T.; Nakano, M. *J. Phys. Chem. Lett.* **2012**, *3*, 145.
289. Minami, T.; Ito, S.; Nakano, M. *J. Phys. Chem. Lett.* **2013**, *4*, 2133.
290. Salem, L.; Rowland, C. *Angew. Chem. internat. Edit.* **1972**, *11*, 92.
291. Bender, C. F.; Dunning, T. H.; Schaefer, H. F.; Goddard, W. A.; Hunt, W. J. *Chem. Phys. Lett.* **1972**, *15*, 171.
292. Buenker, R. J.; Peyerimhoff, S. D. *Chem. Phys.* **1976**, *9*, 75.
293. Brooks, B. R.; Schaefer, H. F. *J. Chem. Phys.* **1978**, *68*, 4839.

294. Daday, C.; Smart, S.; Booth, G. H.; Alavi, A.; Filippi, C. *J. Chem. Theory Comput.* **2012**, *8*, 4441.
295. Sauri, V.; Serrano-Andrés, L.; Shahi, A. R. M.; Gagliardi, L.; Vancoillie, S.; Pierloot, K. *J. Chem. Theory Comput.* **2011**, *7*, 153.
296. Schautz, F.; Filippi, C. *J. Chem. Phys.* **2004**, *120*, 10931.
297. Feller, D.; Peterson, K. A.; Davidson, E. R. *J. Chem. Phys.* **2014**, *141*, 104302.
298. Voter, A. F.; Goodgame, M. M.; Goddard III, W. A. *Chem. Phys.* **1985**, *98*, 7.
299. Oyedepo, G. A.; Wilson, A. K. *J. Phys. Chem. A* **2010**, *114*, 8806.
300. Fratev, F.; Monev, V.; Janoschek, R. *Tetrahedron* **1982**, *38*, 2929.
301. Kollmar, H.; Staemmler, V. *J. Am. Chem. Soc.* **1977**, *99*, 3583.
302. Borden, W. T.; Davidson, E. R.; Hart, P. J. *J. Am. Chem. Soc.* **1978**, *100*, 388.
303. Buenker, R. J.; Peyerimhoff, S. D. *J. Chem. Phys.* **1968**, *48*, 354.
304. Nakamura, K.; Osamura, Y.; Iwata, S. *Chem. Phys.* **1989**, *137*, 67.
305. Van Voorhis, T.; Head-Gordon, M. J. *Chem. Phys.* **2000**, *112*, 5633.
306. Lyakh, D. I.; Lotrich, V. F.; Bartlett, R. J. *Chem. Phys. Lett.* **2011**, *501*, 166.
307. Shen, J.; Fang, T.; Li, S.; Jiang, Y. *J. Phys. Chem. A* **2008**, *112*, 12518.
308. Demel, O.; Shamasundar, K. R.; Kong, L.; Nooijen, M. J. *J. Phys. Chem. A* **2008**, *112*, 11895.
309. Li, X.; Paldus, J. *J. Chem. Phys.* **2009**, *131*, 114103.
310. Deustua, J. E.; Shen, J.; Piecuch, P. *Phys. Rev. Lett.* **2017**, *119*, 223003.
311. Shen, J.; Piecuch, P. *J. Chem. Phys.* **2012**, *136*, 144104.
312. Musiał, M.; Perera, A.; Bartlett, R. J. *J. Chem. Phys.* **2011**, *134*, 114108.
313. Rishi, V.; Perera, A.; Nooijen, M.; Bartlett, R. J. *J. Chem. Phys.* **2017**, *146*, 144104.
314. Levchenko, S. V.; Krylov, A. I. *J. Chem. Phys.* **2004**, *120*, 175.
315. Sancho-García, J. C.; Pittner, J.; Čársky, P.; Hubač, I. *J. Chem. Phys.* **2000**, *112*, 8785.

316. Čársky, P.; Bartlett, R. J.; Fitzgerald, G.; Noga, J.; Špirko, V. J. *Chem. Phys.* **1988**, *89*, 3008.
317. Maksić, Z. B.; Barić, D.; Petanjek, I. *J. Phys. Chem. A* **2000**, *104*, 10873.
318. Eckert-Maksić, M.; Vazdar, M.; Barbatti, M.; Lischka, H.; Maksić, Z. B. *J. Chem. Phys.* **2006**, *125*, 064310.
319. Saito, T.; Nishihara, S.; Kitagawa, Y.; Kawakami, T.; Yamanaka, S.; Okumura, M.; Yamaguchi, K. *Chem. Phys. Lett.* **2010**, *498*, 253.
320. Varras, P. C.; Gritzapis, P. S. *Chem. Phys. Lett.* **2018**, *711*, 166.
321. Voter, A. F.; Goddard III, W. A. *J. Am. Chem. Soc.* **1986**, *108*, 2830.
322. Balková, A.; Bartlett, R. J. *J. Chem. Phys.* **1994**, *101*, 8972.
323. Feynman, R. P. *Phys. Rev.* **1939**, *56*, 340.
324. Sharma, S. *Stochastic perturbation theory to correct non-linearly parametrized wavefunctions*, **2018**, arXiv:1803.04341.
325. Guo, S.; Li, Z.; Chan, G. K.-L. *J. Chem. Theory Comput.* **2018**, *14*, 4063.
326. Guo, S.; Li, Z.; Chan, G. K.-L. *J. Chem. Phys.* **2018**, *148*, 221104.
327. Tsuchimochi, T.; Ten-no, S. L. *J. Chem. Theory Comput.* **2019**, *15*, 6688.
328. Paige, C. C.; Saunders, M. A. *SIAM J. Numer. Anal.* **1975**, *12*, 617.
329. Ring, P.; Schuck, P. *The Nuclear Many-Body Problem*; Springer-Verlag, 1980.
330. Fdez. Galván, I. et al. *J. Chem. Theory Comput.* **2019**, *15*, 5925.
331. Goedecker, S. *Rev. Mod. Phys.* **1999**, *71*, 1085.
332. Nocedal, J.; Wright, S. *Numerical Optimization*; Springer-Verlag, 2006.
333. Sano, T.; l'Haya, Y. J. *J. Chem. Phys.* **1991**, *95*, 6607.
334. Press, W. H.; Teukolsky, S. A.; Vetterling, W. T.; Flannery, B. P. *Numerical Recipes in C++*; Cambridge University Press, 2002.
335. Doye, J. P. K.; Wales, D. J. *J. Chem. Phys.* **2002**, *116*, 3777.
336. Zumino, B. J. *Math. Phys.* **1962**, *3*, 1055.

-
337. Chien, A. D.; Holmes, A. A.; Otten, M.; Umrigar, C. J.; Sharma, S.; Zimmerman, P. M. *J. Phys. Chem. A* **2018**, *122*, 2714.
338. Garniron, Y.; Scemama, A.; Loos, P.-F.; Caffarel, M. *J. Chem. Phys.* **2017**, *147*, 034101.

